The Electrochemistry of Electrochemical Machining

by

Paul Howarth

Ph.D Thesis

The University of Edinburgh

2003

Abstract

Electrochemical machining is a process that has the potential to machine complex shapes at high production rates. However, the expansion of ECM in industry has been impeded by the iterative trial and error approach that is often required to generate process parameters for any one machining set-up. This arises due to the incompleteness of models used to describe the complex physical, chemical and hydrodynamic parameter interdependencies. Such interdependence results in non-ideal effects that distort the transfer geometry between the tool shape and the required workpiece shape. The aim of this thesis is to address some of these problems, working towards developing a predictive stoichiometric model for the chemical interdependencies of ECM that can be applied to advanced alloys and therefore further the use of ECM in industry. This has been achieved by extending the planar tool system to a segmented tool arrangement capable of measuring the chemical parameters (dissolution valencies, n, and overpotentials, V_0) along the flow path length. In addition, electrolyte sampling tubes have also been incorporated into this arrangement enabling the electrolyte to be sampled along the flow path length to determine the conductivity, κ and the pH. This system has been applied to the stainless steel group of alloys. A systematic study of a variety of stainless steels [SS316, SS410, Jethete (J), Duplex (D) and Super Duplex (SD)] has been performed, measuring their electrochemical machining (ECM) characteristics in chloride and nitrate electrolytes. Theoretical current-time analysis using the segmented tool was used to determine the dissolution valency, n, and overpotential, V_0, along the flow path length. Electrolyte samples from the interelectrode gap, taken at intervals along the flow path, and the bulk were analysed for conductivity, pH and the soluble products characterised by visible absorption spectroscopy. The insoluble products were analysed by X-ray diffraction (XRD) and X-ray photoelectron spectroscopy (XPS). The results indicate that the ECM dissolution characteristics of stainless steels are controlled by the surface oxide structure, which is primarily determined by the chromium content of the steel. An interesting "runaway current" phenomena was observed when machining J with nitrate electrolyte where dissolution valencies of $n = 9$ were observed. This phenomenon was also observed when machining pure iron. The effect was found to be caused by a short circuit reaction occurring in the interelectrode gap resulting in inefficient ECM. This short circuit problem was stopped either by using a chloride/nitrate mixed electrolyte or by the addition of a complexing agent such as EDTA. Therefore, an understanding of the dissolution chemistry has proved vital to the successful application of ECM to industrially important modern alloys.

Acknowledgements

I would like to thank the people who have helped me complete the work in this thesis. In particular, thanks go to Andy Mount (my supervisor in the chemistry department) for all his help during the course of my work and for his valuable comments on many drafts of this thesis. Dave Clifton (my supervisor in the mechanical engineering department) for his advice and help carrying out the actual experiments in this work. Also, I would like to thank Dave for allowing me to use some of his Figures and diagrams in this thesis. Derek Jardine was especially helpful as the technician on the project and contributed many ideas and suggestions to this work as well as designing and constructing equipment. James McClennan (postgraduate student) for helping me carry out some of the experiments in this work. Andrew Harrison and his research group (particularly Graeme Robb) for all their help with the XRD work and Ronnie Brown for helping me carry out the XPS work. Finally, I would like to thank my family for feeding and housing me while I spent many hours in my room typing away.

Symbols

A	area of each electrode (segment or total)
f	tool feed rate
t	time
z	gap between the electrodes (perpendicular to the planar electrode surfaces)
z_∞	gap between the electrodes (perpendicular to the planar electrode surfaces) at equilibrium
I	total current
J	current density
κ	electrolyte conductivity
ρ	density of the workpiece material
V	applied voltage
V_0	proportion of voltage required to drive electrochemical reactions at the electrodes (the effective overpotential)
y	thickness of the workpiece (perpendicular to the workpiece surface)
dy/dt	erosion rate
n	average valency of dissolving workpiece
n_i	valency of constituent workpiece element i
x_i	mole fraction of constituent workpiece element i
F	the Faraday
M	average molecular mass of the workpiece
E	potential
m	mass of workpiece surface dissolved by charge Q
U	electrolyte flow rate
I_0	the exchange current for the electrochemical reaction

Subscripts

∞	value as time approaches infinity
i	initial value
t	value at time designated as initial time for fitting purposes
0	value at time zero
f	final value
n	segment number

Contents

Chapter 1

Introduction to machining

1.1 Introduction

This Section introduces modern alloys currently used in the manufacture of hi-tech components such as those used in the aerospace, medical and automotive industries. These materials are very hard and difficult to machine by conventional machining methods and therefore alternative machining processes are required. These processes include chemical machining, specifically electrochemical machining (ECM) and thermal methods, the most important of which is electrode discharge machining (EDM). Currently EDM is the machining process of choice for most manufacturers. However, EDM has limitations and drawbacks and often ECM proves to be more appropriate. As a result ECM has certain niche markets and possible widespread applications throughout the manufacturing industry where other machining processes are not adequate. However, ECM also has its problems. The aim of this thesis is to address some of these problems, working towards developing a predictive stoichiometric model for the chemical interdependencies of ECM that can be applied to advanced alloys and therefore further the use of ECM in industry. The chemical parameters of the ECM process are measured and the dissolution products characterised by Visible Spectroscopy, X-Ray diffraction (XRD) and X-Ray Photoelectron Spectroscopy (XPS) thereby relating the characteristic dissolution parameters of ECM to the dissolution chemistry.

1.2 Modern alloys

The nature of ECM allows it be used for applications where no other machining process is applicable. This is particularly the case in the aerospace industry where new harder and stronger materials are being developed which cannot be machined efficiently with conventional machining methods. The recent introduction of titanium aluminide intermetallics is an example of one of these materials [1]. These alloys offer low density, high stiffness (not bending or changing shape easily), good creep resistance (resistance to the permanent deformation that can occur under stress) and high strength (high resistance to breakage or damage) at a range of temperatures [2, 3], as well as good oxidation and corrosion resistance [4]. These characteristics make titanium aluminide a potentially important material allowing significant weight savings and efficiency gains in high performance components operating at high temperatures. Work has been carried out to examine the properties of machining this alloy using single point cutting [5], grinding [6]

and high speed machining [7]. However, these mechanical techniques are often limited in terms of surface integrity [5], with the formation of a surface layer [6]. This layer consists of a thick oxide layer on the metal surface which is so thick that it can prevent metal machining altogether.

Work has also been carried out to characterise the machineability of this alloy using EDM [8]. EDM was found to produce micro cracking due to thermal recasting and a white layer was found on the machined surface. This very hard recast layer is formed due to the high temperatures involved in EDM, as the sparking process of EDM heats the surface (see Section 1.5). If high currents are used, minute cracks can appear leading to premature fatigue failure. The application of ECM to this material could therefore potentially offer improved characteristics over EDM and other mechanical machining techniques. Additionally a preliminary study carried out as an adjunct to this work on the machineability of gamma titanium aluminide found that ECM gave a favourable surface finish with no residual surface layer with high metal removal rates using a sodium chloride (12 % w/v) and potassium fluoride (1 % w/v) mixed electrolyte [9, 10].

The rapid development over the past 30 years or so of advanced technological industries such as aerospace and nuclear, has been accompanied by an increasing use of these very hard, difficult to machine alloys. Additionally, the use of these materials and the techniques used in these technologically advanced industries are spreading to other industries (automotive and medical) with the result that conventional machining methods are no longer adequate. The metals used for the tools to cut these high strength alloys are often only comparable in strength and hardness to the workpieces themselves; therefore machining is difficult if not impossible. Ultimately, if progress on these advanced materials continues then research and progress into developing suitable machining methods must also be made. The most promising machining method to date is ECM, although its potential has not yet been fully realised.

1.3 Limitations of Conventional Machining

Most power driven machining tools have been developed over the past 200 years [11]. It was only after around 1800 that a recognisable technology of machine tools emerged, which steadily increased in sophistication. Conventional machining of a material involves using a

hardened and tempered (through heating and cooling cycles to get the desired hardness and elasticity) to cut an annealed workpiece, which can also be hardened and tempered after machining.

The principle of conventional machining is that a sharp tool of hard material is moved through a softer material, removing part of this material (Figure 1.1). The harder and sharper the cutting tool then the smaller the force required to cut the workpiece, but other factors are also important. The tool point must be strong enough to withstand the forces to which it is subjected and the tool material must be strong enough to resist abrasion from the machining process. In addition, the work done in machining the workpiece causes the temperature of the tool point and the workpiece to increase. This increased temperature also increases the deformation and wear of the tool. This is due to the relationship between the hardness/strength of a material decreasing with increased temperature [12]. There are two possible mechanisms in which tool wear occurs and both of these can be important:

1. Physical wear, where bits of the tool break off due to the forces involved.
2. Chemical wear, where atoms from the tool diffuse into the chip at high temperature.

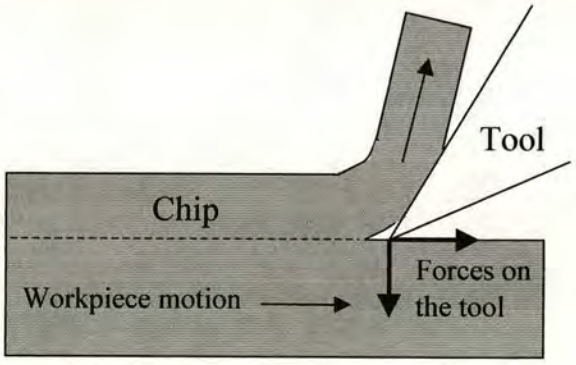

Figure 1.1: Principle of conventional metal cutting (machining). A workpiece is moved against a sharpened tool and part of it is cut away as a chip.

A requirement of the tool for conventional machining is that it is harder then the workpiece. The materials currently used as conventional cutting tools are high-speed steels (HSS), tungsten carbides and ceramic materials. Currently, very hard workpieces can only be cut by grinding, using ceramic grit (alumina, diamond or silicon carbide). Therefore, there is a demand for hard tools – an example is tungsten carbide with a small addition of cobalt. The

cobalt increases tool hardness (makes it more resistant to bending, breaking or piercing) but also increases brittleness (making it liable to break or shatter easily). A major drawback with ceramic tools and the reason for their limited use is their inherent brittleness; therefore, they are unable to cope with the stresses of cutting a workpiece. However, even the newest HSS tools, stellite tools (cobalt based alloys) and hard metal tipped tools (tungsten, tantalum and niobium carbides), have problems with equally hard workpiece materials and the process of machining these hard workpieces is therefore slow and uneconomic [12].

It is relatively easy to cut soft materials (aluminium, wood etc) at very high cutting speeds (15,000 cm min^{-1}). However, as the hardness of the material increases then the economic cutting speed falls. The economic cutting speed can be defined as a balance between the machining rate and the cost of replacing a worn or damaged cutting tool. Therefore very hard materials can only be cut, if at all, with a low machining rate and with a high turnover of cutting tools. This is because the lower the cutting speed, then the lower the temperature of the tool and the harder it will remain, as generally the hardness decreases with increasing temperature. This results in a great difficulty in cutting at economic speeds very hard and strong materials such as titanium alloys, nickel alloys and stainless steels and other similar "difficult to machine" alloys.

Therefore, it is apparent that a new approach to metalworking is required to deal with the problems encountered with new "difficult to machine" alloys. Ideally a method for cutting these materials is required that is unaffected by the hardness of the workpiece.

1.4 New Machining Methods

There are two main areas in which attempts have been made to overcome the problem of machining very hard materials. These are thermal methods and chemical methods of machining, both characterised by the fact that they can machine regardless of the hardness of the workpiece.

1.4.1. Chemical methods

These methods include etching techniques and electrolytic methods such as electrochemical machining (ECM). Chemical machining involves successfully removing each metal atom

from a workpiece by chemical or electrochemical dissolution. Etching [12] can be used to remove metal to reduce the weight of some aerospace components but due to its very nature it is not really suitable as a general purpose machining process as the machining rates are prohibitively slow and machining tends to be indiscriminate, leading to poor shape control. However, the principle of etching can be extended to include electrochemical oxidation, giving ECM. The machining rates achieved for ECM are often around 16 cm^3 min^{-1} [12] and are independent of the hardness of the workpiece or any other physical property of the workpiece as long as the material is a conductor. As well as high machining rates, a good surface finish is usually obtained simultaneously. No tool wear is involved, no residual stresses associated with the process occur, no thermal damage to the workpiece occurs (the maximum possible temperature is around 100 ^0C as the boiling point of the electrolyte will change with the pressure inside the ECM cell) and no burring is observed. Therefore, the process is potentially very attractive as a general purpose machining process.

1.4.2 Thermal Methods

These methods rely on concentrating energy onto a small area of the workpiece to induce the workpiece material to melt or vaporise. The energy may be supplied as heat (flame [13] or plasma [12]), light (ruby lasers [12]) or by electron bombardment (electron beam [14] or electrode discharge machining (EDM) [15]). Machining can be achieved by pulsing the energy source and concentrating the energy on a given area of the workpiece. However, machining using heat can only be used for rough machining and is not suitable for accurate work. Light and electron beam machining methods are capable of very fine cuts but even with greater laser power, it is still uncertain if they can form the basis of an economic general purpose machining process. This is because typical machining rates are very small, typically around 0.008 cm^3 min^{-1} [16]. The only thermal method capable of higher machining rates (5 cm^3 min^{-1} [16]) is EDM which was developed in the 1940's in Russia [17]. The general technique of EDM has progressed steadily since the 1940's and has industrial applications in cavity sinking and for cutting hard materials that were previously very difficult to machine conventionally, as long as the workpiece materials are electrically conducting. The main problem with EDM is that the rate at which metal can be removed and still leave a good surface finish (smooth and aesthetically pleasing) is very limited. It also often results in surface damage making it unsuitable for some applications where components are required to have high structural integrity such as turbine blades. Therefore,

none of the thermal methods offers a complete solution to the problem of machining very hard materials efficiently.

From the above description of thermal and chemical machining methods, the two most promising processes, as modern machining alternatives for conductors are EDM and ECM. Therefore, a more detailed look at EDM would be useful to compare the process with ECM.

1.5 Introduction to Electrode Discharge Machining

Electrode discharge machining (EDM) is much more widely used industrially than ECM. ECM and EDM processes are similar in that they both have the ability to produce complex shapes, with multiple features, using single tooling configurations operating along a single axis. EDM erodes material due to electrical arc discharges between the tool and workpiece. A potential difference is applied between the workpiece and tool with the workpiece being immersed in a dielectric (electrically non-conducting) fluid, which also acts to flush away debris.

The material removal rate and surface finish are all dependent upon the applied voltage, current, discharge rate (number of discharges per second), and melting point of the workpiece [16]. Therefore, it follows that the material removal rate, which can be up to 5 $cm^3\ min^{-1}$, increases as the current increases or the workpiece melting point decreases. A higher discharge rate gives a smoother surface finish. The cutting pattern is Computer Numerically Controlled (CNC) with servo motors positioning the workpiece as the electrode tool discharges (Figure 1.2 and 1.3).

There are two types of EDM for cutting holes, wire and sinker (Figure 1.4). Wire EDM is used primarily for shapes cut out of a flat sheet or plate of metal. The tool is fed through the metal sheet and then moved to give a hole of the desired shape. Sinker EDM is generally used for very small pieces where conventional milling is not practical or very difficult due to the hardness of the material such as in die cast tooling. The tool is fed into a solid workpiece to give the desired size and shape cavity.

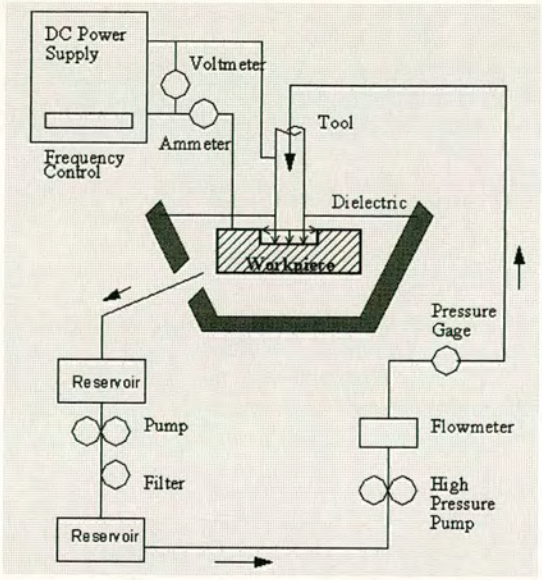

Figure 1.2: Schematic showing all the components necessary for an EDM machine.

Figure 1.3: A CNC Wire EDM Machine

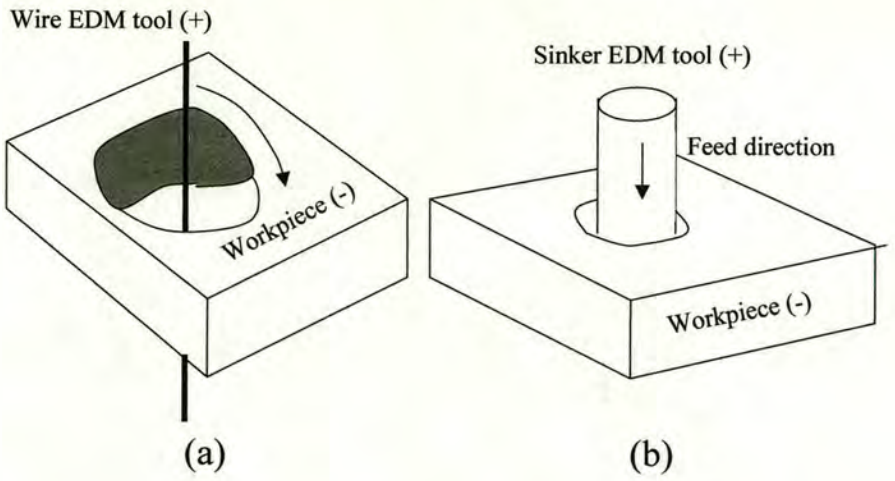

Figure 1.4: Illustration of wire (a) and sinker (b) EDM.

1.5.1 Theory of EDM

Any conductive material can be machined by EDM. The workpiece is biased as the cathode and the tool the anode (opposite to ECM where the workpiece is the anode and the tool the cathode) and a small gap is maintained between the two electrodes. An insulating dielectric fluid is flooded between the two electrodes to provide a controlled amount of electrical resistance in the gap [18].

A pulse of DC voltage is applied between the tool and workpiece and an intense electric field is created at the point where the two electrodes are closest. Because of this field, naturally occurring charged and dipolar microscopic contaminants suspended in the dielectric fluid begin to migrate and concentrate at the strongest point in this field. Therefore, a high conductivity bridge is formed across the gap from these contaminants and particles.

When the pulse is applied the two electrodes charge up like a capacitor. This produces an increase in voltage at the beginning of the pulse and a corresponding sharp increase in current as the charges migrate within the electrodes. This timescale is controlled by the charging time, CR (where C is the capacitance of the electrodes and R is the resistance of the solution) and is in the order of microseconds to milliseconds. Therefore, the power ($P = I \times V$) increases sharply with the increase in current and voltage. Power is energy delivered per second and so this leads to a rise in temperature. Any charged dipolar contaminants would collect in the applied field and only change orientation rather than migrating in the field. In

the field between the electrodes, these contaminants would ionise (promoted by the high temperature) and so discharge occurs resulting in the formation of a spark channel between the two surfaces. The resulting burst in energy results in an increasing temperature and pressure in the spark channel. A small amount of material from the surfaces of both the electrode and the workpiece at the point of spark contact melt and vaporise due to the extremely high temperature of the spark. A bubble then rapidly expands outward from the spark channel fed by the gaseous by-products from the electrode vaporisation. When the electrical pulse is terminated, the spark and heating action are stopped instantly. This causes both the spark channel and, consequently, the vapour bubble to collapse. The violent inrush of relatively cool dielectric fluid results in an explosive expulsion of molten metal from both the electrode and workpiece surfaces, resulting in the formation of a small crater in both surfaces. Small, rapidly solidified balls of material and gas bubbles represent the residue from the cycle. The dielectric fluid acts to remove these by-products from the gap (Figure 1.5).

The entire sequence is very rapid taking anywhere from microseconds to milliseconds. This sequence is repeated from thousands to hundreds of thousands of times each second randomly eroding the workpiece and tool surface, which statistically over many discharges results in uniform erosion of material from both the tool and workpiece. However, tool erosion can be minimised by using a harder and more thermally stable material than the workpiece.

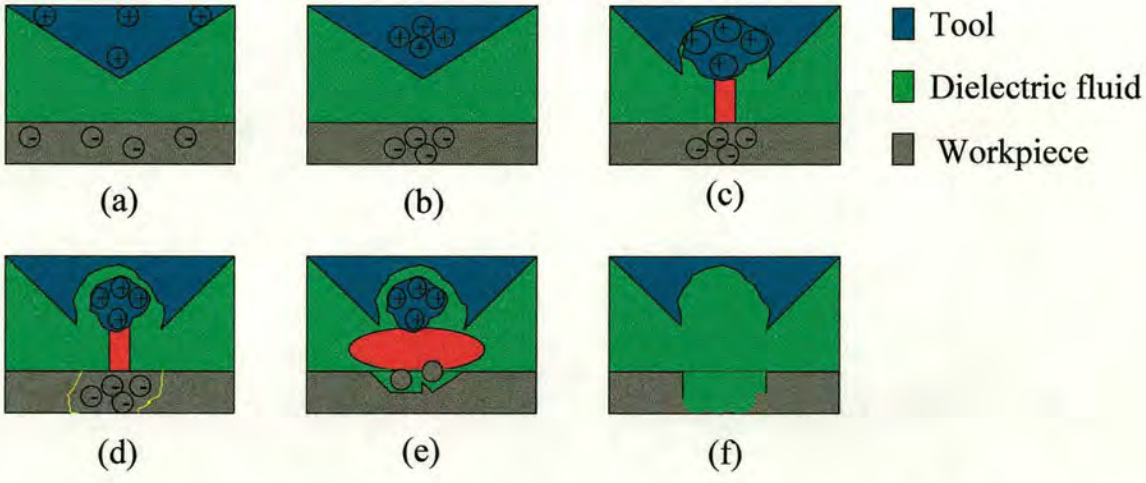

Figure 1.5: Typical series of steps for EDM. a) The energised electrodes approach one another. b) Concentration of the electrical field. c) Creation of an ionised channel between the electrode and workpiece. d) Breakdown of the spark. The workpiece material melts

locally and disintegrates. e) The current is cut off, causing implosion of the spark. f) Evacuation of the metallic particles by flushing with dielectric.

1.6 Electrochemical Machining

Electrochemical machining (ECM) is the process of metal removal by the electrochemical dissolution of a workpiece material. It has many potential advantages over traditional machining methods where high strength, low weight, metallic and intermetallic alloys are used. It can machine a material irrespective of hardness without causing any undue stresses or surface damage [19]. High machining rates and complex shapes are also possible [20, 21, 22, 23, 24]. ECM is carried out by passing a current of the order of 100 A cm^{-2} between an anode and cathode. The workpiece (anode) is machined by the tool (cathode) through a flowing electrolyte. The workpiece is then fed towards the tool at a controlled rate in order to maintain metal removal (Figure 1.6).

The utilisation of ECM in industry has been impeded by the iterative trial and error approach to tool design currently used. Tool shapes are difficult to predict for long electrolyte flow paths or slow electrolyte flow rates and the effects of product accumulation and reactant depletion are not easy to account for. This is due to a lack of understanding of the physical, chemical and hydrodynamic parameter interdependencies. The main hydrodynamic parameter is the Reynolds number, which describes the degree of turbulence in a liquid and is typically very high for ECM at around 10,000. Such an iterative process for tool design is therefore prohibitively expensive resulting in ECM being used for only specialist applications in the aerospace, automotive and medical industries.

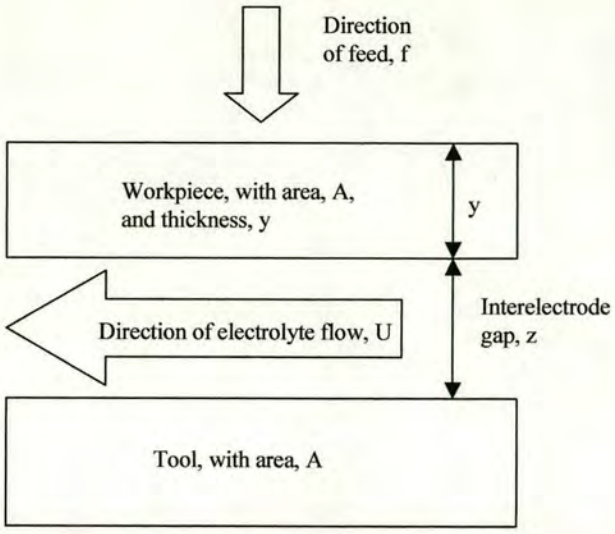

Figure 1.6: The planar ECM system with a single axis feed system and a uniform electrolyte flow path, which is the simplest ECM set up.

1.7 A History of ECM

The Russian, W.Gusseff first proposed an ECM process in 1929 and filed for a patent for an electrochemical metal removal process very similar to modern ECM [25]. Burgess [12] demonstrated the potential of ECM in 1941 and drew attention to the differences between violent mechanical metal removal and steady, non-deforming electrolytic metal removal. However, despite these positive first impressions it was more than 10 years before the process could be sufficiently controlled for use in industry.

It was not until 1954 that the Battelle Memorial Institute in the United States, sponsored by the Cleveland Twist Drill Company, developed an electrochemical method for sharpening carbide tipped drills [26]. The Battelle Memorial Institute then went on to develop a new method based on electrochemical metal removal for the successful machining of curved surfaces of complex gas turbine blades. These early experiments resulted in the production of the first specialised blade machining equipment, which stimulated vigorous and widespread interest. One of these machines was imported into England where Rolls Royce plc made improvements to the machine and became the first British company to use the new technique for the mass production of gas turbine blades [27, 28]. This sparked interest in the United Kingdom and an impetus was given to the further improvement of blade shaping

machines. Meanwhile, other machine tool manufacturers in the USA were also developing electrochemical machine tools at this time as well as British and European manufacturers. However, it was the American company, Anocut Engineering, who were the first to build and market ECM machines designed for a wide range of applications and became the leading supplier of such equipment. At this time the market for this equipment was limited to specialist applications and it was not long before the British company, TI Healy Ltd, started to produce its own range of ECM machines and AEG Elotherm, in Europe, started to produce purpose built modular machines providing a maximum current of up to 400,000 Amps. Additionally, Electrochemical Machining Services Ltd (a spin-off company from TI Healy Ltd), began offering sub-contractor machining facilities in ECM.

Today, Electrochemical Machining Services Ltd and AmTech plc (now owned by the Doncasters Group) are the only two significant companies in the UK that offer ECM sub-contractor facilities. Anocut Engineering plc, in the USA, are still the market leaders in the manufacture of ECM systems and the predominant usage of ECM is still found in the aerospace industry although there are other applications which will be discussed in Section 1.10.

1.8 Comparison of ECM and EDM

Both ECM and EDM are capable of machining materials irrespective of their physical properties but ECM has advantages over EDM. The most significant of these is that ECM has higher machining rates than EDM. These can be as great as 5 to 10 times more than EDM. ECM is also capable of much better surface finishes without leaving the surface damage observed with EDM. This is because ECM avoids the high temperatures involved with EDM, which can produce a very hard surface layer. This surface layer can then crack leading to premature failure of the component. Additionally, there is no tool wear with ECM. Due to the nature of EDM both the tool and workpiece are eroded simultaneously, resulting in new tools being required, which increases long term costs.

In conclusion, ECM is capable of being used as a general purpose, high yield method of producing components, with a potential for a high degree of accuracy and surface finish. However, despite this, currently EDM is the dominant of these two machining processes currently used in industry. The main reason for this is the cheaper initial set-up costs which

are as little as half that of an ECM set-up [12]. To date there have been isolated cases where ECM has been used as opposed to EDM. Two specific cases have been detailed by Goyer [29] in a review of the ECM process.

The first of these is the study of an automotive company who produced hardened steel dies to produce parts for a gearbox assembly. This die had previously been manufactured using an EDM sinking operation. The production time for the die was around 150 hours. This time included hand finishing which was required to remove the EDM recast layer. In heat treatable material, this layer is very hard. After assessing the possibilities of using the ECM process, the company purchased an off-the-shelf ECM system. The operation was then carried out in 35 hours by a sequence in which the approximate die block shape was produced by ECM, followed by a short EDM operation to achieve the final tolerance, and finally finished by ECM to remove the recast layer. Goyer makes the point that switching to ECM for the main machining phase also saved on tooling costs since ECM tools do not wear out. It has already been noted that both the EDM tool and workpiece are eroded (see Section 1.5).

The second example concerned the machining of a sequence of curved sockets into the outer circumference of a stainless steel shroud ring. EDM had originally been considered to machine these pockets. However, in production trials, the estimated cost of the operation was too high (around $270 dollars per ring) and the surface finish obtained, which was in the region of 4.5 μm peak to peak , was considered unacceptably high. By using ECM to cut the slots, the cost of producing the ring was cut by 58 % to $114 per ring and the surface finish was considerably improved to around 0.8 μm peak to peak. Therefore, there can be significant advantages to using ECM, as both machining rates and surface finish can be considerably improved over other machining methods.

Therefore, in conclusion the most promising machining method for new hi-tech alloys is ECM. This is due primarily to the high machining rates obtained as well as the improved surface finish over EDM. However, ECM has its disadvantages and these will now be discussed along with its advantages over other machining processes.

1.9 Advantages and Disadvantages of the ECM process

1.9.1 Advantages

The advantages of ECM over conventional machining methods are [20 - 24]:

1. High metal removal rates

   ECM has removal rates of 10 to 20 cm^2 min^{-1} for large area die sinking operations, which is typically 5 to 10 times greater than rates achieved by EDM and significantly greater than thermal methods such as laser machining (removal rate of 0.008 cm^3 min^{-1}) [16].

2. Complex shapes

   In applications where the required geometry becomes complex and the material being machined is hard, then conventional processes have reduced rates of machining. ECM will often have economic advantages in terms of overall production rates in these cases.

3. High machining rates for hard materials

   As the hardness of the material increases then the overall cost of machining, by conventional means, increases. For very hard materials such as titanium and nickel based alloys, conventional machining is very difficult due to low metal removal rates and high tool wear. ECM can machine materials irrespective of their physical properties and therefore high machining rates can be achieved regardless of the material hardness.

1.9.2 Disadvantages

The early success of ECM in finish machining was both good in that good results came quickly in often difficult and expensive operations and bad in that this early success obscured the many problems associated with the general adoption of ECM as a machining process [30]. If die sinking (producing a hole or recess by sinking a tool into a workpiece) rather than finish machining (machining to the final component tolerance) had been chosen as an initial application then all the current problems associated with ECM would have been

encountered and some progress would have been made to solve them. Finish machining of an aerofoil profile enables tooling configurations to be designed with relatively simple single axis feed paths and uniform electrolyte flow paths whereas applying ECM as a general machining process was found to be more problematic. This is due to the complexities of ECM such as flow geometry, tool design and obtaining the chemical process parameters.

The main problems with employing ECM as an industrial process will now be discussed (although it could be argued that these have been exacerbated by ignorance of the industrial applicability of the technique [31]). These can be considered to be:

1. Expensive set-up costs

   ECM has expensive initial set up costs particularly when compared to EDM. Most ECM machines used today are purpose built and therefore exact costs are difficult to obtain. However, a review was carried out by Kellock [32] in 1982. The actual costs then are less relevant today but the relative costs of ECM and EDM are probably still applicable today. An ECM machine was shown to cost typically twice as much as an EDM machine. However, it is worth noting than an ECM machine is capable of 5 to 10 times the metal removal rate of an EDM machine so in the long term an ECM machine may be better value for money [16].

2. Environmental aspects of ECM

   Hydrogen is the main gaseous product produced from the electrolytic process and therefore needs to be removed from the machining area due to the explosion hazard posed [33]. In addition, there may be concern that certain metals and electrolyte combinations could produce toxic gaseous products (such as chlorine when using a chloride electrolyte). The solid machining products currently assumed to be metal oxides/hydroxides also need to be disposed of [34]. This can be of particular environmental concern if the composition of these products is not known. In addition, currently the soluble products in the electrolyte are often just dumped down the drainage system with no treatment or filtering. These soluble products have been shown in this work to include the chromate ion (Cr(VI)) (see Section 5.4.1). The chromate ion is being phased out of general use by the European Union's End-of-Life vehicle legislation, which intends to reduce the number of heavy metals (including chromium) dumped in landfill sites. This is a long term project aiming to reduce the levels of heavy metals used in products by 85 % by 1st January 2006 [35].

Therefore, dumping Cr(VI) down the drain will no longer be possible without treatment. Identifying the nature of ECM dissolution products (both soluble and insoluble) is therefore extremely important to quantify the viability of the ECM process and this is an aim of the work in this thesis, as an understanding of the nature of these products will go towards quantifying the environmental effects associated with them.

3. Poor Accuracy

ECM is not renowned for being a particularly accurate process. The limitations in practice are due to compromises on machine construction and in process control. Goyer [29] gives the tolerances obtained for the machining of blades for a steam turbine drum as ± 0.05 mm. Typical and achievable tolerances for a range of machining methods are quoted in DeBarr [16]; ± 0.05 mm for ECM, ± 0.003 mm for turning and grinding and ± 0.01 mm for EDM and ruby laser machining. However, the tolerance for ECM can be improved with greater machine rigidity, closer control of machining parameters and appropriate electrolyte selection [16]. This has recently been demonstrated by work carried out at Edinburgh University involving the ECM finishing of tensile test specimens made of titanium aluminide where production run tolerances of ± 0.005 mm were readily achieved [10]. This involved a static tooling system, which in these cases represents a very high rigidity set up. It is therefore possible to achieve very high tolerances.

4. Tool design

Generally, the tool shape is often considered to be the inverse of the required workpiece shape. This would normally be the case in EDM but is not so in ECM. This is partly due the electrolyte flow and conductivity. Predicting the flow characteristics and changes in electrolyte composition and conductivity over long flow paths is currently not possible and therefore unpredictable changes in the interelectrode gap required to maintain machining are observed. Furthermore, for complex workpiece shapes, the electric field distribution between tool and workpiece can become complex. This leads to a complex relationship between tool shape and workpiece shape. Therefore, in this case the exact inverse of the workpiece shape as a tool would not give the desired workpiece shape. This often makes designing a tool shape an iterative trial and error approach, which is a time consuming and costly process, making ECM prohibitively expensive. The current

ineffectiveness of tool design procedures and parameter selection is discussed by Jain [36, 37] and Nilson [38]. A major aim of this work is to move towards an integrated parameterisation and tool design procedure to overcome this problem.

1.10 Current Applications of ECM

The advantages of ECM over conventional machining detailed in Section 1.9.1 make ECM ideally suited to certain applications. These include:

1. Drilling

Electrochemical drilling is particularly useful for producing deep (600 mm), small diameter holes (0.1 mm) in tough or hard components (Figure 1.7). In this case, the high cutting forces associated with conventional machining could break or distort the drill bit whereas in ECM the cutting forces are those associated with the electrolyte supply pressure, which is not usually excessively high [12]. A conventional drill bit would have a very small diameter ~ 0.1 mm and would have to be very short in length to avoid breakage. This type of drill bit is therefore unsuitable for deep holes through hard materials. Electrochemical drilling is used extensively for drilling cooling holes in turbine blades and for other applications in the manufacture of gas turbine engines (see Section 1.10.1) [39, 40]. The tool is usually a metal tube with insulation around the outside edge to prevent shorting. Electrolyte is fed through the inside of the tubular tool to allow efficient electrolyte flow at the machining site, which gives accurate machining. It should be noted that as the hole diameter is generally larger than the tool thickness, a small burr is seen in the workpiece where the electrolyte exits the tool (Figure 1.7).

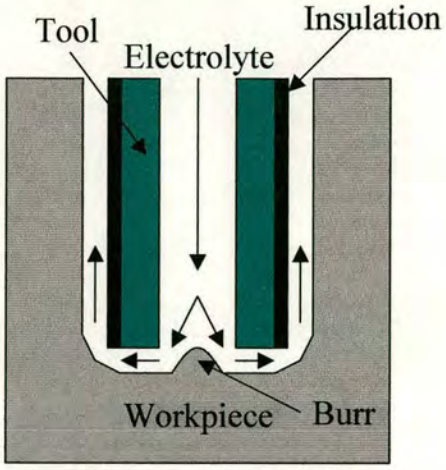

Figure 1.7: Diagram of ECM drilling.

2. Shaping or cavity sinking

ECM is a good cavity sinking and shaping process. Cavity sinking is a term used to define the process of sinking a tool into a solid workpiece to produce a hollow or hole whereas shaping is used to describe the contouring of a workpiece into a given shape. The main application of shaping is the contouring of components, particularly blades, for gas turbine engines in which the smooth, sweeping surfaces of the blades are difficult to produce by conventional machining methods (Figure 1.8) [41].

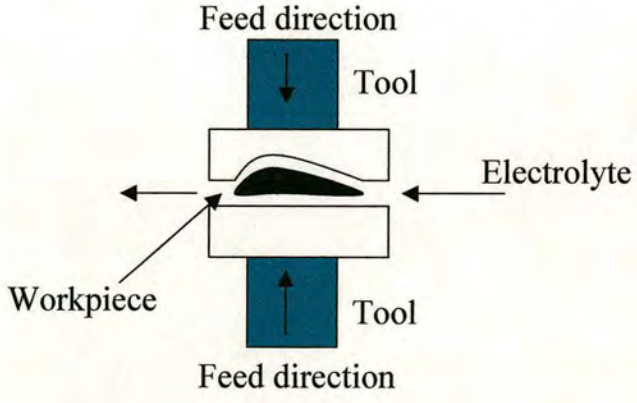

Figure 1.8: ECM shaping of a turbine blade.

3. Cutting and milling

ECM is particularly useful for cutting very hard materials and is able to produce machined surfaces that are stress free and highly polished compared to conventional machining [42]. ECM can produce relatively high quality surfaces in a single pass operation, thereby avoiding milling.

Some of the most important current uses of ECM will now be discussed in more detail.

1.10.1 ECM drilling of holes

The drilling of holes for cooling purposes in turbine blades is another example of where realistic machining alternatives are limited. Only ECM can be used efficiently as it imparts no surface stress to the component [12], thereby preventing the failure of the blade. These holes enable gaseous coolant to be passed through the body of a blade and out through other holes on the leading and trailing edges of the blade to form a protective cooling envelope. Blades with these cooling holes can operate in temperatures that would otherwise cause the blade to melt. Cooling holes for low specification blades can be formed by placing ceramic core inserts into the blade casting. However, in the case of high specification blades, ECM can be used. Tools in the form of fine tubing are used to produce holes to the required specification (length and position of holes) as shown in Figure 1.9.

Figure 1.9 shows an example of these holes machined by ECM through a Pegasus turbine blade. It is very important that the crystalline integrity of the alloy is not affected as this could lead to component failure. Other drilling techniques such as laser drilling and EDM are unacceptable as they disrupt the integrity of the crystal structure (see Section 1.5).

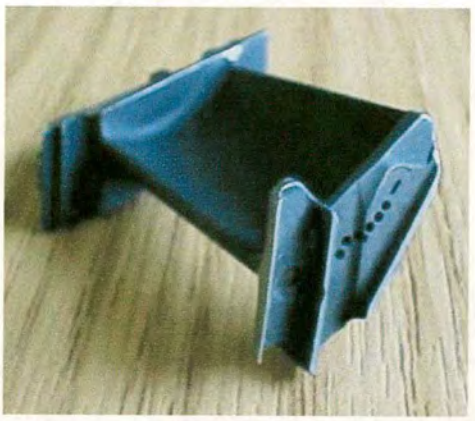

Figure 1.9: Pegasus turbine blade with axial cooling holes produced by ECM.

1.10.2 Weld defect sampling

ECM can be applied in weld defect sampling where conventional methods cannot easily be used. Weld defect sampling is carried out when a defect is found which is then removed to prevent further growth and/or to obtain a sample of the defect for subsequent analysis. Analysis of these weld samples can provide valuable information concerning the structure from which the weld was taken. The residual life of the structure can be estimated or the nature of the defect can be determined. This includes the origin of the defect i.e. was it produced during use or present at the time of manufacture? An alternative to ECM is grinding; however, grinding will destroy the defective section by its very nature, destroying the sample and precluding subsequent analysis. In addition, grinding is impractical in certain locations such as sub-sea. A sub sea ECM weld defect sampling system has been developed at Edinburgh University [31, 43]. A summary of the process is given here.

An integrated sampling tool and non-destructive testing (NDT) system was used. This allowed the weld inspection to be carried out, removal of the defective area and the determination of the nature of the repair required. ECM was applied to enable the removal of the defect area in combination with an Alternating Current Field Measurement (ACFM) system that was used to ensure that the defect had been completely removed. The ACFM system used a uniform input current, arranged to flow in a direction normal to the expected crack direction, and required measurement of two components of the magnetic field, one parallel to the crack (B_x) and one normal to the surface under inspection (B_z). The presence of a surface breaking crack disrupts the uniform current flow, which in turn produces perturbations in both components of the magnetic field measured by the sensors. The B_z field responds to circulation in the current flow, which is in a clockwise direction around one crack end and anticlockwise around the other end. In this way, the B_z signal exhibits a peak and a trough, the separation of which determines the length of the crack.

The ECM sampling tool consisted of a Section of "U" shaped tubing of the form shown in Figure 1.10 (right). The tube was traversed into the workpiece and around and under the weld defect, removing a "scoop" sample containing the weld defect. The electrolyte was supplied into the machining zone in the direction of feed through a groove in the tube. The sampled site and recovered sample are shown in Figure 1.10 (left). The integrated ECM tooling/ACFM system is shown operating in position on a tubular weld section whilst being submerged in a test tank (Figure 1.11).

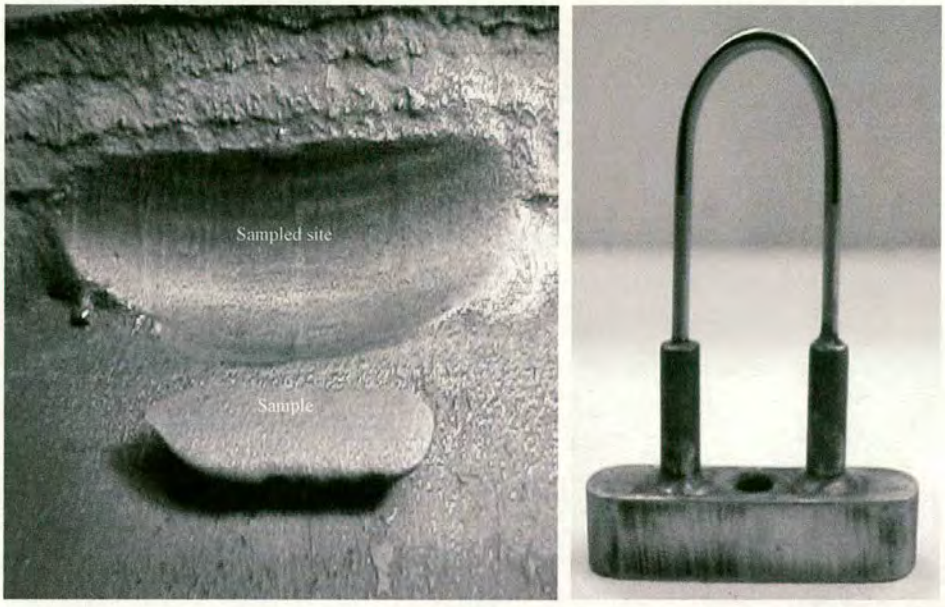

Figure 1.10: Sampled site in welded section and removed sample (left) and "U-shaped" ECM sampling tool (right).

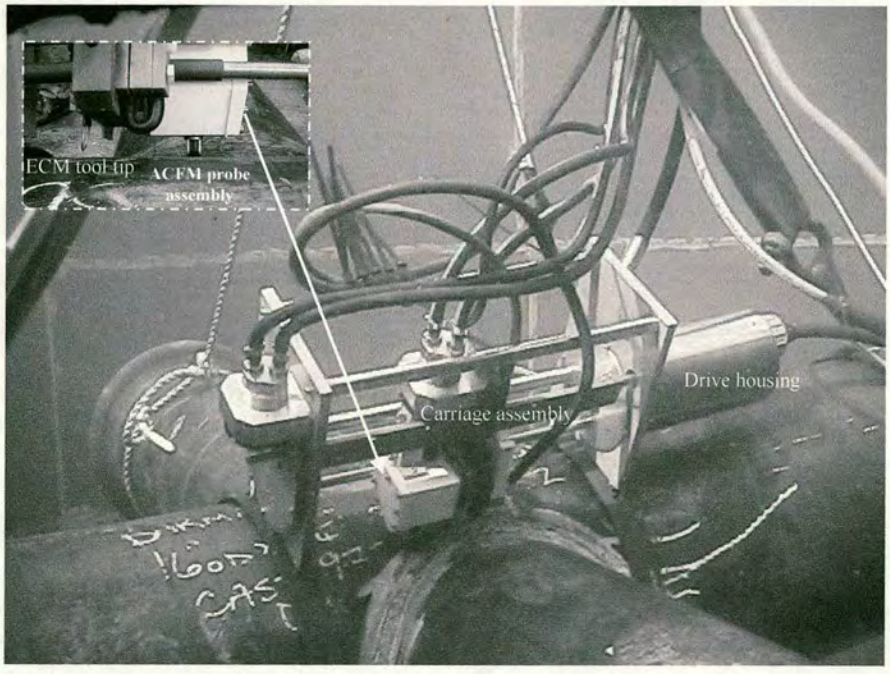

Figure 1.11: ECM/ACFM system during submersed operation in test tank with a close up of the ECM tool (retracted) and ACFM probe (deployed) aligned at the weld

The application of ECM in this case has the advantage that additional stresses will not be conveyed into the machined zone and that the surface at the sampled site after machining will be of high structural integrity. A further advantage is that the ECM system can be applied without the use of bulky mechanisms and can be easily deployed using a Remotely Operated Vehicle (ROV) thereby reducing costs.

1.10.3 Removing a plug and cutting an oil pipe sub sea

This project was "proof of concept" to determine whether a plug could be removed from a pipe and whether the pipe could be cut using ECM [44]. The only problem with this project was that it was to be carried out sub sea on an oil pipe. The aim was to use ECM to machine away the thread of the plug. The plug could not be removed manually as it had been welded in place and no other viable alternative was available. The options were to bring the pipe tree to the surface which was prohibitively expensive, to use explosives which could be dangerous or to try ECM. Two possibilities were apparent when considering the tooling options for carrying out the first part of the project, which was to remove the plug. These options were either direct sinking or indirect sinking, which are illustrated in Figure 1.12.

1.10.3.1 Direct and Indirect sinking

Direct sinking is where the axes of the plug housing threads are used as the line for ECM erosion along the direction of tool feed (Figure 1.12a). Indirect sinking is where a larger diameter tool is sunk outside the axes of the plug housing threads (Figure 1.12b). The tool in this case has a large inner lip so that machining erodes inwards through the header housing towards the thread using a combination of feeding the tool and static machining in order to control the machined area.

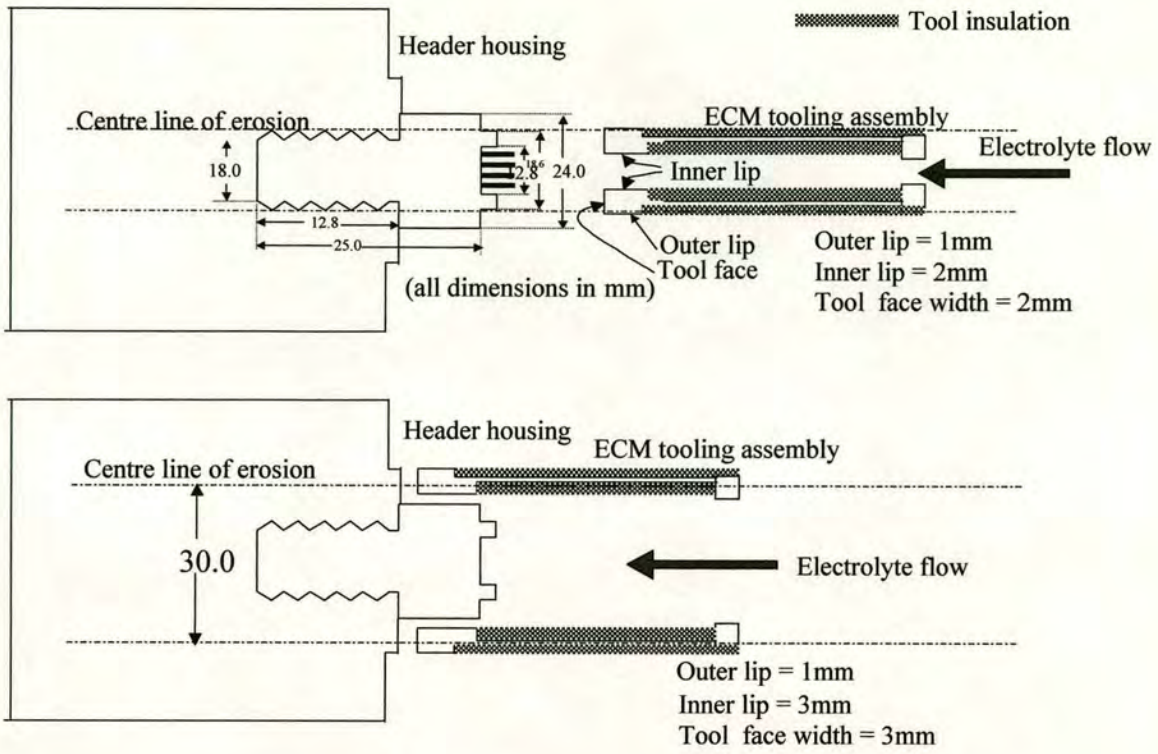

Figure 1.12: a) direct sinking b) indirect sinking of the tool to remove the plug.

The advantage of direct sinking is the greater predictability in knowing when the plug thread had been removed (as the line of erosion is directly through the thread), but the disadvantage is that more machining is required (as machining starts at the top surface of the plug as in Figure 1.12a). Therefore, the total feed distance will be greater than indirect sinking. Indirect sinking has an advantage in terms of reduced overall feed distance (since the tool starts machining at the header housing rather than the top of the plug, Figure 1.12b). However, the disadvantage is that the machining parameters must be controlled to prevent significant machining of the header housing after the threads have been machined. This would result in longer machining times and higher machining currents as excess material from the plug and header housing is needlessly removed. Therefore, the results using the direct and indirect methods for removing the plug are shown in Figure 1.13.

Figure 1.13: Showing header housing mock-up after machining using indirect (on left) and direct (on right) ECM sinking.

When machining in the indirect mode, using the tooling dimensions in Figure 1.12b, then a taper was produced on the plug. This taper is produced because the top end of the thread is being actively machined for longer and the field lines and electrolyte flow are difficult to predict. Because of these interactions, when using indirect sinking, predicting the point at which the thread is completely removed will be dependent upon a complex interaction of tooling and process parameters. Thus although the indirect mode of removal has lower machining times, the direct mode is easier to control and parameterise (in terms of having high confidence of removing all the thread). Therefore, the direct mode of operation appears to be easier to deploy as well as providing greater predictability (in terms of machining times and knowing when the plug is removed) and therefore was the preferred method of removing the plug.

1.10.3.2 Cutting through the outer casing of the pipe

In addition to machining the plug, another task was to machine through the 6 mm thickness of the outer housing of the pipe (see Section 1.10.3) using a static tool carried out by this author in collaboration with Clifton [44]. The ECM tool had been designed to slice around the full 76 mm diameter of the outer casing of the pipe using a segmented cylindrical tooling plate in a single operation. The electrolyte supply and exit channels were symmetrically positioned around the tool plate as can be seen in Figure 1.14.

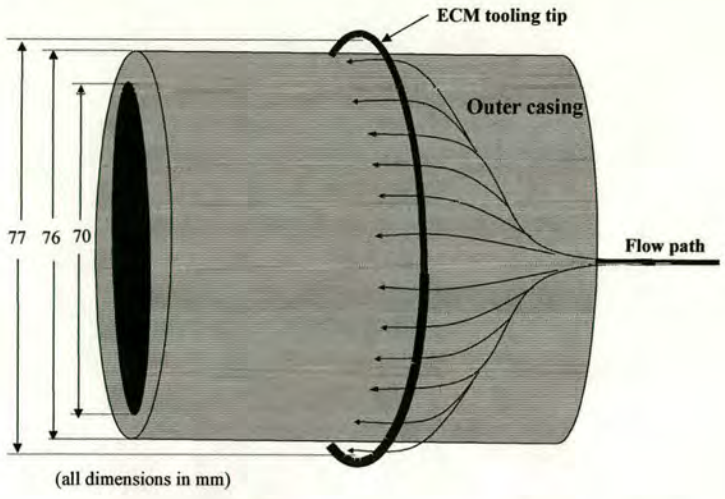

Figure 1.14: Tooling configuration and dimensions for ECM slicing of outer casing

Depending on the concentration of the electrolyte used, then this determined the length of time taken to cut through the pipe but it was possible using equivalent sea water salt concentration (equivalent to 0.51 M NaCl). If machining sub-sea then it is advantageous not to have to take electrolyte down to the required depth so using the surrounding sea water would be preferable. Therefore, it was shown to be possible to cut the pipe in a single pass using sea water as electrolyte.

1.11 The parameterisation of ECM planar dynamics

The current level of parameterisation in ECM will now be discussed. The important parameters in ECM are the electrolyte conductivity, κ, the workpiece overpotential, V_0, and the workpiece dissolving valency, n. An initial assumption in the basic planar ECM model (see Section 2.8.1) is that ideal conditions exist within the interelectrode gap. Ideal conditions can be defined as the electrolyte conductivity, valency and overpotential all being constant across the workpiece surface and insensitive to changes in machining parameters such as voltage, feed rate, electrolyte flow rate and current. If this was the case, then the interelectrode gap along the flow path should be constant. The theoretical model which relates all of these parameters together becomes complicated when ideal conditions break down. Actual ECM does not always have constant parameters and a lack of understanding of the interrelationships between these parameters can lead to inaccuracy in component machining as well as the possibility of damaging the electrodes. Work carried out to examine

each of the ECM parameters will now be examined dealing with each in turn and then current ECM models will be discussed.

1.11.1 Electrolyte conductivity

In the ECM theory (discussed more thoroughly in Section 2.6) the overall current in ECM is governed by migration of ions in the gap where the current, I, is given by

$$\frac{I}{A} = \frac{(V - V_0)\kappa}{z} \tag{1.1}$$

The current, I, is determined by the values of conductivity, κ, the interelectrode gap, z, and the effective voltage $(V - V_0)$ where V_0 is the overpotential (as in Section 1.11.2, see Section 2.6 for a more thorough explanation) Therefore, conductivity, κ, is given by

$$\kappa = \sum_i c_i u_i z_i F \tag{1.2}$$

where for each ion type, i, c is the concentration of the ion, u is the mobility of the ion, z is the charge number and F is Faraday's constant. For a 1:1 salt MX eg NaCl or $NaNO_3$, then $\kappa = cu_+F + cu_-F$ where $z_+ = 1$ and $z_- = 1$.

The ion mobility, u, increases with temperature, and therefore κ increases (viscosity, η, decreases and the hydrodynamic radius slightly decreases). Significant amounts of gas bubbles (H_2 in ECM) could cause voids in the electrolyte, decreasing c (the overall concentration) and hence κ. However, if gas is dissolved which could be the case at the elevated pressures in the gap during ECM, it is neutral and so will not affect the conductivity, κ, as concentration, c, of the ions will remain essentially unchanged (the only effect will be changes in η due to dissolved gas affecting $u_{+/-}$ and hence κ, but this effect will probably be small). Therefore, the temperature of the electrolyte, the gaseous products and the changes in composition of the electrolyte are the only things that could significantly affect the conductivity during ECM.

The basic ECM model (see Section 2.8.1) assumes that the only significant contribution to heating within the gap is Joule heating due to the passage of the electrolysing current through

the electrolyte. Heat generated due to viscous friction and heat lost by conduction through the electrodes is ignored. At the far end of the flow channel, where the conductivity is higher (higher temperature due to Joule heating), the current density will also be greater than at the inlet. This will cause an initial high rate of dissolution, which will cause an opening out of the gap at this point. Steady state conditions are reached after a given time in which the value of current density is constant along the length of the gap.

The basic model neglects the effects of gaseous products within the interelectrode gap, which can reduce the conductivity of the electrolyte. It has been shown [45] that the temperature rise along the gap cannot only be attributed to the effects of Joule heating. It was suggested that in addition to resistive heating, increased resistivity due to the accumulation of hydrogen and localised evolution of steam bubbles occurred. It was suggested that such bubbles, which form due to boiling within very localised turbulent voids, have properties of very high resistivity. Once these begin to form then the additional heating within these areas cause a runaway effect, resulting in increasing gap taper towards the exit end of the flow channel.

Hopenfeld and Cole [46] have examined the hydrodynamic and thermodynamic mechanisms in ECM. In particular, this study has detailed the distribution of electrolyte conductivity, for the case of a planar interelectrode gap, through examining the influence of an accumulation of non-conducting gaseous products along the axis of electrolyte flow. Their work has demonstrated experimentally that at any one point in the gap, for fixed conditions of flow, that the relationship between the current density and applied voltage, for a range of gap sizes typical in ECM (0.4 to 0.8 mm) is linear, and therefore obeys Ohm's Law.

The basic ECM model and the predictions of Hopenfeld and Cole have been extended further in a study by Thorpe and Zerkle [47]. In this investigation, Thorpe and Zerkle, produce a direct analytical solution to describe ECM dynamics. Most significantly, they address the heterogeneous nature of gap dynamics, by allowing for the possibilities that the various layers (gaseous electrolyte, solid dissolution sludge, and pure electrolyte) do not necessarily move through the gap at the same velocity. In their conclusions, Thorpe and Zerkle point out that because of the heterogeneous nature of transfer effects in ECM that it is unlikely that a full analytical description of gap dynamics will be achievable. They point out that their own analytical model could be force fitted to experimental data, to obtain the value of the valency, n, and hence approach modelling ECM dynamics semi-analytically.

The work mentioned above makes certain simplifying assumptions about the linearity and homogeneity of temperature and pressure distribution within the gap. The testing of such assumptions through experimental validation is considered difficult to achieve, due to the small dimensions, and high pressures and temperature gradients involved in ECM. However, a few studies have been directed to provide at least some indications of the variation and complexity of the parameter functions involved. Pramanik [48] has carried out a series of measurements on the pressure distribution in the case of a planar parallel electrode configuration, 100 mm long by 40 mm width. The results exhibit a general trend of an increase in pressure towards the centre of the flow channel and then a decrease towards the exit (as would be expected assuming that the flow exits the gap to atmospheric pressure). A significant feature of their results is the observation that a small sharp pressure drop, to slightly below ambient, occurs a few millimetres into the flow field. This feature was noted over the full range of gaps and flow volumes used in their experiments. There is no detailed explanation or analysis of these results.

Another assumption is that heat losses from the gap through the tool via conduction are ignored. Jain and Murgan point out [49] that the tools used in ECM are usually made from materials with a high thermal conductivity, such as copper and brass. Therefore, the thermal loss through the tool could be significant. Their investigation shows that for tool materials of low thermal conductivity, such as stainless steel, temperature gradients show close correlation to theory developed by neglecting conduction through the electrodes. However, when they compare the same theory for tooling made of a good thermal conductor, such as copper, they observed significant deviation from the theory. Therefore, heat loss through conduction in the tool can be an important factor.

For all these reasons it is difficult to come up with a comprehensive model of conductivity changes for all ECM conditions. Therefore, conductivity changes are minimised in this work by using a high flow rate to give ideal conditions.

1.11.2 Overpotential

Variation of the overpotential, V_0, with the type of electrolyte used in ECM is common. However, overpotential values can also be sensitive to process parameters when using a single electrolyte. For example, Landolt [50] has carried out trials using a copper anode and a 1M sulphuric acid electrolyte. Over a current density range with a maximum of 39 A cm^{-2}, Landolt observed Tafel behaviour (linear dependence between current density and overvoltage). Davydov [51] has reported similar dependencies during dissolution of nickel in nitrate electrolyte. These effects are small, in the region of 0.1 V over an order of magnitude increase in current density, and can often be neglected in ECM applications where voltages of several volts are applied. However, significant variations have been observed when machining some of the stainless steels in this work (see Section 5.5.2).

1.11.3 Current efficiency and valency

There is general confusion in the field of ECM on whether a change in dissolution efficiency and/or a change in valency state is occurring [52]. A change in efficiency will be due to competing electrochemical reactions such as oxygen evolution at the workpiece and/or redox reactions of the dissolution products in the interelectrode gap not resulting in metal dissolution. This increased current, if it is assumed it results from the ECM reaction, can lead to artificially high values of the valency, n. In fact, the observed valency, n_{obs} under these conditions can be thought of as $n_{obs} = n/e$ where n is the true ECM valency and e is the fractional efficiency of the dissolution process. It is worth mentioning that nonsensical valencies can be produced in many cases such as with Jethete, due to the confusion between n and n_{obs} (see Chapter 6 where n = 9 was reported). Also, if the high valency produced was actually due to the ECM reaction then it would be expected that the interelectrode gap would decrease. However, this is not the case as has been found in this work (see Section 6.5). Many authors have reported current efficiency dependencies. Landolt [53] reported that when machining nickel in a 1 M $NaClO_3$ electrolyte, the dissolution efficiency falls rapidly from close to 100 %, at current densities of 30 A cm^{-2} and above, to below 20 % as the current density drops below 10 A cm^{-2}. Dependencies between current efficiency and both flow velocity and current density during the dissolution of iron in sodium nitrate electrolyte have also been reported [54, see Section 6.5]. Current efficiencies of ~ 70 % have been reached for low flow velocities of in the region of 1 m s^{-1}. For higher flow velocities, of up to

10 m s^{-1}, an increase in efficiency towards 100 % as the current density increases has been reported.

Bejar and Gutierrez [55] measured the rate of change of gap to determine the relationship to the current efficiency. Their method involved measuring the value of current density in the case when the cathode is held static and the anode dissolves thereby increasing the gap. They then measure the rate of change of gap, dz/dt, at predefined intervals (using a mechanical probe and presumably by interrupting the process to make each measurement) and relating this measurement to the current occurring at that time. This relationship is based on the application of Faraday's laws (see Section 2.8). The value of dz/dt is computed by fitting a simple exponential relationship to the experimental data. At low current densities (less than 20 A cm^{-2}), their results show current efficiency dependencies with gap size, current density, temperature and flow velocity. At a higher current density of around 30 A cm^{-2}, they report that the efficiency levels off at around 80% (the valency in this case is assumed to be divalent).

Several authors have also reported chemical valency sensitivity to process parameters. For example, it has been reported by Moir and Harvey [56, 57] that a transition from Fe^{3+} Cr^{6+} to Fe^{2+} Cr^{3+} dissolution occurred when machining a stainless steel (316) anode in sodium chloride electrolyte (20% wt/wt). This transition is observed as a change on the anode surface from a smooth, bright area, which is associated with Fe^{3+} Cr^{6+} dissolution, to a pitted grey surface, which is associated with Fe^{2+} Cr^{3+} dissolution. Although Moir and Harvey do not give a detailed reasoning of why this valency change occurs, they do, however, correlate this transition with flow rate and/or current density. Specifically, they report that a boundary, corresponding to the transitions between Fe^{3+} Cr^{6+} to Fe^{2+} Cr^{3+}, moves along the flow path in proportion to the increase in flow volume (over the range 2.5 to 8.0 l min^{-1}).

1.11.4 Modelling parameter interdependencies

Throughout the ECM literature few attempts have been made in the area of modelling parameter interdependencies in ECM. It is suggested that the reason for this is in part due to the complexities of the problem, but also due to the lack of available analysis techniques. There have been two studies which have attempted, at least in part, to address these issues and these will be briefly discussed.

Khairy [58] has developed a system in which a hierarchically structured knowledge based system (KBS) can be applied for optimising process operation in ECM. In this approach, the need for detailed analytical models can be avoided by defining a structure that enables updating of limits over which specified parameter relationships are valid. For example, a particular feature which forms a part of an overall profile (i.e. a step or pocket etc) is given certain attributes which define process relationships for that feature. The system can then provide an assessment as to whether, for example, the flow velocity regime that can realistically be achieved over the complete component profile will successfully provide the required dissolution characteristics for that particular feature. Khairy demonstrates use of the KBS strategy applied to a single machining system (steel in a NaCl electrolyte) and reports success in the generation of appropriate processing parameter set-ups. In order to apply such an approach to a wide range of ECM systems, Khairy suggests that the database would need to be expanded based upon information from other workers and reference works such as the machine data handbook [59]. The problem with this approach is that it would require extensive database input in order to describe the process complexities to the required degree. The work of others and available reference works do not, in general, provide the required level of detail. It is however suggested that the KBS approach could form a useful component in an overall system for ECM representation.

Two studies [60, 61] have addressed the parameter independence complexity problem by use of a response surface methodology (RSM) based approach with specific application to tubular electrodes. In this system parameter interdependence is specified using two empirically derived functions. These functions, based around second order polynomial surfaces, map the primary machining criterion of overcut and metal removal rate to the primary machining parameters of electrolyte conductivity, electrolyte flow rate, machining voltage and gap size. To achieve this representation a series of trials (31 in the example given) are carried out to determine the order and value of the coefficients for the surface functions. It has been demonstrated [61] how these surface functions can be used to correctly predict parameter relationships at values that were outside the range of the coefficients determined during trials. This predictive parametric approach appears to provide a good degree of modelling accuracy, at least for the specified system characterised. The question arises, however, as to whether these methods could be effectively applied to give a general description independent of the system type. Neither of the two studies provide a clear answer to this question.

1.11.5 Conclusions

The models described relating the parameter interdependencies have failed to provide the level of resolution necessary for a complete description of the interelectrode gap characteristics. This is due to the complexities and heterogeneous nature of ECM.

Most of the work on design and process modelling in ECM has not attempted to include modelling of non-ideal phenomena. Such work has provided a useful insight into the general form of tool to workpiece transfer characteristics. Specifically, such work has provided insight into the limitations of ECM (i.e. the range of shapes that can be machined) and also for estimating the removal envelope required for forming specified shapes. Those workers who have attempted to incorporate non-ideal effects into their tool design/process simulation systems have reported a limited degree of success, but only when applying their systems to relativity simple shapes. Approaches that use non-conformal tools are aimed at niche ECM applications and will not therefore expand its general usage.

The work in this thesis uses a developed theoretical model (see Section 2.8.2) to measure and relate the ECM parameters and applies this theory to a family of alloys, specifically stainless steels.

1.12 Active and Passive electrolytes

The electrolytes most commonly used in ECM can be put into two categories. These are *active* electrolytes, which include halogens (specifically chlorides and chlorates), and *passive* electrolytes which include nitrates. The terms used to describe the electrolytes depend on the nature of the electrolyte and the way in which they interact with the ECM machining surface. Chloride electrolytes are known to act chemically in the machining process in that the chloride ions incorporate themselves into the oxide layer of the material being machined (see Section 5.5) and as a result affect the way in which that material dissolves, as observed in the case of stainless steels (see Section 5.2). Chloride is also able to form complexes with dissolving metal ions, thereby stabilising them. However, nitrate electrolytes are not known to have any such effects on the machining of materials as nitrate is regarded as a poor ligand. They are not known to have a significant effect on the oxide layer and thereby affect machining. The two main electrolytes used throughout this thesis are NaCl and $NaNO_3$ and

these will be discussed in more detail in Section 5.2 as the effect each electrolyte has on machining is significantly different. More detail on NaCl, $NaClO_3$ and $NaNO_3$ electrolytes can be found in [62, 63]. Additionally, the two main electrolytes used industrially are NaCl (used by Rolls Royce) and $NaNO_3$ (used by Doncasters) primarily because they are cheap.

1.13 The Development of Stainless Steels

This thesis looks specifically at using ECM to machine stainless steels. Stainless steels were chosen because it had previously been observed [56, 57] that stainless steels show some interesting behaviour when being machined by ECM. This is because they have a surface oxide layer that significantly affects their dissolution characteristics. Therefore, an introduction and background to stainless steels is given here.

1.13.1 The history of stainless steels

The inventor of stainless steel, Harry Brearley, was born in Sheffield, England in 1871. His father was a steel melter, and after a childhood of hardship, he left school at the age of twelve getting a job washing bottles in a chemical laboratory. He became an expert in the analysis of steel and its production through years of private study and night school. Having already established his reputation for solving metallurgical problems, Brearly was given the opportunity in 1908 to set up the Brown Firth Laboratories, which was financed by the two leading Sheffield steel companies of the day. This was a highly innovative idea for its time; research for its own sake on the problems of steel making.

In 1912 Brearly was asked to help in the problems being encountered by a small arms manufacturer, whereby the internal diameter of rifle barrels was eroding away too quickly because of the action of heating and discharge gases. Brearly was therefore looking for a steel with better resistance to erosion, not corrosion. As a line of investigation he decided to experiment with steels containing chromium, as these were known to have a higher melting point than ordinary steels. Chromium steels were already at that time being used for valves in aero engines as chromium steel valves were lighter than their carbon steel counterparts.

Using first the crucible process and then more successfully an electric furnace, a number of different melts of 6 – 15 % chromium with varying carbon contents were made. The first true

stainless steel was created on the 13th August 1913. It contained 0.24 % carbon and 12.8 % chromium. Brearly at this time was still trying to find a more wear resistant steel and in order to examine the grain structure of the steel he needed to etch samples before examining them under the microscope. The etching reagents he used were based on nitric acid and he found that the new steel strongly resisted chemical attack. He then exposed samples to vinegar and other food acids such as lemon juice and found the same result.

At that time table cutlery was silver or nickel plated. Cutting knives were made of carbon steel, which had to be thoroughly washed and dried after use, and even then rust stains would have to be rubbed off using carborundum stones. Brearly immediately saw how this new steel could revolutionise the cutlery industry, then one of the biggest employers in Sheffield but he had great difficulty convincing his more conservative employers. On his own initiative, he had knives made at a local cutler, R F Mosley. Initially, Brearly referred to his invention as rustless steel. However, Ernest Stuart, the cutlery manager of Mosley's referred to the new knives as stainless after he had failed to stain them with vinegar during his experiments. Corrosion resisting steel would be really the better term as ordinary stainless steels do suffer corrosion in the long term in hostile environments.

Other claims have been made for the first invention of stainless steel, based upon published experimental papers that indicated the passive layer corrosion resistance of chromium steels with a 9 % chromium content for engineering purposes. Brearley's contribution was that having concluded by purely empirical means he immediately seized on the practical uses of the new material.

Within a year of Brearley's discovery Krupp in Germany were experimenting by adding nickel to the steel mixture. Brearley's steel could only be supplied in the hardened and tempered condition whilst the Krupp steel was more resistant to acids, was softer and more ductile and therefore easier to work with. There is no doubt that but for Brearley's chance discovery, the metallurgists at Krupp would soon have made the discovery themselves. From these two inventions, just before the First World War, the 400 series of martenistic and 300 series of austenitic stainless steels were developed.

The first world war largely put a halt to the development of stainless steel, but in the early 1920's a wide variety of chromium and nickel combinations were tried including 20/6, 17/7 and 15/11. Brearly then left Brown Firth Laboratories over a dispute regarding the patent

rights to his invention of stainless steel, and joined another Sheffield company, Brown Bayleys. His successor at the Brown Firth Laboratories was Dr W H Hatfield, who is credited with the invention in 1924 of 18/8 stainless steel (18 % Cr, 8 % Ni) that, with various additions, still dominates in the production of stainless steel today. Dr Hatfield also invented 18/8 stainless steel with titanium added, now known as 321.

Most of the standard grades still in use today were invented in the period 1913 to 1935, in Britain, Germany, America and France. Once these standard grades became accepted, the emphasis changed to finding cheaper, mass production methods and popularising the use of stainless steels. This tended to stifle the development of new grades. However, after the Second World War, new grades with a better weight to strength ratio were required for jet aircraft, which led to the development of the hardened grades such as 17:4 PH. From the 1970's onwards the duplex stainless steels began to be developed. These have greater corrosion resistance and strength than the grades developed in the 1920's and show great potential for increasing the use of stainless steel.

1.14 Classification of Stainless Steels

There are four categories of stainless steel. A short description of each is now provided.

Austenitic (304 and 316)

Austenitic grades of stainless steel were developed for use in both mild and harsh, corrosive environments and are chromium-nickel alloys. Austenitic is the name derived from the type of crystal structure from which it is comprised. Stainless 304 (18 % Cr – 8 % Ni) is the most common steel and is used more than any other. Due to their relatively high chromium content, austenitic stainless steels form a passive surface film to provide protection against corrosion. The addition of nickel stabilises the austenitic crystal structure and decreases the tendency of the material to crack due to stress corrosion. Nickel also promotes repassivation in case the protective surface oxide film is damaged. The material is non magnetic.

Ferritic (430)

Ferritic steels (type 430) contain only iron and chromium and have the same crystal structure as iron. The material is magnetic and cannot be hardened. Higher levels of corrosion and oxidation resistance can be achieved by adding more chromium and molybdenum.

Martensitic (403, 414 and 420)

Martensitic steels have low chromium, no nickel and high carbon content. These steels may be heat treated to have favourable characteristics of high strength and toughness as well as reduced corrosion. The material is magnetic.

Duplex stainless steels (D and SD)

Molybdenum, nitrogen and copper are added to the iron-chromium-nickel system with very low carbon content to give Duplex steels. This provides a system with equal ferrite and austenitic phases in the microstructure. This material offers twice the strength of austenitic (300 series) stainless steel and increased corrosion resistance over martensitic stainless steel (400 series).

1.15 Function of Alloying Elements

Various alloying elements are added to stainless steels to improve corrosion performance and/or to modify and improve the mechanical or physical properties of the stainless steel. There are several hundred different stainless steels, all formulated to provide specific properties of corrosion resistance, weldability or mechanical properties. The main elements added are given here with a brief description of their role along with typical amounts of each element found in the steels used in this thesis. The full composition of the steels is given in Table 1.1.

Alloy	Fe	Cr	Ni	Mo	Mn	Cu	C	S	P	Si	N	V	W
J	80.63[b]	12.50[a]	3.00[a]	2.00[a]	0.90[a]	-	0.13[a]	0.02	0.03	0.35	0.04[a]	0.40[a]	-
SS410	85.50	12.75	0.23	0.01	0.72	0.08	0.14	0.02	0.04	0.49	0.02	-	-
SS316	70.09	17.00	8.00	2.50	2.00	-	0.12	0.05	0.05	0.02	-	-	-
D	63.52[b]	23.00[a]	6.50[a]	3.50[a]	2.00[a]	0.20[a]	0.03[a]	0.02[a]	0.03[a]	1.00[a]	0.20[a]	-	-
SD	61.20	25.58	6.98	3.57	0.63	0.60	0.02	-	0.02	0.47	0.26	-	0.65

Table 1.1: Composition in atomic weight percent of the stainless steels jethete (J), SS316, SS410, duplex (D) and super duplex (SD), [a]maximum amount, [b]minimum amount.

Chromium (12.50 – 25.58 %)

Chromium is the element that makes stainless steel stainless. It is essential in forming the passive surface oxide film. Other elements can influence the effectiveness of chromium in forming or maintaining the film, but no other element by itself can create the properties of stainless steel. At about 10.5 % chromium, a weak film is formed and will provide mild atmospheric protection. By increasing the chromium content to 17 – 20 %, which is typical in the type 300 series of austenitic stainless steels, the stability of the passive film is increased. Further increases in the chromium content will provide additional protection (eg ~ 25 % Cr in super duplex). At elevated temperatures, the chromium reacts with the oxygen in the air to form a thick, visible layer. The colour and thickness of the chromium oxide will depend on the temperature and time exposure. The chromium oxide layer is visible and is thick enough to be scraped off as opposed to the relatively thin, transparent, protective passive film seen at low temperatures.

Nickel (0.23 – 8.00 %)

Nickel stabilises the austenitic structure (the grain or crystal structure) of the stainless steel and enhances the mechanical properties (ductility, formability and weldability) and fabrication characteristics. A nickel content of 8 – 10 % and above will decrease the tendency of the material to crack due to stress corrosion. Nickel also promotes repassivation in case the protective surface oxide film is damaged.

Manganese (0.63 – 2.00 %)

Manganese, in association with nickel, performs many of the functions attributed to nickel. It also interacts with the sulphur in stainless steel to form manganese sulphites, which increases the resistance to pitting corrosion. By substituting manganese for nickel and then combining it with nitrogen, strength is also increased.

Molybdenum (0.01 – 3.57 %)

Molybdenum, in combination with chromium, is reported [64, 65] to be very effective in stabilising the passive film in the presence of chlorides. It is effective in preventing crevice or pitting corrosion. Molybdenum, next to chromium, provides the largest increase in corrosion resistance in stainless steel. 316 is the most common Mo stainless steel. However, from work carried out in this thesis (see Section 5.2.2) on comparing J (2.00 % Mo) and SS410 (0.01 % Mo) no such stabilisation effect in the presence of chlorides was observed. Both J and SS410 gave similar current responses.

Carbon (0.02 – 0.14 %)

Carbon is used to increase strength. In the martensitic grade, the addition of carbon facilitates hardening through heat treating.

Nitrogen (0.02 – 0.26 %)

Since around 1970 Nitrogen has been used to stabilise the austenitic structure of stainless steel. This enhances its resistance to pitting corrosion and strengthens the steel. In duplex stainless steels, nitrogen promotes the re-formation of austenite at higher temperatures and helps maintain an acceptable austenite-ferrite phase balance. Using nitrogen makes it possible to increase the molybdenum content up to 6 %, which improves corrosion resistance in chloride environments.

Titanium and niobium

Titanium and niobium are used to reduce the sensitisation of stainless steel. When stainless steel is sensitised, intergranular corrosion can occur. This is caused by the precipitation of

chrome carbides during the cooling phase when parts are welded. This depletes the weld area of chromium. Without chromium the passive film cannot form. Titanium and niobium interact with carbon to form carbides, leaving the chromium in the steel so a passive film can form.

Copper (0.08 – 0.60 %) and aluminium

Copper and aluminium, along with titanium can be added to stainless steel to promote hardening. Hardening is achieved by heating to and maintaining a temperature of 900 ^{0}C to 1150 ^{0}C. These elements form a hard intermetallic microstructure during the heating process at this elevated temperature.

Sulphur (0.02 – 0.05 %)

Sulphur (forms sulphides particularly MnS) is added to stainless steels to aid machining by enhancing the mechanical properties of the steel (ductility, formability and weldability).

1.16 The Oxide Film

As stainless steels are only stainless due to their protective oxide layer then it is worth discussing this layer, as this could greatly affect a steels ECM characteristics. For a wide variety of applications, stainless steel competes with carbon steels supplied with protective coatings as well as other metals such as aluminium, brass and bronze. The success of stainless steel is because it has a unique advantage. The chromium in the stainless steel has a great affinity for oxygen and will form a film of chromium rich oxide on the surface of the steel at a molecular level. The two main contributors to this layer are Chromium and Molybdenum [64] but the effect of Mo on the steels used in this work (see Section 5.5) was not apparent. Surface films on stainless steels are considered to have a duplex character with an inner oxide region rich in chromium and an outer oxide region rich in iron [64, 65, 66, 67]. This duplex character was not observed when performing XPS on the unmachined stainless steel surface in this work (Section 5.4.3). However this could have been due to the way the samples were prepared or other factors discussed in Section 5.4. The preferential dissolution of iron in Fe-Cr alloys causes the formation of a chromium enriched region, the concentration of Cr being maximum close to the metallic substrate [68]. The Cr rich inner

region maintains the passivity of stainless steels [65 - 68, 69]. This layer is described as passive in that it does not react or influence other materials, tenacious in that it clings to the layer of steel and is not transferred elsewhere and self renewing in that if it gets damaged or is forcibly removed then more chromium from the steel will be exposed to the air and form more chromium oxide.

Therefore, looking at the oxide layer on pure chromium may provide insight into the oxide layer on stainless steel. The protective oxide layer on chromium is composed of Cr_2O_3 [70] that acts as a barrier between the metal and the environment. The oxide is a p-type semiconductor and grows by diffusion of cations from the metal to the oxide/solution interface [71]. The active Cr surface is assumed to be covered by a surface hydride where Cr dissolves through this layer in the active state as divalent ions [71]. The surface hydride layer is oxidised to a layer of chromium (III) hydroxide during the active to passive transition [71]. It has been shown [72, 73] that film growth prevails over dissolution of the metal through the pure Cr in the passive state.

It has been found using recent applications of advanced in situ surface analysis techniques [74, 75, 76, 77] that the anodic films formed on iron, chromium and Fe-Cr alloys have a nanocrystalline structure, which resemble that of the corresponding bulk oxides. From these studies, it has also been found that molybdenum as well as chromium is very important in influencing the surface film in stainless steels. Alloying with molybdenum influences both the composition and structure of the passive film on ferrous alloys. It has been proposed [78] that Mo(IV) probably occupies Cr(III) positions in the oxide layer and eventually diminishes the degree of hydration of that layer. In addition, higher dissolution rates in the passive state have been measured for alloys containing a high amount of Mo. This indicates that Mo facilitates the selective dissolution of Fe through the passive film [69]. At higher potentials, it is reasonable to assume that Mo(VI) is segregated in the outermost layers of the film or absorbed at the film/solution interface as molybdate species that catalyse the transpassive dissolution of Cr from the alloys [79, 80].

Two theoretical approaches on the influence of molybdenum on the stability of chromium passive films are: the bipolar film model of Clayton [65, 81, 82, 83] and the point defect model (PDM) for the growth and breakdown of passive films proposed by Macdonald [84, 85, 86]. Both models imply that there is a separation of charges in the barrier layer. According to Clayton et al [66 – 70], injected cations are accumulated at the metal/film

interface, and molybdate ions at the film/solution interface. However, Macdonald et al [85 – 86] assumed there is an accumulation of oxygen vacancies (positive charge) at the metal/film interface and a corresponding accumulation of cation vacancies (negative charge) at the film/solution interface. However, neither model is complete as they do not take into account the possible effect of the degree of hydration of the passive film on its defect structure.

Therefore, the protective surface film formed on stainless steels is due mainly to chromium forming chromium oxide (probably Cr_2O_3). If molybdenum is present in the steel, then this greatly aids the stability of the surface film by occupying Cr(III) sites in the film, thereby reducing the degree of hydration in the layer which can lead to breakdown of the film. The importance of this film on the dissolution characteristics of the stainless steels will be discussed in Section 5.5.1.

1.17 Product Characteristics and Applications

Stainless steel can be selected for use compared to other materials for a number of different reasons, not just its resistance to corrosion. These include:

- Aesthetic qualities - It can be polished to a satin or mirror finish.
- Dry corrosion occurs to steel at higher temperatures where it oxidises or scales up. Stainless steel is far more resistant to this than ordinary carbon steel and grades such as 310 (25 % chromium, 20 % nickel) were specifically developed for use at high temperatures.
- Liquids are not contaminated by contact with stainless steels, because of the passivating surface oxide layer.
- Weight savings can be made, as thinner sections and more innovative design structures can be used, with cost savings.
- Anti corrosion coatings are avoided as these are often fire hazards or have a low melting point.

These attributes of stainless steels give them applications in the following areas:

The most common everyday use of stainless steel is in cutlery. Very cheap cutlery is made out of grades 409 and 430, with the finest Sheffield cutlery using specially produced 410 and

420 for the knives and grade 304 (18/8 stainless with 18 % chromium and 8 % nickel) for the spoons and forks. The different grades are used as 410/420 can be hardened and tempered so that the knife blades will take a sharp edge, whereas the more ductile 18/8 stainless steel is easier to work and therefore more suitable for objects that have to undergo numerous shaping, buffing and grinding processes such as forks and spoons.

Large amounts of stainless steel are used in food production and storage. The most commonly used grades are 304 and 316. Typical uses would be dairies, milk storage, ham curing and frozen and salted fish storage. Whereas 304 is used for normal temperatures and acid concentrations, 316 is used for harsher environments. For example, 304 is used in cheese production, but where salted ham is being prepared 316 is used. For low concentrations of phosphoric acid (one of the constituents of cola) 304 is used, but at higher temperatures and concentrations 316 is used. Food slicers are made of 420 and 440. Very often in food production, stainless steel is used not because the food itself is corrosive but the use of stainless steel allows for faster and more efficient cleaning. For example in ice cream production 316 is specified so that strong anti bacteriological cleaning and rinsing systems can be used. One of the great advantages of stainless steel is that it imparts no taste to the food that it comes into contact with. This has created one interesting anomaly. Traditional wine making uses barrels of oak. The newer wine producing nations use very large vats and storage containers of stainless steel as this gives them far greater economies of scale. However, in conventional winemaking the acid of the wine dissolves some of the wood to give an oak body taste. Using stainless steel vats, oak chips have to be deliberately put into the vats to create the same effect and satisfy traditional wine drinkers.

The pumping and containment of oils, gases and acids has created a large market for stainless steel tanks, pipes, pumps and valves. The storage of dilute nitric acid was one of the first major success stories for 18/8 stainless steel as it could be used in thinner sections and was more robust than other materials. Special grades of stainless steel (duplex and super duplex) have been developed to have greater corrosion resistance. These are used in desalination plants, sewage plants, offshore oil rigs, harbour supports and ships propellers.

Architecture is a growing market. Many modern buildings use stainless steel for cladding. When reinforced concrete first started to be used, it was considered that the carbon steel used would not rust, as cement, derived from limestone, is alkaline. However, constantly using grit salt on bridges can rust the steel thus expanding the cracks in the concrete. This is

thought to occur because of the production of carbonate/carbonic acid from carbon dioxide in the air and sulphuric acid from acid rain making the pH more acidic. The chloride from the salt would attack the stainless steel oxide layer therefore weakening it and making it more susceptible to attack from an acidic environment. Stainless steel reinforcing bars, although initially expensive are proving to have a very good life cycle and therefore reduces the overall long term cost. The low maintenance cost and anti vandal characteristics of stainless steel provides a growing market in public transport, ticket machines and street furniture.

The nuclear power industry uses large quantities of stainless steel, often specified with a low cobalt content, for both power generation and radiation containment. Special louvered ventilation shafts are made, which are designed to be used in emergencies to seal off plants for years if necessary. Steam and gas turbines use stainless steel because of its corrosion resisting and heat resisting qualities.

Clean, cast stainless steel is used for medical implants and artificial hips. Medical equipment such as orthopaedic beds, cabinets and examination machines are made as standard from stainless steel because of its hygienic and easy clean qualities. Pharmaceutical companies use stainless steel for pill funnels and hoppers and piping creams and solutions. Cars are making increasing use of stainless steel, primarily for exhaust systems (409) and catalytic converters, but also for structural purposes.

With greater attention being made to achieving low long term maintenance costs, less environmental impact and greater concern with life costs, the market for stainless steel continues to grow.

1.18 Product Characterisation

When carrying out ECM of steel, dissolution products from the steel accumulate in the electrolyte tank and it has been shown (see Section 5.5) that these species can have a dramatic effect on the dissolution characteristics of the steel being machined. Additionally, the environmental concern about the disposal of these products is very important and needs to be addressed. An aim of this work is to quantify these soluble and insoluble dissolution products and therefore provide insight in to their chemical nature. The insoluble products

were therefore analysed by X-Ray diffraction (XRD) and X-Ray photoelectron spectroscopy (XPS). A discussion of these two analysis techniques is provided here.

1.18.1 X-Ray Diffraction (XRD)

X-Ray Diffraction (XRD) is the most widely used and least ambiguous method for the precise determination of the positions of atoms in solids. Molecular shapes including detailed bond lengths and angles can be determined experimentally from XRD. Therefore, the technique seemed ideal for determining the structure of the dissolution products.

X-Rays, which are electromagnetic radiation with wavelengths of around 100 pm (1 Å), may be produced by bombarding a metal with high energy electrons. The electrons decelerate as they plunge into the metal and generate radiation with a continuous range of wavelengths called Bremsstrahlung (Bremse – brake, strahlung – ray). Superimposed on the continuum are a few high intensity, sharp peaks. These peaks arise from collisions of the incoming electrons with electrons in the inner shells of the atoms. A collision expels an electron from an inner shell, and an electron of higher energy drops into the vacancy, emitting the excess energy as an X-Ray photon.

1.18.1.1 The Bragg Law

Wilhelm Röntgen discovered X-rays in 1895. Seventeen years later Max von Laue suggested that they might be diffracted when passed through a crystal, for by then he had realised that their wavelengths are comparable to the separation of lattice planes. Laue's suggestion was confirmed almost immediately by Walter Friedrich and Paul Knipping, and has grown since then into a very strong analytical technique [87, 88].

The earliest approach to the analysis of diffraction patterns produced by crystals was to regard a lattice plane as a mirror, and to model a crystal as stacks of reflecting lattice planes of separation, d, The model makes it easy to calculate the angle a single crystal must make to the incoming beam of X-rays for constructive interference to occur. It has also given rise to the name reflection to denote an intense spot arising from constructive interference.

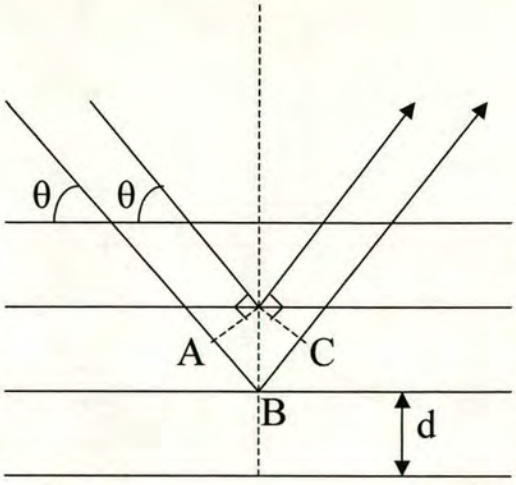

Figure 1.15: The conventional derivation of the Bragg law treats each lattice plane as reflecting the incident radiation. The path lengths differ by AB + BC, which depends on the glancing angle θ. Constructive interference occurs when AB + BC is equal to an integral number of wavelengths.

The path length difference of the two rays in Figure 1.15 is

$$AB + BC = 2d \sin\theta \tag{1.3}$$

where θ is the glancing angle and d is the lattice spacing. For many glancing angles the path length difference is not an integral number of wavelengths, and the waves interfere destructively. However, when the path length difference is an integral number of wavelengths (AB + BC = nλ), the reflected waves are in phase and interfere constructively. It follows that a bright reflection should be observed when the glancing angle satisfies the Bragg law

$$n\lambda = 2d \sin\theta \tag{1.4}$$

Reflections with n = 2, 3, ….etc are called second order, third order, and so on; they correspond to path length differences of 2, 3, ….etc wavelengths. XRD powder diffraction is used for the analysis of samples in this work and will be discussed in Section 2.13.

1.18.2 Scanning Electron Microscopy (SEM) and X-Ray Photoelectron Spectroscopy (XPS)

In the study of the structure of materials, it is important to analyse the surface to determine both the composition (the amount and type of elements present) and the oxidation state (or valency). It can also be important to measure how these properties vary with depth to probe composition and/or structural differences between the interface and the bulk. Therefore, this is particularly important for determining the chemical composition of the steel dissolution particles and for determining the composition of the surface oxide layer. However, before examining the technique of XPS, it would first be useful to briefly look at another surface analysis technique, scanning electron microscopy (SEM), as this is the main alternative to XPS. SEM provides a direct image of the topographical nature of the surface from the emitted secondary electrons. The technique involves focusing a probe beam (a beam of high energy electrons, typically 10 - 50 keV in energy) to obtain spatial localisation.

1.18.2.1 SEM Theory

The technique involves scanning the primary electron beam across the surface. This causes electrons of a wide range of energies to be emitted from the surface in the region where the beam is incident (Figure 1.16). These electrons will include backscattered primary electrons and Auger electrons (Auger electrons are produced when an ionised atom relaxes via electrons with a lower binding energy dropping into the core hole. The energy thus released can be converted into an X-ray or emit an electron known as an Auger electron) but the vast majority will be secondary electrons formed in multiple inelastic scattering processes. The secondary electron current reaching the detector is recorded and the microscope image consists of a plot of this current, I, against probe position on the surface. The contrast in the micrograph arises from several mechanisms, but first and foremost from variations in the surface topography. Consequently, the secondary electron micrograph is virtually a direct image of the real surface structure [89, 90].

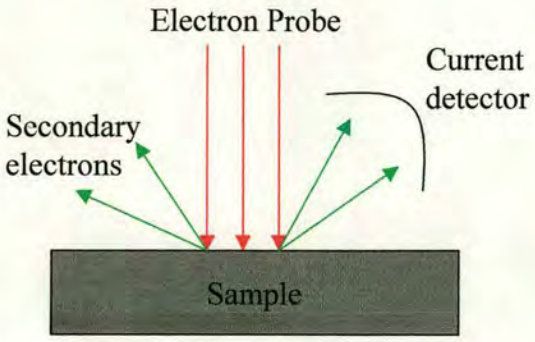

Figure 1.16: Diagram of SEM technique.

The attainable resolution of the technique is limited by the minimum spot size that can be obtained with the incident electron beam, and ultimately by the scattering of this beam as it interacts with the substrate. With modern instruments, a resolution of better than 5 nm is achievable. This is more than adequate for imaging semiconductor device structures, for example, but insufficient to enable many supported metal catalysts to be studied in any detail [91].

1.18.2.2 Problems with SEM

A particular problem faced by analysts using SEM is that their samples contain many different elements containing rough surfaces (the steel dissolution particles can be rough as can parts of the machined steel surfaces, particularly SS316 with chloride electrolyte), and this may interfere with quantitative analysis. However, the quantitative information at every point in the image may not be essential as association of specific types of qualitative information with each point may be more informative [92].

These 'associative' or pattern recognition techniques are very powerful, but they do require that a lot of effort be expended on a particularly small area. This can result in radiation or other forms of damage, and it is always possible that the required information could have been determined faster by another technique. Also, the electron energies used are often large (to make smaller wavelengths to study smaller features) which means that more surface charging will occur (more than XPS) on the sample and is particularly important when analysing insulating samples such as oxides (as is the case in this thesis). SEM is only semi-quantitative, and typically only works well for heavier elements, as the scattering of

electrons depends on atomic number. Thus O and N cannot be easily detected quantitatively (unlike XPS) [93]. Often, conducting gold is sputtered onto the surface to overcome both these problems, but this changes the sample under analysis and is of no use if the surface oxide film is be analysed.

1.18.2.3 XPS Introduction

X-ray Photoelectron Spectroscopy (XPS) was developed in the mid 1960s by K. Siegbahn (who received the Nobel Prize for Physics in 1981 for his work on XPS) and his research group [94, 95]. XPS is based on the photoelectric effect outlined by Einstein in 1905 where a photon impinging on a metal surface causes the ejection of electrons from that surface. XPS is in principle a simple process where a photon of energy ($E = h\nu$, where h is Plancks constant and ν is the frequency of the photon), penetrates the surface and is absorbed by an electron with a binding energy, E_b, below the vacuum level. This electron then leaves the solid with a kinetic energy ($h\nu - E_b$). In the simplest case the energy distribution of the photoemitted electrons should be the energy distribution of electron states in the solid surface shifted up in energy by $h\nu$. However, this simplified picture is not the case in reality as it is more complicated due to the probability of the photon being absorbed by all the electron states not being the same. This leads to different absorption cross sections (or sensitivity factors), however, these have been measured and tabulated to enable quantification of elemental composition. Any photon whose energy exceeds the work function of the solid ($h\nu > \phi$) can be used for photoelectron spectroscopy thus excluding near ultraviolet, visible and higher wavelength radiation. For XPS, Al K_α (1486.6 eV) or Mg K_α (1253.6 eV) are often the photon energies of choice. Other X-ray lines can also be chosen such as Ti K_α (2040eV).

The XPS technique is highly surface specific due to the short range of the photoelectrons that are excited from the solid. The energy of the photoelectrons leaving the sample are determined using a concentric hemispherical analyser (CHA) and this gives a spectrum with a series of photoelectron peaks. The binding energy of the peaks are characteristic of each element. The peak areas can be used (with appropriate sensitivity factors) to determine the composition of the materials surface and the shape of each peak and the binding energy can be slightly altered by the charge on the element. This makes the binding energy sensitive to oxidation state and chemical environment of the emitting atom hence XPS can provide

chemical bonding information. XPS is not sensitive to hydrogen or helium, but can detect all other elements.

1.18.2.4 XPS as core level spectroscopy

Core level spectroscopy [96] is used to provide a compositional analysis of a surface. Because core levels are essentially characteristic in their energy of the atomic species (despite the energy shifts) the observation of certain binding energy peaks in an XPS spectrum can be taken as an indication of the presence in the surface region of a particular elemental species. Thus an XPS spectrum should present information from which the composition of the surface region may be determined; the additional information on exact peak positions may then be capable of indicating the chemical state of some of these component elements. The usefulness of XPS for compositional analysis depends on how sensitive the technique is and how easily the technique can be made quantitative.

A primary component of both questions is the photoionisation cross section for different atomic species. Additionally the availability of accessible energy levels is important. A photon energy in excess of 1 keV, photoemission from some energy levels of all elements is possible and in most cases several levels are accessible. The character of these levels varies as does the proximity of the photon energy to the photoemission threshold for the various levels.

Quantitative studies are possible using XPS as a means of compositional analysis and by taking great care in the mode of calibration, analyses accurate to 5 % are possible.

1.18.2.5 Advantages and disadvantages of XPS

Advantages:

- Non destructive.
- Argon ion beam sputtering allows depth profiling of surface.
- Quantitative method for elemental composition.
- Sensitive.
- Chemical shift gives information about oxidation states and chemical environments.

- Extensive databases of chemical shift information.
- Sampling depth typically 20 – 100 Å.
- Detection of all elements heavier than Li including O and N (SEM can not do this).

Disadvantages:

- Monochromatic X-ray sources have low flux.
- Sampling depth varies with electron KE and material (surface sensitive).
- Spectra complicated by secondary features – X-ray satellites, extrinsic losses, final state effects (software available to analyse these features).
- Surface charging in insulators shifts E_b scale (not an issue due to the flood gun on the machine used which fires low energy electrons to minimise charging).
- Cannot detect H, He with good sensitivity. This is a problem as the technique is being used to analyse oxides and hydroxides and is not capable of discriminating between O^{2-} and OH^-. However, the stoichiometry difference may allow $M(OH)_n$ or $MO_{1/2}$ for M^{n+} to be indirectly measured.

Therefore, overall XPS has the potential to provide a lot of useful information both on the solid dissolution products and on the machined surface. The advantages outweigh the disadvantages especially as some of the disadvantages can be solved by the machine itself or the software available.

1.19 Aims of this work

This Section is to explain the precise aims of this work. Before going into detail it would be both appropriate and useful to summarise the current level of knowledge concerning ECM.

1.19.1 Drawbacks of conventional ECM

Current problems with ECM include the lack of a coherent theoretical model and the lack of suitable measurement techniques for easy determination of ECM parameters. Also, information cannot be extrapolated to other materials. For example, one set of machining parameters may work very well for stainless steel but when applied to titanium aluminide the material may passivate and sparking may occur damaging the electrodes. The lack of a

model is because the machining process as well as the machining parameter interdependencies are not completely understood. This therefore leads to iterative trials when deciding on the best way in which to proceed when machining a material. Therefore, for industrial use of ECM this is both time consuming and costly which is often unacceptable. Currently, there is no convenient method of measuring all the information required to elucidate changes in ECM parameters e.g. is efficiency or valency changing? What are the dissolution products? What is the dissolution mechanism? Therefore, this work involves the development of experimental equipment that enables measurement of the ECM parameters, dissolving valency, n, electrolyte conductivity, κ, and the workpiece overvoltage, V_0, and enables information to be gained concerning the chemical nature of the dissolution reaction and products (see Section 5.5).

1.19.2 ECM Parameterisation

The current level of parameterisation of ECM was discussed in Section 1.11. Currently, there is a lack of a complete understanding of the ECM parameters and their interdepencies if any. Therefore, one of the primary aims of this work is to extend the chronoamperometric method (see Section 2.8.2) to enable the ECM parameters (n, κ and V_0) to be determined for a family of stainless steels. The electrolyte conductivity is measured along the flow path length and in the bulk electrolyte by a novel electrolyte sampling system (see Section 3.5.5). Therefore, the experimental system used in this work allows all the important physicochemical parameters to be independently determined.

1.19.3 Chemical understanding of the ECM process

Currently, there is very little understanding about the chemical process of ECM and another aim of this work is to understand the process of electrochemical dissolution under ECM conditions. Typical ECM conditions are a 0.4 mm electrode gap, 24 V applied between the electrodes producing ~100 A cm^{-2} depending on the workpiece material, electrolyte flow perpendicular to the electrodes at 50 m s^{-1} and 15 bar pressure. These conditions are therefore extreme and little previous work on electrochemical kinetics and mechanisms has been carried out under these conditions. One of the further aims of this work is therefore to determine the electrochemistry of the ECM process at a fundamental level. If these dissolution reactions are understood then this may go some way towards developing a

complete predictive model. This work looks at the stainless steel family of alloys, and correlates their dissolution behaviour with the composition and structure of the protective surface oxide layer through the application of analytical techniques such as XPS and XRD.

1.19.4 Process and tool design modelling

Although the precise aim of this work is not to develop an ECM tool model, this work is part of a broader project with the general aims of producing an integrated approach for tool design in ECM. The proposed method is to produce a system for automatically generating the required parameters and modelling data, through a single test arrangement taking only a few minutes. Then this information will be combined with numerical tool design systems already developed and a tool design for a desired workpiece shape will be produced. This will avoid the dependence on techniques that attempt to model the tool form through the generation of complete empirical ECM data models or those that attempt to develop fully applicable analytical models. Therefore, before a tool model can be designed and applied, it is first necessary to understand the process which is to be modelled and the aim of this work is to determine and model the chemical processes occurring during machining. An understanding of these processes is required for the development of a predictive stoichiometric model that can be applied to advanced alloy compositions.

As the work carried out in this thesis is aimed at allowing tool design for ECM to be made quicker, easier and more accurate, then it would be useful to briefly look at current process simulation and tool design techniques. In general process simulation is achieved as follows:

Based upon an initial tool design and initial relative tool position, these techniques compute the electric potential distribution within the gap determined as a solution to the Laplace Equation [31]. This solution is then applied to the determination of the current density at spatial intervals on the workpiece surface. The erosion rate can then be determined by applying Faraday's laws (see Section 2.8). An intermediate workpiece shape is then established using the erosion rate distribution and a pre-defined temporal interval. The tool position is then incremented according to a pre-selected feed rate and the computation repeated to calculate the next stage in the evolving workpiece shape. These iterations are repeated until the desired workpiece is achieved in the transient state or until the current

density distribution, and therefore the workpiece shape, becomes invariant with time (the equilibrium condition).

In the majority of the work on process simulation, several simplifying assumptions are made. These assumptions, which can be collectively termed as ideal conditions, ignore any variation in fundamental machining parameters. Within the general grouping of ideal process simulation techniques, different methodologies have been developed for representation of the tool and workpiece surface and the way in which the field distribution is modelled. For example, the finite element technique is applied using a rectangular mesh [97, 98, 99, 100, 101] and alternatively a triangular mesh [102, 103] for representing and incriminating nodal descriptions of the electric field distribution. In these latter cases, the use of a triangular mesh is reported to improve the accuracy of the computed workpiece shape. In the work reported in [99] the finite element algorithm is employed in conjunction with an optimisation formulation. This optimisation process minimises the deviation between each computation of the workpiece shape, from that which is required, to produce a more accurate simulated shape.

As a variation to applying the finite element technique to solve the simulation problem, several workers have applied other methodologies such as finite difference techniques [104, 105] and the boundary element method [106, 107, 108]. Improved accuracy and reduced computation times have been reported in this latter case.

1.19.4.1 Tool design for ECM

Tool design methodologies (the so-called inverse problem) attempt to compute the tool shape by calculating the tool form as an equipotential boundary relative to the required workpiece shape (also assumed to be highly conducting and therefore an equipotential boundary using the values of conductivity, κ, appropriate to the electrolyte in the gap and with $(V-V_0)$ being equal to the potential difference between the two equipotential surfaces). In the case of many workpiece examples there is found to exist a family of tool form solutions of which only some can actually be manufactured. For specified machining conditions, however, parameters can usually be defined that will ensure that only realisable tools are generated. For the case of ideal conditions, workers have addressed the tool design problem using a number of different strategies. For example, using numerical boundary element methods [109, 110] and also as a Cauchy problem for the Laplace Equation solved

by analytical continuation [111]. However, this work not does take into account variations in overpotential, V_0, conductivity, κ, and dissolution valency, n, along the flow path length.

Therefore, there is no current and complete method for modelling the ECM process accurately and producing the required tool geometry to produce a given component to the required tolerance. The work of this thesis goes some way towards facilitating this goal by investigating the ECM chemistry and providing new experimental techniques for measuring and parameterising ECM across the whole range of industrially applicable ECM conditions.

The structure of this thesis is therefore as follows. Chapter 2 outlines the theory of electrochemical machining including the chemical reactions at the tool and workpiece as well as the chronoamperometric theory used to analyse the current transients. Chapter 3 outlines the experimental equipment used in this work and Chapter 4 compares the single planar tool with the planar segmented tool looking at the advantages and disadvantages of each. Chapter 5 outlines the work carried out on the family of stainless steels, looking at the dissolution characteristics of the different steels as well the effect of different electrolytes. Chapter 6 outlines the work carried out on J and looks specifically at the abnormally high current densities observed and proposes a mechanism by which this is occurring and a solution to the problem. Finally, Chapter 7 concludes the results in this work and looks at possible future work.

Chapter 2

Theory of Electrochemical Machining

2.1 The ECM reaction

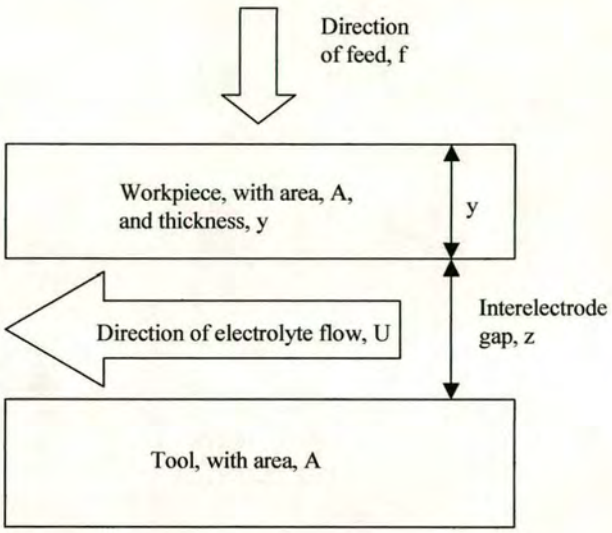

Figure 2.1: Planar ECM system.

An electrolytic cell uses external electrical energy from an external voltage source to apply a potential difference (voltage) between two electrodes (Figure 2.1). This is the type of cell used in ECM and allows the direction and rate of the electrode reaction to be controlled by the voltage, converting electrical energy into chemical energy. This is different to a galvanic cell that transforms energy obtained in a spontaneous chemical reaction into electron movement in an external circuit. ECM involves passing a current between two electrodes (tool and workpiece) through a flowing electrolyte. The reactions are heterogeneous and take place at the interface between the electrodes and the electrolyte. During ECM the workpiece oxidises and the general electrode reaction at the workpiece can be represented as the dissolution of a metal, M

$$M \rightarrow M^{n+} + ne^-$$

Equation 2.1

with a corresponding reduction reaction of water (from the electrolyte) at the tool of

$$2H_2O + 2e^- \rightarrow H_{2(g)} + 2OH^-_{(aq)}$$

Equation 2.2

The workpiece is then fed towards the tool at a controlled rate in order to maintain metal dissolution (Figure 2.1).

2.2 Single Electrode (Workpiece or Tool) at Equilibrium

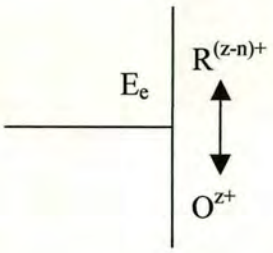

Figure 2.2: Diagram of a single electrode system where a species O is reduced to a species R.

Firstly considering a single electrode at equilibrium (Figure 2.2) where the general redox reaction is

$$O^{z+} + ne^- \leftrightarrow R^{(z-n)+}$$

Equation 2.3

then the Nernst Equation can be used to describe this system at equilibrium

$$E_e = E^\theta + \frac{RT}{nF} \ln \frac{a_0}{a_R}$$

Equation 2.4

where E_e is the potential of the electrode at equilibrium and E^θ is the standard electrode potential under standard conditions (usually at a stated temperature, often T = 298 K, and all reagents having an activity, a, equal to 1 and are in their standard physical states). The standard state involves reactions at a platinum electrode for solution redox species or at a pure metal electrode where the electrode material is part of the redox reaction. Therefore, for the example of pure iron dissolution, a pure iron workpiece is required, and the reduction reaction is

$$Fe^{2+}_{(aq)} + 2e \rightarrow Fe_{(s)}$$

Equation 2.5

which can be represented by the Nernst Equation as

$$E_e = E^{\theta}_{Fe^{2+}/Fe} + \frac{RT}{2F} \ln a_{Fe^{2+}}$$

Equation 2.6

with pure iron being used as the electrode. However, when looking at an alloy, as is most frequently the case with ECM, then E^{θ} is not appropriate, as the metal elements constituting the alloy are not in their standard states. Therefore, looking at the reduction of iron in an alloy, the Nernst Equation can be written as

$$E_e = E'_{Fe^{2+}/Fe} + \frac{RT}{2F} \ln a_{Fe^{2+}}$$

Equation 2.7

where E' is the equivalent of the standard electrode potential when using the alloy.

This is also the case for the reaction of solution redox species. For example, for the tool reaction

$$2H_2O + 2e^- \rightarrow H_{2(g)} + 2OH^-_{(aq)}$$

Equation 2.8

the corresponding Nernst Equation for the reaction at a Platinum electrode is

$$E_e = E^{\theta}_{H_2O,H_2,OH^-} + \frac{RT}{2F} \ln \frac{1}{\frac{p_{H_2}}{p^{\theta}} a_{OH^-}^{\ 2}}$$

Equation 2.9

where p_{H_2} and p^{θ} are the partial pressure of hydrogen gas and the standard partial pressure of 1 atmosphere respectively. The reaction at a tool alloy electrode and not Platinum, will again involve E', with the equivalent of the standard electrode potential in the Nernst Equation

$$E_e = E'_{H_2O,H_2,OH^-} + \frac{RT}{2F} \ln \frac{1}{\frac{p_{H_2}}{p^\theta} a_{OH^-}^{\ 2}}$$

Equation 2.10

2.3 Two Electrode System at Equilibrium

Now considering a two electrode system at equilibrium where no overall current flows (I = 0), one can build on the one electrode system just described and the total applied voltage, V, can be written as

$$V = E_w - E_T$$

Equation 2.11

where E_w is the potential at the workpiece and E_T is the potential at the tool (as the system is at equilibrium, then there is no migrational voltage (an IR drop is required to pass current in the gap) (Figure 2.3).

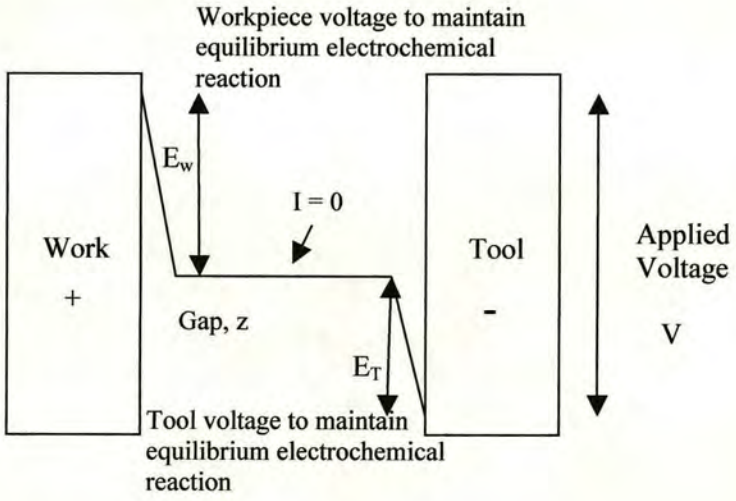

Figure 2.3: Diagram of a two electrode system where I = 0.

Throughout, the subscripts W and T will denote the workpiece and tool respectively. Therefore, from the one electrode system using iron as the dissolving workpiece material (Equation 2.5), the potential at equilibrium at the workpiece, $E_{e,w}$ can be written (Section 2.2) as

$$E_{e,w} = E'_w + \frac{RT}{2F} \ln a_{Fe^{2+}}$$

Equation 2.12

and for the tool, considering the reaction

$$2H_2O_{(l)} + 2e \rightarrow H_{2(g)} + 2OH^-$$

Equation 2.8

the reaction at the tool can be written as

$$E_{e,T} = E'_{H_2O,H_2,OH^-} + \frac{RT}{2F} \ln \frac{1}{\frac{p_{H_2}}{p^\theta} a_{OH^-}^{\ 2}}$$

Equation 2.10

where p_{H_2} / p^θ is the activity (fugacity) of hydrogen, p^θ = 1 atmosphere and p_{H_2} is the partial pressure of the hydrogen gas in atmospheres. Therefore in this case

$$V = V_e = E_{e,w} - E_{e,T}$$

Equation 2.13

where V_e is the voltage at equilibrium.

This is the system in equilibrium, with no current flowing at either electrode. However, in order to get oxidation at the workpiece and reduction at the tool, a more positive potential is required at the workpiece and a more negative potential at the tool. This will require an increase in the overall value of the applied voltage V above V_e to drive these reactions. The extra voltage required to drive these reactions can be calculated in the simplest case by means of Butler-Volmer kinetics.

2.4 The kinetics of one and two electrode systems

If a more positive potential than V_e is applied in order to cause the workpiece to oxidise then Figure 2.3 can be modified to Figure 2.4.

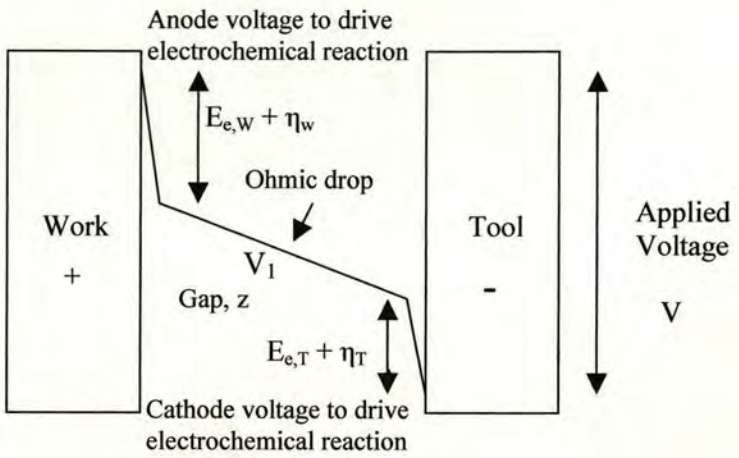

Figure 2.4: The potential distribution across a typical ECM cell away from equilibrium where $V_0 = E_{e,w} - E_{e,T} + \eta_w - \eta_T$.

The anode (η_w) and cathode (η_T) voltages are required to drive the surface electrochemical reactions (Figure 2.4) and V_1 is the ohmic voltage (IR, where R is the resistance of the solution) which drives ion migration in the bulk electrolyte to maintain the current, I. Chronoamperometric analysis of ECM dissolution allows determination of the surface voltages without this term (i.e $V_0 = V - V_1$, where V is the applied potential (Section 2.8), and hence this does not need to be considered).

Determining the current for a one electrode system can be done using the Butler-Volmer Equation [112]. It would first be useful to discuss the origin of the Butler-Volmer Equation particularly the transfer coefficient, α and the overpotential, η. The transfer coefficient is a measure of the fractional distance along the reaction co-ordinate at which the transition state for a reaction is found.

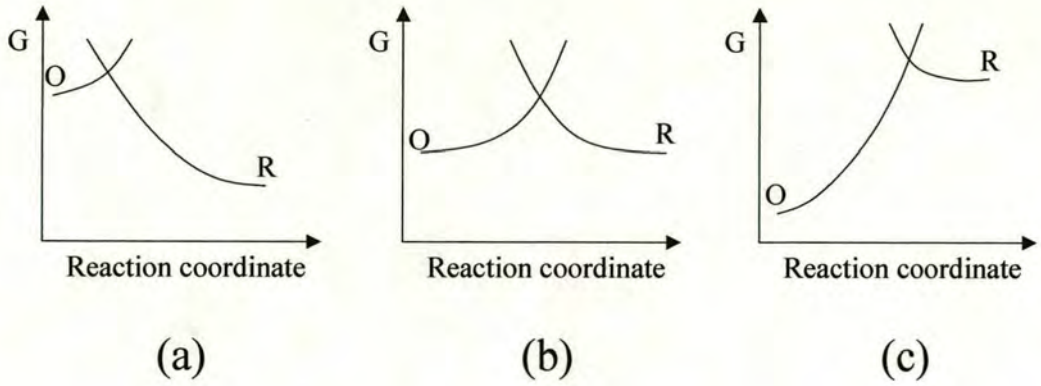

Figure 2.5: Free energy potential surfaces for (a) $\alpha = 0$, (b) $\alpha = 0.5$ and (c) $\alpha = 1$.

The value of α ($0<\alpha<1$) reflects the sensitivity of the transition state to the drop in electrical potential at the electrode surface between the metal and the solution. The free energy potential surface for a reduction is simply the mirror image of that for an oxidation with respect to the reaction coordinate, and hence

$$\alpha_{ox} = 1 - \alpha_{red}$$

Equation 2.14

where α_{ox} and α_{red} refer to the transfer coefficients for the oxidation (right to left in Figure 2.5) and reduction (left to right) reactions respectively.

If α is close to zero then the transition state resembles the reactants in its potential dependence whereas when it approaches unity the transition state resembles the products. α is typically found to be close to 0.5 for many reactions, suggesting the transition state has intermediate behaviour between reactants and products.

For electrolysis to occur at an electrode, a potential different in value from the equilibrium potential E_e for the reaction in question must be applied to the electrode in order to initiate the electrode reaction; more positive for an oxidation and more negative for a reduction. The deviation of E from this equilibrium potential, E_e is quantified by the term overpotential, η, where

$$\eta = E - E_e$$

Equation 2.15

as when $\eta = 0$, i.e. $E = E_e$ then no overall current will flow.

2.5 The Butler-Volmer Equation

The relationship for the net current, I, flowing at an electrode at which the general reaction

$$O^{z+} + ne^- \leftrightarrow R^{(z-n)+}$$

Equation 2.3

is occurring is given by

$$I = I_0\left(\frac{[R]_0}{[R]_{bulk}}\exp\left\{\frac{(1-\alpha_{red})nF\eta}{RT}\right\} - \frac{[O]_0}{[O]_{bulk}}\exp\left\{\frac{-\alpha_{red}nF\eta}{RT}\right\}\right)$$

Equation 2.16

This is the Butler-Volmer Equation, which is fundamental to electrode kinetics [112]. It predicts how the observed current varies as a function of the overpotential, η, and the transfer coefficients, α_{ox} and α_{red}, which are interrelated through Equation. 2.14 and therefore only one variable. The first term in Equation 2.16 refers to the oxidation reaction, with its potential sensitivity controlled by $\alpha_{ox} = 1 - \alpha_{red}$. The second term refers to the reduction reaction, controlled by α_{red}, with the balance of these two terms giving the overall current at the electrode. I_0 is the exchange current, which is the magnitude (equal) of the oxidation and reduction currents at equilibrium, when $\eta = 0$. If the solution under investigation is well stirred (as in ECM, Section 2.7) the surface concentrations of the reactants will be equal to their bulk values ($[R]_0 = [R]_{bulk}$ and $[O]_0 = [O]_{bulk}$). Under these conditions the first term in Equation 2.16 simplifies to

$$I = I_0\left(\exp\left\{\frac{(1-\alpha_{red})nF\eta}{RT}\right\} - \exp\left\{\frac{-\alpha_{red}nF\eta}{RT}\right\}\right)$$

Equation 2.17

Now let us consider each of the electrodes in the ECM system in turn. As large currents are flowing at the electrodes in ECM then η at the workpiece (denoted η_w for the workpiece

overpotential) is large and positive and the oxidation reaction dominates the reduction reaction. Hence from Equation 2.17 the current can be expressed as

$$I_w = I_{0,w}\left(\exp\left\{\frac{(1-\alpha_{red,w})n_w F\eta_w}{RT}\right\}\right)$$

Equation 2.18

where the subscript w again denotes the reactions at the workpiece. At the tool reduction dominates and η_T is large and negative and the current is given by

$$I_T = -I_{0,T}\left(\exp\left\{\frac{-\alpha_{red,T}n_T F\eta_T}{RT}\right\}\right)$$

Equation 2.19

where the subscript T denotes reactions at the tool.

Since the currents at each electrode must be of equal magnitude then $I_w = -I_T$. Therefore, for a simple dissolution reaction a summary diagram can be drawn to show the components which make up V_0 for ECM (Figure 2.6).

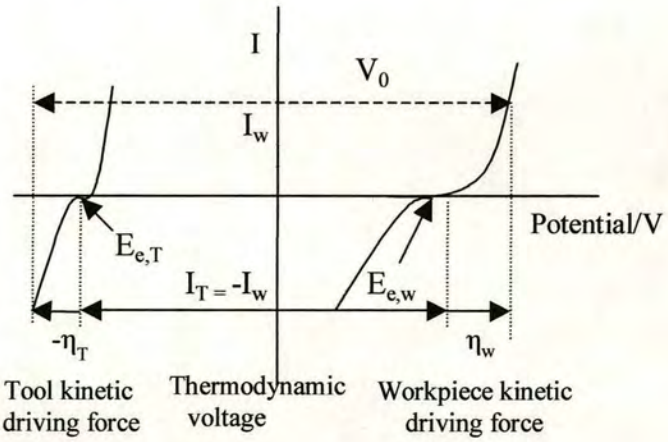

Figure 2.6: A diagram showing the electrode components of V_0.

Therefore, a summary of the overall contribution to V_0 (Figure 2.6) in this case can be expressed as

$$V_0 = E_w - E_T = E_{e,w} - E_{e,T} + \eta_w - \eta_T$$

Equation 2.20

where η_w (workpiece) is the overpotential at the electrode to drive the workpiece reaction at the ECM current I_w, and $-\eta_T$ (tool) drives the reaction at the tool with the same magnitude of current ($-I_w$).

Since the overpotential terms are functions of I, it can be seen that V_0 is also a function of I. However, the exponential dependency of I on η means that small changes in the overpotential, η can cause large changes in the current, I (Equations 2.18 and 2.19). If the thermodynamic terms ($E_{e,w}$ and $E_{e,T}$) are large, as the change in I during ECM is often relatively small (a factor of 2 or 3) then changes in these overpotential terms can be small and can lead to apparently constant V_0 values within experimental error during ECM (from Equation 2.20). This often simplifies modelling, but makes measuring changes in V_0 with I experimentally difficult (see Section 5.5.2 for measurements of V_0 with I).

Equation 2.20 is derived assuming simple electrode kinetics, without such complications as the presence of resistive surface oxide films which hinder the electrochemical reaction. No such surface oxides would be expected on the tool due to the reductive conditions; however, this is not the case for metal oxide coated surfaces such as stainless steel workpieces, where a resistive layer hinders metal ion dissolution. In this case, an IR resistive component could be added to Equation 2.20 where R is the resistance of the surface layer.

$$V_0 = E_{e,w} - E_{e,T} + \eta_w - \eta_T + IR_w$$

Equation 2.21

If the resistance, R, were independent of I, then a linear relationship of this term in V_0 with current, I, for the film might be expected whilst Tafel behaviour gives an exponential dependence of I on the overpotential terms. This means that measuring the dependence of I on V_0 could give insight into which system dominates. Dissolution is often assumed to be controlled by Tafel like behaviour, but with a reduced slope, as the proportion of the electric field drops at the oxide surface.

The Point Defect Model (PDM) [113] can be applied to explain the growth of the surface oxide layer. When the applied voltage, V, exceeds the most negative electrode potential at

which the passivating film is formed electrochemically (usually equal to or more positive than the equilibrium potential of formation of the oxide) then a continuous passive film will form on the surface of the metal (workpiece in this case). The film can be assumed to be an oxide of composition $MO^{x/2}$ (where "x" represents "x" negative charges). It is assumed that the passive film contains a high concentration of point defects. The major point defects in the oxide film are V_M^x (metal vacancy), V_O^{n+} (oxide vacancy), e (electron) and h (electron hole). According to the PDM the rate of the oxide growth and breakdown is dependant upon the migration of these vacancies. The growth of the oxide film has been shown [84 - 86] to be linearly dependent with potential. Therefore, the higher the applied potential the thicker the resulting oxide film. Metal dissolution is due to the diffusion of metal cations or cation vacancies through the film. However, it is worth noting that this work was carried out at much lower currents than used in ECM.

It must also be remembered that the Butler-Volmer Equation (Equation 2.16) has been derived and established at much lower current densities than those used in ECM. Therefore, the applicability of this fundamental relationship between η and I also needs to be established under these conditions which is an objective of this work. Additionally, measurements of the variation of V_0 with I may be important in parameterising the system (Section 5.5.2).

2.6 Conductivity

The conductivity of the solution in the interelectrode gap is important in determining the magnitude of the migrational voltage, V_1, and hence the migrational field which determines the ECM gap. This conductivity is the result of the movement of all ions in solution under the influence of an electric field. Considering an isolated ion type, i, then the force on each ion due to the electric field is

$$F = z_i eE$$

Equation 2.22

where $z_i e$ is the charge on each ion, and E is the electric field strength. This force is counterbalanced by a viscous force given by Stokes' Equation

$$F = 6\pi\eta r_i v_i$$

Equation 2.23

where η is the solution viscosity, r_i the radius of the solvated ion and v_i the velocity. Therefore, the maximum velocity, v_i, without any other retarding effects is

$$|v_i| = \frac{z_i eE}{6\pi\eta r_i} = |u_i E|$$

Equation 2.24

where u_i is the ion mobility, which is the proportionality coefficient between the velocity and electric field strength. Smaller, more highly charged ions will therefore have a higher mobility. The relationship between conductivity and mobility can be obtained by calculating the ionic flux, j_i, which is the number of moles of ions that pass through a 1 cm^2 plane per second.

$$j_i = v_i c_i$$

Equation 2.25

where v_i is the velocity, and c_i is the concentration. Therefore, for the solution (which contains various ions) the overall measured conductivity, κ, is given by the charge carried by all the ions, or

$$\kappa = F\sum_i z_i c_i u_i$$

Equation 2.26

Assuming independent migration of each ion (at high dilution, Kohlrausch, [88]), the molar conductivity of each ion type ion, λ_i is given by

$$\lambda_i = \frac{\kappa_i}{c_i} = z_i u_i F$$

Equation 2.27

and the electrolyte molar conductivity, Λ, is

$$\Lambda = \sum_i n_i \lambda_i = \frac{\kappa}{c}$$

Equation 2.28

where c is the overall concentration of the salt which gave rise to the ions when dissolved. Hence $c = c_i/n_i$ where n_i is the stoichiometry of ions in the salt i.e. for NaCl, $n_{Na} = 1$, $n_{Cl} = 1$, and therefore, for a 1:1 salt (those used in this thesis are 1:1 salts) then

$$\Lambda = \lambda_{M^+} + \lambda_{X^-}$$

Equation 2.29

The measurement of the conductivity of an electrolyte solution is species selective. Individual ionic conductivities can be calculated only if the conductivity (or mobility) of one ion is known. If various ions are present and at high ionic strengths, where ion interaction is important and difficult to model, as in ECM, calculation is extremely difficult. In addition, individual ionic conductivities can vary with solution composition and concentration, except at infinite dilution, where ionic interaction does not affect ion migration due to infinite separation of ions. In this case, experimental measurement of the ionic conductivity of the solution is required.

2.7 Hydrodynamic electrodes

2.7.1 Mass transport in ECM

Hydrodynamic electrodes [114] work under forced convection of the electrolyte and the channel hydrodynamic electrode (Figure 2.7) is the closest example to the flow conditions in an ECM cell. The ECM cell can be thought of as two channel electrodes (workpiece and tool) facing each other on the opposite side of the channel.

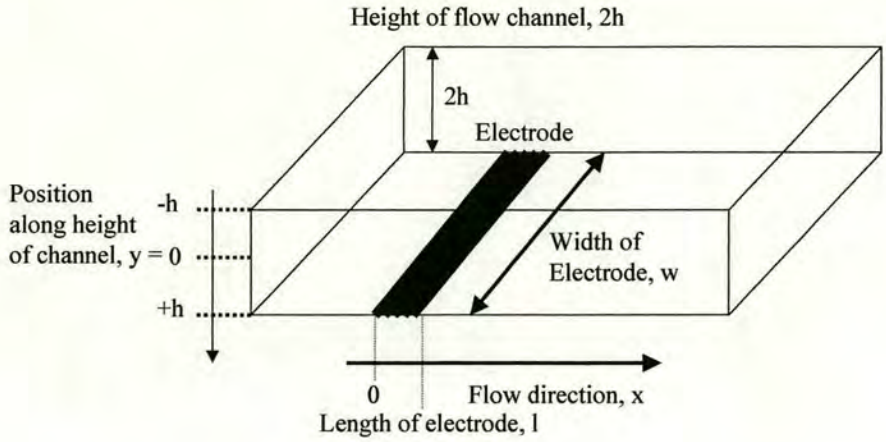

Figure 2.7: Diagram representing a channel electrode including all the terms.

It can be shown that irregular, chaotic motion characterises the turbulent flow in a channel cell under conditions typical for ECM. The Reynolds number, Re is a dimensionless parameter which is related to the cell geometry and the solution velocity and describes the state of the electrolyte flow. Re is given by

$$Re = \frac{v_0 h}{\nu}$$

Equation 2.30

where v_0 is the velocity at the centre of the channel, h is half the channel height, and ν is the kinematic viscosity of the solution. For Re < 2000 the flow is smooth and laminar. However, once the Reynolds number, Re > 2000 [115, 116, 117], then the flow pattern through the channel is no longer smooth and steady but instead there is an irregularly fluctuating motion superimposed upon the main electrolyte flow stream.

In virtually all channel electrode studies, the flow is chosen to be laminar. However, in ECM where high flow rates and high pressures are normal, then it is unlikely the flow will be laminar and Re is likely to be much higher than Re = 2000. Using Equation 2.30, a typical value of, Re, can be calculated for the ECM cells used in this work. For a flow rate of 16.0 l min^{-1} through a cell of width 1.50 cm and height (interelectrode gap) of 0.040 cm, the interelectrode channel area is 1.50 cm x 0.040 cm = 0.060 cm^2. A flow rate of 16.0 l min^{-1} or 16,000 cm^3 min^{-1} or 267 cm^3 s^{-1} gives a flow velocity, v_0 = 267 cm^3 s^{-1}/0.060 cm^2 = 4440 cm

s^{-1}. Therefore, substituting these Figures in Equation 2.30 and using the kinematic viscosity of water as 0.01 $cm^2\ s^{-1}$ then

$$Re = \frac{4440\ cm\ s^{-1} \times (0.040/2\ cm)}{0.01\ cm^2\ s^{-1}} = 8900$$

Therefore, Re is of the order of 9000 and under these ECM conditions where high electrolyte flow rates and high pressures are usual, then the flow regime is turbulent. A complete theoretical description of mass transport under these turbulent conditions is impossible [118]. Therefore empirical models have to be used, where a simplified representation of turbulence is considered. The fully developed turbulent velocity profile can be represented by the empirical Equation [119, 120]

$$\frac{v_x}{v_0} = \left(\frac{h-y}{h}\right)^{\frac{1}{n}}$$

Equation 2.31

where h is half the height of the flow channel, y is the height variable in the flow channel such that y has values between -h and +h, v_x is the velocity of flow in the x direction at a particular value of y and the velocity at the centre of the flow path, h = 0 is v_0 (see Figure 2.7). If 4000 < Re < 100,000 then the velocity distribution can be described by Equation 2.31 with n = 7 and is said to follow the $1/7^{th}$ power velocity distribution law [120] which is shown in Figure 2.8.

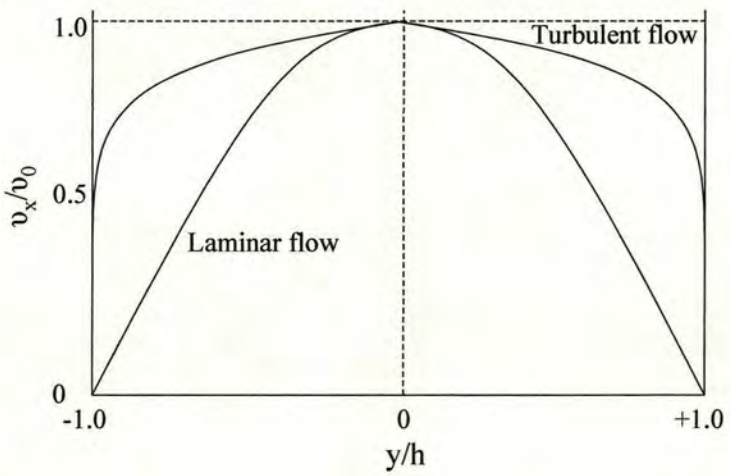

Figure 2.8: Comparison of laminar (Re < 2,000) and turbulent ($1/7^{th}$ power) (4,000 <Re <100,000) velocity distributions.

Therefore greater rates of mass transport (within the vicinity of the tube walls) are possible with turbulent rather than laminar flow. Usually, the effect of friction at the walls of the channel will be to slow down the flow in their vicinity but due to the turbulence this effect is less pronounced than in a laminar flow system (see Figure 2.8). The entry length required to establish turbulent flow is also much shorter than under laminar conditions and is typically 40 – 80 h at equilibrium [120]. The entry length, l_e can therefore be estimated by multiplying the interelectrode gap by 40 and is typically found to be between 4 mm and 8 mm for an interelectrode gap of 0.40 mm under ECM conditions. Note that one segment length in the ECM experiments with a segmented tool (Section 3.6) has a length of 5.70 mm, which indicates that the establishment of turbulent flow will typically occur within the length of the end segment in the system. Therefore, it might be expected that segments 1 and 7 (which fall within the entry length limits) would have different hydrodynamic regimes to those of segments 2 to 6 (see Section 4.3).

Von Karmen [121] has identified three zones within the turbulent boundary (see Figures.2.8 and 2.9).

1. The laminar sublayer, close to the wall of the tube, where the flow may be considered to be laminar because of the turbulent eddies being damped down by the walls. In this region, v_x varies linearly with the distance (height) from the electrode surface.

2. A transition region in which flow changes from laminar to turbulent.

3. A turbulent core, where v_x varies according to the one seventh power velocity distribution law (Figure 2.8).

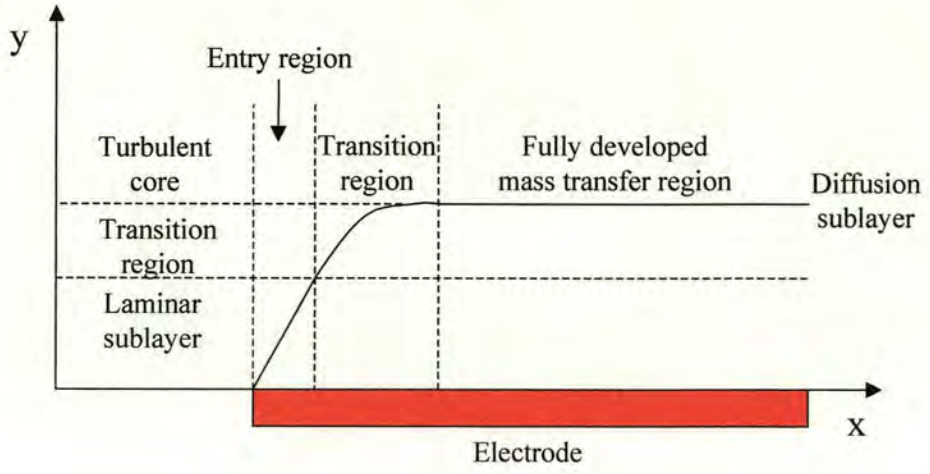

Figure 2.9: Diagram showing the 3 mass transport regions for turbulent flow as a function of distance along the flow path length of the electrode, x.

The contribution of each of the zones within the turbulent boundary layer, as a function of distance along the flow path length of the electrode need to be considered. If a species undergoes electrochemical reaction at the electrode, then comparing the extent of the resulting concentration boundary layer relative to the mass transport boundary layer (Figure 2.9) is important in determining the nature of the mass transport of this species as a function of x. At short distances from the upstream edge of the electrode, in the entry region, l_e, mass transport to the electrode can be considered to be relatively large, and controlled by transport across the laminar sublayer. However, as the electrolyte moves downstream, the diffusion sublayer is extended to greater distances from the electrode surface, decreasing the rate of diffusional mass transport and the contribution of the turbulent eddies to the transport process is seen to be increasingly important. Eventually, at a sufficient distance downstream, mass transfer becomes independent of x and the diffusion sublayer maintains a constant thickness. This is termed the "fully developed mass transport region". In this region, mass transport to and from the electrode is invariant with x and the electrode can be considered to be uniformly accessible. Therefore, this could be a reason why small hydrodynamic effects are observed on entry (segment 1) and exit (segment 7) of the electrolyte flow for Cell 2000 (see Section 4.5) as the entry length is likely to be between 4 and 8 mm, comparable to the size of one segment (5.70 mm).

Therefore, laminar flow is only established in the laminar sublayer close to the electrode during ECM. The high degree of turbulence in the core flow of ECM also increases the efficiency of mixing of products from tool and workpiece, which acts to minimise

compositional variation and ensure constant solution conductivity across the interelectrode gap.

2.8 Electrochemical machining theory

The factors affecting the electrochemical rates and reactions at electrodes have been discussed. Now the theory concerning ECM parameterisation will be examined. The rate at which the workpiece dissolves and the current produced are given by Faraday's laws of electrolysis which state:

1. The mass of any given substance, which is liberated or dissolved because of electrolysis, is proportional to the quantity of electric charge that has flowed.

2. The ratio of the numbers of moles of any two different substances liberated or dissolved in electrolysis because of equal quantities of charge flowing is equal to the reciprocal of the ratio of their respective valencies.

Therefore, the amount of material deposited or dissolved at an electrode is proportional to the sum of the charge passed and inversely proportional to the valency of the dissolving material. These laws can be combined and quantitatively expressed assuming 100 % efficiency (the concept of efficiency will be discussed in Section 2.11).

For the general oxidation and dissolution of a metal, M, then

$$M_{(s)} \rightarrow M^{n+}_{(aq)} + ne^-$$

Equation 2.1

The charge passed for a given amount of material dissolved, Q, can be shown to be

$$Q = \int_0^t Idt = \frac{nFm}{M}$$

Equation 2.32

where I is the current passed (A) and t is the time (s). F is the Faraday, and so nF is the number of moles of electrons required to remove 1 mole of material, m is the mass of material removed and M is the atomic mass of the element dissolved. Therefore, the mass of material dissolved is

$$m = \frac{ItM}{nF}$$

Equation 2.33

Equation 2.33 incorporates the atomic mass of the material dissolved but this only applies to a pure element. Materials machined by ECM are more frequently alloys. In this case, M represents the molecular mass of the alloy rather than the atomic mass of an element, where

$$M = \sum_i x_i M_i$$

Equation 2.34

and x_i and M_i are the mole fraction and atomic masses of each individual element in the alloy. Therefore, in this case, M can be considered to be the mass of 1 mole of the alloy. In this case, n is therefore the overall valency of the alloy

$$n = \sum_i x_i n_i$$

Equation 2.35

2.8.1 Simple theory for a planar ECM system

All the process characterisation outlined in this thesis is based on a planar ECM system (Figure 2.10). The workpiece is fed towards the tool at a feed rate, f. The interelectrode gap, z has electrolyte flowing through at a volume flow rate, U. The area of each electrode is given by A. As the workpiece approaches the tool then the interelectrode gap decreases until it stabilizes at a value z_∞ known as the equilibrium gap. At this equilibrium condition the feed rate is equal to the workpiece dissolution rate and the gap is constant.

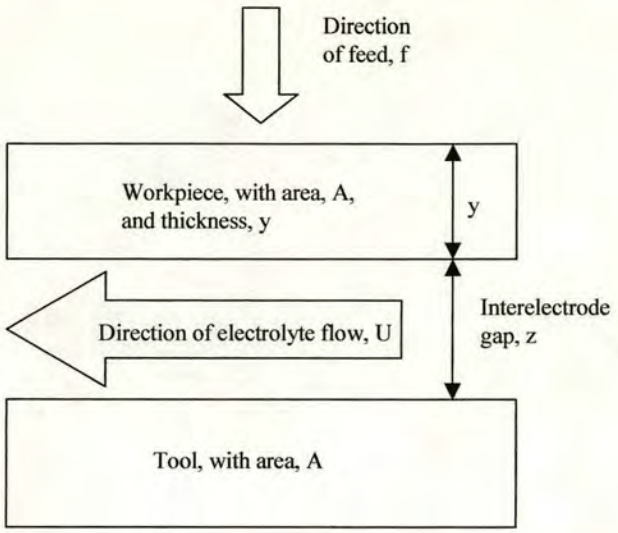

Figure 2.10: Planar ECM system

The simplest analysis of this system assumes ideal conditions. In this case, the following assumptions are made for the planar ECM system

1. The conductivities of the tool and the workpiece are large compared with that of the electrolyte so that the tool and workpiece can be considered as equipotential surfaces (since these are typically metals or metal alloys).

2. The volume flow rate is high enough so that the number of ions produced and consumed during the ECM reaction is negligible compared to the number of ions flowing past the electrodes, ensuring a constant concentration of electrolyte. This means that the composition and hence the conductivity of the electrolyte, κ, are constant and do not change on passing through the interelectrode gap. Therefore, product formation has a negligible effect on the overall electrolyte composition. It is also assumed that mixing is sufficient to ensure a constant conductivity throughout the gap (Section 2.7).

3. It is assumed that all the current produced is generated from the dissolution of the workpiece and not from any side reactions. Therefore, the current efficiency for ECM dissolution is assumed to be 100 %.

In this case, the mass of material removed per unit time, dm/dt is given by

$$\frac{dm}{dt} = A\frac{dy}{dt}\rho$$

Equation 2.36

where ρ is the density and dy/dt is the erosion rate of the workpiece. Therefore by differentiating Equation 2.33 with respect to time and combining with Equation 2.36 the thickness of material removed from a given area per unit time is

$$\frac{dy}{dt} = \frac{IM}{AFn\rho}$$

Equation 2.37

When equilibrium is reached, denoted by the subscript ∞, the feed rate, f, equals the dissolution rate dy/dt and

$$f = \frac{I_\infty M}{AFn\rho}$$

Equation 2.38

Rearranging Equation 2.38 allows the overall dissolution valency at equilibrium to be calculated. This is the Equation used throughout this thesis to calculate valency.

$$n = \frac{I_\infty M}{fAF\rho}$$

Equation 2.39

The current from the workpiece of area, A, across the electrolyte with conductivity, κ, can also be related to the voltage, $V - V_0$, available across the gap, z, to drive the migration current as

$$I = \frac{\kappa(V - V_0)A}{z}$$

Equation 2.40

where V_0 which is defined in this work as the component of the voltage required at the electrodes to drive the electrochemical reactions which is therefore unavailable to drive migration in the gap (see Section 2.5).

At any time the rate of change of gap will be given by the balance of the erosion rate of the workpiece and the feed rate

$$\frac{dz}{dt} = \frac{dy}{dt} - f$$

Equation 2.41

Substituting Equations 2.37 and 2.39 into Equation 2.41 gives

$$\frac{dz}{dt} = \frac{\kappa(V - V_0)M}{\rho F n z} - f$$

Equation 2.42

or

$$\frac{dz}{dt} = \frac{k}{z} - f$$

Equation 2.43

where

$$k = \frac{\kappa(V - V_0)M}{\rho F n}$$

Equation 2.44

The significance of k is that it is the combined ECM machining parameter, which defines the value of z_∞ for any given value of f. Therefore, k is a combined parameter containing the parameters that govern the dissolution process. These parameters are the applied voltage between the electrodes, V, the overvoltage, V_0, the dissolution valency, n, and the electrolyte conductivity, κ. It is these parameters that control the dissolution characteristics of ECM and it is therefore important to be able to measure these parameters in order to gain insight into the dissolution process. Traditional electrochemical voltammetric measurements have provided some insight into the electrochemical dissolution process but at much lower current densities (< 1 A cm^{-2}) than those used in ECM (100 A cm^{-2}). It is not obvious that parameters obtained from these measurements can be directly applied to the high current high voltage process of industrial ECM. For example, it has been shown that oxide layer thickness and structure on steel workpieces are dependent upon voltage at low V and therefore V_0 may change [114] and/or the kinetics and mechanism of transpassive dissolution may also be different at greater I and hence V and V_0. Therefore, in the absence of experimental evidence, traditional voltammetric measurements cannot be applied with confidence to

ECM, and voltammetric measurements at conditions applicable to ECM are required (see Section 2.5).

There have been some previous attempts to determine the physical parameters (n, κ and V_0) that give insight into the chemical processes occurring during ECM. It has been shown [122] when machining at a constant current with no tool feed that the overvoltage and conductivity can be determined from the intercept and gradient respectively of a linear graph relating I_0 and V, using

$$I_0 = \frac{\kappa(V - V_0)A}{z_0}$$

Equation 2.40

The valency was determined through comparing the mass of material dissolved with the charge passed (assuming constant valency throughout). This is a valid method for determining the chemical parameters but it could only be performed by repeated ex situ measurements as the experiment had to be stopped in order to measure the mass of material removed. Such static measurement techniques require repeated time-consuming measurements to check for interparameter dependencies, which often make complete parameterisation impractical. Therefore, an electrochemical method for analysing current-time transients [123] and obtaining the chemical process parameters in real time ECM conditions has been developed and used throughout this thesis. This will now be explained in more detail.

2.8.2 Chronoamperometric analysis

Taking Equation 2.43 as the time dependent description of the ECM planar system at equilibrium, as the current, I_∞ (i.e. I when $t \rightarrow \infty$) is constant, the interelectrode gap, z, is constant at z_∞ and $dz/dt = 0$ and the feed rate, f, is equal to the dissolution rate, dy/dt. Therefore, from Equation 2.43

$$f = \frac{k}{z_\infty}$$

Equation 2.45

Combining Equations 2.43 and Equation 2.45 gives

$$\frac{dz}{dt} = k\left[\frac{1}{z} - \frac{1}{z_\infty}\right]$$

Equation 2.46

As

$$\frac{1}{z} - \frac{1}{z_\infty} = \frac{z_\infty - z}{zz_\infty}$$

Equation 2.47

by substitution of Equation 2.47 into Equation 2.46, one obtains

$$\left(\frac{zz_\infty}{z_\infty - z}\right)dz = kdt$$

Equation 2.48

Integrating from $t = 0$, $z = z_0$ to $t = t$, $z = z$, one obtains

$$\int_{z_0}^{z} \frac{zz_\infty}{(z_\infty - z)} dz = \int_{t_0}^{t} kdt$$

Equation 2.49

If $\alpha = z_\infty - z$ then $d\alpha = -dz$ and $z \rightarrow \alpha = z_\infty - z$ and $z_0 \rightarrow \alpha_0 = z_\infty - z_0$. In this case $zz_\infty \rightarrow z_\infty(z_\infty - \alpha)$ and on substituting into Equation 2.43

$$-\int_{(z_\infty - z_0)}^{(z_\infty - z)} \frac{z_\infty(z_\infty - \alpha)}{\alpha} d\alpha = \int_{t_0}^{t} kdt$$

Equation 2.50

which rearranges to (assuming k is independent of t and I)

$$-z_\infty^{\,2} \int_{(z_\infty - z_0)}^{(z_\infty - z)} \left(\frac{1}{\alpha} - \frac{1}{z_\infty}\right) d\alpha = k(t - t_0)$$

Equation 2.51

and therefore

$$-z_\infty^{\,2}\left\{\left[\ln\alpha\right]_{z_\infty-z_0}^{z_\infty-z}-\left[\frac{\alpha}{z_\infty}\right]_{z_\infty-z_0}^{z_\infty-z}\right\}=k(t-t_0)$$

Equation 2.52

which gives

$$\ln\left[\frac{z_\infty-z_0}{z_\infty-z}\right]+\frac{z_0-z}{z_\infty}=\frac{k(t-t_0)}{z_\infty^{\,2}}$$

Equation 2.53

At equilibrium the gap can be expressed in terms of the feed rate, f, as z_∞ = k/f (from Equation 2.45) and this can be substituted into Equation 2.53 so that the RHS becomes $f^2(t - t_0)/k$ and one obtains

$$\ln\left[\frac{1-\frac{z_0}{z_\infty}}{1-\frac{z}{z_\infty}}\right]+\left(\frac{z_0}{z_\infty}-\frac{z}{z_\infty}\right)=\frac{f^2(t-t_0)}{k}$$

Equation 2.54

Equation 2.54 defines the gap-time system function. This function can be fitted to gap-time data using an iterative computation from which the equilibrium gap is determined from z at t $\rightarrow \infty$ and k are also determined once initial values of z_0 and t_0 are chosen. However, in this thesis a variation of this Equation is used where the current data is used rather than the gap data. From Equation 2.40 the appropriate values of I_0 with $z = z_0$ at $t = t_0$, I with z = z and I_∞ with $z = z_\infty$ can be substituted into Equation 2.54, to give

$$\ln\left[\frac{1-\frac{I_\infty}{I_0}}{1-\frac{I_\infty}{I}}\right]+\left(\frac{I_\infty}{I_0}-\frac{I_\infty}{I}\right)=\frac{f^2(t-t_0)}{k}$$

Equation 2.55

Equation 2.55 can then be used to perform chronoamperometric analysis by non-linear regression with iterative fitting of the I and t data to obtain f^2/k (and hence k). I_∞ is determined as I at long t. This fitting is carried out in this work using the Levenberg-

Marquardt algorithm in Origin 6.1 (OriginLab). To avoid double layer and other charging effects seen at short times after the voltage V is applied, the initial time (t_0) and current (I_0) are usually chosen to be the earliest time after the voltage is applied when stable machining conditions were reached with a slowly rising value of I. Therefore, k can be determined for any specified feed rate, f. For non-ideal conditions when k is not constant, deviations in the fit of Equation 2.55 to experimental data would be observed. It should be emphasised for this treatment that the assumption that k is constant under ideal conditions is only valid if V_0 does not vary appreciably with I (Section 2.5).

A series of theoretical curves can be produced using Equation 2.55 for the dimensionless current transients which would be obtained at different values of I_0/I_∞ that correspond to different values of the start gap with respect to the equilibrium gap (z_∞/z_0) as a function of dimensionless time (f^2t/k). Figure 2.11 shows the theoretical relationship both when $I_0 > I_\infty$ and when $I_0 < I_\infty$. These two conditions produce very different current transients. When $I_0 > I_\infty$ then the dz/dt term is much greater then the f term in Equation 2.41. I varies with $t^{-1/2}$ initially therefore producing a relatively steep decrease in current until the equilibrium current is reached. When $I_0 < I_\infty$ (large initial gap) then the dissolution current is low and remains low until the feed closes the gap to near to the equilibrium gap, where a rise in current to the equilibrium current is observed producing an S-shaped curve (Figure 2.11).

In ECM the condition where $I_0 < I_\infty$ is generally used as this ensures a large start gap and therefore reduces the possibility of shorting, sparking and electrolyte breakdown. When using constant voltage (see Section 1.5) these processes can severely damage the electrodes. Therefore, rising S-shaped current transients are typically observed.

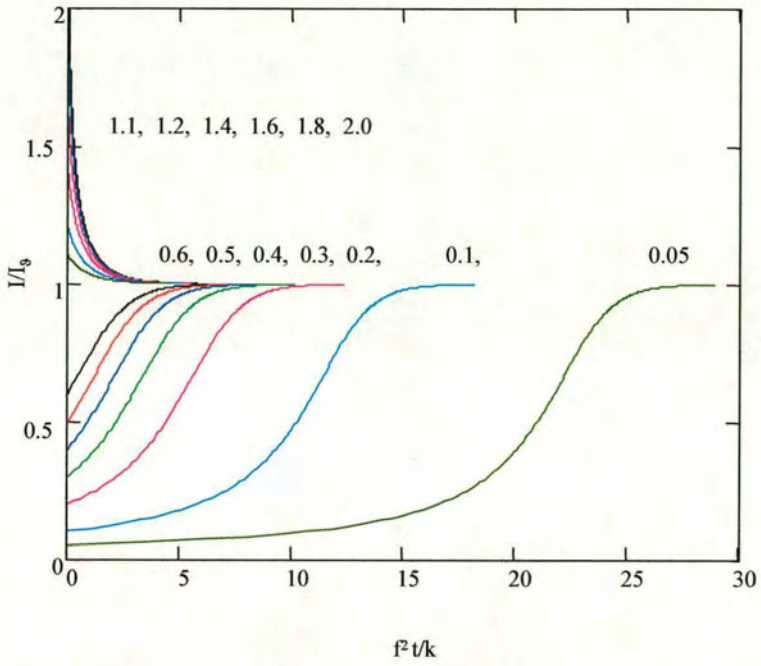

Figure 2.11: Theoretical normalised current (I/I_∞) vs. normalised time (f^2t/k) curves for ECM using Equation 2.55. Values of initial normalised current (I_0/I_∞) are shown on the diagram for each curve.

The mean dissolution valency can be calculated by

$$n = \frac{I_\infty M}{fAF\rho}$$

Equation 2.39

V_0 can also be calculated from rearranging Equation 2.44 to give

$$V_0 = V - \left(\frac{\frac{k}{f^2} nF\rho f^2}{\kappa M} \right)$$

Equation 2.56

As k/f^2 is produced by an iterative fit to Equation 2.55 then this value can simply be entered into Equation 2.56 to give V_0. In addition V_0 can be obtained using k/f^2 and I_0/A.

$$\frac{k}{f^2} = \frac{\kappa(V - V_0)M}{\rho F n f^2} \propto (V - V_0)$$

Equation 2.44

and

$$\frac{I_0}{A} = \frac{\kappa(V - V_0)}{z_0} \propto (V - V_0)$$

Equation 2.40

as z_0, the starting interelectrode gap is constant. When k/f^2 and I_0/A are plotted against V, if straight-line graphs are obtained which intercept on the V axis at a common point, then this indicates a constant value of V_0, given by the intercept.

Therefore, the valency, n and the overpotential, V_0 can be determined from this chronoamperometric analysis. The conductivity, κ, can also be obtained from Equation 2.40. This can also be measured ex-situ (with a conductivity meter allowing a test of the constant conductivity assumption of the derivation). This enables the independent measurement of all three chemical parameters for a system with an invariant value of k. Note that it is also possible to extend this approach to measure variation in the value of k throughout an ECM process by iterative fitting of the current-time data over short time segments of the current-time transient, where the variation in k is sufficiently small to ensure that the assumption of constant k for the data is valid. Comparison of the values of k for each of these segments then enables the variation of k with I and t to be studied [124].

2.9 Theoretical treatment of segments 2 to 6

It has been shown that segments 2 –6 behave as the single planar tool in that unusual effects are not observed (see Section 4.3). Therefore, Equations 2.39 (determine n), 2.56 (determine V_0), 2.44 (determine k/f^2) and 2.40 (determine I_0/A) can all be applied to segments 2 – 6 and the experimental results fit the theoretical Equations. However, this is not the case with segments 1 and 7 for Cell 99. The current-time response of these segments will now be discussed.

2.10 Theoretical treatment of segments 1 and 7 for Cell 99

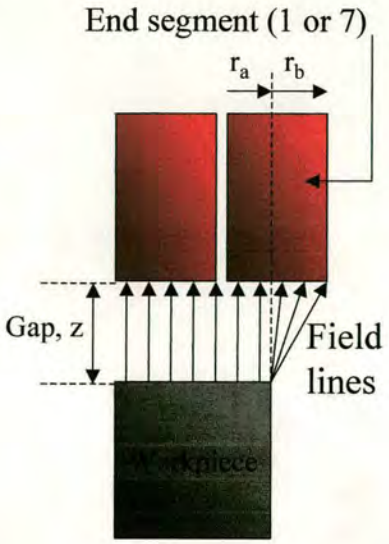

Figure 2.12: A diagram showing r, z and the field lines for segment 1 and 7 in Cell 99.

The current from the overhanging segments 1 and 7 in Cell 99 due to migration can be modelled as two distinct areas [124]. The first has a width, r_a, and depth, l, (the depth of all the segments) and is where the segment and workpiece lie directly over one another and have normal field lines. This area would be expected to behave in a similar manner to segments 2-6 (Section 2.9). The second is concerned with the overlapping part of the segment with width, r_b, and depth, l, which will produce non normal field lines (see Figure 2.12 for r_a and r_b). The overall current for either segment 1 or 7, $I_{1,7}$, determined by migration can be approximated as the sum of two terms (assuming a constant interelectrode gap, z across the segments)

$$I_{1,7} = \frac{\kappa(V - V_0)r_a l}{z} + \kappa(V - V_0)l\int_0^{r_b}\frac{1}{\sqrt{r^2 + z^2}}dr$$

Equation 2.57

where the segment width, r, is equal to the sum of r_a and r_b. Substituting r/c =tan u, then

$$I_{1,7} = \frac{\kappa(V - V_0)r_a l}{z} + \kappa(V - V_0)l\int_0^{\tan^{-1}\frac{r_b}{c}}\sec u\,du$$

Equation 2.58

Integrating 2.58 gives

$$I_{1,7} = \frac{\kappa(V - V_0)r_a l}{z} + \kappa(V - V_0)l\left[\ln\left(\tan^{-1}\frac{r_b}{c}\right) + \frac{r_b}{c}\right]$$

Equation 2.59

and therefore

$$I_{1,7} = \frac{\kappa(V - V_0)r_a l}{z} + \kappa(V - V_0)l\left(\ln\frac{\sqrt{2r_b{}^2 + z^2}}{z}\right)$$

Equation 2.60

Now $lr_n = A_n$, the area of segment n = 2, 3, 4, 5 or 6, where r_n is the width of any of the segments n. By substituting from Equation 2.60, then

$$I_{1,7} = \frac{I_n}{r_n}\left[r_a + B\ln\left(\frac{\sqrt{2r_b + B^2}}{B}\right)\right]$$

Equation 2.61

where

$$B = \frac{z_\infty I_{n,\infty}}{I_n} = \frac{\kappa(V - V_0)A_n}{I_n}$$

Equation 2.62

I_n and $I_{n,\infty}$ are the current and equilibrium current (as t approaches infinity) for any of the segments n = 2, 3, 4, 5 or 6 and z_∞ is the equilibrium distance between the tool and workpiece. Therefore, B can be determined at any time for any segment n from the current I_n and either the values of z_∞ and $I_{n,\infty}$ or the values of κ and V_0 and the area of the segment, A_n. This allows the calculation of $I_{1,7}$ at any time from Equation 2.61 using the calculated values of B and measured values of r_a, r_b, r_n and I_n. However, $I_{1,7}$ corresponds to the current that would be observed whilst maintaining a planar workpiece. This will only apply at the onset of machining as at the end of the workpiece (segments 1 and 7) the increased migrational flux from the overlapping tool will lead to increased machining and an increasingly pronounced workpiece curvature at these points. This has been observed experimentally.

This curvature acts to increase the workpiece-tool distance and decrease the machining current. At longer times, machining conditions approach equilibrium where there is no further change in the workpiece shape and hence the tool-workpiece separation or the currents for any segment with time. Under these conditions, as the amount of metal dissolved from the workpiece per unit area by each segment will be the same and will exactly balance the feed rate, the currents for segments 1 and 7, $I_{1,7}$, will be given by

$$I_{1,7} = \frac{I_n r_a}{r_n}$$

Equation 2.63

with the particular conditions as $t \rightarrow \infty$ of

$$I_{1,7} = \frac{r_a}{r_n} I_{n,\infty}$$

Equation 2.64

where $I_{1,7,\infty}$ and $I_{n,\infty}$ are the equilibrium machining currents for segments 1 or 7 and a neighbouring segment, n, respectively. The experimental current time transients obtained for segments 1 and 7 should be described by Equation 2.61 at short times and Equations 2.63 and 2.64 at long times, with a transition between these limiting values at intermediate times. The validity of this model has been tested in this work and this has been shown to apply to the ECM of In718 under ideal conditions (see Section 4.5)[124].

2.11 Efficiency

The theoretical chronoamperometric treatment assumes 100 % efficiency, with all anode current being due to the dissolution reaction. However, electrochemical side reactions may occur which would produce more current. For example, the production of oxygen has previously been observed to occur at the workpiece [125] depending on the experimental conditions. In this case the number of electrons passed per atom in generating M^{n+} would be greater then n. In addition, the reduction products from the tool and oxidation products from the workpiece may react together in the gap regenerating materials which can be further oxidised and reduced at the workpiece and tool respectively. This can be considered to be

essentially a short circuit reaction (see Section 6.6). The total current passing between the electrodes is then the total of that resulting in workpiece dissolution and these other reactions such as oxygen production. In this case, the efficiency of ECM can be expressed as

$$\text{efficiency} = \frac{\text{actual metal removal rate}}{\text{theoretical metal removal rate}} \text{x } 100$$

Equation 2.65

Without the complication of these side reactions, under ideal conditions the observed valency n_{obs} equals the actual valency, n, which in ECM is the number of electrons produced per mole of dissolving material and corresponds to the number of moles of electrons removed for a mole of workpiece atoms (giving M^{n+} on average). However, if the dissolution reaction is not the only reaction occurring and side reactions are important then the number of electrons per mole of dissolving material, n_{obs}, calculated form Equations 2.37 and 2.39 would be higher than expected chemically and the calculated valency for the ECM current would deviate from the valency of the dissolving atoms (see Section 6.6). Therefore, an efficiency term, e, can be incorporated into these Equations to take this into account. This replaces the n term by n_{obs}, the observed or calculated valency where $n_{obs} = n/e$, where e is the fractional efficiency. If $e = 1$ only the dissolution reaction occurs. If $e < 1$ other reactions occur and the observed ECM valency is not equal to the dissolution valency of the atoms, n. Therefore, when $e \neq 1$ the ideal dissolution valency can only be determined from the ECM current with a knowledge of e.

Ultimately, it is often not possible to be confident about the dissolution efficiency without independent measurements of the dissolution valency of the workpiece atoms. This is because unless the side reaction is not governed by migration, the ECM current-time analysis will still apply and n_{obs} will be the only valency parameter which can be obtained. Just such an independent measurement is outlined in Section 5.4, where the dissolution valency of chromium was determined by Visible Spectroscopy as Cr(VI). However, the exact dissolution valency cannot always be determined by ex situ measurements. There is often a dependence of e on such parameters as current (see Section 6.6) and flow rate as the degree to which short circuit reactions will be important will depend upon the concentration of products and the distance apart of the electrodes at which they are produced, and these vary with such parameters as current, voltage and flow rate, which vary throughout the experiment. Insensitivity of the measured value of n_{obs} to these parameters can often be used

to discount significant efficiency effects. It is important that for this work, efficiency has been observed to increase with flow rate as the concentration of products in the gap decreases and would be expected to approach e = 1 at flow rate values lower than those used throughout this work except where products are deliberately allowed to accumulate and be recycled e.g. (Section 5.5) [126, 127, 128, 129]. Measurements on the nature and amount of the ECM products as a function of the ECM current have been used to test this assumption (Section 5.5). Furthermore, the relatively high flow rates employed in this work tend to ensure electrolyte flow effects on the current distribution are negligible.

2.12 Determining efficiency changes

When the valency is equal to $n_{obs} = n/e$ and the height of the workpiece is taken to be h, during machining from Equations 2.36 and 2.37

$$\frac{dy}{dt} = -\frac{dh}{dt}$$

Equation 2.66

and substituting into Equation 2.37 with $n_{obs} = n/e$ gives

$$I = -\frac{A\rho nF}{Me}\frac{dh}{dt}$$

Equation 2.67

I can be integrated with respect to time to give Q, passed between an initial time, i, and a final time, f,

$$Q_f - Q_i = \int_{I_i}^{I_f} I dt$$

Equation 2.68

Integrating Equation 2.68 and substitute by Equation 2.67 therefore gives

$$Q_f - Q_i = -\frac{A\rho nF}{Me}\int_{h_i}^{h_f}\frac{dh}{dt}dt$$

Equation 2.69

where f and i denote the final and initial values of those variables and therefore

$$Q_f - Q_i = -\int_{h_i}^{h_f}\frac{A\rho nF}{Me}dh$$

Equation 2.70

which simplifies to

$$Q_f - Q_i = -\frac{A\rho nF}{Me}(h_f - h_i)$$

Equation 2.71

Therefore, a plot of Q vs h results in a graph with a gradient of $-A\rho nF/Me$. If a linear plot is obtained with a negative slope, then n/e is unchanged and can be calculated over a large range of I and z (a good indicator of $e = 1$). If $e < 1$ a dependency of e on I and z (or t) would be expected. If this is the case, and all other variables in the slope can be assumed to be constant, the gradient at any time can be used to calculate n/e, thereby demonstrating the variation in e.

2.13 X-Ray Diffraction (XRD) powder method

Laues's [130] original X-Ray diffraction method consisted of passing a broadband beam of X rays into a single crystal, and recording the diffraction pattern photographically. The idea behind the approach was that a crystal might not be suitably orientated to act as a diffraction grating for a single wavelength, but, whatever its orientation, the Bragg law [131, 132] would be satisfied for at least one of the wavelengths if a range of wavelengths was used.

An alternative technique to Laue's was developed by Peter Debye and Paul Scherrer [88] and independently by Albert Hull [88], who used monochromatic radiation and a powdered sample. When the sample is a powder, at least some of the crystallites will be orientated so

as to satisfy the Bragg condition for each set of planes (hkl). For example, some of the crystallites will be orientated so their (111) planes, of spacing d_{111}, and give rise to a diffracted intensity at the glancing angle θ (Figure 2.13). The crystallites with this glancing angle will lie at all possible angles around the incoming beam, so the diffracted beams lie on a cone around the incident beam of half angle 2θ. Other crystallites will be orientated with different planes satisfying the Bragg law. They give rise to a cone of diffracted intensity with a different half angle. In principle, each set of (hkl) planes gives rise to a diffraction cone, because some of the randomly orientated crystallites will have the correct angle to diffract the incident beam. This was the technique used to analyse the solid dissolution products of the stainless steels.

Powder diffraction techniques are used to identify a sample of a solid substance by comparison of the positions of the diffraction lines and their intensities with a large data bank (the powder diffraction file, which is maintained by the Joint Committee on Powder Diffraction Standards, JCPDS, and contains information on over 30,000 substances).

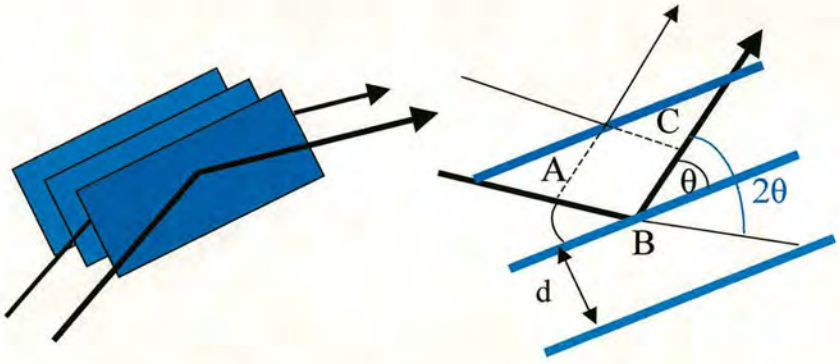

Figure 2.13: A set of planes around the direction of the incident beam give diffracted rays that lie on a cone. Two of these diffracted rays are shown here for clarity. The full powder diffraction pattern is formed by cones corresponding to reflections from all sets of (hkl) planes that satisfy the Bragg law. A reflection at a glancing angle θ gives rise to a reflection at a glancing angle 2θ to the direction of the incident beam.

For many glancing angles the path length difference is not an integral number of wavelengths, and the waves interfere destructively. However, when the path length difference is an integral number of wavelengths (AB + BC = nλ), the reflected waves are in phase and interfere constructively. It follows that a bright reflection should be observed when the glancing angle satisfies the Bragg law

$$n\lambda = 2d\sin\theta$$

Equation 2.72

Reflections with n = 2, 3, ...etc are called second order, third order, and so on; they correspond to path length differences of 2, 3, ...etc wavelengths.

2.14 X-Ray Photoelectron Spectroscopy (XPS) theory

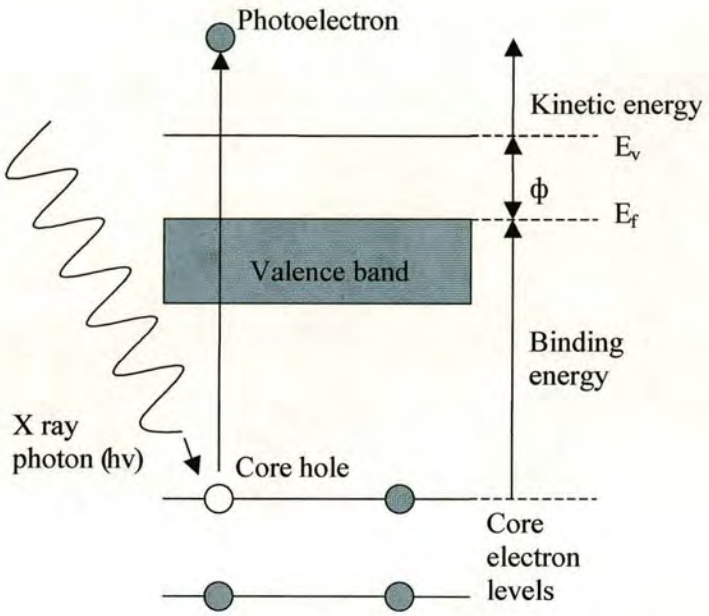

Figure 2.14: Diagram illustrating the three steps involved in XPS. E_f is the energy of the Fermi level, E_v is the energy of the vacuum level and ϕ is the workfunction of the surface.

In XPS, an incident beam of monochromatic X-ray photons each with energy, hυ, is fired at the sample material (Figure 2.14). When a photon collides with an electron it must either be reflected with no reduction in energy or it must give up all its energy to the electron. The latter case is the one of interest in XPS where a core electron can absorb a photon (this process is very fast, ~ 10^{-16} s). The energy of a single photon cannot be shared amongst electrons therefore the number of electrons emitted by a surface is proportional to the number of incident photons. Einstein reasoned that some of the energy imparted by the photon is used to release an electron (core electron in this case) from the surface (overcoming the binding energy, E_b) and that the remaining energy appears as kinetic energy of the emitted electron, hence for an atom, A

$$A + h\nu \rightarrow A^+ + e^-$$

Equation 2.73

Conservation of energy then requires that

$$E(A) + h\nu = E(A^+) + E(e^-)$$

Equation 2.74

Since the electron's energy is present solely as kinetic energy (KE) this can be rearranged to give the following expression for the KE of the photoelectron

$$KE = h\nu - (E(A^+) - E(A))$$

Equation 2.75

The final term in brackets, represents the difference in energy between the ionised and neutral atoms, and is generally called the binding energy (E_b) of the electron. Photoemission can be therefore grouped into 3 steps

1. Absorption and ionisation (initial state effects)
2. Response of atom and creation of photoelectron (final state effects)
3. Transport of electron to surface and escape (extrinsic losses)

These 3 steps will now be discussed in more detail.

If some of the incident photon energy is used to overcome the binding energy (the strength of interaction between the electron (with its quantum numbers n, m, l, s) and the nuclear charge) of the electrons then the kinetic energy of the photoelectron can be shown to be

$$KE = h\nu - E_b$$

Equation 2.76

where $h\upsilon$ is the energy of each incident photon of frequency, υ and KE is the maximum kinetic energy of the emitted electrons. Many of the emitted electrons are involved in collisions on their way out of the surface and therefore emerge with energy which is less than the maximum. It is worth noting that the binding energies (E_b) of energy levels in solids

are conventionally measured with respect to the Fermi-level of the solid, E_f rather than the vacuum level, E_v. This involves a small correction to Equation 2.76 in order to account for the work function ($\phi = E_v - E_f$) of the solid. Therefore, Equation 2.76 can be written as

$$KE = h\nu - E_b - \phi$$

Equation 2.77

where ϕ can be defined as the minimum amount of energy that has to be given to an electron to release it from the surface. If the KE of the photoelectron increases then it follows that E_b will decrease. A range of KE's can be produced from a solid if the valence band is broad. However, as each element has a unique set of core levels then the measured KE of the photoelectrons emitted from these levels can be used to fingerprint elements. ϕ can be determined for each XPS machine and E_b can be measured quantitatively if $h\upsilon$ is fixed by the variation in KE and Equation 2.77. E_b is characteristic of a specific element and its environment and charge (also gives oxidation state). Therefore, XPS can determine specific elements as well as quantitatively measuring the amount of that element present in the sample being tested (see Section 1.18.2).

Chapter 3

Experimental equipment

3.1 ECM experimental configuration

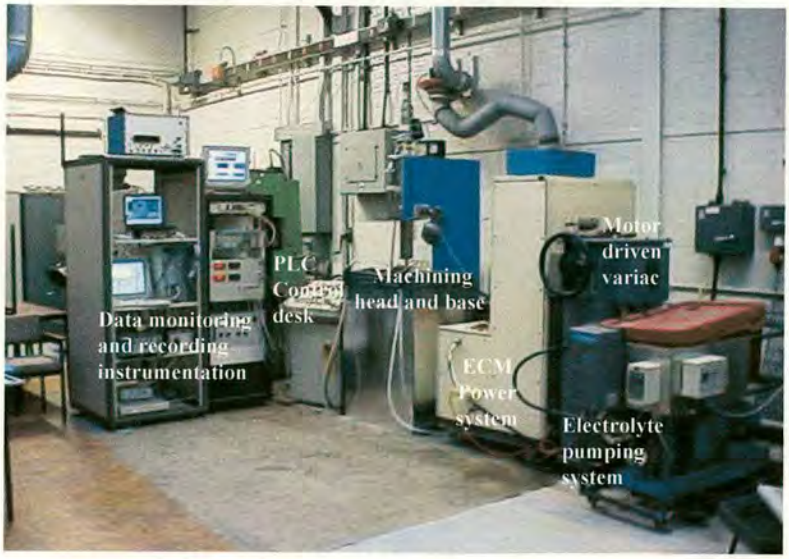

Figure 3.1: View of entire ECM system.

The experimental set-up currently used is shown in Figure 3.1 and is the experimental equipment assembled by Clifton [31]. When the ECM project began there was no off-the-shelf experimental equipment available with the desired flexibility in signal processing and control. Therefore, it was decided to build a complete ECM system in house including all ECM tooling systems and machine cells.

The aim of the in house ECM system was to be able to monitor and control machining parameters and variables. It was also desirable that the reconfiguration of the monitoring and control systems could be readily achieved with minimum adjustment. This was achieved through the design and implementation of a fully customised programmable logic controller (PLC) and a computerised data logging system. Therefore, the system can be divided into:

1. Electrolyte supply system
2. ECM power system
3. Feed control system
4. Parameter monitoring and control / data acquisition system

The design, development, set-up, calibration and operation of these systems will now be described in more detail.

3.1.1 ECM electrolyte flow system

It is very important that stable dissolution is maintained across the workpiece area for the successful application of ECM. In order to achieve this, dissolution products need to be removed and ion depletion minimised such that conductivity is not significantly affected. In addition, the electrolyte flowing through the interelectrode gap heats up primarily due to Joule heating. This could cause local voids in the flow due to vaporisation and, in extreme cases, boiling of the electrolyte. To avoid these effects stable dissolution was maintained by flowing the electrolyte through the interelectrode gap at a sufficiently high rate. Under higher flow rates, changes in conductivity and heating of the electrolyte along the flow path length could be assumed to be negligible and ECM occurs under these ideal conditions. Therefore, reducing the flow rate below high electrolyte flow rates can be regarded as moving towards non-ideal conditions.

There is no clear definition as to what is considered a sufficiently high rate to ensure ideality but flow velocities reported as 30 – 55 m s^{-1} have previously been shown to be sufficient [12]. The higher end of the flow velocity would be required for high dissolution currents and/or long complicated flow paths in order to reduce non-ideal effects. However, a requirement of the ECM system was that the flow velocity could be varied to induce non-ideal conditions and that the flow was smooth i.e. without any pulsation, as this could cause physical movement of the electrodes and/or turbulent or inhomogeneous velocity distributions. The pressure associated with velocities in the range of 30 – 55 m s^{-1} has been reported [12]. For flow passing through a 0.25 mm deep, 40 mm long channel in a planar configuration (similar to the dimensions of the flow path used in this thesis) with a mean flow velocity of 30 m s^{-1} then the inlet pressure would be around 8 bar. This is in agreement with observed pressures in this thesis although the pressure on occasions has been observed to increase to as much as 20 bar (before the cell started to leak electrolyte).

The volume of flow required to achieve flow velocities of 30 m s^{-1} can be calculated from the cross-sectional area of the flow channel multiplied by the velocity of flow. The gap dimensions for the following examples are based on observed gaps with the equipment used throughout this thesis. For a flow velocity of 28 m s^{-1} through an area of 6 x 10^{-6} m^2 (0.4 mm interelectrode gap by 15 mm gap width), a flow volume of 1.67 x 10^{-4} m^3 s^{-1} (10 l min^{-1}) is required. Therefore, flow rates in the order of 10 l min^{-1} can often be considered to be a lower limit for ideal conditions under typical experimental ECM conditions.

The requirements of any pump system would therefore be to produce flow rates at least up to 30 l min^{-1}. A flow rate of 20 l min^{-1} (55 m s^{-1} through a 0.4 mm interelectrode gap by 15 mm gap width) would produce the maximum velocity (55 m s^{-1}) required for ideal flow conditions. The ability to deal with pressures of up to 40 bar and corrosive, oxygenated salt solutions containing metal particulates are also requirements.

3.1.1.1 Selection of a suitable electrolyte pump

The lack of an optimum pumping system for ECM was discussed by Bennett [16]. After reviewing the pumping systems available at the time (1968), it was concluded that "none of them were suitable for pumping corrosive electrolytes at the capacity required in an electrochemical machine". However, pumping technology has improved since the late 1960's and a wide range of pumping options were considered. The criterion for the system were those indicated in Section 3.1.1 and that the system could provide maximum flexibility in terms of controlling the flow velocity. The pumping systems currently available for pumping low viscosity liquids can be placed in two groups: those operating through rotodynamic principles and those operating through positive displacement principles [133]. For a more mathematical description, see Douglas [134].

Rotodynamic systems can be grouped into axial and centrifugal systems. The output (characterised by flow volumes and pressures achieved) is controlled by rotational velocity for both systems. However, axial systems show a steep decrease in efficiency when operating outside a specified optimum flow capacity. Therefore, this type of pump was not suitable for ECM, where a wide range of flow velocities is required. Centrifugal systems are able to provide more broadly defined flow volume/pressure characteristics in which efficiency gradually falls off [134], resulting in stability being maintained over a wider range of flow volumes. The resulting pressure variation as the gap closes towards equilibrium during ECM is not likely to produce large efficiency changes. Therefore, centrifugal systems are the pumps commonly employed in commercial ECM systems. An examination of the specifications of available centrifugal pumps was carried out. However, although the flow volumes required for ECM could be attained, the pressures required for the system could not readily be achieved i.e. above 25 bar. This would limit the system, resulting in stable dissolution at very small gaps (0.2 mm and below) being difficult to maintain. Another requirement of the system was that the flow rate could be easily and accurately varied. However, fine flow rate adjustment would not be possible with centrifugal pumps and also,

electrolyte would readily come into contact with the working parts of the pump therefore causing corrosion. Centrifugal pumps used commercially in ECM systems have to be regularly serviced and in extreme cases replaced after one or two years. Therefore, this type of pump was not thought to be suitable.

Positive displacement pumps were also considered and only reciprocating piston pumps were capable of delivering the required flow volumes. In this case changing the reciprocating rate changes the flow rate. The problem with this type of pump is that due to the reciprocation, pulses of flow are produced which is undesirable, as pulses can move the electrodes due to the pressure fluctuation as well as pulsing the electrolyte flow giving a flow regime which would be undefined. It is possible to smooth out the pulses by applying a damper. However, the damper must be pre-set to operate at a particular pulse rate and therefore flow rate. This type of set-up would not allow the flow rate to be varied during an experiment and so the piston pump/damper system was not considered to be viable.

After considering all the options available a diaphragm pump was chosen for use in the ECM system. This combined the high flow rates of the centrifugal pump with the high pressure capability of positive displacement systems without the pulsing. The pump used was a Hydracell D-25XL (Wanner Engineering Inc. USA). Another advantage of this pump was that all its metallic parts were isolated from the fluid therefore any possibility of corrosion and/or salt precipitation was negated. The pump can also provide high flow pressures of up to 70 bar with flow capacities of up to 45 l min^{-1}. Therefore, this pump was easily able to deal with the flow rates and pressures associated with ECM.

Figure 3.2 shows the pump along with the flow system. This consists of a 3.3 KV motor driven by an S3 frequency inverter (PIV electronics, Netherlands) to enable pump speed and hence flow rate control. The electrolyte was contained within a 60 l tank situated above the pump. The electrolyte was maintained at a constant temperature ± 1 °C by use of a TN2-1KV heater/temperature sensor (Therm-o-level Ltd, UK) which worked in parallel with a water driven heat exchanger. A PDH13 high pressure filter (Pall process filtration Ltd, UK) was placed on the outlet side of the pump in order to remove precipitated solids greater in diameter than 10 μm. This filter was not used for the work detailed in this thesis as the resulting pressure drop from flowing the electrolyte through the filter was found to be too great, and the effect of accumulated particulate products on ECM was to be investigated.

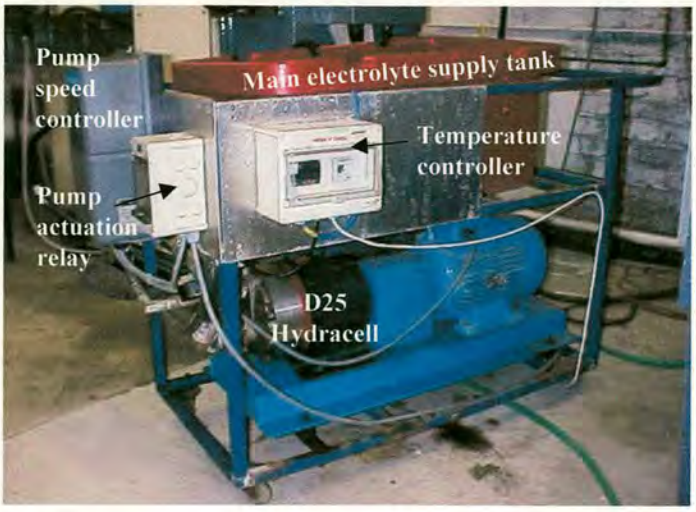

Figure 3.2: Flow system assembly incorporating pump speed controller and electrolyte tank with temperature controller.

3.2 Power System

The main requirement for the power supply system was that it could supply a voltage across the interelectrode gap and maintain this voltage irrespective of the dissolution current. Therefore an RDOA 100/240/415 3 phase variac power supply (Bonar Brentford Electric Ltd, UK), and an isolating transformer/rectifier (Goodyear Ltd) with an output of 600 A at 45 V was chosen.

Voltage control could be achieved by using regulating transistors and associated control electronics for low currents (100 A). However, using this method in ECM, where currents are much higher, would be impractical due to excessive inefficiencies and heat build up within the electronics. Therefore, the voltage was controlled by mechanically maintaining the specified voltage. This was achieved by manually adjusting the displacement between the primary and secondary stages of the variac transformer. This system, when under manual control, was found to be accurate to within ± 0.1 V.

For the efficiency experiments (see Section 6.2), the voltage needed to be more accurately determined. Therefore, a different power supply was used. This was a Farnell Stabilised Power supply Type H30/100. This had an output of 100 A at 30 V with independent control of both current and voltage. However, due to the low maximum current the supply could

take, the workpiece area had to be reduced (1 cm^2) to retain the high current densities associated with ECM. The voltage could then be kept constant to within ± 0.01 V.

3.3 Feed and Control System

The feed, flow and ECM voltage were all controlled from a central system console. This was achieved by an S5-100U programmable logic controller (PLC) (Siemens plc) programmed with S5-ladder program assembly software, which can sequence and control ECM operations. These include:

1. Timed sequencing of flow, ECM power and tool feed

   Sequencing was required so that no damage was inflicted on the tooling assembly. This was accomplished by first initiating the flow at a sufficient rate to maintain stable dissolution, then applying the voltage and tool feed across the interelectrode gap simultaneously. This ensured that dissolution was initiated at the starting interelectrode gap.

2. Selection and adjustment of voltage and flow parameters

   Control signals were generated by the PLC for setting and adjusting the voltage and flow rate (by setting the pump speed) during an experiment. This enabled experiments to be carried out in which either voltage or flow variations were required.

3. Tool feed control and positioning

   Feed reference signals at pre-defined values were generated by the PLC which drive the feed by a DC D110 servo controller which powers a 33 D-series servo/tacho motor (Unimatic plc). The start and stop positions of the feed were controlled by limiting switches connected to the PLC.

4. Current and sparking protection

   The PLC contains a comparator, which detects excessively high dissolution currents. High currents occur when the feed rate, or overvoltages are too high and the workpiece gets very close to the tool. This can result in an electrical discharge between the two electrodes (sparking). Alternatively, the interelectrode gap may

become full of machining products e.g. gases and/or metal particles to such an extent that the conductivity of the electrolyte is severely reduced, or the workpiece may passivate, both of which lead to dissolution failure. In this case, the current will fall and the workpiece can approach and touch the tool. However, this system can detect a sudden increase in current due to either the electrodes touching or getting extremely close, shut down the system and sound an alarm, thereby minimising any damage.

An important requirement for the tool feed system was high stability as well as high positional accuracy. Stability was achieved using a speed compensated pulsed width modulated MSM series servo driver (Infranor Ltd, Switzerland) which drove a DC motor/tacho system enabling highly accurate velocities to be achieved. High positional accuracy was achieved through a ground anti backlash ball screw (6 mm pitch) system. The ball screw was connected to the motor via a 100:1 anti backlash gearbox. This high ratio ensures that the motor velocity is high thereby producing high torque whilst the tool feed rate is relatively low (usually 1 mm min^{-1}). This enables high precision control of the feed rate to be obtained.

The base and head of the ECM machine were donated to the project by AmTech Ltd. Rigidity is provided by means of an I-beam as well as box construction and four symmetrically positioned linear bearings situated along the length of travel (Figure 3.3).

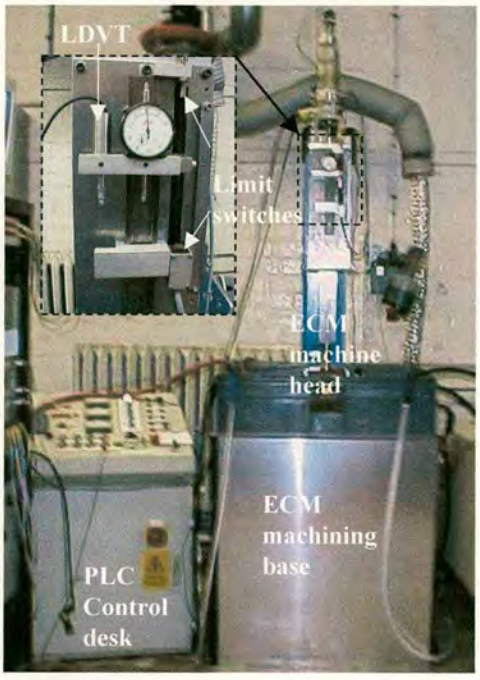

Figure 3.3: PLC control desk and machining base (insert shows LDVT tool position sensor and limit switches).

3.4 Data Acquisition and Parameter Control and Monitoring

All the process parameters and variables were measured and logged using the following systems:

1. Dissolution currents (total and segmented)

   The current was monitored using split core, type 200 SID Hall effect transducers (LEM-HEME, Switzerland) that provide data at an RMS accuracy of ± 1 %. The segment current monitoring array is shown in Figure 3.4.

2. Tool feed rate

   Feed was monitored using a digital to analogue (DAC) module that processes signals from an EC6-CW25C incremented optical encoder (Omron ltd, UK) connected to the drive shaft directly. This produces 1000 pulses per revolution. Therefore, with the 6 mm pitch ball screw and 100:1 gear ratio, 16,000 pulses mm^{-1} travel were produced with a recording resolution of ± 0.01 mm.

3. Flow rate

This was measured using an NT13 (CT Platon Ltd, UK) turbine type flow rate meter with a capacity of 4 to 30 l min^{-1} and an accuracy of ± 1 %.

4. Voltage

This was measured using a type 3192 Hall effect voltage transducer (LEM-HEME, Switzerland) with an accuracy range of ± 1 %.

5. Electrolyte pressure

The inlet and outlet pressures were monitored using a piezoelectric PTX1400 pressure transducer (GEMS Transinstruments Ltd, UK) ± 1 % over the range 0 to 40 bar. The outlet pressure was atmospheric pressure (1 bar) in all the experiments carried out in this work.

6. Tool position

Data was recorded using an LDVT DG2.5 (Solartron Metrology Ltd, UK) with a total travel of 5 ± 0.005 mm. This data was used in the computation of interelectrode gap values. In this case it was important to measure the tool position with a high degree of accuracy as this translates to accuracy in the gap values.

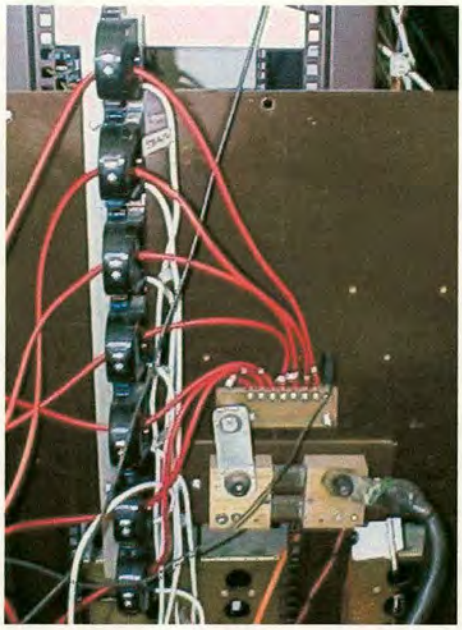

Figure 3.4: Hall-effect transducer array for monitoring of individual segment currents.

A completely programmable parameter monitoring and logging system was also developed. A diagram of this system is shown in Figures 3.5 and 3.6. All sensor and transducer signals are routed through a central board shown in Figure 3.7. This central board allows the system to be reconfigured and allows the signals to pass to additional monitoring equipment such as oscilloscopes and multimeters without interrupting the main data monitoring system. The data was logged using a PCI – 20377 W multifunction data acquisition board (Burr Brown inc, USA). This was located inside an Optiplex GX100 PC (Dell inc, USA). Visual Designer (Burr Brown inc, USA) was used to write a flow diagram, which was subsequently compiled to produce an executable program to log and compute all the system parameters in real time. Various programs were written to incorporate monitoring of different parameters. The program is icon based and enables the flexible logging, manipulation and analysis of data.

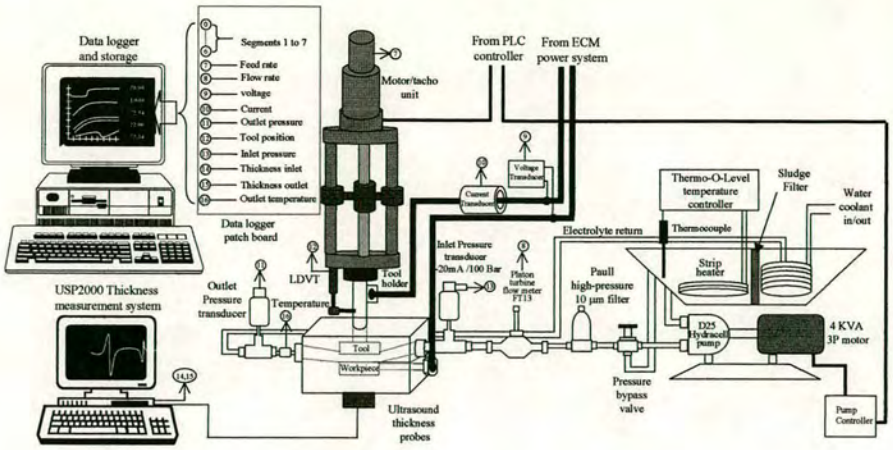

Figure 3.5: Detailed Schematic showing system monitoring and transducer arrangement.

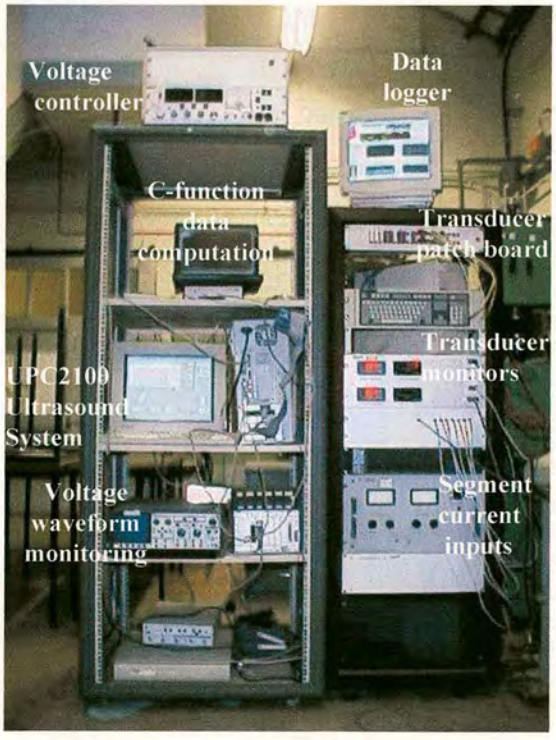

Figure 3.6: System monitoring and data logging arrangement.

Figure 3.7: Patchboard for routing of parameter signals to data logger and/or diverting to monitors.

3.5 ECM flow and tooling configuration

Commercial ECM systems usually enclose the tool and workpiece electrodes with semi open flow systems in a machining chamber where the chamber confines the electrolyte flow. It is assumed that there will be some electrolyte loss between entering the chamber and leaving it. However, this type of system would make it difficult to control and monitor the flow velocity and therefore volume through the interelectrode gap. This is undesirable in the system described here, where electrolyte flow is an important variable. The electrode enclosure will be described as an ECM cell throughout this thesis. The cell consists of the tool and workpiece enclosed in a block arrangement with the feed column and side cheeks (used to direct the electrolyte flow) directly attached to the electrodes (Figure 3.8). Therefore, the ECM cell used for the experiments here fully enclosed the electrodes resulting in no significant electrolyte loss and no alternative pathway for electrolyte flow. These cells have been designed so that the electrode configurations can be interchangeable, which increases the flexibility of the system. There are currently two ECM cells in use. These cells are named cell 99 and cell 2000 (from the year of development). The tooling configurations and specifications of these two cells will now be described.

3.5.1 Tool Configurations

The interelectrode gap is defined by the ECM cell, which maintains a uniform flow path irrespective of the workpiece/tool position (cell 99 feeds the tool towards the workpiece whereas cell 2000 feeds the workpiece towards the tool). Maintaining a uniform electrolyte

flow path enables the flow volume and therefore the flow velocity through the cell to be controlled. In addition, the flow rate must be sufficient so that there are no adverse flow effects in the machining area. Edge effects are known to produce instability in most dissolution systems and can result in passivation along the edge of the flow field [31]. These problems are addressed in the design of the ECM cell. The general electrode arrangement is shown in Figure 3.8.

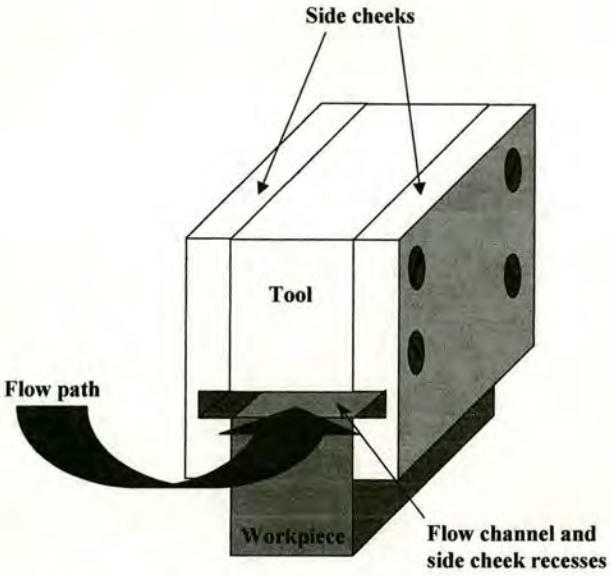

Figure 3.8: General tool and workpiece configuration. The recesses are shown exaggerated for clarity.

The workpiece and tool are encapsulated by insulating side cheeks attached to the tool. These protrude from the tool to encompass the workpiece and therefore guide the electrolyte through the interelectrode gap (Figure 3.8). Therefore, the electrolyte is prevented from flowing around the outside of the side cheeks and flows entirely through the interelectrode gap. Two small recesses of 0.1 mm depth are also present in the side cheeks at the workpiece edge (exaggerated for clarity in Figure 3.8) where the side cheek is level with the tool. These are designed to remove the flow edge effects which may affect machining of the workpiece edge. The volume of these recesses was deliberately kept to a minimum and ensured that less than 1 % of the total flow volume went through these recesses, minimising their effect on the overall velocity. Electrolyte flow should therefore be uniform over the entire machined surface.

The planar tool and feed system shown in Figure 3.9 provides the flexibility required to machine planar or 2-D shapes by replacing the tool. It also incorporates the side cheeks for

channelling the electrolyte flow. An extension of this planar system is the use of a planar-segmented tool. This splits the tool into seven segments and is shown in Figures.3.10 and 3.11. The segments are numbered sequentially from 1 to 7 with segment 1 being at the flow inlet and 7 at the flow outlet. The reason for this tool arrangement is so that multiple chronoamperometric data can be collected and correlated to position along the flow path. The tool segments were insulated from one another by 0.05 mm mica spacers. The segments are held together by two insulated brass bolts. Each of the segments was powered separately by one of an array of seven power connection pins. These pins were screwed into the individual sections at one end with the other end secured to the main feed block. The power cables were secured to each of the pins by purpose made miniature spigot clamps. An array of seven Hall effect transducers were used for independent monitoring of the current flowing through each segment.

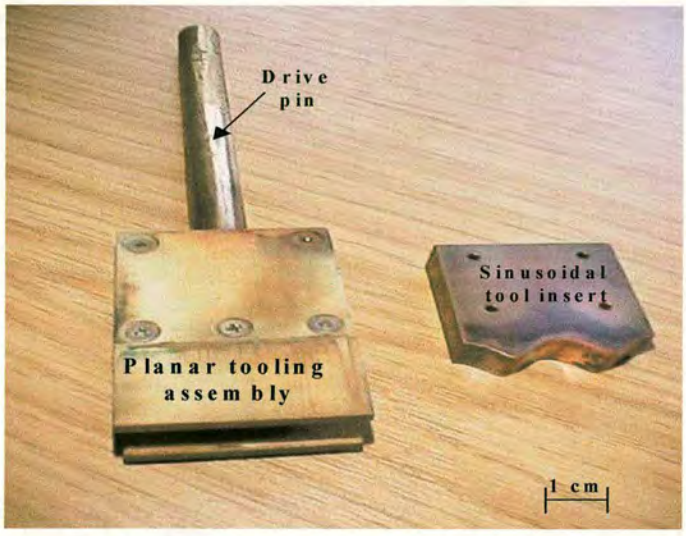

Figure 3.9: Planar tooling together with 2-D sinusoidal tool insert.

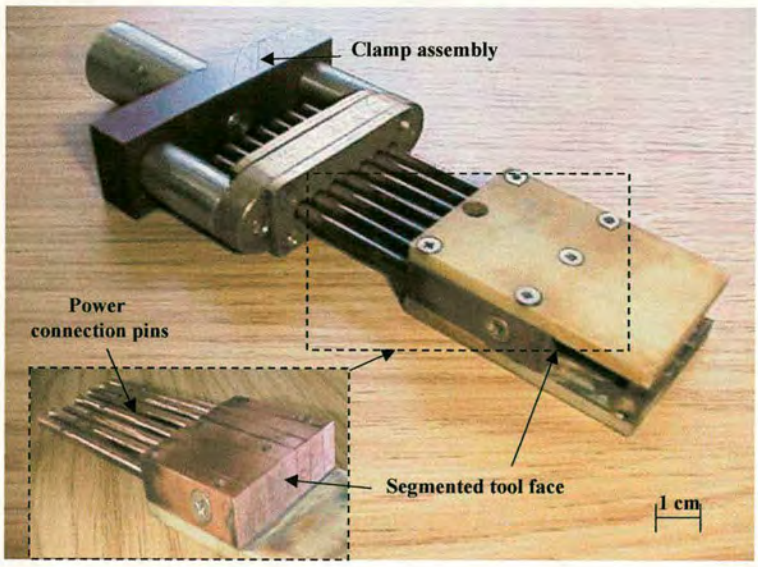

Figure 3.10: Segmented tooling system.

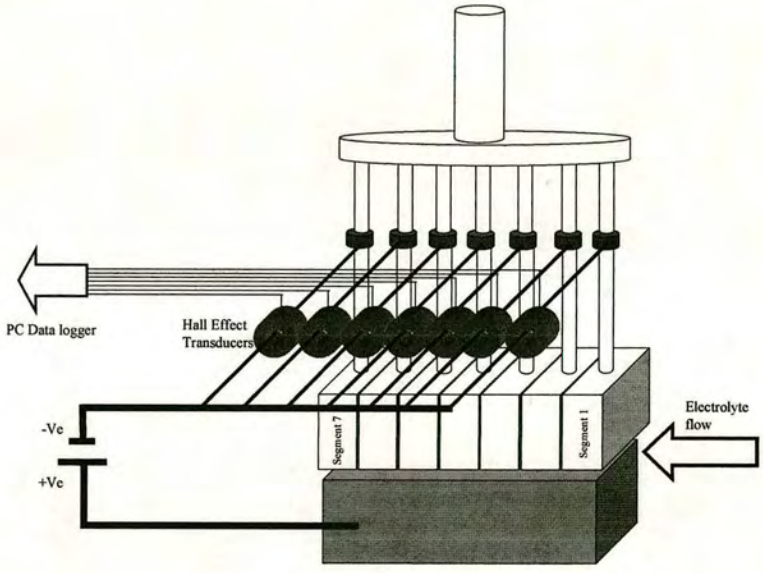

Figure 3.11: Segmented tooling arrangement showing power distribution and monitoring arrangement

3.5.2 Cell Configurations

The design of each new cell was to allow it to fulfil certain experimental requirements. Throughout the progression of the project these requirements changed and hence, each new cell was an enhancement of the general features of previous cells. These features will now be

described in more detail. Cell 2000 represents the latest stage of cell development and therefore only this system is described in detail with regards to set up and system operation.

3.5.2.1 Flow path variance

It is generally known in ECM that the electrolyte flow path inlet and outlet conditions can affect dissolution characteristics. Therefore, in order to simulate ideal conditions the flow path conditions should be invariant with time. This particularly requires that the flow path conditions are the same irrespective of the tool and workpiece positions.

Figure 3.12 shows the flow path conditions for the two different configurations used in cell 99 and 2000. Cell 99 had the tool feeding towards a fixed workpiece, whereas cell 2000 had the workpiece feeding towards a fixed tool. These changes seem to be minor, however, they had a major effect on the flow geometry through the interelectrode gap.

The flow path in cell 99 is illustrated in Figure 3.12a and 3.12b. The initial condition enables the interelectrode flow channel to be aligned with the flow inlet but as machining occurs and the tool is fed towards the workpiece then the flow inlet and interelectrode flow channel are no longer aligned, resulting in a distortion of the flow path.

This problem was minimised in cell 2000, where the workpiece and tool positions are reversed, Figure 3.12c and 3.12d. The interelectrode flow channel now remains in line with the flow inlet regardless of the position of the workpiece. When feeding the workpiece at a constant rate (the most common experimental situation), an initial transient period will occur when the gap height will vary and the workpiece edge will move slightly relative to the flow inlet. However, this will only be a small displacement and certainly when near equilibrium machining, when the feed rate equals the erosion rate, this relative displacement will be zero, and the flow path geometry will be fixed.

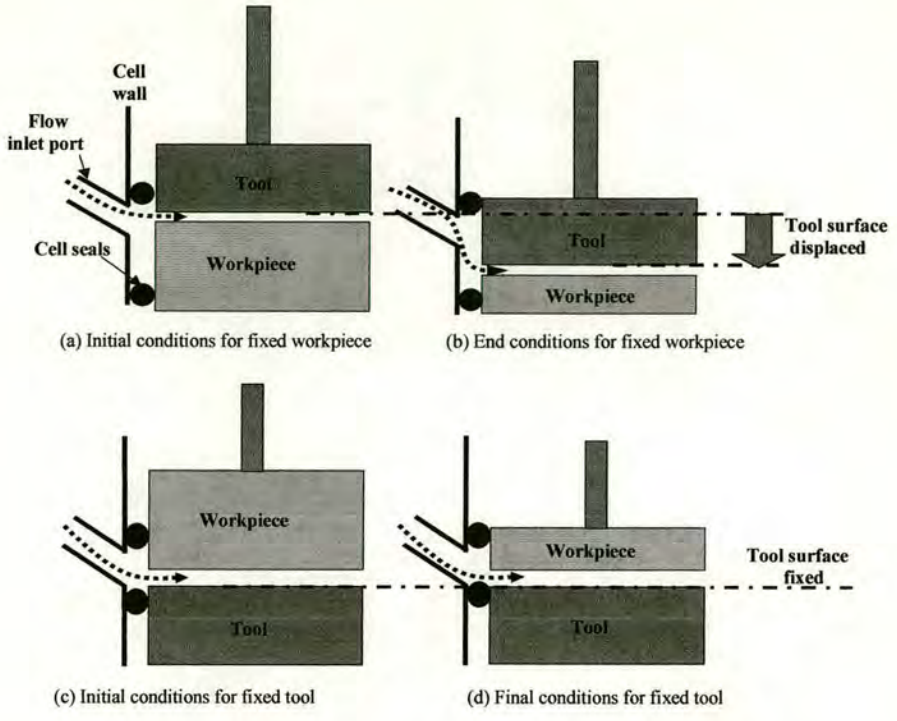

Figure 3.12: Showing flow variation for fixed workpiece or tool configurations.

3.5.3 Cell 99

Cell 99, shown in Figure 3.13, is split into three sections consisting of the top plate, central section and bottom plate. The bottom plate enclosed and clamped the workpiece electrode, the central section enclosed and defined the flow path, and the top section guided and located the tooling arrangement. All three sections were clamped together by symmetrically positioned toggle clamps. Bayonet type quick-release flow connectors were used to attach inlet and outlet flow ports. The use of quick release connectors improved set-up times, since it was found that if the flow connectors were left attached during a tool retraction, then bending of the drive pin could result (this was particularly the case when using the segmented tooling assembly).

Workpiece power was fed through the walls of the lower cell plate via a brass bolt that also acted to clamp the workpiece in position. Cell 99 also incorporated an LDVT position sensor attached to the tooling feed pin and an ultrasound probe (described in Section 3.5.4) attached centrally to the workpiece enclosed within the cell. The main body of the LDVT, containing the sensing coil, was clamped directly to the machine head whilst the sliding pin, containing the transmitting core, was screwed into a rigid mounting plate that was securely attached to

the cell top plate. Mounting the LDVT assembly directly on the cell, and not at a remote position on the machine feed axis, ensures that any compliance in the drive/feed system was not misinterpreted as a change in tool position. During later experiments, this problem was overcome, in the case of cell 2000, by use of an anti-backlash ball screw.

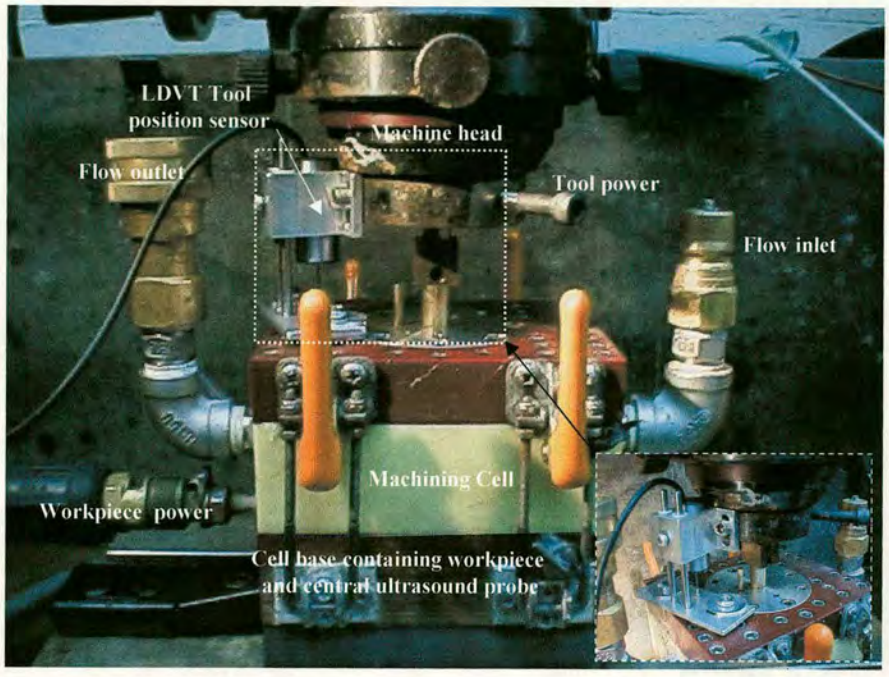

Figure 3.13: Cell 99 shown with LDVT sensor in position.

3.5.4 Ultrasound system

The main additions to cell 2000 were the incorporation of ultrasound probes to measure the workpiece height during machining, allowing the interelectrode gap to be inferred, and the addition of electrolyte sampling tubes. These additions will now be discussed in more detail.

The ultrasound system is relatively complex. All the work carried out on setting up the ultrasound system was carried out by Clifton and therefore more detail can be found in references 135 and 34. A brief overview of the system is provided here.

The ultrasound system used was a non-destructive measurement device based on the principle that sound energy will be partially reflected and partially transmitted when encountering a discontinuity within the elastic properties of a material (commonly correlated

to density discontinuities) or across the boundary of two joined materials. A USPC2100 (Krautkramer Ultrasonics UK Ltd) flaw detection system was used for the ultrasound measurements. This system had a claimed measurement resolution of 0.005 mm. The system also provided a multi-channel upgrade that enabled measurements to be made at several points in parallel. This was exploited in cell 2000 by using two ultrasound probes (CLF4 (Buehler Krautkramer Ltd) piezoelectric/perspex delayline probes) placed at segments 2 and 6. The perspex delay line acted as an interface between the probe face and the surface through which detection was required. The ultrasound probe assembly was therefore an arrangement consisting of the ultrasound transmit/receiver transducer connected in series with a perspex delay line tip.

The ultrasound configuration used in this thesis is shown in Figure 3.14 with the ultrasound probe attached to the bottom of the workpiece. This surface is where the initial reflection occurs (termed the primary interface reflection, IR_p). The ultrasound is directed through the workpiece with further reflections occurring at the workpiece surface/electrolyte interface (termed the primary backwall reflection, BR_p) and also a second reflection (termed the primary gap reflection, GR_p) occurring, through the electrolyte, at the tool surface/ electrolyte interface.

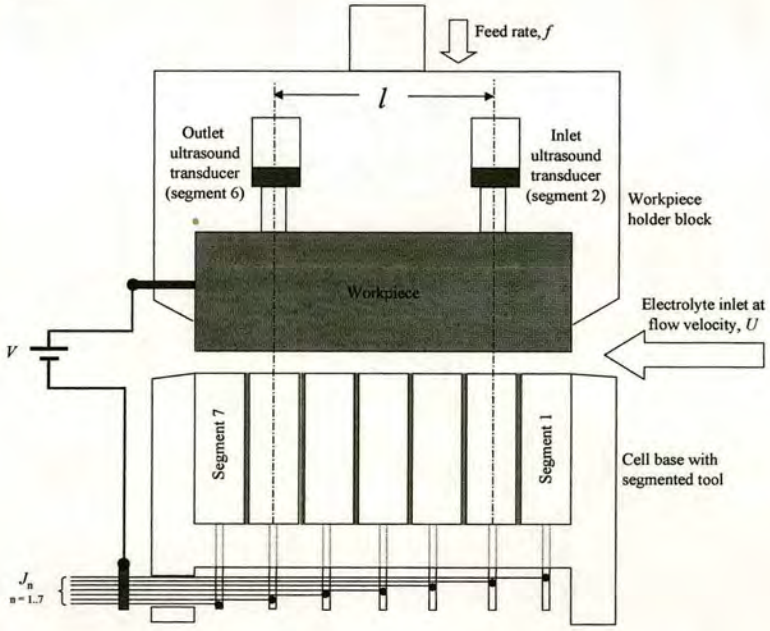

Figure 3.14: Ultrasound configuration.

The Perspex delay line acts to "clean" the sound signal by dampening the sound energy as it is transmitted from the transducer face to the surface of the workpiece material (the IR_p signal).

3.5.4.1 Application of ultrasound to ECM gap measurement

The problem of applying the ultrasound system to gap measurement was which configuration would be most effective, direct or indirect gap measurement. A direct gap measurement refers to the use of ultrasound to measure time-of-flight data directly across the gap (the time-of-flight data are amplitude vs. time signals representing the received ultrasonic pulse) by measuring the time difference between BR_p and GR_p and using the velocity of sound in the electrolyte to calculate the gap, z. Indirect gap measurement refers to using IR_p and BR_p and the velocity of sound in the workpiece to measure the workpiece height and using the difference between the measured tool face position and the workpiece height, h, to give the interelectrode gap. Indirect measurements require that the initial tool position needs to be accurately pre-set and its position monitored throughout the measurement. The direct measurement has the advantage that prior knowledge of the initial set-up position and continuous tool position monitoring is not required. A series of tests were carried out in order to assess which of these options would be most effective.

The feasibility studies of applying ultrasound to the direct measurement of the ECM gap were carried out using cell 99. Cell 99 was modified to include an ultrasound probe sprung loaded against the workpiece surface and positioned at the centre of the flow field. The aim of these experiments was to assess whether the ultrasound could be transmitted, through the workpiece material and then through the electrolyte within the gap, with sufficient signal power so that assessment of the gap size could be achieved. However, it was concluded that the direct method was not feasible. This was because the gap could be measured when the power was off but the small signal disappeared when machining began making it impossible to measure the gap in real time directly. This was most probably due to reflection or scattering of the ultrasound signal in the interelectrode gap from regions of varying electrolyte density (due to H_2 gas bubbles, local concentration gradients and/or localised heating).

Indirect measurement of the ECM gap could be achieved by subtracting tool position data from the measurement of the workpiece height as machining proceeded. Therefore, the

reflection occurring at the workpiece surface/electrolyte interface could be used to produce a continuous output of workpiece height, h, which could be combined with the linear differential voltage transducer (LDVT), to give the tool face position, y. The difference between tool position and the workpiece height would then give the interelectrode gap. The indirect gap measurement method was found to be feasible and therefore it is used throughout this thesis.

Visual Designer data analysis/logging software has been used to compute these gap values using the LDVT and USPC2100 ultrasound output signals. Gap values are measured and logged using the following procedure:

1. The initial gap, z_0, was set, usually at 0.800 ± 0.005 mm.
2. The workpiece height signal was measured by the ultrasonic probe and input into Visual Designer as h_o.
3. The LDVT was adjusted to zero its output and a constant offset parameter was added in the software to give a value of y such that $z_0 = y - h_0 = 0.800$ mm.
4. The gap, z, was calculated dynamically during the experiment as $z = y - h$.

It was concluded that this indirect method of measuring the interelectrode gap by ultrasound could be used reproducibly, and was found to be accurate to within ± 0.015 mm when comparing gap values to cast measurements (see Section 3.6) and also by correlation with current-time data [31].

3.5.5 Electrolyte sampling tubes

The central block in cell 2000 was modified to include tubes so that electrolyte could be sampled from the interelectrode gap. It was hoped that by sampling electrolyte, information regarding the dissolution products of ECM could be gained by subsequently analysing the electrolyte samples (see Section 5.4.1). Three polyurethane tubes were used with an inside diameter of 0.40 mm and a length of 300 mm. These were positioned along the flow path length above segments 2, 4 and 6 at equal spacing, to enable samples to be taken along the flow path (Figure 3.15). The tubes were located with their inside edge at the edge of the tool surface. At equilibrium gaps greater than the tube diameter (0.40 mm), the samples from these tubes will therefore be unrepresentative of the overall electrolyte composition in the

gap and will be expected to contain more products from the tool reaction than the workpiece reaction. Gaps significantly less than 0.40 mm might be expected to contain slightly more products from the workpiece reaction. Typical flows from these tubes were both calculated and measured as being less than 1% of the total electrolyte flow, which enabled sampling without significant perturbation of the electrolyte flow. Electrolyte conductivity was measured using a 4010 conductivity meter (Jenway). This incorporated a temperature probe such that all conductivity values were produced at a constant reference temperature of 25 °C. pH measurements were performed using a Hydrus 300 digital meter (Fisherbrand).

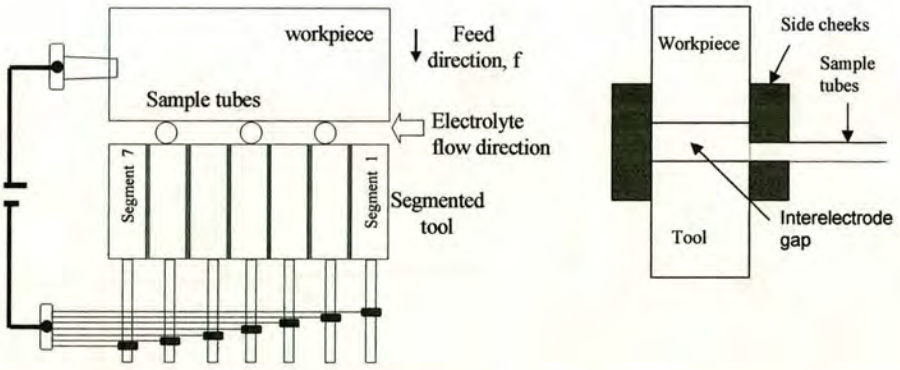

Figure 3.15: Experimental configuration of the segmented tool system (a) front view (b) end view from the end face of segment 7 (flow out of page). The positions of the tubes used to sample the flow are shown (O).

3.6 Cell 2000

Cell 2000 consists of three main elements:

1. A tooling block
2. A workpiece holder/feed pin assembly
3. The main cell enclosure

Cell 2000 used a three-sectioned design and incorporated an inverted feed arrangement in which the workpiece was attached to the drive system (and not the tool as used in cell 99) and was fed towards the stationary tool. This arrangement had several advantages over cell 99, most notably the improved flow path (Section 3.5.2). The other advantages include:

1. Greater rigidity
2. Easier and faster set-up
3. Improved sealing
4. The removal of the need for sliding feed pins on the segmented tool, which had previously been difficult to seal
5. The addition of two ultrasound probes
6. The addition of electrolyte sampling tubes

Cell 2000 was used on the Doncasters machining base that was fitted with an anti-backlash ball screw. The system was very rigid which allowed the LDVT position sensor to be positioned on the main screw assembly, remote from the cell. This arrangement improved the set-up time when using this cell.

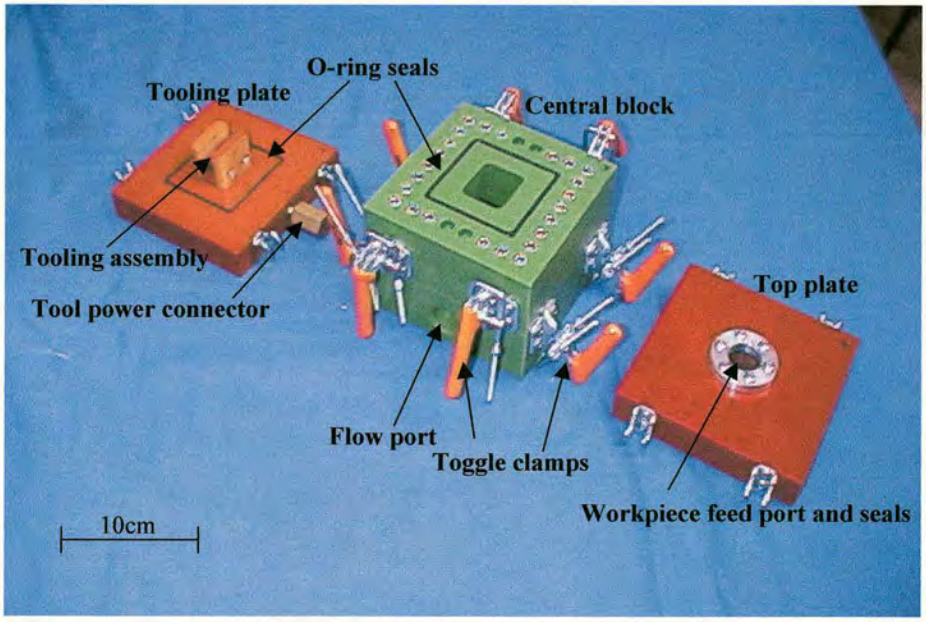

Figure 3.16: Component parts of cell 2000.

Figure 3.16 shows the main cell enclosure split into its three sections. These are a tooling plate, the central block and a top plate. The tooling plate was positioned at the bottom of the cell and was used to locate the tooling assembly. Two tool assemblies were designed for this system, a planar tool and a segmented tool. A single release bolt enabled the systems to be readily interchanged. A tool power connector passed through and locked to the tooling plate that provided the current to the tool. The central block located, via the tool side cheeks, to line up the tooling plate relative to both the workpiece assembly and the flow feed ports.

Eight toggle clamps were situated symmetrically around the sides of the central block; half of these act to pull and seal the central block onto the tooling plate and the other set clamp the top plate onto the central block. The workpiece feed port acted to locate and seal the workpiece in alignment, via the central guide channel, with the tooling face.

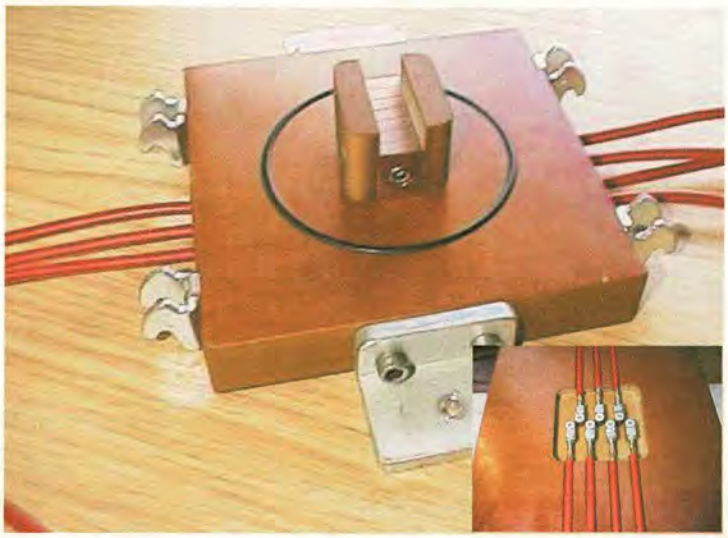

Figure 3.17: Segmented tooling plate for cell 2000 with underside view (insert) showing individual segment connections arrangement.

The tooling plate was changed when carrying out experiments using the segmented tool by replacing the planar tooling assembly with the segmented assembly as shown in Figure 3.17. Power connections are made to each of the seven segments with pins that pass through the plate and locate with individual power cables (see Figure 3.17).

Detailed views of the cell 2000 workpiece/drive pin assembly are shown in Figure 3.18 (a) to (d). It incorporated the ultrasound probes which were used for some experiments into the body of the workpiece assembly. These probes were situated symmetrically about the centre of the flow channel (aligned opposite segments 2 and 6). Two springs were secured to the drive pin end plate (Figure 3.18a) and acted to align the probes flat against the underside of the workpiece. This was required to achieve the maximum power for received ultrasound pulses (as set up trials [31] had indicated that the power of the ultrasound could be significantly reduced if the contact alignment between the probe and the workpiece surface was not exactly parallel). The spring arrangement was also required to ensure that an appropriate amount of contact pressure was achieved (by adjustment of the spring compression length) at the probe tip/workpiece interface. The tool holder assembly was

sealed by use of a silicon rubber compound and cap screws which attached the workpiece holder block to the drive pin end plate. The probe contact points were sealed so that electrolyte could not reach them, at the back-end of the workpiece, as shown in Figure 3.18b. Location of the workpiece firmly against the seal was achieved by tightening the clamping bolt that was part of the clamping tool arrangement as shown in Figure 3.18c. After locating the workpiece on this seal the workpiece clamps screws were tightened to secure the workpiece in position prior to removal of the clamping tool.

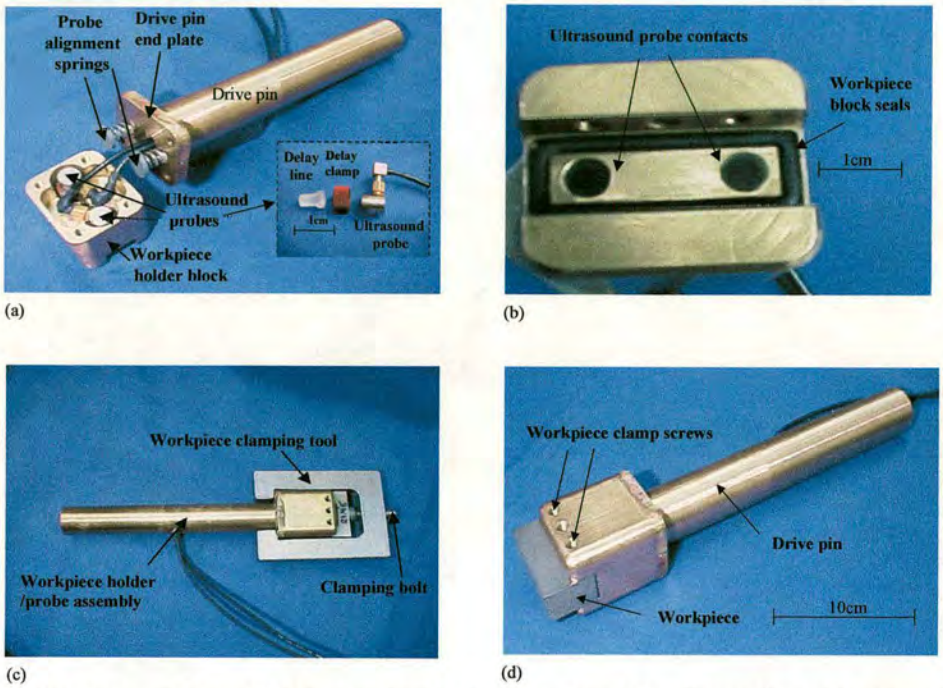

Figure 3.18: Views of Cell 2000 workpiece/drive pin assembly illustrating; (a) internal view of workpiece block showing encapsulated probes, (b) probe contact points and block seals, (c) procedure for workpiece clamping, (d) completed assembly.

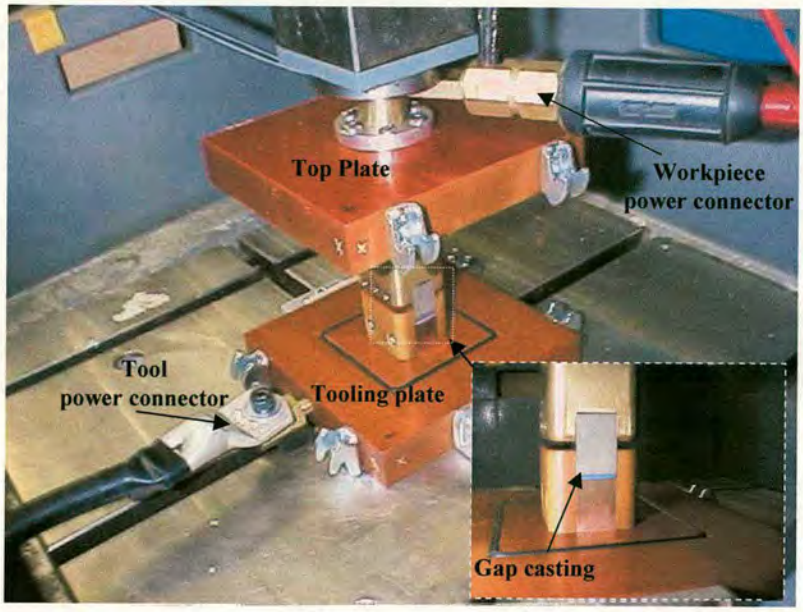

Figure 3.19: Cell 2000 gap measurement procedure.

The three block configuration of cell 2000 aided the accurate pre-setting of the interelectrode gap before a machining experiment. The procedure (Figure 3.19), involved first removing the cell central block and then aligning the tool and workpiece electrodes within the side cheek sections. The cell top and bottom plates were then located and clamped to the machined head and the table respectively. A feeler gauge was then used to set the position of the tool face at the required initial gap relative to the workpiece face. A polyether casting solution (Permadyne) was then injected into the tool/workpiece gap. The close-up insert in Figure 3.19 shows the casting compound as solidification was occurring. After solidification (around two minutes), the gap casting was removed from the gap and the casting thickness measured at intervals along the flow axis using a micrometer. The casting was used to provide accurate confirmation of the gap setting and to ensure that the gap was parallel along the machining axis. Where the gap was not parallel (usually due to the initial workpiece specimen not being accurately machined) then an initial stage of ECM machining could be carried out, before the actual experiment, in order to flatten the workpiece relative to the tool surface. Once the initial gap dimensions were confirmed the gap was then measured on the computer monitoring system (according to Section 3.5.4.1).

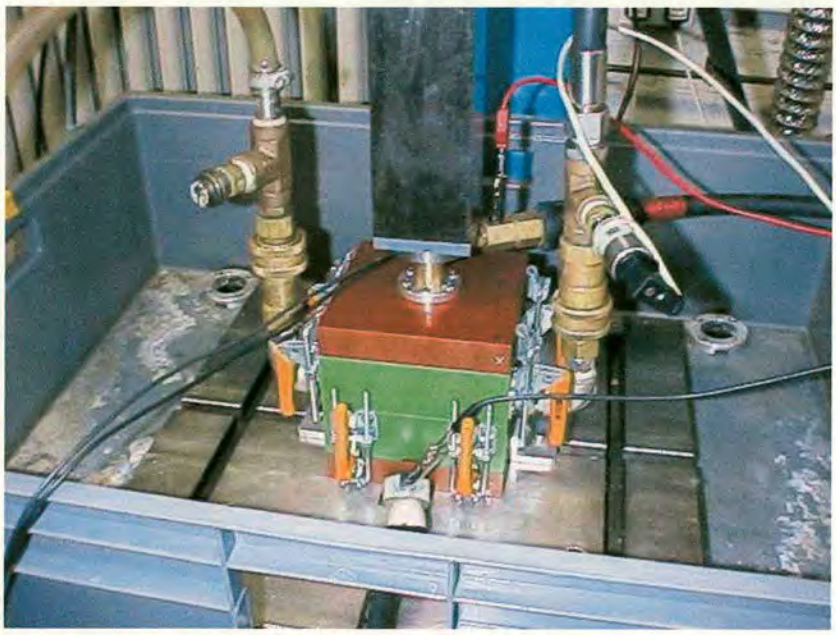

Figure 3.20: Cell 2000 assembled in machine enclosure.

Once the initial set-up procedures were carried out the central section of the cell was positioned on the tool plate and pulled onto the lower seals via the lower toggle clamps. The workpiece plate was then fed back into the set-up position (by re-zeroing the LDVT output) and the remaining four toggle clamps fastened to ensure isolation of the flow channels within the cell and also sealing of the cell against electrolyte loss into the machining chamber. Finally, before beginning an experiment, flow inlet/outlet, electrode power connections and gap voltage monitoring clips were attached to the cell in the arrangement as shown in Figure 3.20.

3.7 Experimental conditions

Unless otherwise stated the experimental conditions used throughout this thesis were as follows.

The workpiece material was the stainless steel of choice as described in Chapter 5. The initial interelectrode gap was 0.800 ± 0.005 mm and a constant voltage of 24.0 ± 0.1 V was applied between the tool and workpiece. The gap was set either by a feeler gauge or by the polyester casting material. The workpiece (or tool) feed rate was kept constant throughout at 1.00 mm min^{-1}. The electrolyte flow rate was either 20.0 l min^{-1} (high flow) although this was reduced to 16 l min^{-1} for some experiments to prevent too high a pressure building up

(no adverse affects were observed to occur with this reduction in flow rate) or 8.0 l min^{-1} (low flow) and the electrolyte was usually recycled. A reservoir of 60 litres of electrolyte was used with an initial temperature of 30 ^{0}C. The electrolytes used throughout were a 15.0 % weight/volume solution of sodium chloride or a 21.7 % solution of sodium nitrate (each 2.56 mol dm^{-3}; Anderson, Gibb and Wilson) as appropriate.

3.8 X-Ray Diffraction Experimental

The XRD machine used to carry out analysis on the solid dissolution products was a Philips PW1730 diffractometer with a flat-plate, theta-2theta geometry Xpert system using an optically-encoded goniometer. The X-rays were generated from a copper K(alpha) radiation source with doublet wavelengths of 1.540560 and 1.544390 Ångstroms. The data recording and analysis was by Philips PC-APD and PC-Identify software respectively, both MS-DOS programs. An in-situ heater was used which was an Anton Paar Infra red temperature controlled heating unit.

XRD scans were performed on the powdered solid products of ECM. Prior to XRD the samples were placed in a centrifuge to separate the solid from the electrolyte. Then the solid was washed with distilled water several times to remove any traces of salt which may have been present and placed in a vacuum dessicator until dry. This dried powder was then X-rayed.

Initial scans were performed at room temperature and the scan time was kept relatively short at 1 hour. It should be remembered that the signal to noise ratio was relatively low, and the spectra obtained were full of noise, but even so no clear peaks could be seen. Therefore, it was suspected that the solid dissolution products could be nanocrystalline leading to large amounts of peak broadening and no XRD spectrum. Therefore, it was decided to anneal the sample. However, the temperature at which the samples would anneal to the extent that peaks could be observed was not known. Therefore a series of scans where the temperature was incremented upwards were performed. This involved heating the sample to the specified temperature, allowing it to stabilise at that temperature and then performing the scan, then increasing the temperature and repeating the process. This cycle was performed and the temperature at which SS316 particles gave a discernable spectrum was at 600 ^{0}C, with the intensity of the spectrum increasing up to a temperature of 800 ^{0}C. Therefore, all the

remaining samples were annealed at a temperature of 800 ^{0}C. However, the risk of annealing at such a high temperature is that the sample may oxidise with O_2 in the air and form the thermodynamic end product which in the case of Fe (which was present in all the steels used) is Fe_2O_3 (Haematite). Therefore, in order to minimise the risk of oxidising the product and changing it, the sample was annealed under a fast flowing stream of Argon gas. Therefore, the Argon stream was used for all the samples.

3.9 X-Ray Photoelectron Spectroscopy Experimental

The XPS machine used to carry out analysis of the steels was a Thermo VG Scientific Sigma Probe XPS instrument. The X-ray source, data acquisition and sample movement were all computer controlled. An inert ion gas gun (Argon) was used to remove surface contamination and etch away surface layers to analyse the bulk sample with depth. An ultra high vacuum (UHV) of 10^{-8} mbar was used which was automatically controlled. In addition a flood gun was used which fired electrons at the sample to prevent surface charging. The analysis software used was a windows based data system called Avantage also provided by VG Scientific.

The solid workpiece samples were quickly wiped with aqua regia (1 part by volume of nitric acid to 3 parts by volume of hydrochloric acid) to remove any traces of dirt or fingerprints to minimise the amount of carbon on the surface. The samples were only wiped with aqua regia to avoid dissolving or significantly altering the surface oxide layer. The samples (powder and solid) were then placed in the sample chamber until a vacuum was reached. The sample holder was then inserted into the measurement chamber where the sample was irradiated with X-rays. The solid samples were sputtered with argon atoms so that a depth profile could be obtained.

The sputtering could be performed by applying between 1 and 5 keV incident energy to the Ar atoms. However, for the samples analysed in this thesis 3 keV and 1 μA were applied for 1 minute which produced an analysis area of 1 mm^2 giving an average sputter rate of 10 nm min^{-1} or 0.166 nm s^{-1} for an unspecified steel sample. Therefore, different elements will have different sputter rates, so, as the depth of the surface oxide layer is unknown in the stainless steel samples then this sputter rate is only a guide to the depth being sputtered. Therefore, 10 nm per sputter is only an average depth etched into the surface.

Chapter 4

Extension of the Planar Tool System to a Segmented Tool for the Analysis of ECM

4.1 Introduction

The object of this section is to show that both the planar and segmented tools can be used to collect current-time (chronoamperometric) data which can be analysed to obtain ECM parameters for any workpiece material. In these experiments the workpiece material, Inconel 718 (In718), was chosen because simple ECM electrochemical dissolution characteristics has previously been observed for the planar tool [31, 123]. These data were chronoamperometrically processed using the theory derived in Section 2.8.2, which gives the combined ECM parameter k. This can be deconvoluted to give V_0 and n for a given workpiece. Theoretical current-time transients are produced which should have the same shape as the experimental transients. Therefore, the closeness of the fit determines the accuracy of the theory. The validity of applying this theory to the planar and segmented tools is tested here. It has already been demonstrated that the planar tool can be used to obtain ECM parameters [123]. This Section looks into if the segmented tool can be used in a similar manner to obtain these parameters at several points along the flow path length. Note that in these experiments cell 99 was used with either the planar or segmented tool unless stated otherwise (see Section 3.5.3 for details on cell 99).

4.2 Planar tool results for In718

Typical current transients for In718 with nitrate and chloride electrolytes using the planar single tool are shown in Figures 4.1 and 4.2. This confirms that the planar single tool can be used to obtain good chronoamperometric fits to In718 data. It is also satisfying that the values of V_0 and n obtained from these data are in reasonable agreement with those values obtained previously [123] i.e. $n = 3.0 \pm 0.2$, V_0 (chloride) $= 3.0 \pm 0.4$, V_0 (nitrate) $= 5.4 \pm 0.4$. This is good agreement with previous work [123] and the closeness of fit confirms the previous observations that it is likely that there is little variation in k either with current or along the flow path length. The In718 system can therefore be considered to be ideal for the initial characterisation and comparison of the planar single tool and planar segmented tool systems.

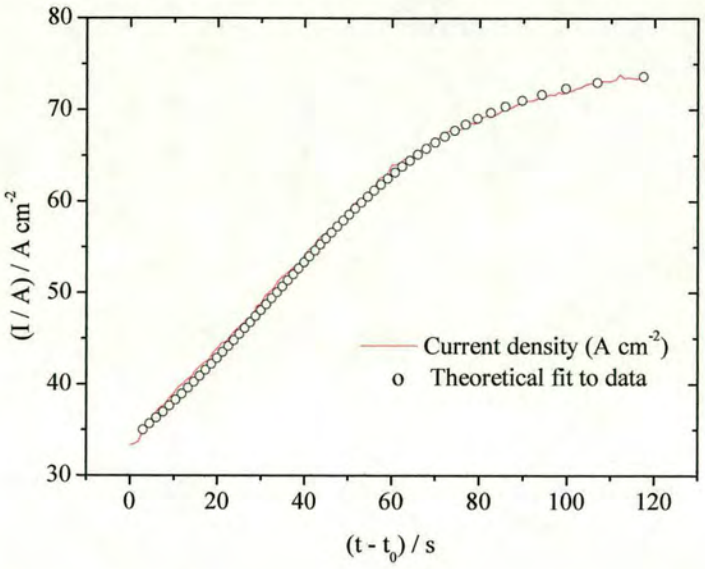

Figure 4.1: Experimental current time data with theoretical fit for the planar tool for In718 in nitrate electrolyte at U = 16.0 l min^{-1} and V = 20.0 V. n = 3.1 ± 0.2 and V_0 = 7.1 ± 0.8 V.

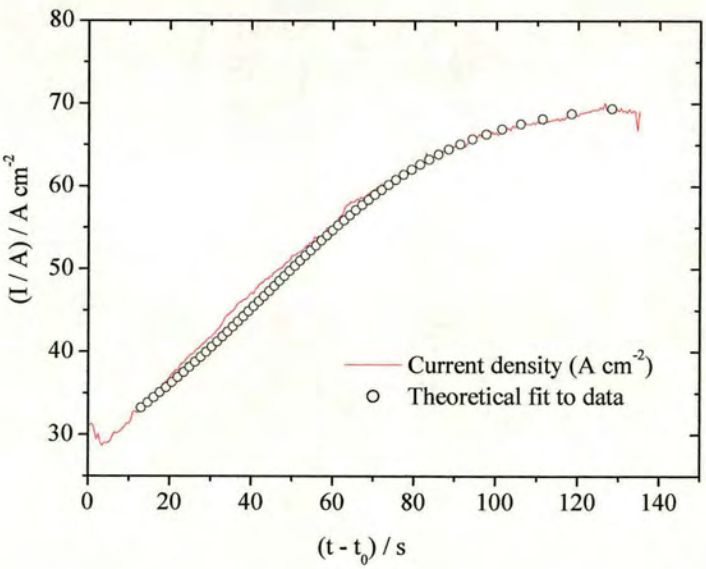

Figure 4.2: Experimental current time data and the theoretical fit for the planar tool for In718 in chloride electrolyte at U = 16.0 l min^{-1} and V = 16.0 V. n = 3.1 ± 0.2 V_0 = 3.4 ± 0.9 V.

4.3 Segmented tool results for In718

The chronoamperometric responses for the segmented tool with In718 and nitrate electrolyte are shown in Figures 4.3 to Figure 4.8 and with chloride in Figure 4.9. Only segments 2 to 6 are shown here as segments 1 and 7 have different characteristics to segments 2 to 6, which will be discussed in Section 4.5.

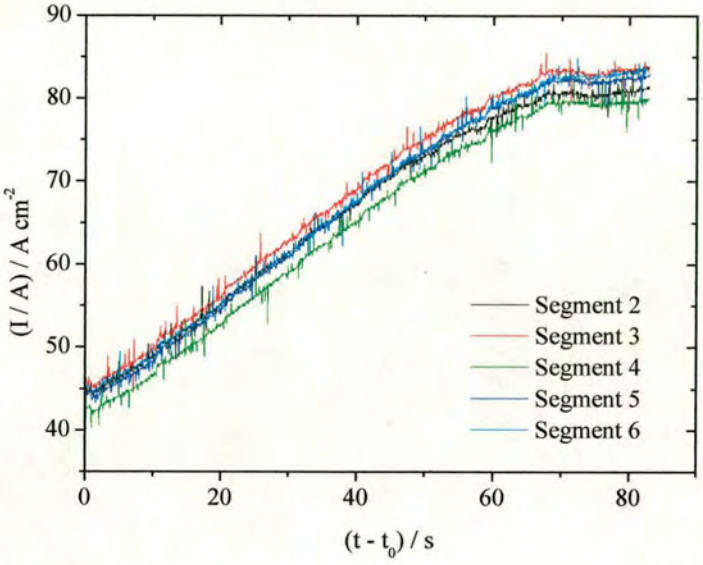

Figure 4.3: Experimental current time data for the segments 2 and 6 for In718 in nitrate electrolyte at U = 18.0 l min^{-1} and V = 20.0 V.

The fits for segments 2 – 6 are now shown for In718 with nitrate electrolyte although it is clear from Figure 4.3 that the segments are the same shape and rise to the same current. Therefore, it would be expected that the theoretical fit to the transients would be similar giving a similar value of k and therefore of V_0 and n.

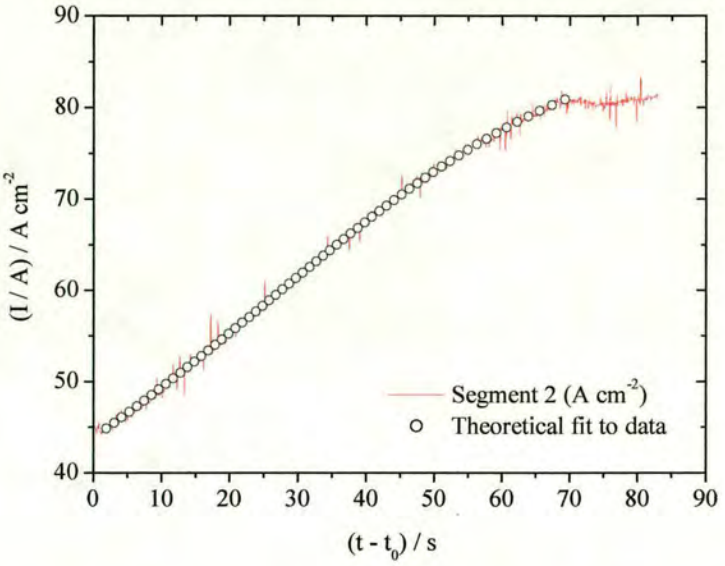

Figure 4.4: Experimental current time data and theoretical fit for segment 2 for In718 in nitrate electrolyte at U = 18.0 l min^{-1} and V = 20.0 V. n = 3.1 ± 0.1 and V_0 = 7.9 ± 0.8 V.

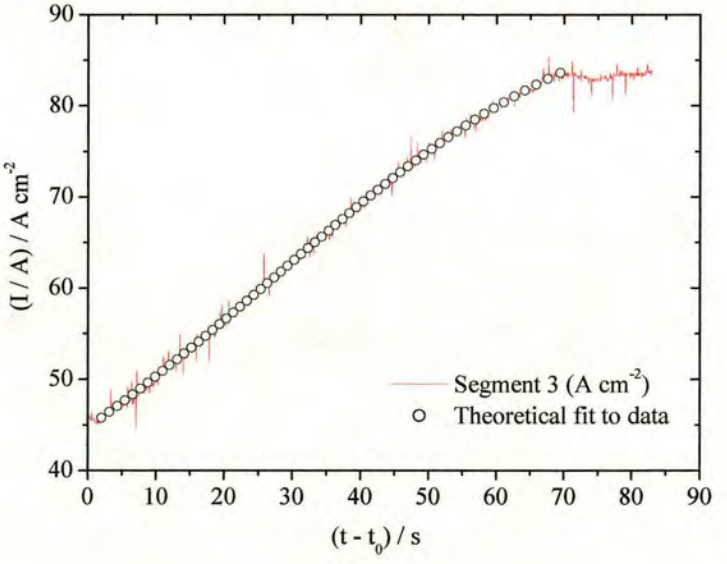

Figure 4.5: Experimental current time data and theoretical fit for segment 3 for In718 in nitrate electrolyte at U = 18.0 l min^{-1} and V = 20.0 V. n = 3.1 ± 0.1 and V_0 = 7.9 ± 0.8 V.

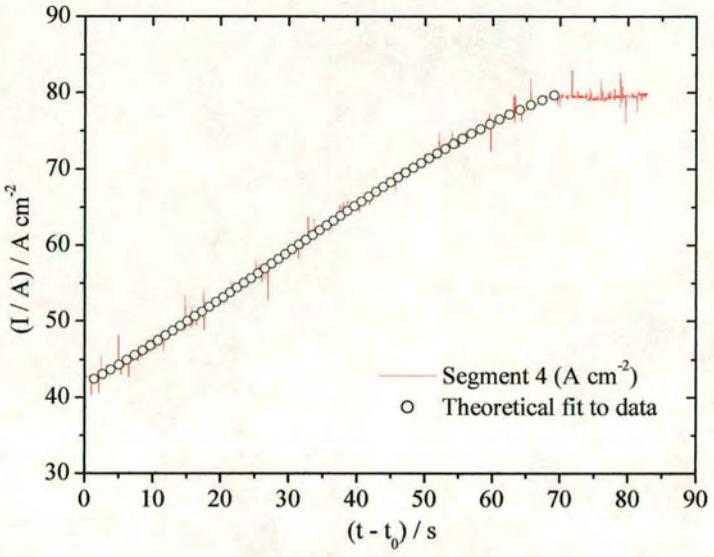

Figure 4.6: Experimental current time data and theoretical fit for segment 4 for In718 in nitrate electrolyte at U = 18.0 l min^{-1} and V = 20.0 V. n = 3.1 ± 0.1 and V_0 = 8.0 ± 0.8 V.

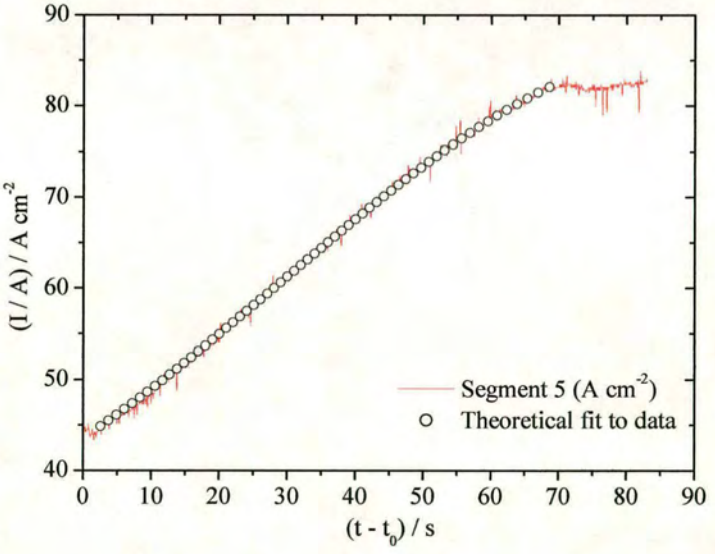

Figure 4.7: Experimental current time data and theoretical fit for segment 5 for In718 in nitrate electrolyte at U = 18.0 l min^{-1} and V = 20.0 V. n = 3.1 ± 0.1 and V_0 = 7.8 ± 0.8 V.

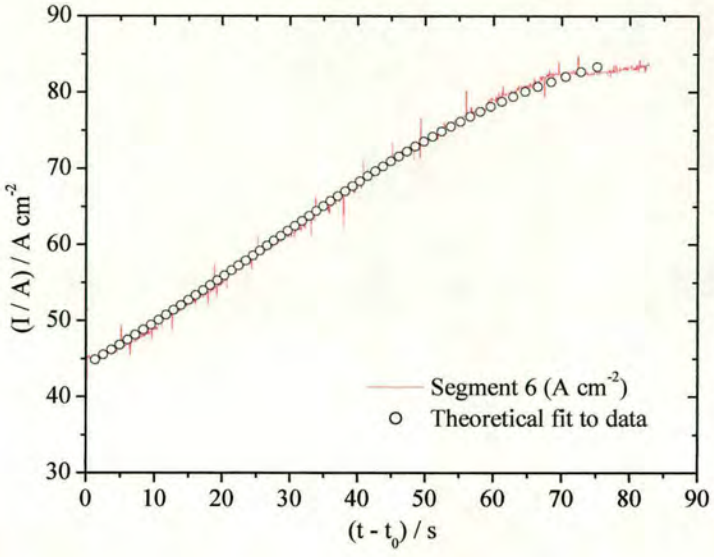

Figure 4.8: Experimental current time data and theoretical fit for segment 6 for In718 in nitrate electrolyte at U = 18.0 l min^{-1} and V = 20.0 V. n = 3.1 ± 0.1 and V_0 = 7.9 ± 0.8 V.

Theoretical fits to segments 2 – 6 were done for all the segmented tool current transients throughout this work and the results are presented where appropriate. However, from now on only selected representative fits are shown in each figure for clarity.

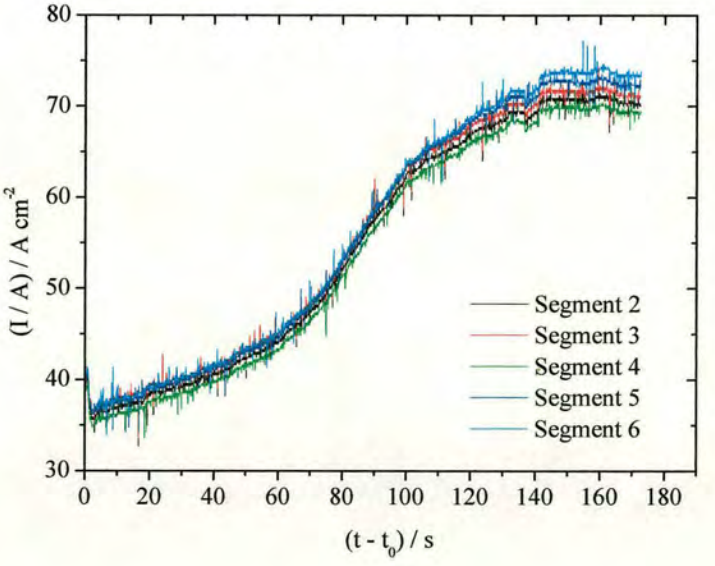

Figure 4.9: Experimental current time data for the segments 2 and 6 for In718 in chloride electrolyte at U = 20.0 l min^{-1} and V = 16.0 V. n = 3.1 ± 0.2 and V_0 = 3.5 ± 0.9 V.

4.4 Discussion of planar and segmented tool results

Using the measured values of ρ and M for In718, it was possible to calculate the dissolution valency and the overpotential using Equations 2.39 and 2.56 in Section 2.2.2 using the theoretical chronoamperometric analysis. The dissolution valency using the planar single tool was n = 3.1 ± 0.2 for both chloride (I_∞/A = 70 ± 2 A cm^{-2}) and nitrate (I_∞/A = 75 ± 2 A cm^{-2}) electrolytes. Using the segmented tool, dissolution valencies of n = 3.1 ± 0.2 were again obtained for both chloride (I_∞/A = 72 ± 2 A cm^{-2}) and nitrate (I_∞/A = 78 ± 2 A cm^{-2}) electrolytes. Therefore, the observed valencies for In718 are internally consistent with Fe dissolving as Fe (III), Cr as Cr (III) and Ni as Ni (III), which are all chemically reasonable [123]. V_0 values obtained from the planar tool were V_0 = 3.4 ± 0.9 V and V_0 = 7.1 ± 0.8 V for chloride and nitrate respectively. The total overvoltages obtained from the segmented tool were V_0 = 3.5 ± 0.9 V and V_0 = 8.1 ± 0.8 V for chloride and nitrate respectively as shown in Table 4.1. The segment overvoltages are given in Table 4.2 for both electrolytes. The value of V_0 was calculated using a value of κ = 0.20 S cm^{-1} previously found in [123] and confirmed in this work by conductivity measurements (see Section 5.4).

Tool	Valency	V_0 total
Planar (Cl^-/NO_3^-)	3.1±0.2 / 3.1±0.2	3.4±0.9 / 7.1±0.8
Segmented (Cl^-/NO_3^-)	3.1±0.2 / 3.1±0.2	3.5±0.9 / 8.1±0.8

Table 4.1: Comparison of the valency and total overvoltages for In718 between the planar and segmented tools.

Segmented Tool	V_0 Seg 2 (V)	V_0 Seg 3 (V)	V_0 Seg 4 (V)	V_0 Seg 5 (V)	V_0 Seg 6 (V)
Chloride electrolyte	3.5 ± 0.9	3.6 ± 0.9	3.6 ± 0.9	3.5 ± 0.9	3.0 ± 0.9
Nitrate electrolyte	7.9 ± 0.8	7.9 ± 0.8	8.0 ± 0.8	7.8 ± 0.8	7.9 ± 0.8

Table 4.2: Comparison of the overvoltages for segments 2 - 6 for In718 with chloride and nitrate electrolytes using the segmented tool.

Therefore, there is good agreement between the planar and segmented tool calculated overvoltages and valencies within experimental error. The chloride experiments were performed at a voltage of V = 16.0 V and the nitrate experiments at V = 20.0 V both with

high enough flow rates (16 – 20 l min^{-1}) to ensure ideal conditions [123], with the conductivity remaining constant. The conductivity, κ, was found to be 0.20 ± 0.01 S cm^{-1} (by theoretically calculating the conductivity of the electrolyte in [123]), which is in good agreement with measured conductivities (see Section 5.4). This good agreement confirms that the products of the electrochemical machining process do not significantly alter the conductivity of the solution as machining progresses (see Section 5.4). It should be noted that the total overvoltage calculated from the planar tool is representative of the average dissolution overvoltage over the entire workpiece area, whereas the values for each segment represent the value for its own individual workpiece area. These values between the planar and segmented tool are in good agreement within experimental error and therefore as expected these indicate little change in ECM characteristics along the flow path length.

Both the planar single tool and segmented tool show the same trends in results in that the overvoltage with nitrate is higher than with chloride. This can be explained by the increase in the ligating ability of chloride ions compared to nitrate ions. Chloride ions tend to form relatively strong complexes with the dissolving species at the workpiece and this would lead to a decrease in the free energy of dissolution and hence a decrease in the oxidation potential. Additionally, chloride ions can disrupt the oxide layer [136, 137] by inserting into the oxide lattice, introducing vacancies and disrupting the structure. Removing or compromising the oxide layer reduces the kinetic barrier to dissolution (and hence V_0) and therefore ions can be ejected more easily (see Section 5.5.1). The Point Defect Model (PDM) [84 - 86] has been used to describe the mechanisms by which the surface oxide layer can be maintained or disrupted. This is discussed in more detail in Section 5.5.1.

The single planar tool was used to establish that (with the possible exception of the very ends of the electrodes) a normal field existed between tool and workpiece. Cell 99 contains seven segments numbered sequentially from 1 to 7 with segment 1 being at the flow inlet and 7 at the flow outlet (Figures 4.10 and 4.11). The tool segments are insulated between one another by very thin, 0.05 mm, mica spacers. Therefore, it can be considered that each segment acts as an entire planar tool where the process parameters for that portion of the workpiece immediately below the segment can be determined, and with successive segments allowing their mapping along the entire flow path. Therefore, any variations in the process parameters can be observed across the workpiece surface. As in the planar single tool the electric field lines can be assumed to be parallel; however, where the segments are separated by mica spacers for insulation, no current can flow, and the field lines must be non-normal. The

results demonstrate that this effect can be considered to be very small, due to the small area of these insulating spacers (0.0075 cm^2 compared to the segment area of 0.70 cm^2). The region below the mica spacer cannot have exactly parallel field lines as dissolution occurs but if z is much greater than the spacer distance then the field lines are almost parallel and would approximate to the normal field line situation, with the effective area of the segment (the area of workpiece dissolved by field from the segment) including half a mica insulating spacer at each segment edge.

The variation in parameters between the segments provides additional information and shows that the overvoltage when machining with nitrate appears to be constant across the whole workpiece surface area within experimental error. The main effect when using nitrate would be expected to be a very small but possibly significant increase in the values of I_0 and k/f^2 with increasing segment number [124], which may be observed due to a very small increase in conductivity (due to thermal and/or compositional changes). When machining with chloride the same trend is observed. The V_0 values are generally constant along the flow path length within experimental error. However, for any set of experimental measurements, there is a consistent increase in k from segment 2 to segment 6. There is no statistical difference between any two segments e.g. 2 and 3, 4 and 5 within experimental error etc but there is a small but significant monotonic increase in k/f^2 from segment 2 to segment 6. This monotonic increase is within experimental error but is consistently reproducible. This infers that there is a small but significant change in k which could be attributed to the overvoltage decreasing down the flow path length showing that the surface oxide barrier layer is getting weaker and therefore dissolution is occurring more easily, as either V_0 decreases or κ increases. This could be consistent with e.g. H_2 products progressively weakening the barrier surface oxide layer along the flow path length (see Section 5.5). It could also be due an increase in κ due to a temperature increase or compositional change inducing a conductivity increase along the flow path length. (Chloride ions would be expected to weaken the oxide layer equally effectively along the flow path length and so a variation of V_0 would not be expected due to chloride ions with flow path length). This small but significant change in k would not have been possible to detect with the single planar tool but the monotonic nature of this change with each successive segment allows its detection, and therefore shows the success of the segmented tool in measuring changes in k along the flow path length. Therefore, the segment current densities of 2 – 6 are in good agreement with the planar system. However, segments 1 and 7 cannot be included into this analysis. The reason for this will now be explained and discussed.

4.5 Analysis of Segments 1 and 7 for In718

Plotting all the segments for In718 with nitrate (Figure 4.10) and chloride (Figure 4.11) it can be seen that segments 1 and 7 are significantly lower that segments 2 – 6.

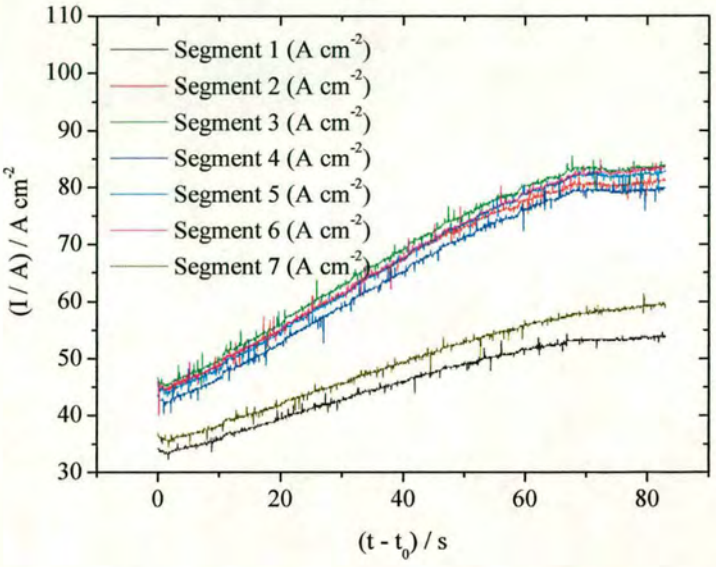

Figure 4.10: Experimental current transients for segments 1 to 7 for In718 with nitrate electrolyte at U = 18.0 l min^{-1} and V = 20.0.

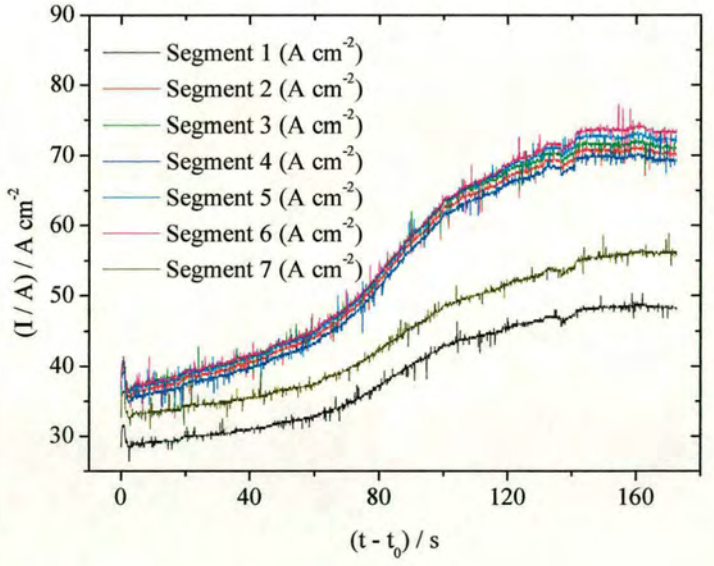

Figure 4.11: Experimental current transients for segments 1 to 7 for In718 with chloride electrolyte at U = 18.0 l min^{-1} and V = 20.0 V.

The segmented tool used in cell 99 contained overlapping segments as shown in Figure 4.12. Segments 1 and 7 slightly overhang the workpiece at each end and therefore the field lines are not parallel at the corner of the workpiece. This leads to an increased density of field at the corner of the workpiece and therefore an increase in the initial migrational current and therefore more erosion taking place at these points. This should result in a rounding over of the edge of the workpiece at each end, which was experimentally observed. Additionally, due to the segment overhanging the workpiece then there was less workpiece surface area machined by these segments and so the current at segments 1 and 7 would be expected to be lower than the other segments, which is again observed (Figure 4.10 and 4.11).

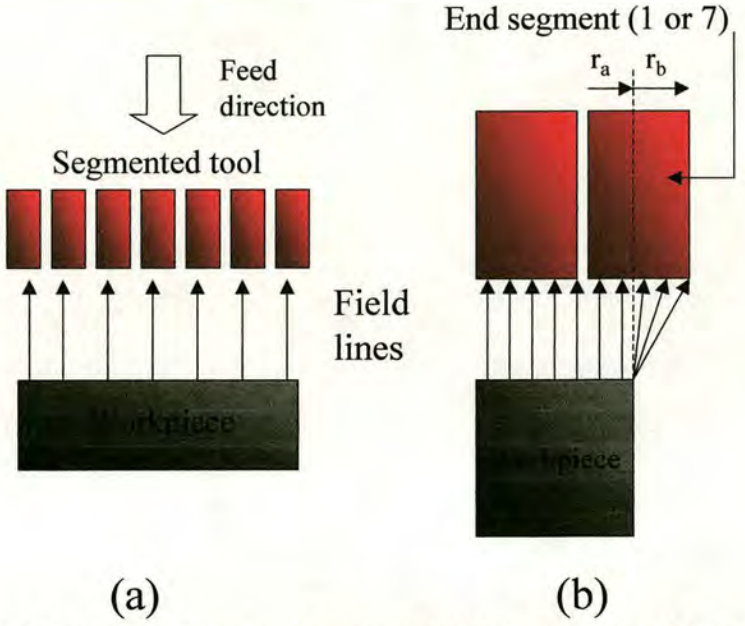

Figure 4.12: (a) A diagram showing the segmented tool used in cell 99 with the parallel electric field lines. The spaces in between each segment represent the mica spacers and are exaggerated for clarity, (b) close up of the end segment (1 or 7) is shown with the parallel field lines and non parallel field lines due to the tool overlapping the workpiece.

The extra complication caused by these overlapping effects can be modelled as shown in Section 2.10. The current from segments 1 or 7, $I_{1,7}$, corresponds to the current that would be observed whilst maintaining a planar workpiece. This will only apply at the onset of machining as at the end of the workpiece (segments 1 and 7) the increased migrational flux from the overlapping tool will lead to increased machining and an increasingly pronounced workpiece curvature at these points. This curvature acts to increase the workpiece-tool distance and decrease the machining current. At longer times, machining conditions

approach equilibrium where there is no further change in the workpiece shape. Therefore, the current at long and short times can be modelled as shown in Figures 4.13 and 4.14.

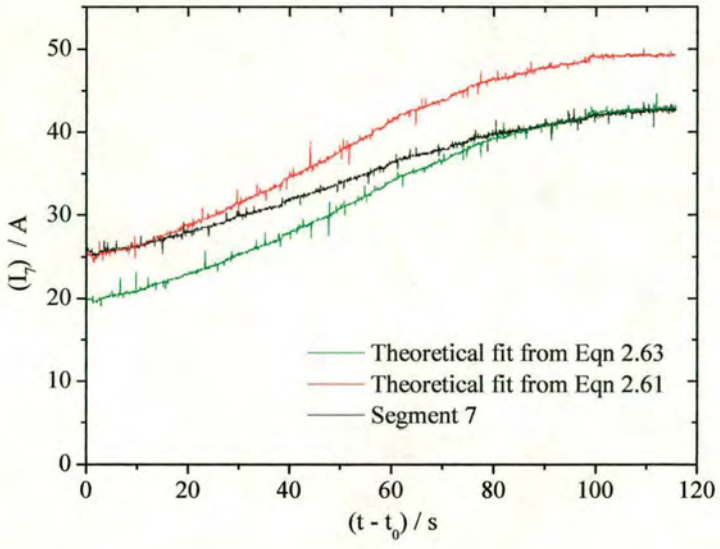

Figure 4.13: Comparison of experimental current transients for segment 7 with the theoretical transients produced from Equation 2.61 at short times and 2.63 at long times for In718 in nitrate electrolyte at high U (16 l min^{-1}) and V = 20.0 V.

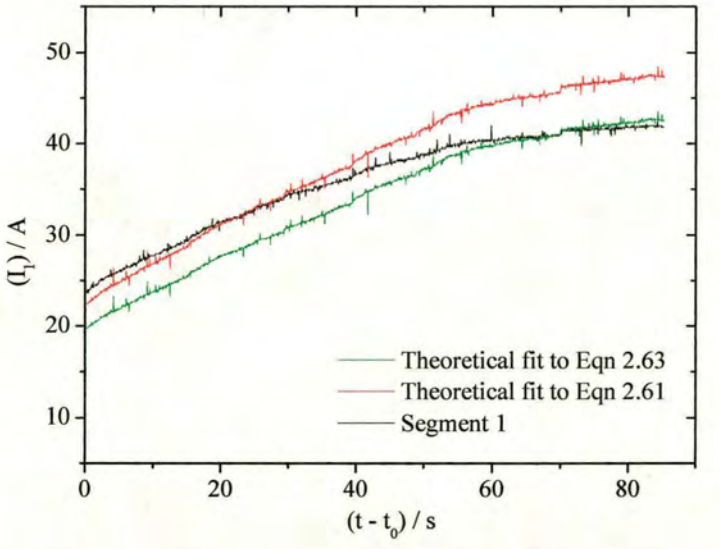

Figure 4.14: Comparison of experimental current transients for segment 1 with the theoretical transients produced from Equation 2.61 at short times and 2.63 at long times for In718 in nitrate electrolyte at high U (22 l min^{-1}) and V = 20.0 V.

In addition to the observed rounding of the workpiece ends, the inlet and outlet hydrodynamics may also have an effect on segments 1 and 7. As observed in Figure 3.12 the flow regime for cell 99 is not particularly smooth and the flow path would be expected to be turbulent (see Section 3.5.2). Also, the entry length, l_e, which is the length required to establish fully turbulent flow was calculated to be between 4 and 8 mm where one segment length is 5.7 mm. Therefore, in the entry length region, the flow is not well defined and therefore cannot be modelled or even approximately modelled. This uncertainty in the flow could therefore lead to uncertainty in the results from the inlet (segment 1) and outlet (segment 7) segments in addition to the rounding effect. It is interesting that despite this, the observed fits of the experimental current-time data to the two limiting cases determined in Section 2.10 is good, which suggest that these hydrodynamic effects are not large under these conditions.

4.6 Conclusion

Cell 99 has been used to demonstrate that chronoamperometric analysis and can be used for both the planar single tool and segments 2 – 6 from the planar segmented tool to make measurements of n and V_0 in an ECM system. However, segments 2 – 6 can also be used to measure variation along the flow path length whereas the planar single tool only provides average values across the tool surface. Segments 1 and 7 are harder to analyse theoretically to produce quantitative data due to the overlapping segments, but the limiting ECM current-time data at short and long times for these segments still appear to be controlled by simple migration. Segments 1 and 7 can therefore also in principle be used to examine inlet and outlet erosion due to non-normal field lines, enabling parameterisation and modelling. However, other effects such as electrolyte flow at the inlet and outlet may also cause a small perturbation to these segments. It is difficult to judge whether these effects are important, as a complete theoretical analysis of segments 1 and 7 current transients was not possible. Therefore, a main reason for producing cell 2000 was to avoid these overlapping edge effects, thereby simplifying analysis to see if segments 1 and 7 could be used for parameterisation under these conditions. Results from Cell 2000 will now be examined.

4.7 Cell 2000

Cell 2000 was made so that segments 1 and 7 did not overhang the workpiece and therefore each segment had approximately equal area. This was confirmed by the fact that current transients were observed that all rose to the same equilibrium current density. Machining of Duplex stainless steel with NaCl electrolyte is shown as an example in Figure 4.15. As with In718, Duplex is not known to exhibit any unusual surface effects during ECM (as it is later shown to give a constant V_0 along the flow path length, see Section 5.2.1).

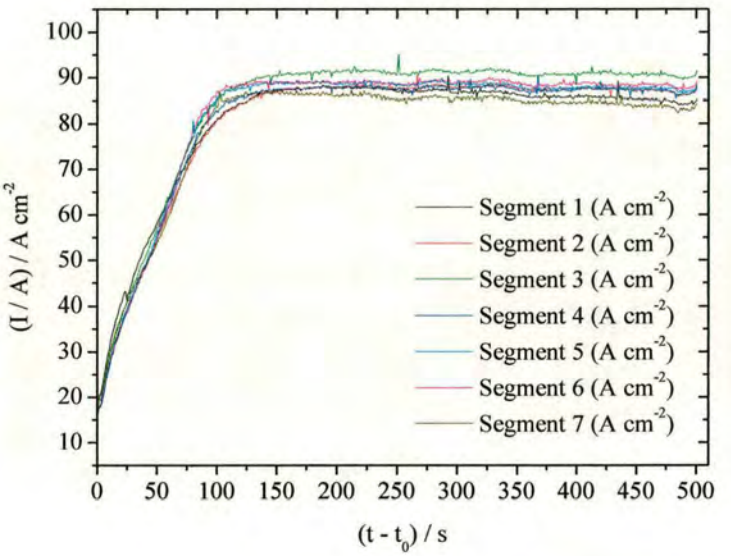

Figure 4.15: Experimental current transients for Duplex stainless steel showing segments 1 to 7 for with chloride electrolyte at U = 8.0 l min^{-1} and V = 24.0.

Initially all the segment current densities are approximately the same, however, as machining progresses, the currents for segments 1 and 7 can be seen to decrease slightly from the remaining segments. However, this decrease is extremely small in comparison with cell 99 (Figures 4.10 and 4.11) where segment 1 and 7 currents were completely different to segments 2 - 6. Therefore, this confirms that the main cause in the difference between segments 1 and 7 and 2 – 6 is the overlapping end segments [138]. Additionally, cell 2000 has improved flow geometry over cell 99 (see Section 3.5.2), which may decrease flow effects but entry length problems would still be expected. These entry length effects may be apparent at larger times with the smallest gaps e.g. where segments 1 and 7 currents are always slightly lower than 2 – 6 (Figure 4.15). Therefore, because of these minor entry length and exit length problems and the resulting segment 1 and 7 current variations,

segments 1 and 7 will not be used in the following chronoamperometric segment analyses; however it should be noted that the difference is very small between segments 2 – 6, and that analysis of segments 1 and 7 may be possible. Indeed, at early times all the currents are the same and no significant edge effects are observed. (Figure 4.15).

4.8 Conclusion

It has been demonstrated that the analysis of chronoamperometric ECM data obtained using a planar workpiece/planar tool and a planar workpiece/planar segmented tool can be used to characterise the dissolution of metals under industrially relevant ECM conditions and to obtain relevant process parameters. The results presented here show that the segmented tool allows these parameters to be measured along the electrolyte flow path length. Cell 99 has been shown not to be as effective for quantitative edge ECM analysis as cell 2000 due to the extra complexity in the analysis of the overhanging end segments, possibly coupled with a poor entry and exit flow regime. Segments 2 to 6 in cell 99 are consistent with the chronoamperometric theory developed for a single planar tool, but segments 1 and 7 are harder to parameterise due to non-normal field lines and the influence of progressive workpiece rounding. However, this cell 99 system could find uses in the analysis of such edge machining effects. Cell 2000 can in theory be used to analyse the response of all 7 segments but again the inlet and outlet segments appear to suffer from minor hydrodynamic problems, which makes analysis of these segments more prone to error at larger times. With this caveat, Cell 2000 is therefore capable of providing information about the ECM parameters along the entire flow path length. Combined with the chronoamperometric analysis technique, the segmented tool in Cell 2000 is a powerful method for measuring the electrochemical dissolution characteristics of various workpiece materials. This system will therefore now be used to examine the electrochemical dissolution properties of stainless steels.

Chapter 5

The ECM of Stainless Steels

5.1 Introduction

To date there has been little systematic study of the effect of changes in elemental composition on the ECM characteristics within a family of alloys. This is addressed here by studying the family of stainless steels. This is because as well as their prevalence in manufacturing, previous studies [56, 57] have indicated a valency change in stainless steel (SS316) under certain ECM conditions. It has already been established [123] that for Ti 6/4 alloy (predominantly titanium) and In718 alloy (predominantly nickel), dissolution is determined by the energetics of expulsion of the metal ions from the surface oxide. This indicates that changes in the surface oxide during ECM of SS316 should cause measurable changes in the dissolution process. Stainless steels are iron chromium alloys, typically greater than 10 atomic % chromium [64]. This chromium induces the formation of a protective oxide film on the metal surface. As the chromium content is increased, then the passive film becomes thicker (and/or denser) and more stable, being able to resist more aggressive chemically corrosive agents such as acidic or oxygenated chloride solutions. In addition, other alloying elements such as Nickel and Molybdenum are added to stainless steels in order to further enhance the corrosion resistance, weldability and ductility (see Section 1.15). During ECM, it is reasonable to expect that the metal dissolution characteristics of stainless steels would be determined by the surface structure. The object of this work is to test this expectation by performing a systematic study under ECM conditions, measuring the ECM characteristics of a variety of stainless steels and correlating these with the steel composition.

5.2 Results and discussion

The results presented in this work are a systematic analysis of ECM of a family of stainless steels. Both chemical and electrochemical parameters have been determined along the flow path length. The importance of the surface oxide layer is categorised in terms of the steels chromium content as this primarily determines the strength of the oxide layer.

5.2.1 ECM of Super Duplex (SD) and Duplex (D)

SD (25.58 % Cr) and D (23.00 % Cr) are both high chromium steels, with chromium contents greater than 20%. For each electrolyte and all segments analysed (segments 2-6, see Chapter 4), both steels machined with equilibrium currents which produce an overall valency, n = 3.8 ± 0.1 (Figures. 5.1, 5.2 and 5.3) across the entire workpiece surface. From Equation 2.39, this is consistent with dissolution of iron in its high valency state (Fe(III), n_{Fe} = 3) and of dissolution of chromium in its high valency state (Cr(VI), n_{Cr} = 6), if it is assumed that the minor elements in the alloy (i.e. all elements excluding Fe and Cr, Table 1.1) dissolve with an average valency of n = 3 ± 1. This is both chemically reasonable and consistent with previous interpretations of the ECM valencies of stainless steels [56, 57]. For these and all subsequent electrolyte and steel systems, since it can be assumed that ECM dissolution is occurring under ideal conditions, substitution of the values of k/f^2, f, κ, ρ, V, M, n and F into Equation 2.56 enabled V_0 to be calculated for each current-time transient. Representative values for these and all other steels are tabulated in Table 5.3.

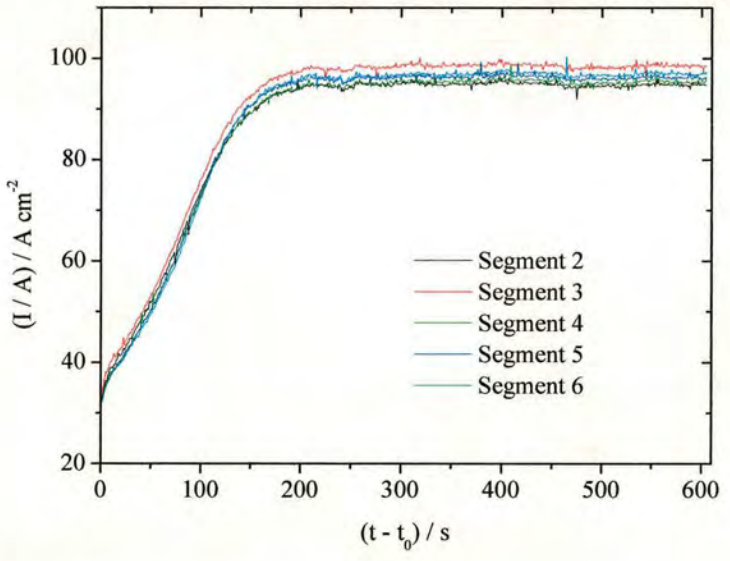

Figure 5.1: Experimental current transients for segments 2-6 for ECM of SD at high U (20 l min^{-1}) with chloride electrolyte. All segments can be seen to have similar profiles and I_∞ values, producing n = 3.8 ± 0.1 and V_0 = 9.6 ± 0.8 V.

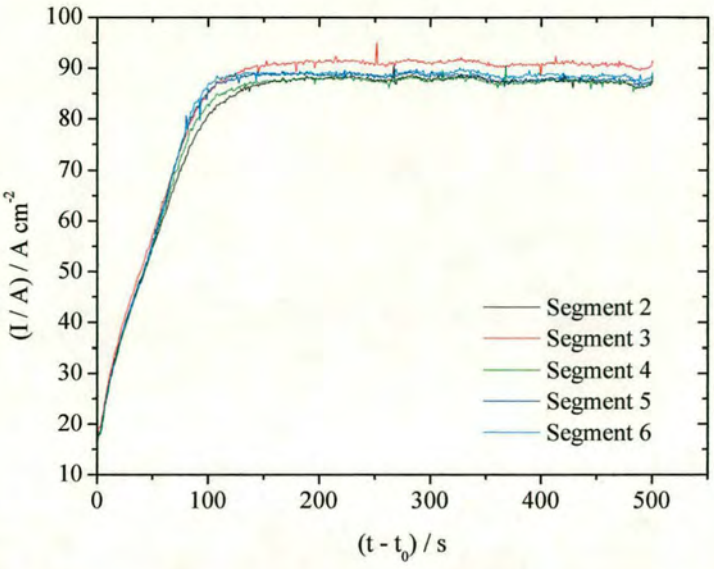

Figure 5.2: Experimental current transients for segments 2-6 for ECM of D at low U with chloride electrolyte. All segments can be seen to have a similar profiles and I_∞ values, producing $n = 3.8 \pm 0.1$ and $V_0 = 9.2 \pm 0.8$ V.

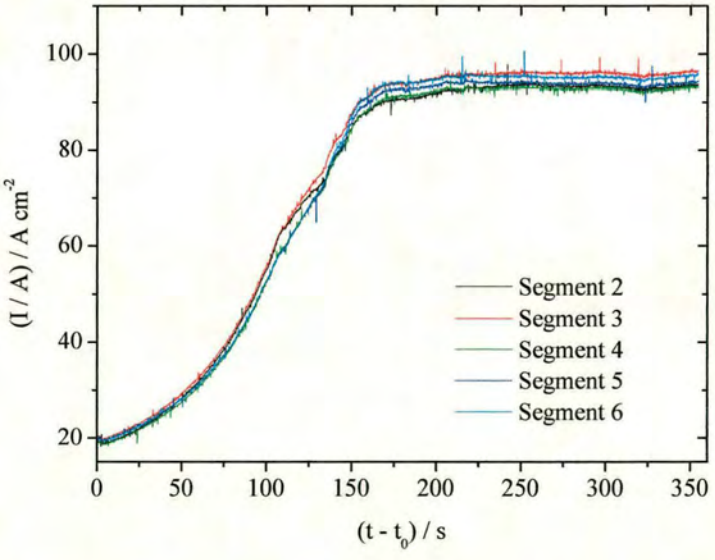

Figure 5.3: Experimental current transients for segments 2-6 for ECM of D at high U for nitrate electrolyte at a start gap of 1.6 mm. All segments can be seen to have similar profiles and I_∞ values, producing $n = 3.8 \pm 0.1$ and $V_0 = 15.7 \pm 0.5$ V.

5.2.2 ECM of jethete and SS410

Jethete (12.50 % Cr) and SS410 (12.75 % Cr) are both relatively low chromium steels, containing less than 15 % chromium. When carrying out ECM with nitrate electrolyte, a valency of n = 3.5 ± 0.1 was obtained for segments 2-6 for both materials (Figures 5.4 and 5.5) This is again consistent with dissolution of iron and chromium in their high valency states (Fe(III), $n_{Fe} = 3$ and Cr(VI), $n_{Cr} = 6$) across the entire workpiece surface, as this value is within experimental error of the mean valency of n = 3.4 which would be expected if the minor elements in these steels dissolved with a chemically reasonable average valency of n = 3. However for chloride electrolyte, dissolution with a lower valency occurs (Figs. 5.6 and 5.7) giving n = 2.1 ± 0.1, obtained from Equation. 2.39. As iron is the major elemental component in these steels, this indicates that in this case iron dissolution is occurring in its low valency state (Fe(II), $n_{Fe} = 2$) and also suggests that chromium (and some of the minor elements) may be dissolving in lower valency states than with nitrate. The average valency can be subdivided into individual valencies, n_i, and mole fractions, x_i, for each element, i, in the alloy to give

$$n = \sum_i n_i x_i \tag{5.1}$$

An efficiency of 100% (a fractional efficiency, e, of 1) was assumed throughout the work presented here (see Section 2.11). It has been postulated previously [56, 57] that Cr dissolves as Cr(III), $n_{Cr} = 3$ under these conditions. These results would be consistent with this postulation if the average valency of the minor elements were n = 2 ± 1 (Table 1.1).

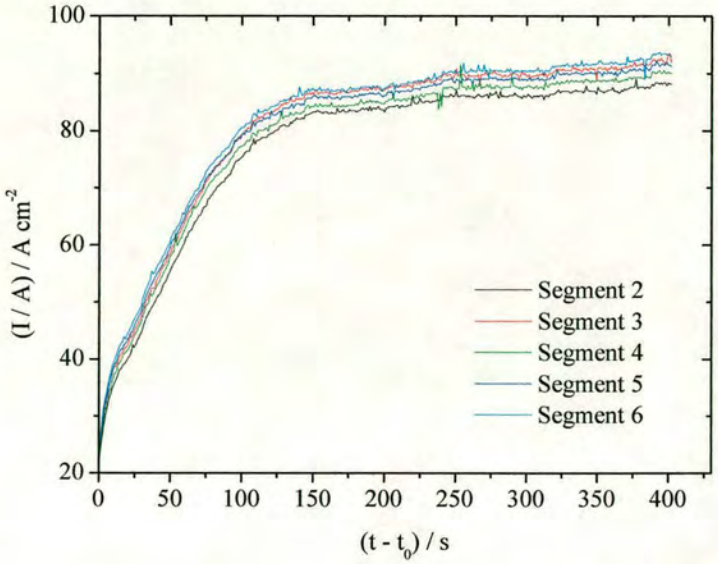

Figure 5.4: Experimental current transients for segments 2-6 for ECM of J at high U with nitrate electrolyte. All segments can be seen to have similar profiles and I_∞ values, giving n = 3.5 ± 0.1 and V_0 = 7.5 ± 0.9 V.

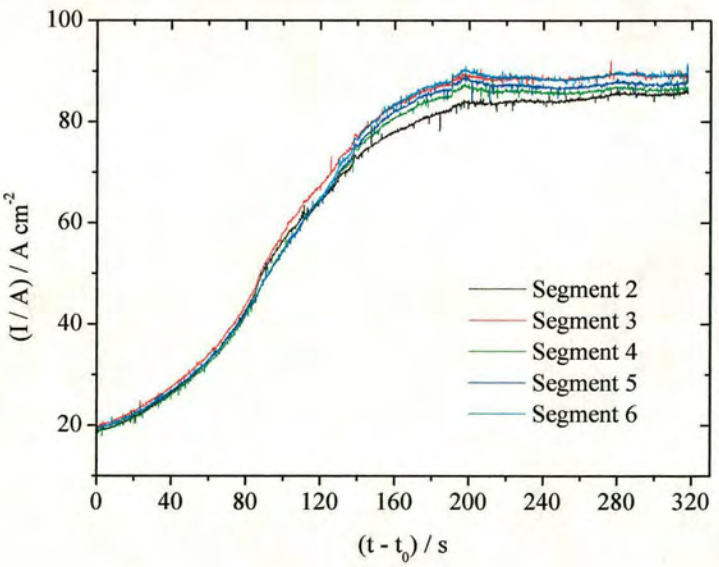

Figure 5.5: Experimental current transients for segments 2-6 for ECM of SS410 at high U with nitrate electrolyte at a start gap of 1.6 mm. All segments can be seen to have similar profiles and I_∞ values, giving n = 3.5 ± 0.1 and V_0 = 9.5 ± 0.8 V.

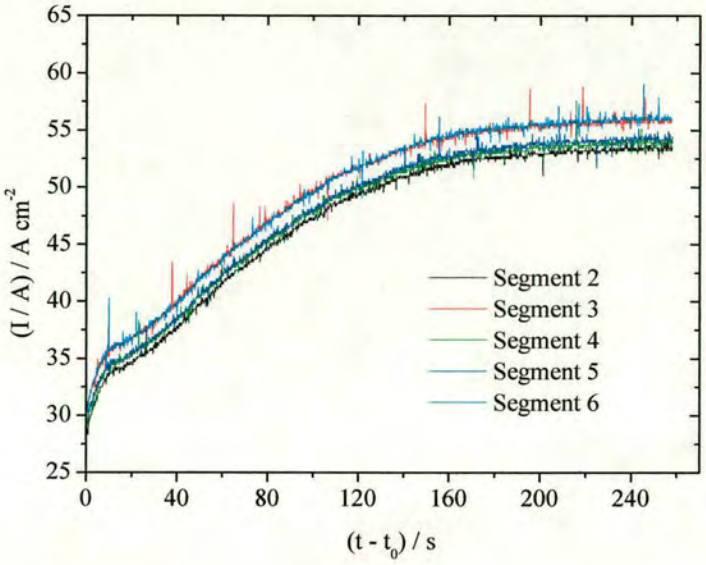

Figure 5.6: Experimental current transients for segments 2-6 for ECM of J at high U with chloride electrolyte at a start gap of 1.3 mm. All segments can be seen to have similar profiles and I_∞ values, giving $n = 2.1 \pm 0.1$ and $V_0 = 5.6 \pm 0.9$ V.

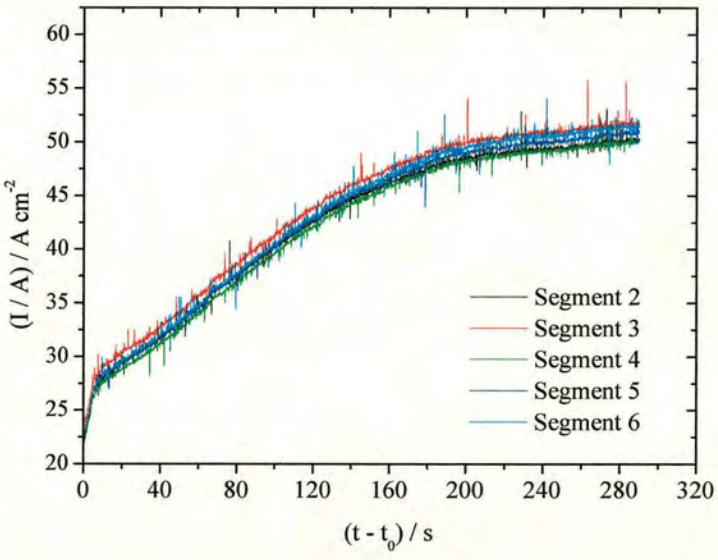

Figure 5.7: Experimental current transients for segments 2-6 for ECM of SS410 at high U with chloride electrolyte at a start gap of 1.6 mm. All segments can be seen to have similar profiles and I_∞ values, giving $n = 2.1 \pm 0.1$ and $V_0 = 4.0 \pm 1.0$ V.

5.2.3 ECM of SS316

SS316 (17.00 % Cr) contains an intermediate chromium content higher than the low chromium steels (> 15%) but lower than the high chromium steels (< 20%). When carrying out ECM with nitrate electrolyte, an average valency of n = 3.6 ± 0.1 was obtained for segments 2 - 6 (Figure 5.8).

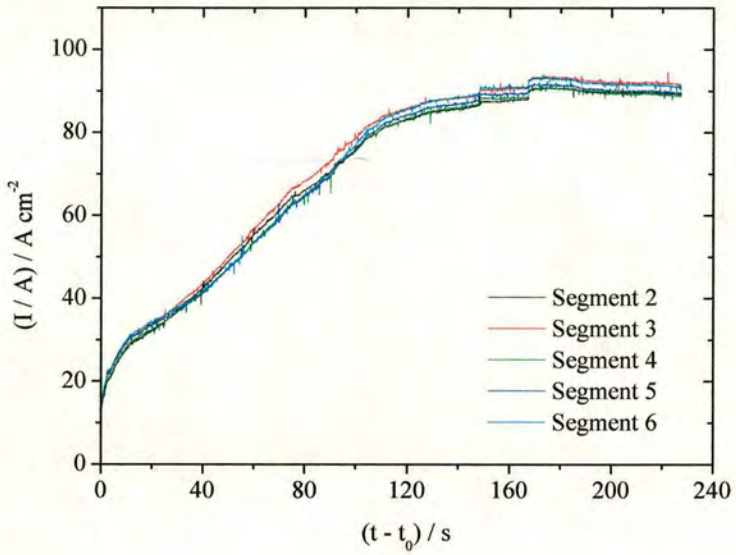

Figure 5.8: Experimental current transients for segments 2-6 for ECM of SS316 at high U with nitrate electrolyte at a start gap of 1.0 mm. n = 3.6 ± 0.1 and V_0 = 9.7 ± 0.8 V for all segments as they can be seen to have similar profiles and I_∞ values.

Within experimental error, this is again consistent with dissolution of iron and chromium in their high valency states (Fe(III), n_{Fe} = 3 and Cr(VI), n_{Cr} = 6), if the overall valency of the minor elements is n = 3 ± 1. For chloride at high U, at short times, (t - t_0) < 400 s, (Figure 5.9) a similar value of n within experimental error was obtained as for nitrate.

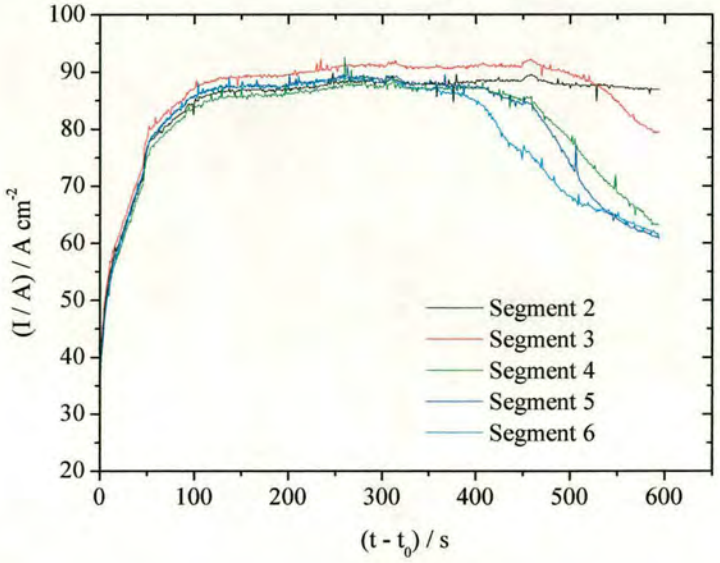

Figure 5.9: Experimental current transients for segments 2-6 for ECM of SS316 at high U (20 l min^{-1}) with chloride electrolyte. n = 3.6 ± 0.1 and V_0 = 5.7 ± 0.9 V for all segments as they can be seen to have similar profiles and I_∞ values.

However, at longer times ((t - t_0) > 400 s), significant variations in segment current were obtained, which indicates, from Equation. 2.39, significant changes in valency with time along the flow path length. A smooth, shiny surface with high dissolution valency (n = 3.5 ± 0.1) was found near the inlet of the flow path whereas a rough, dull, pitted surface was found with low dissolution valency (n = 2.1 ± 0.1) towards the outlet of the flow path (Figure 5.10).

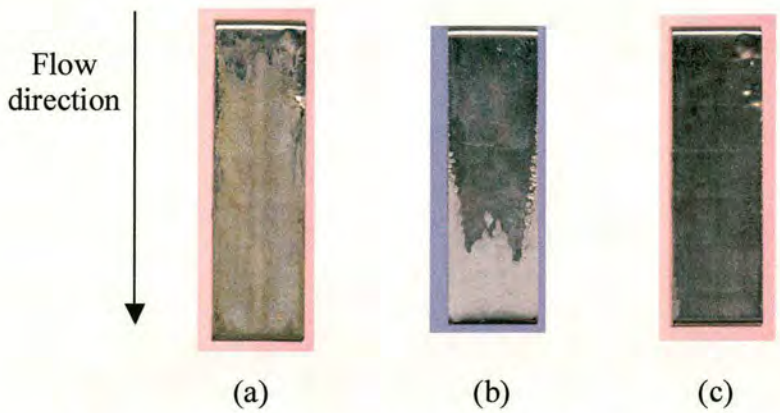

Figure 5.10: Photographs of the machined surface of SS316 with varying flow rates of chloride electrolyte (a) 10.0 l min^{-1} (majority of the surface is dull and pitted), (b) 16.0 l min^{-1} (the surface is split between dull and shiny) and (c) 22.0 l min^{-1} (the majority of the surface is smooth and shiny).

Similar results have been previously observed [56, 57, 139] and it was previously suggested [56, 57] that the smooth, shiny surface is characteristic of iron and chromium dissolving in their high valency states (as Fe(III), $n_{Fe} = 3$ and Cr(VI), $n_{Cr} = 6$) and the dull, rough, pitted surface is characteristic of iron and chromium dissolving in their low valency states (as Fe(II), $n_{Fe} = 2$ and Cr(III), $n_{Cr} = 3$) [56, 57]. As has been seen previously [123], the observed decrease in valency corresponded to the progressive change in electrode surface appearance, as dull, pitted patches spread upstream across the electrode surface from the downstream end of the workpiece [123].

When carrying out ECM under low U (8 l min^{-1}) with chloride, at very short times ($t - t_0$) < 50 s) ECM currents indicative of high valency machining were obtained for segments 2- 6 (Figure 5.11).

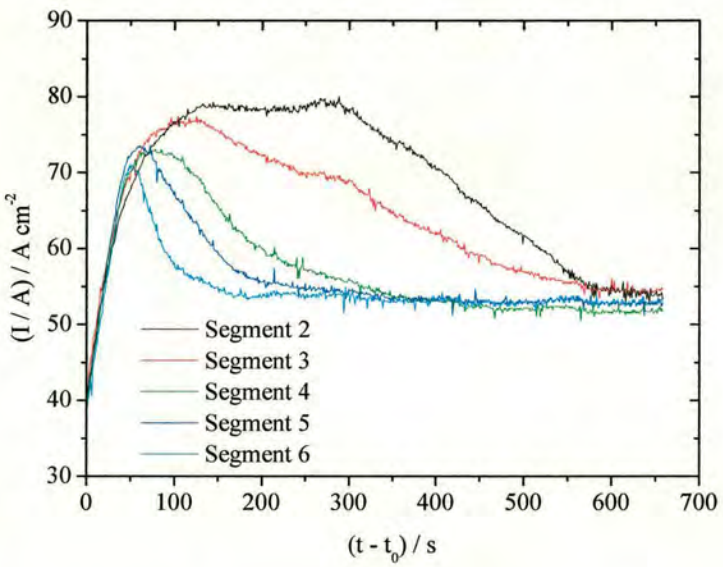

Figure 5.11: Experimental current transients for segments 2-6 for ECM of SS316 at low U (8 l min^{-1}) with chloride electrolyte.

As with high flow, progressive growth of the dull, pitted surface occurred and spread upstream from the downstream end of the workpiece (Figure 5.8). However, the progressive onset of low valency machining was initiated typically much quicker (less than 50 s for segment 6 in Figure 5.11) than at high flow (400 s in Figure 5.10). This is again indicated by the progressive decrease in segment currents (indicating a progressive decrease in valency) from segments 6 through to 2. On each segment, these currents asymptotically approached with time the equilibrium current expected for an average valency $n = 2.1 \pm 0.1$. Within

experimental error, this is again (see Section 5.2.2) consistent with dissolution of iron and chromium in their low valency states (Fe(II), $n_{Fe} = 2$ and Cr(III), $n_{Cr} = 3$), if the overall valency of the minor elements is $n = 2 \pm 1$.

5.3 Effect of Electrolyte Recirculation on SS316

The chloride high U recirculation experiment (Figure 5.10) showed significant changes in valency only after 400 s. This was a much longer time than the time to reach equilibrium machining conditions; however, complete recirculation of the electrolyte should have occurred after of the order of 180 seconds (the time taken to cycle 60 l of electrolyte through the ECM system at 20 l min^{-1}), and so it is likely that these valency changes could be a result of accumulating electrolyte products. To test this hypothesis, SS316 was machined in chloride again at high U without electrolyte recirculation (Figure 5.12). At high flow the ECM currents corresponded to a valency $n = 3.6 \pm 0.1$ ($I_\infty/A = 88 \pm 3$ A cm^{-2}) consistent with Fe(III), $n_{Fe} = 3$ and Cr(VI), $n_{Cr} = 6$ dissolution at all times. This indicates the importance of recirculation, and the resulting product accumulation, in determining the dissolution valency at high flow. Similar experiments carried out at low U produced similar current-time transients for segments 4, 5 and 6 (Figure 5.13) to those observed when recycling the electrolyte (Figure 5.10). This is to be expected as the recirculation experiments established that valency changes on these segments were observed well before complete electrolyte recirculation had been achieved. However, the most downstream segments, 5 and 6, showed a more rapid decrease in valency for the recirculated experiments, and the upstream segments 2 and 3 showed a markedly decreased valency change without electrolyte recirculation.

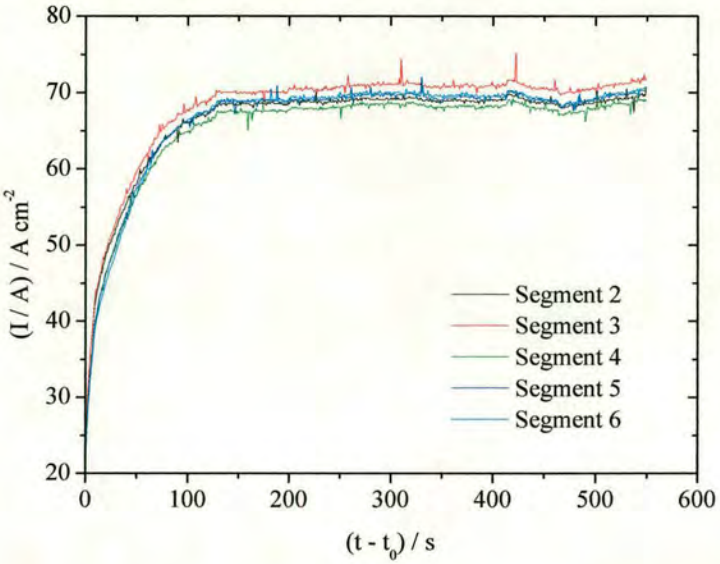

Figure 5.12: Experimental current transients for segments 2-6 for ECM of SS316 at high U with chloride electrolyte without recycling. n = 3.6 ± 0.1 and V_0 = 5.7 ± 0.9 V for all segments as they can be seen to have similar profiles and I_∞ values.

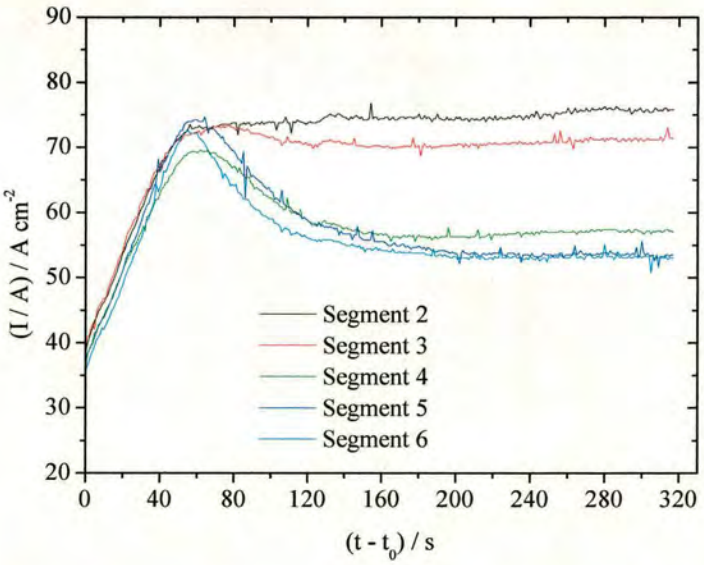

Figure 5.13: Experimental current transients for segments 2-6 for ECM of SS316 at low U with chloride electrolyte without recycling.

These results suggest that the cause of the surface transition is the build up of products in the electrolyte to a critical concentration. At high U, the concentration of products accumulating in the gap in the electrolyte is much less than at low U. This would mean that critical product

concentration could be achieved at the downstream end of the flow path at low U in both recirculated and non-circulated electrolyte, producing similar changes in valency on segments 4-6 in both cases (as seen in Figures 5.12 and 5.13). However, for the upstream segments at low U and for all segments at high U, product accumulation in the gap may have to be augmented by product accumulation in recirculating electrolyte in order to attain the critical product concentration necessary to induce the change in valency. Hence, these changes would only be expected for recirculated electrolyte (as seen in Figures.5.12 and 5.13).

5.4 Characterisation of the ECM products of Stainless Steels

Analysis of the electrolyte composition before ECM, along the flow path length during ECM (from inlet tube, middle tube and outlet tube) and in the recirculating tank after ECM were performed. For all experiments and all samples the conductivity of the electrolytes were measured as $\kappa = 0.20 \pm 0.2$ S cm^{-1} at 25°C within experimental error (Table 5.1). These values are in agreement with those measured for bulk chloride and nitrate electrolyte previously both before and during ECM [123], and indicate that conductivity is not a sensitive measure of the degree of product accumulation in these systems. It is to be remembered that the overall conductivity merely measures the sum of the individual ionic conductivities in the electrolyte (see Section 2.6). Therefore, for all reactions that produce and consume ions, significant conductivity changes would be expected only when there is significant product accumulation and there are significant differences in conductivity between the reactants and the products.

Steel	Segment 2	Segment 4	Segment 6	Bulk
D, low U, Cl^-	0.18	0.19	0.18	0.19
SD, low U, Cl^-	0.21	0.20	0.21	0.21
D, high U, NO_3^-	0.19	0.19	0.20	0.20
J, high U, Cl^-	0.20	0.19	0.19	0.20
J, high U, NO_3^-	0.20	0.20	0.20	0.20
SS410, low U, Cl^-	0.20	0.20	0.21	0.21
SS410, high U, Cl^-	0.21	0.20	0.20	0.21
SS410, high U, NO_3^-	0.20	0.20	0.19	0.20
SS316, high U, Cl^-	0.19	0.19	0.20	0.20
SS316, low U, Cl^-	0.18	0.19	0.19	0.20
SS316, high U, NO_3^-	0.19	0.20	0.21	0.20

Table 5.1. Table of conductivities (S cm^{-1} ± 0.02) for the different steels and electrolytes corrected to 25 ^{0}C.

pH measurements of these electrolyte samples have also been carried out, and typical values are given in Table 5.2.

Steel/Flow conditions and electrolyte	pH (IT)	pH (MT)	pH (OT)	pH Bulk (before/after)
D – High U, Cl	8.74	10.02	2.65	-
SD – High U, Cl	6.38	10.40	3.52	-
J - High U, Cl	***10.83***	***10.40***	***6.23***	-/6.04
J –High U, NO_3	***9.08***	***8.69***	***7.26***	-
SS410 – High U, NO_3	***10.09***	***8.02***	***10.39***	8.63/9.18
SS410 – High U, Cl	***10.58***	***10.37***	***9.47***	6.80/8.82
SS316 – High U, NO_3	10.02	8.53	10.08	8.66/8.77
SS316 – High U, Cl	10.59	11.42	2.75	7.7/6.8
SS316 – Low U, Cl	***11.50***	***11.68***	***7.02***	7.41/9.91

Table 5.2. A comparison of selected electrolyte sample pH values obtained when carrying out equilibrium ECM of steels under different flow regimes. The inlet (IT), middle (MT) and outlet (OT) sample tubes are located with their inside edge at the edge of the tool surface. At

equilibrium gaps greater than the tube diameter (0.4 mm), the samples from these tubes will therefore be unrepresentative of the overall electrolyte composition in the gap and will be expected to contain more products from the tool reaction than the workpiece reaction. Gaps significantly less than 0.4 mm would be expected to contain more products from the workpiece reaction. Those samples with gaps greater than 0.4 mm are therefore shown in italics and bold.

The bulk pH of the electrolyte was typically found to lie in the range pH = 8 ± 1 both before and after ECM experiments. This is consistent with the expected pH variation of electrolytes prepared with soft Edinburgh tap water. However, it can be seen from Table 5.2 that the pH of samples taken from the inlet, middle and outlet tubes were often significantly outside this range. Although thorough mixing of these electrolyte samples would be expected in these sample tubes, for those ECM experiments with equilibrium gaps significantly greater than 0.4 mm, the tubes would be expected to sample electrolyte from closer to the tool surface than the workpiece. The pH values of these samples are shown in bold and italics. It is clear from Table 5.2 that these pH values tend to be greater than those for experiments that sample electrolyte products from both the workpiece and the tool. This is to be expected, as at the tool the reduction reaction

$$H_2O_{(aq)} + e^- \rightarrow \frac{1}{2}H_{2(aq)} + OH^-_{(aq)} \tag{5.2}$$

is most likely to occur, generating hydroxide ions and increasing the local pH. At the workpiece, the general reaction

$$M_{(s)} \rightarrow M^{n_m+}_{(aq)} + n_m e^- \tag{5.3}$$

occurs, with each metal ion, M, dissolving with its own characteristic valency, n_m. For some of these metals their valencies could also be sufficiently high to induce proton production from water molecules in their solvation shell

$$M^{n_m+}(H_2O)_{y(aq)} \rightarrow M^{(n_m-x)+}(OH)_x(H_2O)_{y-x(aq)} + xH^+_{(aq)} \tag{5.4}$$

which would generate an acidic pH near the workpiece. Along the electrolyte flow path length, electrogenerated products will tend to both diffuse and migrate from their respective electrode towards the opposite electrode. Away from the thin laminar diffusion layer present at each electrode surface [140], turbulent flow enhances their mixing (see Section 2.7), and the reaction

$$M_{(aq)}^{n_m+} + n_m OH_{(aq)}^- \rightarrow M(OH)_{n_m(s)} \qquad (5.5)$$

would be expected to occur, producing soluble and insoluble metal hydroxides and (following dehydration) metal oxides. Such reactions would be expected to produce a significantly lower pH near the centre of the gap compared to near the tool, as hydroxide ions are consumed. Overall, this would produce more acidic pH values for the outlet (and middle) tubes than the inlet tube, if significant reaction according to Equation 5.5 occurs within the sampling volume of the sample tube. Such increases in acidity are indeed found (Table 5.2), indicating the importance of Equation. (5.5) within the interelectrode gap during ECM.

5.4.1 UV/Visible Absorption Analysis

Visible absorption measurements have also been performed on the inlet, middle and outlet samples to identify and characterise absorbing metal dissolution products in the electrolyte. A series of spectra for the electrolyte samples obtained during the equilibrium machining of SD, J, SS410 and SS316 in nitrate electrolyte and D in chloride electrolyte are shown in Figures 5.14 to 18. The absorption spectra were obtained from the inlet, middle and outlet electrolyte sampling tubes and from the bulk electrolyte after machining. The close correspondence of these spectra to the visible absorption spectrum of a reference basic chromate ion (CrO_4^{2-}) solution is strong evidence that chromate is present in each sample. For a constant current density and electrochemical reaction type across the workpiece surface, the concentration of stable products should increase linearly with flow path length. This linear increase in absorption is observed from the sampling tubes (which are equally spaced along the flow path length) in Figures 5.14, 5.15 and 5.16. For SS410 the increase in absorption between neighbouring tubes, when compared with the absorption peak height of the chromate calibration solution of known concentration, gives an average increase in chromate concentration between neighbouring tubes of 1.4×10^{-4} M (Figure 5.14).

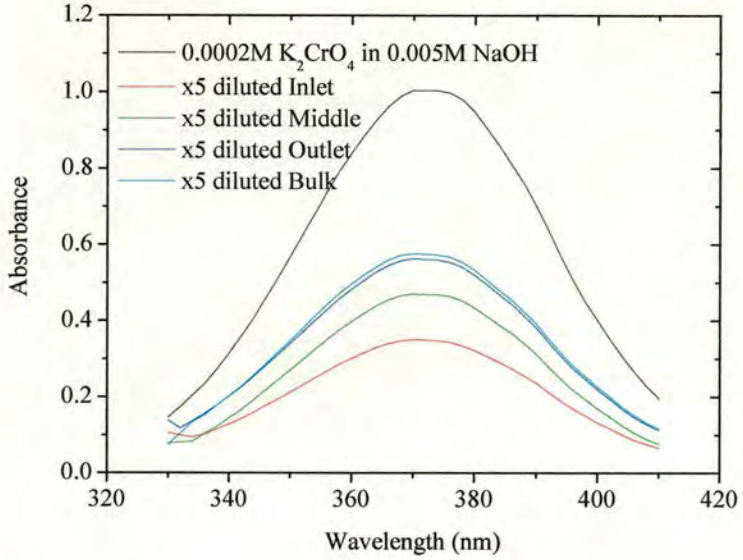

Figure 5.14: The visible absorption spectra of samples taken from the sample tubes for ECM of SS410 at high U with nitrate electrolyte. These samples were diluted by a factor of 5. Also shown is the spectrum of 2.0×10^{-4} M CrO_4^{2-} in 5.0×10^{-3} M NaOH.

By considering the equilibrium ECM current, the average valency n, the electrolyte flow rate U and the composition of SS410, a theoretical increase in chromate concentration has been calculated between neighbouring tubes as 1.5×10^{-4} M. The reasonably close correspondence of this calculated value to the experimentally observed value indicates that chromate is the major chromium product of ECM dissolution in this case, and is stable in the electrolyte. This is consistent with the observation that $n_{cr} = 6$ (Section 5.2.1). Furthermore, the bulk electrolyte concentration was 5.7×10^{-4} M, whilst extrapolation of the linear concentration gradient to the upstream edge of the workpiece gave the inlet electrolyte concentration as 3.5×10^{-4} M. This difference in chromate concentration between the inlet and the bulk samples also strongly suggest either that complete electrolyte mixing has not occurred in the bulk electrolyte reservoir during ECM when these electrolyte samples were taken or that there is some reaction with slow kinetics between CrO_4^{2-} and other ECM products in the reservoir.

For SS316 the increase in absorption between neighbouring tubes, when compared with the absorption peak height of the chromate calibration solution of known concentration, gives an average increase in chromate concentration between neighbouring tubes of 1.7×10^{-4} M (Figure 5.15).

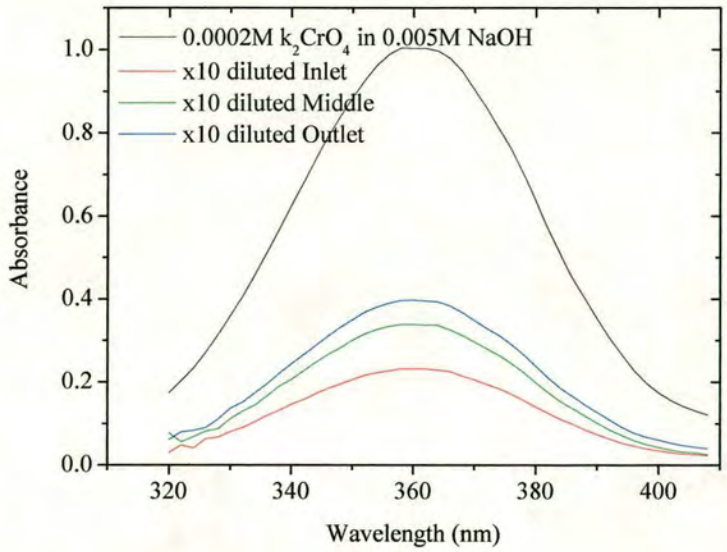

Figure 5.15: The visible absorption spectra of samples taken from the sample tubes for ECM of SS316 at high U with nitrate electrolyte. These samples were diluted by a factor of 10. Also shown is the spectrum of 2.0 x 10^{-4} M CrO_4^{2-} in 5.0 x 10^{-3} M NaOH.

By considering the equilibrium ECM current, the average valency n, the electrolyte flow rate U and the composition of SS316, a theoretical increase in chromate concentration has been calculated between neighbouring tubes as 2.0 x 10^{-4} M. The close correspondence of this calculated value to the experimentally observed value also indicates that chromate is the major chromium product of ECM dissolution in this case, and is stable in the electrolyte. This is again consistent with the observation that $n_{cr} = 6$.

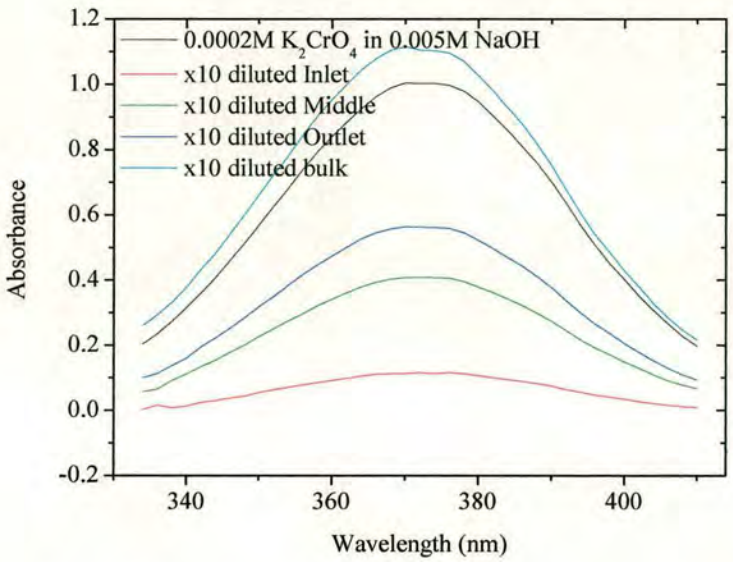

Figure 5.16: The visible absorption spectra of samples taken from the sample tubes for ECM of SD at high U with nitrate electrolyte. These samples were diluted by a factor of 10. Also shown is the spectrum of 2.0 x 10^{-4} M CrO_4^{2-} in 5.0 x 10^{-3} M NaOH.

An experiment was also carried out performing the ECM of SD with nitrate electrolyte. In this experiment the electrolyte was recycled for a long time to give 8.2 mm of machining and therefore a large build up of products in the electrolyte tank. The increase in absorption between neighbouring tubes, when compared with the absorption peak height of the chromate calibration solution of known concentration, gave an average increase in chromate concentration between the inlet and middle tubes of 5.8 x 10^{-4} M. The observed increase between the middle and outlet tubes was 2.8 x 10^{-4} M. This compares to a theoretical increase in chromate concentration between neighbouring tubes of 3.1 x 10^{-4} M. Therefore, the expected difference in chromium concentrations is observed between the middle and outlet tubes but not between the inlet and middle tubes. Therefore, it might be expected that as the amount of products in the electrolyte build up then more and more chromate would enter the ECM cell thus increasing the concentration. The amount of chromate in the bulk was measured as 2.2 x 10^{-3} M. Therefore, if 8.2 mm of machining occurred, the amount of chromate expected in the bulk after this amount of machining can be calculated. The flow rate was 20 l min^{-1} and a theoretical increase in chromate of 3.1 x 10^{-4} M was expected between the sampling tubes. The three sampling tubes are placed in the centre of their corresponding segments (see Section 3.5.5) and therefore sample at 1.5, 3.5 and 5.5 segment lengths i.e. two segments apart. Therefore, by extrapolation the chromate content expected

after passing through all 7 segments is 7/2 x 2.5 x 10^{-4} M = 8.8 x 10^{-4} M. The electrolyte passes entirely through the system in 60 l / 20 l min^{-1} = 3 mins which corresponds to 3 mm of machining. The chromate concentration in the bulk electrolyte was measured as 2.2 x 10^{-3} M. This corresponds to (2.2 x 10^{-3} M / 8.8 x 10^{-4} M) x 3 mm = 7.5 mm of machining. The actual amount of material removed was 8.2 mm, in reasonable agreement with this calculated value. Therefore, it would appear that chromate is stable in the bulk electrolyte solution. Therefore, the low chromium content in the inlet sampling tube appears to be anomalous as the experimental and theoretical concentrations of both chromate in the bulk and the values of and difference between chromate concentrations for MT and OT correspond. This indicates that ECM of SD with nitrate also results in the accumulation of stable CrO_4^{2-} product.

In contrast to nitrate, ECM experiments with the low and intermediate chromium level steels in chloride electrolyte showed no detectable absorption corresponding to chromate in the electrolyte samples, which suggests alternative chloro-substituted dissolution products. However, the high chromium steels (D, SD) did show absorption spectra consistent with CrO_4^{2-} ion. This is most probably due to the high chromium content in these steels which forms a thick, strong protective oxide layer. When machining with nitrate then this is unable to disrupt the oxide layer and therefore Cr(VI) species are produced which are soluble and can be detected with UV/Vis spectroscopy, whereas chloride is well known to attack surface oxide layers usually resulting in their compromise and low valency machining (see Section 5.5). The growth and disruption of the surface oxide layer can be explained by the point defect model (PDM) [84 – 85] described in Section 5.5. This results in lower oxidation states of chromium being produced, most likely Cr(III) species which do not have strong UV/Vis absorption spectrum and are therefore not detected with UV/Vis. Therefore, with the high chromium steels the oxide layer remains intact, and the higher oxidation state, CrO_4^{2-} dissolution species are observed which are soluble in solution and is therefore able to be detected with UV/Vis spectroscopy. This is further evidence that the surface oxide layer remains intact, and that chromium content and chloride ion concentration work antagonistically in affecting the surface oxide layer. For Duplex (D) with chloride, the increase in absorption between neighbouring tubes, when compared with the absorption peak height of the chromate calibration solution of known concentration, gives an average increase in chromate concentration between the inlet and middle tubes of 2.0 x 10^{-4} M (Figure 5.17).

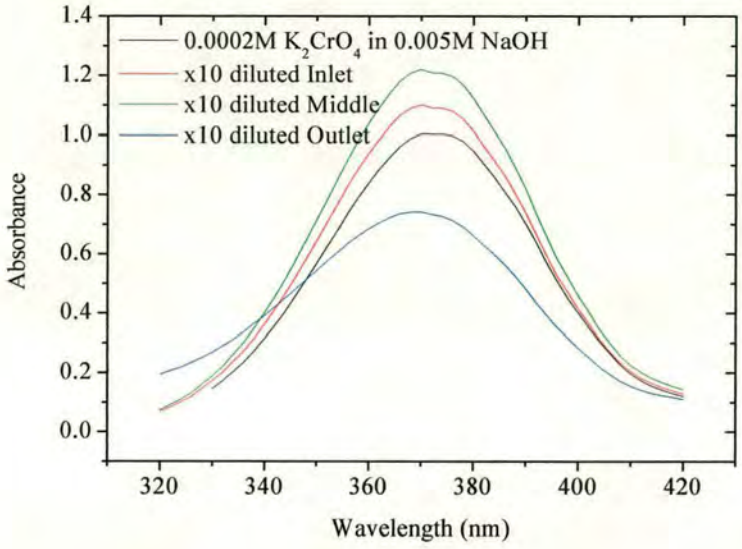

Figure 5.17: The visible absorption spectra of samples taken from the sample tubes for ECM of D at high U with chloride electrolyte. These samples were diluted by a factor of 10. Also shown is the spectrum of 2.0×10^{-4} M CrO_4^{2-} in 5.0×10^{-3} M NaOH.

However, the outlet tube concentration dropped, being 9.0×10^{-4} M lower than the middle sampling tube. This is most likely due to the fact that CrO_4^{2-} ions are stabilised in alkaline environments but the pH from the outlet tube in this case is highly acidic, at pH = 2.65 (Table 5.2), therefore destabilising the CrO_4^{2-} ion and therefore may cause it to drop out of solution as solid chromic oxide, CrO_3 resulting in a decrease in the concentration. It is interesting that there is an increase in the tail of the absorption at high energy (low wavelength) for OT, which would be consistent with increased scatter due to the formation of suspended solid particulate products. By considering the equilibrium ECM current, the average valency n, the electrolyte flow rate U and the composition of D, a theoretical increase in chromate concentration has been calculated between neighbouring tubes as 3.0×10^{-4} M. The reasonably close correspondence of this calculated value to the experimentally observed value between tubes IT and MT indicates that chromate is the major chromium product of ECM dissolution in this case, and is stable in the electrolyte at high pH. This is consistent with the observation that $n_{cr} = 6$. Additionally, some of the CrO_4^{2-} may form CrO_3 due to the acidity of the electrolyte, therefore explaining why all the chromium is not found as CrO_4^{2-} dissolved in the electrolyte along the flow path length (from MT to OT).

An interesting deviation in behaviour was observed when machining J with nitrate. In this case, the absorption spectra for J do not appear to follow the same linear increase in

chromate concentration along the flow path length as for other steels. This may be related to the distinctive ECM characteristics of J when machining with nitrate electrolyte (see Chapter 6). The concentration of chromate ions from all the sampling tubes, IT, MT and OT were found to be very similar at around 2.0 x 10^{-3} M. However, if soluble CrO_4^{2-} were produced during machining, a theoretical increase between sampling tubes of 1.4 x 10^{-4} M is expected. Again, the expected bulk concentration of chromate can also be calculated from the amount of J machined during the recycling experiment. An increase in chromium concentration across all seven segments of 7/2 x 1.4 x 10^{-4} M = 4.9 x 10^{-4} M in the time for a complete electrolyte cycling. The electrolyte passes entirely through the system in 60 l / 20 l min^{-1} = 3 mins which corresponds to 3 mm of machining. 7.65 mm of machining was performed and therefore the theoretical bulk concentration is (7.65 mm x 4.9 x 10^{-4} M) / 3 mm = 1.3 x 10^{-3} M. It appears that more chromium is observed in the sampling tubes than is theoretically produced. This is clearly impossible. The reason for this can be seen when looking more closely at the observed spectra. It is clear that unlike the previous experiments, these spectra have a markedly different shape from the reference CrO_4^{2-} spectrum, particularly with reduced absorption in the wavelength region up to 360 nm. This shape change is indicative of the presence of another soluble optically absorbing product in this case. This unknown product has an unknown extinction coefficient, and in this case absorbance measurements cannot therefore be used to obtain concentrations of soluble products as previously. This underlines the importance of ensuring that the absorbance values obtained are solely due to CrO_4^{2-} to enable quantitative analysis, by comparing the shape of the reference and experimental visible absorption spectra.

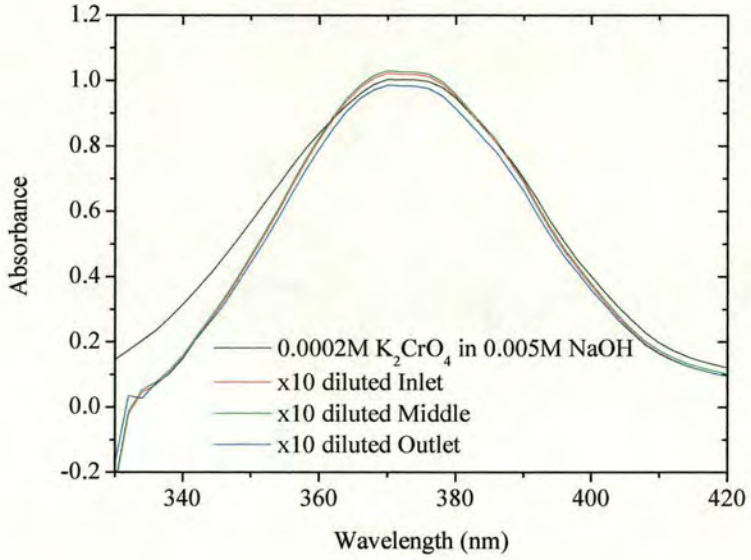

Figure 5.18: The visible absorption spectra of samples taken from the sample tubes for ECM of J at high U with nitrate electrolyte. These samples were diluted by a factor of 10. Also shown is the spectrum of 2.0×10^{-4} M CrO_4^{2-} in 5.0×10^{-3} M NaOH.

5.4.1.1 Summary

From all the spectra from the different steels it appears that the main chromium species produced is Cr(VI) when machining with nitrate, which is soluble and the amount of CrO_4^{2-} detected corresponds to the amount of chromium in the steel. When machining with chloride with low chromium steels, then in general a different lower valency chromium species is produced due to the disruption of the oxide barrier layer by the chloride ion. This low valency chromium species does not show significant UV/Visible absorption and therefore no chromium species are detected. However, when machining high chromium steels the protective oxide layer remains intact even in the presence of chloride, and CrO_4^{2-} is again observed as the major dissolution product. When machining J with nitrate, other soluble product(s) are formed which absorb in the visible and complicate the observed UV/visible spectrum, making quantitation of ECM products difficult. Further work is required to identify the nature and visible absorption characteristics of this (these) product(s).

5.4.2 XRD Analysis

A selection of some of the solid dissolution products from Section 5.4.1 have also been analysed by X-ray diffraction (XRD) and X-ray Photoelectron Spectroscopy (XPS) (see Section 5.4.3). Solid products were annealed (Section 3.3) and the resulting patterns compared with a database of patterns to match the peaks and therefore characterise the spectra. As the samples were thoroughly washed and dried before annealing, no salt (from the electrolyte) was expected in any of the patterns observed. XRD patterns of the analysed solid dissolution products are shown in Figures.5.19 to 5.21 and show patterns obtained for the low chromium steels (SS410 and J), Figures.5.22 and 5.23 are those for the high chromium steels (SD and D) and Figures.5.24 and 5.25 are those for the intermediate chromium steel (SS316).

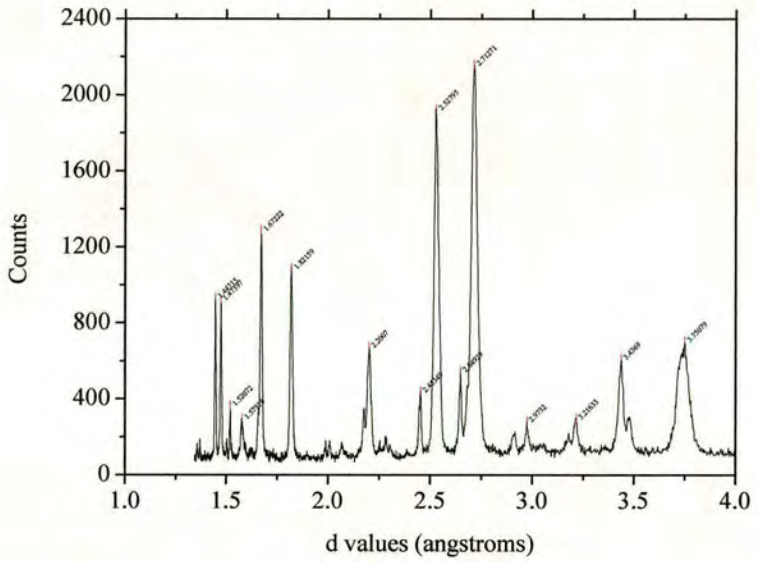

Figure 5.19: XRD pattern for SS410 with chloride electrolyte annealed at 800°C under an Argon stream. The d values of all the major peaks are marked.

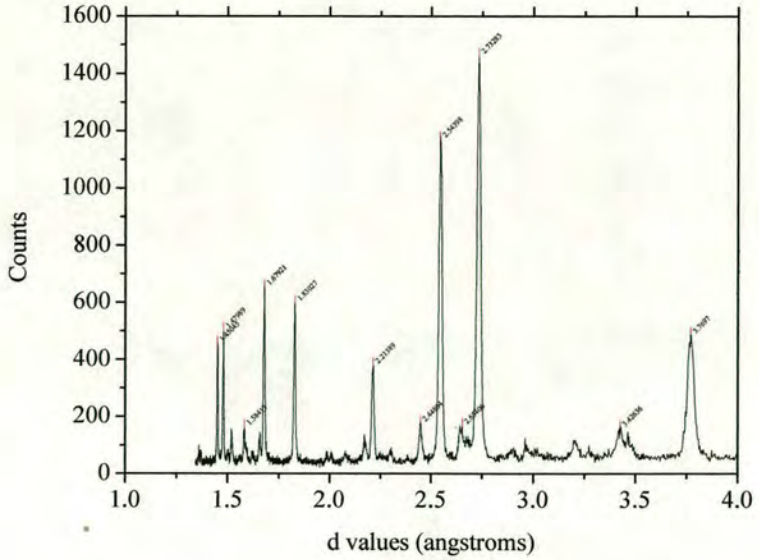

Figure 5.20: XRD pattern for SS410 with nitrate electrolyte annealed at 800°C under an Argon stream. The d values of all the major peaks are marked.

The pattern for SS410 appear to be very similar for both chloride (Figure 5.19) and nitrate (Figure 5.20) electrolyte. Comparing the pattern to that of haematite (Figure 5.26) shows these peaks (Fe_2O_3 peaks d = 3.74, 2.72, 2.53, 2.20, 1.82, 1.67, 1.58, 1.48, 1.45) to be present in both of these SS410 patterns as well as some additional peaks. As Fe is the main component in the steel then this result is consistent with the steel composition. The other peaks are probably mixed metal oxides with similar structures to haematite as similar peak patterns were found for similar structures to haematite but with different lattice dimensions.

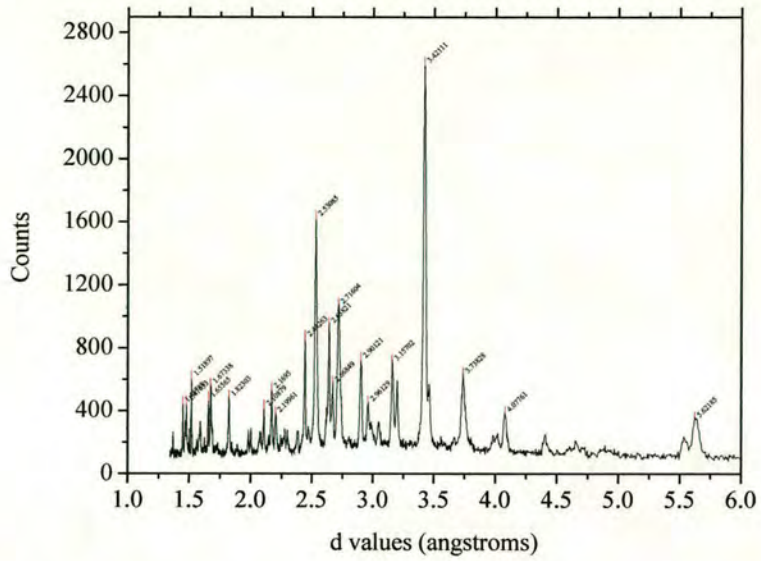

Figure 5.21: XRD pattern for J with nitrate electrolyte annealed at 800°C under an Argon stream. The d values of all the major peaks are marked.

However, the J pattern with nitrate (Figure 5.21) appears to have some haematite present but there are a large number of additional peaks. It has not been possible to fully identify these due to the complexity of the spectra. These are also observed in the Fe with nitrate pattern (Figure 5.27). Haematite appears to be present as well as additional products. This could be because the dissolution products when machining with chloride or nitrate are different as has been postulated (Section 5.4.1). It is likely that there are a lot of mixed metal oxides present in nitrate ECM and oxychlorides in chloride electrolyte ECM. Only Cr(VI) has been identified in the electrolyte solution through visible spectroscopy (Figures.5.14 to 5.18). Therefore, the remaining steel elements are likely to be in the solid oxide and oxychloride products, giving rise to structures that produce the other lines.

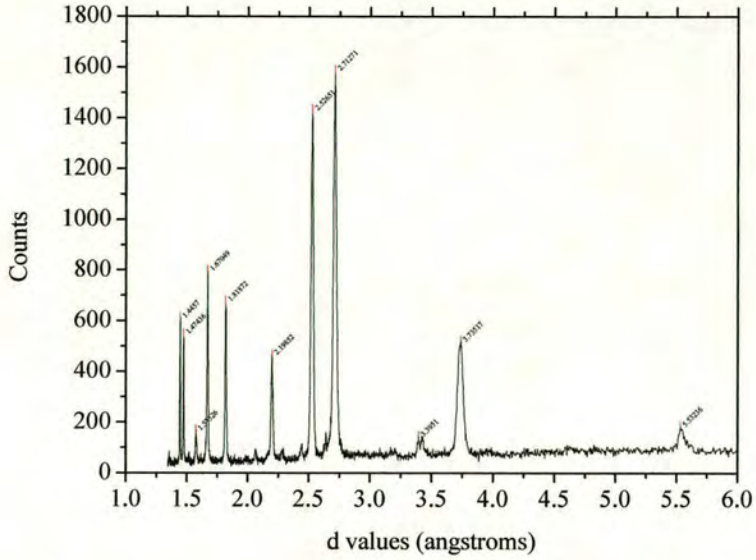

Figure 5.22: XRD pattern for SD with chloride electrolyte annealed at 800°C under an Argon stream. The d values of all the major peaks are marked. Note that only the pattern for SD was analysed as a representative spectrum, as both the high chromium steels (SD and D) produce similar patterns under ECM conditions with both electrolytes used.

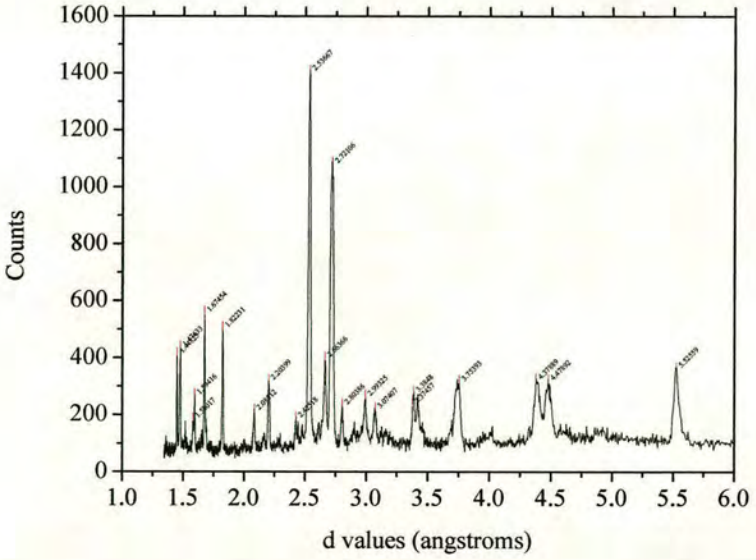

Figure 5.23: XRD pattern for SD with nitrate electrolyte annealed at 800°C under an Argon stream. The d values of all the major peaks are marked.

The pattern for SD with nitrate and chloride again appears to be very similar to the corresponding Fe patterns. This could suggest that the dissolution products are of the generic

formula M_2O_3 for elements of valency 3 producing lattices which may be distorted by doping metal sites with the alloy elements present. Again, SD with nitrate exhibits more peaks which probably represents the difference in products between chloride and nitrate.

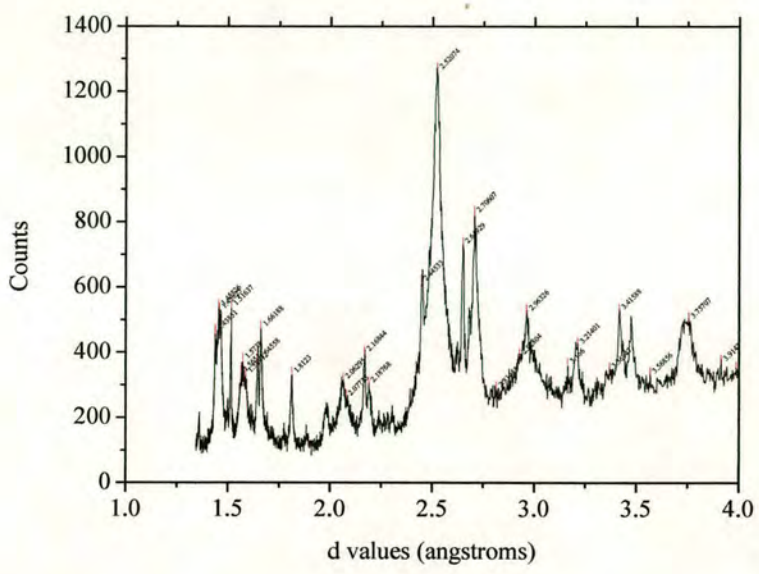

Figure 5.24: XRD pattern for SS316 with chloride electrolyte annealed at 600°C under an Argon stream. The d values of all the major peaks are marked.

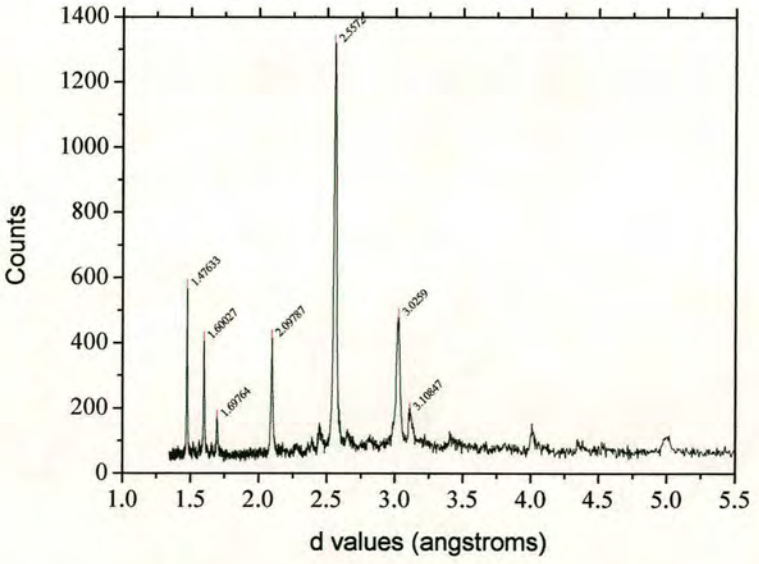

Figure 5.25: XRD pattern for SS316 with nitrate electrolyte annealed at 800°C under an Argon stream. The d values of all the major peaks are marked.

The pattern of SS316 with chloride appears to be broader than the previous patterns but again the peaks correspond to haematite as well as additional peaks, which cannot be unambiguously identified. The reason for this broadness is not known exactly but it could be due to the sample having smaller particles or due to Cl^- substituting O^{2-} in the lattice, creating further lattice distortions. The nitrate pattern does not correspond to haematite but to magnetite (Fe_3O_4) containing mixed oxidation states of Fe (Fe(II) and Fe(III)). As electrochemical dissolution of SS316 occurs with an iron valency of 3 under these conditions (Section 5.2.3), this result suggests partial reduction of Fe(III), most probably by the H_2 tool products, may be occurring in bulk electrolyte. This indicates the Argon stream in the XRD annealing process is efficient enough to prevents oxidation by oxygen from the atmosphere as in this case all the sample would oxidise to the thermodynamically most stable haematite phase Fe_2O_3 (Fe(III)). Therefore, these results show that different products are produced when machining different steels and additionally confirms that the XRD Argon flow stream can be used to prevent sample oxidation during annealing.

As Fe is the main component of all of the steels then it would be useful to compare the spectra of Fe solid dissolution products when machining with ECM using chloride and nitrate electrolytes.

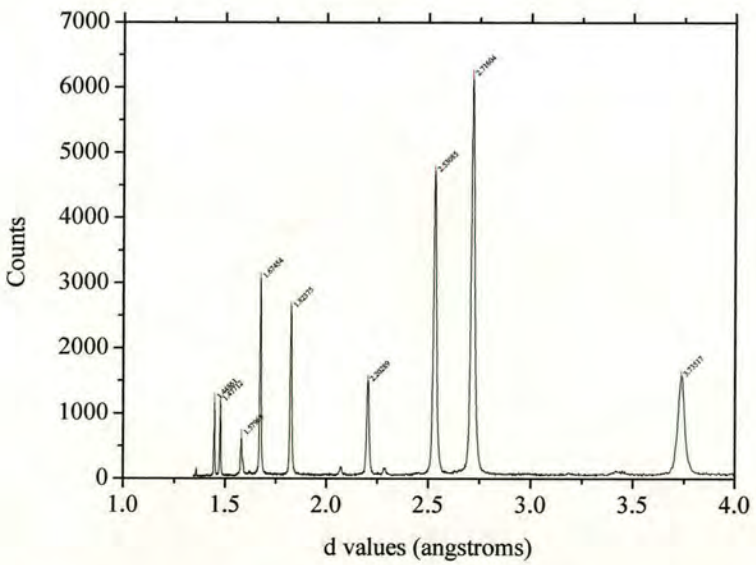

Figure 5.26: XRD pattern for Fe with chloride electrolyte annealed at 800°C under an Argon stream. The d values of all the major peaks are marked and these correspond exactly to Haematite (Fe_2O_3).

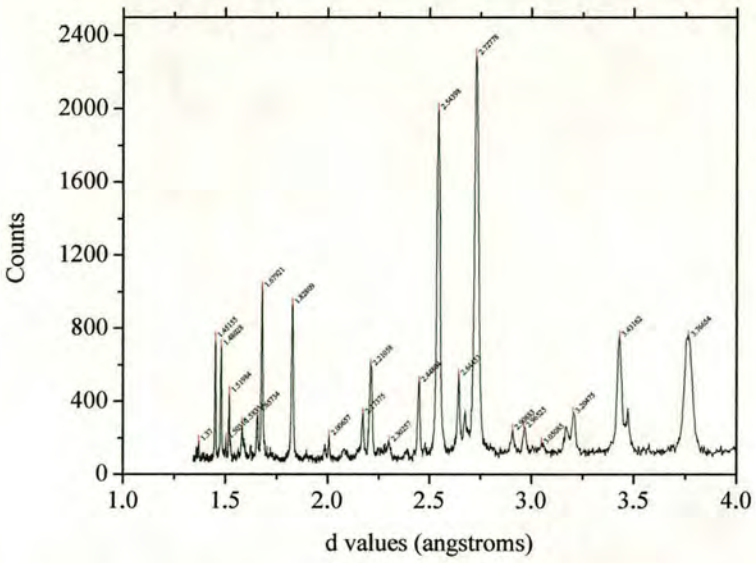

Figure 5.27: XRD pattern for Fe with nitrate electrolyte annealed at 800°C under an Argon stream. The d values of all the major peaks are marked.

Therefore, due to the complexity of the spectra it has not been possible to identify all of the compounds present in all of the spectra. Similarities are observed when compared with the spectra of Fe dissolution products. Therefore, it seems likely that the spectra contain a mixture of metal oxides. The predominant structure in most of the spectra is haematite with the formula Fe_2O_3. It is possible that distorted Fe_2O_3 structures may also be present in these samples with Fe alloyed with other metals, M (often M^{3+} but also M^{n+}) which would account for distortions in the lattice parameters and hence peak broadening and peak multiplets and also the other metal elements present in the steels. It is also possible Cl^- (when using chloride electrolyte) might replace O^{2-} in the structure to also produce further distortion. It has been possible to compare the samples when using nitrate and chloride electrolytes and some differences can be observed indicating differences in the dissolution products when using these electrolytes, consistent with the different co-ordinating properties of the anions. However, it has not been possible to precisely characterise the composition and structure of the solid dissolution products using XRD.

5.4.3 XPS Quantitation of Oxide films

XPS probes core energy levels to provide a compositional analysis of a surface. Because the binding energies of core levels are essentially characteristic of the element, elemental analysis is possible by measuring the kinetic energy of the emitted photoelectrons and knowing the energy of the incident X-rays (see Section 2.14). The observation of certain binding energy peaks in an XPS spectrum can therefore be taken as an indication of the presence in the surface region of a particular elemental species. The exact peak position may then be used to indicate the oxidation state of these elements. However, the usefulness of XPS for compositional analysis depends on how sensitive the technique is and how easily the technique can be made quantitative. A primary parameter which determines both of these is the photoionisation cross section of the elemental orbital. Additionally the availability of accessible energy levels is important. The penetration depth of the X-rays is normally very long compared with those of the escaping photoelectrons (with a photon energy in excess of 1 keV) and as the energy of the X-rays are relatively high, photoemission from some energy levels of all elements is possible and in most cases several levels are accessible. Quantitative studies are possible using XPS as a means of compositional analysis and by taking great care in the mode of calibration analyses accurate to 5 % are possible [141].

Before examining the XPS results for the steel particles after machining, it would be useful to test the capabilities of XPS and assess whether such accuracies are readily achievable for steels by examining some results for a steel that has not undergone machining. SS316 (intermediate chromium steel) was examined, analysing the elemental composition of the surface chromium rich oxide layer as it is removed by sputtering.

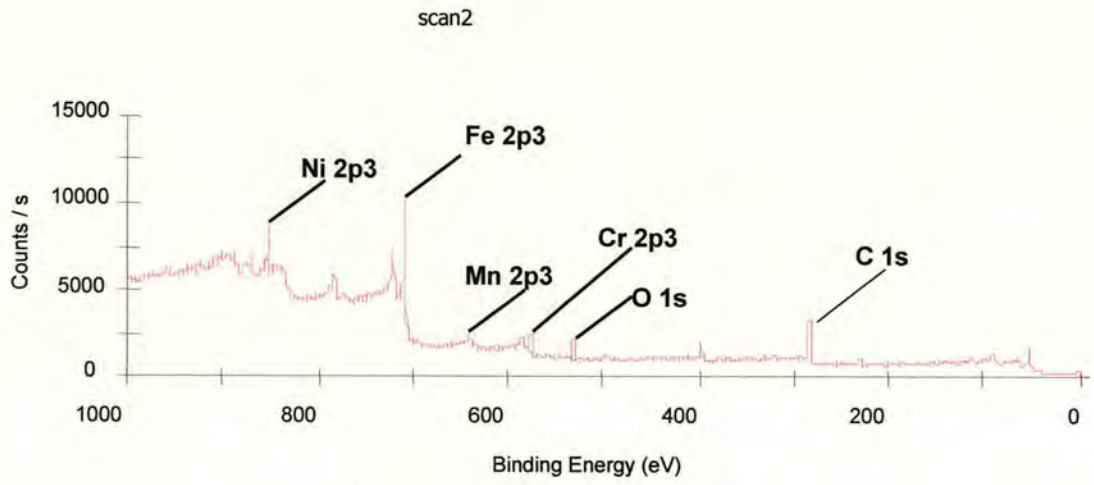

Figure 5.28: XPS pattern of SS316 without any machining after 2 scans and 1 sputter at 3 keV and to approximately 12 nm depth.

Figure 5.28 shows the XPS spectrum for SS316. These results were obtained after the steel surface was sputtered to a depth of approximately 12 nm by argon ions (see Section 3.9 for discussion on the sputtering of surfaces with Ar^+ ions). This was performed because the stainless steel surface was often contaminated by grease and fingerprints due to handling and gave spectra dominated by adventitious carbon without at least 1 sputter period. The spectrum is dominated by sharp emission peaks and it is also evident that there is still a large peak present due to carbon, indicating that the steel surface is still contaminated but to a much lesser degree than without any sputtering. In addition, a number of other features are observed. The most obvious general feature is the steps in intensity to the higher binding energy side of XPS peaks. This can be attributed to inelastic tail losses and scattering following original excitation of the relevant core level. The inelastic loss tails reflects the fact that while the surface sensitivity shown by the directly emitted (no loss) photoemission peak is defined by the electron inelastic scattering mean free path for the escaping electron, the depth of photoionisation is related to the much weaker absorption of the incident X-ray photons. Escape energies in XPS are high, typically around 500 – 1400 eV and therefore a large low energy secondary peak causes a severe loss of signal to background ratio at low kinetic energies (high E_b). The XPS spectrum therefore has a stepped structure as at high kinetic energies (low E_b) there are few primary electrons of sufficient energy to create further electrons by inelastic scattering, while each new discrete emission opens up a new channel of primary electrons to be inelastically scattered. These individual inelastic tails can be probably attributed primarily to photoionisation events occurring at depths below the surface

layer much greater than the mean free path for inelastic scattering. Thus, only inelastically scattered electrons from these photoionisation events can be detected outside the surface. This effect is particularly pronounced in photoemission because of the deep penetration of the incident photon beam relative to the escaping depth of the escaping electrons.

The results in table 5.3 were obtained from this experiment, after the steel surface was sputtered to a depth of approximately 12 nm by argon ions (see Section 3.9 for the sputtering of surfaces with Ar^+ ions).

Name	Observed At.%	Specified At.%	Metal At.%	Centre BE/eV ± 0.5 eV	Valency
Fe 2p3	32.16	70.09	55.97	709.5	2
Cr 2p3	16.68	17.00	29.03	577.0	3
Ni 2p3	6.10	8.00	10.62	854.0	2
Mn 2p3	2.52	2.00	4.39	641.0	3
O 1s	42.54	-	-	530.5	-2

Table 5.3: Composition atomic % of SS316 for 2 XPS scans after 1 sputter (to 12 nm depth) at 3 keV and 1μA sputter current.

It has previously been found [142] that the passive film on stainless steels (specifically SS316 and SS304) were comprised primarily of $Cr(III)_2O_3$ and $Fe(III)_2O_3$ which would be expected to give a metal:oxygen ratio of 40 %:60 % if this were the case. However, the results actually give a ratio of 57.5%:42.5%. This lower than expected oxygen composition may indicate the presence of a lower valency metal oxide. When comparing the Metal At.% and Specified At.% columns then it can be observed that at approximately 12 nm into the surface of the unmachined SS316 sample that as may be expected (Section 1.16), Cr is enriched close to the surface (29 % compared to 17 % in the bulk steel) while Fe is depleted (from 70 % in the bulk steel to 55 % close to the surface). Ni and Mn are also slightly enriched. In order to determine the valency of the elements detected the binding energies of the elements have been compared to those of other compounds in the NIST XPS database [143]. Typical Fe, Cr and Ni compounds and their binding energies for 2p3 orbitals as reported in this database are given in Table 5.4.

Fe(0)	**$Fe(II)Cl_2$**	**Fe(II)O**	**$Fe(III)_2O_3$**	**$Fe(III)Cl_3$**
707.0 eV	710.6 eV	710.7 eV	711.3 eV	711.6 eV
Cr(0)	**$Cr(III)O_2^-$**	**$Cr(III)_2O_3$**	**$Na_2Cr(VI)_2O_7$**	**$Cr(VI)O_3$**
574.0 eV	577.0 eV	577.1 eV	579.9 eV	580.1 eV
Ni(0)	**Ni(II)O**	**$Ni(II)OH_2$**	**$Ni(III)_2O_3$**	**$Ni(II)Cl_2$**
853.0 eV	854.4 eV	855.5 eV	856.0 eV	856.7 eV

Table 5.4: Typical Fe, Cr and Ni compounds and their respective binding energies and metal oxidation states.

Therefore, the measured binding energy of an element was compared to the NIST database of these compounds to determine the oxidation state. Typical Fe (II) and Fe (III) binding energies for 2p3 orbitals are 710.6 eV and 711.6 eV respectively and Cr (III) and Cr (VI) are 577.0 eV and 580.0 eV respectively for 2p3 orbitals. However, Ni (II) and Ni (III) compounds are closer in binding energies with no definite distinction between +2 and +3 oxidation states making their quantification more difficult.

These relative amounts of the main elements are different to those when the surface has been sputtered to a depth of approximately 80 nm (Table 5.5). Here the amounts are much closer to those found in the bulk steel and the amount of oxide is significantly reduced with the observed binding energies consistent with the metal oxidation states being 0. Therefore, the depth of the oxide layer on stainless steel 316 appears to be of the order of 80 nm.

Name	Observed At.%	Specified At.%	Metal At.%	Central BE/eV ± 0.5 eV	Valency
Fe 2p3	52.29	70.09	66.36	707.00	0
Cr 2p3	14.80	17.00	18.78	574.33	0
Ni 2p3	11.13	8.00	14.12	853.07	0
O 1s	21.20	-	-	530.03	-2

Table 5.5: SS316 after 8 scans and 7 sputters at 3 keV, shows main elements on surface comprising surface oxide layer.

Therefore, two (Fe and Cr) of the three main elements (Fe, Cr and Ni) present in the steel are very close to their specified amounts with Ni possibly slightly enriched. However, if the oxide layer had been completely removed there should be no oxygen present on the steel surface, but it can be observed that some O is still present (although the amount is

significantly reduced). This could be because there is still some oxide present on the steel after 7 sputters (i.e that the alloy/oxide interface is somewhat diffuse) and/or maybe that O is diffusing into the steel due to an increase in the temperature as a consequence of the sputtering process. However, even with these effects, this depth can be considered to be of the order of the depth of the oxide layer. The fact that the elemental composition of SS316 as measured by XPS is in close correspondence with the actual bulk composition of the steel confirms that in this case, it is possible to use XPS to compare the relative amounts of metal elements to gain insight into the relative elemental compositions in these systems.

It can be noticed on comparison of the elements measured by XPS and those given as specification of the steel when purchased (Table 1.1) that elements with less than 2 % composition are not present in the XPS results. The reason for this is the signal-to-noise ratio which is controlled by the amount of data points acquired at each point of the spectrum. Integrating the signal for longer and/or running repeated numbers of scans increases the signal-to-noise (by $N^{1/2}$, where N is the number of data points) so running 4 times as many scans increases the signal to noise by a factor of 2. However, this process would have taken a long time to sufficiently resolve the spectra for elements of 2 % and less. Therefore, due to time restrictions the required number of scans to fully resolve the spectra was not carried out and the accuracy of the results were determined by the signal to noise ratio which was fixed by the number of scans performed. The experiment as ran could not identify the minor peaks and the results therefore give information about the major peaks. Therefore, throughout the results all elements with less than 2 % composition are not included.

It can also be noted (Table 5.5) that after several sputters no Mn is detected which is not the case after 1 sputter (Table 5.3). Therefore, it is likely that as 2.00 % Mn is given as specification in the bulk steel then after several sputters the concentration of Mn approaches 2 % and is not possible to be detected. Therefore, the main elements present in the steel that can be detected with confidence are Fe, Cr and Ni. It would be expected that these elements would also be detected in the dissolution particles.

5.4.3.1 Measuring the Oxide thickness through sputtering

It is not possible at this time to quantify the reported duplex character of surface oxide films [64 - 67], however a rough estimation of the oxide layer thickness is possible by calculating the depth sputtered through the oxide layer and then looking at the results to see when the

metal oxidation states return to 0 and the oxygen content is minimised (Section 5.4.3). SS316 was sputtered at 3 KeV and 1 μA for 1 minute.

This was calculated to give a sputtering depth of 12 ± 2 nm using data provided in the XPS handbook [144] gained from sputtering a stainless steel surface (type unspecified) and then measuring the resulting depth of sputter (see [144] for more information). This took into account the different sputtering rates of different metals and their oxides. For comparison of oxide depths for different steels (Section 5.5.1) the number of sputter periods is assumed to have a linear relationship to the depth of sputter enabling a comparison of the relative oxide thickness. However, there may be some deviation from this, especially when sputtering through relatively soft oxide layers into relative hard alloy, when the sputtering rate may be expected to vary. Also different steels have slightly different oxide compositions, which may lead to some variation in the sputtering rate of different oxide surfaces. These effects mean that the quoted sputter depths should be considered approximate.

5.4.3.2 XPS analysis of iron

From the results presented in Chapter 6, it is clear that both pure iron and J show increasing ECM currents at equilibrium when using nitrate electrolyte. It is postulated that this effect is due to accumulating solid iron oxide products, which can catalyse the short-circuit reaction between the products from the tool and workpiece (see Section 6.2). Therefore, analysis of the solid particulate products from the ECM of pure iron was carried out to compare with those from J and the other steels. The ECM experimental conditions were as given in Section 3.7. The results for the analysis are shown in Figure 5.29.

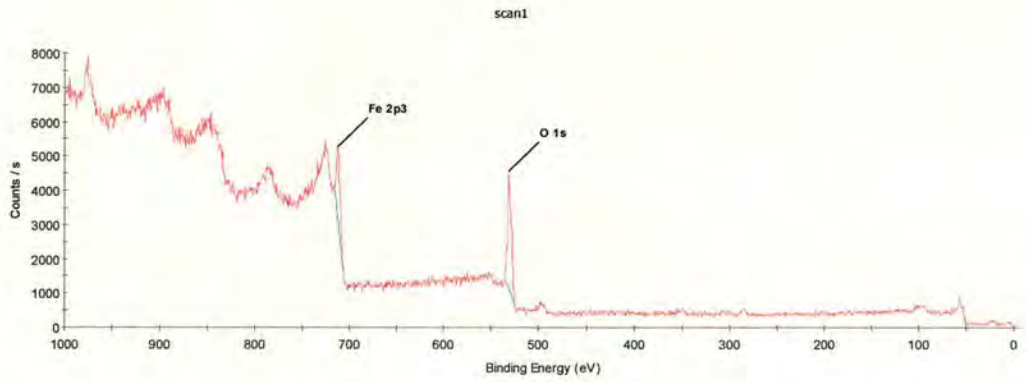

Name	Observed At.%	Specified At.%	Centre BE/ eV ± 0.5 eV	Valency
Fe 2p3	14.08	99.99	712.50	+3
O 1s	85.92	-	531.50	-2

Figure 5.29: XPS spectra with table of results for Fe solid dissolution particles machined with nitrate electrolyte.

It is clear that the particles consisted of Fe and O as expected. The oxidation state of Fe is +3 as expected (see Section 5.2), indicating that the product is most likely Fe_2O_3. The observed binding energy of the O 1s orbital (531.5 eV) has a comparable binding energy to the O 1s orbital in Fe_2O_3 (531.3 eV) from the NIST database [143], providing strong evidence that the major iron product is Fe_2O_3 (haematite). This is also consistent with the XRD results (see Section 5.4.2), but it is worth remembering that these results have been obtained without annealing, which supports the hypothesis (see Section 6.6) that it is Fe_2O_3 particles that are implicated in the catalytic effect. For Fe_2O_3, it would be expected that the ratio of Fe:O that would be obtained would be 40%:60%. It is clear from these results in Figure 5.29 that the measured Fe:O ratio is considerably lower than this, and even lower than that expected for the completely hydrated oxide, iron(III) hydroxide ($Fe(OH)_3$), which would give a ratio of 25%:75%. This supports the idea that quantitative XPS of these oxide particulates tends to underestimate the amount of metal (M), perhaps due to a difference in the escape depth of the O and Fe photoelectrons (see Section 5.4.3.4). It is also interesting to note the lack of any carbon of valency zero, C(0), in the spectrum. This is evidence that the carbon is not deposited in these oxide films as carbonates due to the incorporation of CO_2 from the atmosphere (which in any case would not lead to a carbon valency of zero) or due to C(0) contamination arising from the filtering process. Thus carbon present in the oxide products

of steels must be from the inherent carbon in the steel (see Sections 5.3.4.4, 5.3.4.5 and 5.3.4.6). All steel particulate products from machining with nitrate electrolyte show significant C(0) in the product, as all the steels have carbon as a constituent (Table 1.1). This is not the case with pure Fe and therefore no carbon is observed.

5.4.3.3 Summary of the XPS Capabilities

All elements with less than ~2 % composition in the stainless steel cannot be reliably detected with the standard configuration and data acquisition times used in these experiments.

Therefore, with this point in mind then the stainless steel dissolution particles were analysed with XPS. XPS analysis was performed on the solid dissolution products washed (described in Section 3.9) but unlike for XRD no annealing was carried out on the samples as it was hoped that it would enable the elements and oxidation states present in the particles to be identified and quantified (Section 5.4.1 and 5.4.2). From the XRD spectra (see Section 5.4.2) it appeared that a variety of metal oxides were present but it was not possible to identify all the different oxides due to the complexity of the spectra. A large selection of particles for each of the samples was analysed and therefore a good average approximation of composition was expected. This was to negate any effects due to inhomogeneity of the particles, although a homogeneous distribution of particles was observed in the optical microscope during imaging. As the unmachined surface of SS316 has been analysed with good results and the capabilities of the XPS process determined, then SS316 dissolution particles when using nitrate electrolyte will be examined first.

5.4.3.4 XPS spectra of the dissolution products of SS316 with nitrate electrolyte

The XPS spectra obtained from SS316 dissolution particles when using nitrate electrolyte is shown in Figure 5.30.

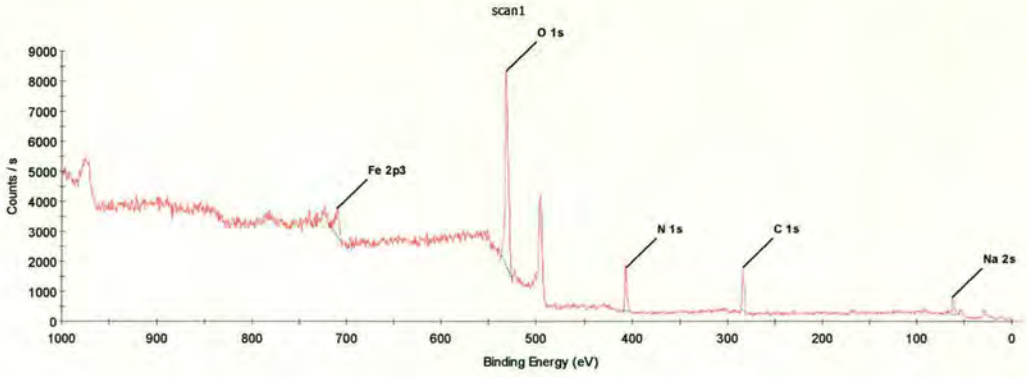

Name	Observed At.%	Specified At.%	Centre BE/ eV ± 0.5 eV	Valency
Fe 2p3	2.41	70.09	710.24	+3
N 1s	11.44	-	406.35	+5
C 1s	19.60	0.12	283.57	0
O 1s	46.54	-	531.97	-2
Na 2s	20.02	-	61.94	+1

Figure 5.30: XPS spectra with table of results for SS316 solid dissolution particles machined with nitrate electrolyte.

Fe(III) is detected as expected from the ECM chronoamperometric analysis (Section 2.8.2) when machining SS316. It can be noted that some Na and N were found indicating that some nitrate electrolyte was still present due to insufficient washing. Note that Na may have larger than expected % as it has a very low binding energy, therefore if $NaNO_3$ were present and N is 11% (from table), then it would be expected that O was 33%.

It should be noted that in this and every subsequent spectrum of the dissolution particles there is a peak at 500 eV which is unidentified. No result was obtained on entering the binding energy of this peak into the NIST database. Therefore, the peak is probably an Auger peak from another element or a secondary peak caused by primary scattered electrons causing secondary electron transitions.

The first striking feature about these particle XPS results is the high amount of oxygen present and the very low amount of metal. The binding energy of oxygen is consistent with Fe_2O_3. As observed with the UV/Vis results (Section 5.4.1) then when using nitrate electrolyte with SS316, CrO_4^{2-} is produced which is a stable and soluble dissolution product and therefore it is expected that little or no Cr would be present in the solid particles.

However, Fe and Ni would be expected (from SS316 results) but no Ni was found and a very low amount of Fe was detected.

When analysing these steel dissolution particles, it is clear that there is significant additional oxygen in the sample, and that the constituent elements from the alloy are present at much less overall elemental abundances than those found before oxidation. One reason for this may be that quantitative analysis is easiest for monolayers or thin film layers on surfaces. This is because in thick oxide films, the escape depth, and hence the escape probability at a given depth, of the photoelectrons depends on the electron energy, as higher energy electrons are more likely to avoid energy loss processes and emerge from the surface as a photoelectron of unchanged energy. Therefore, for a fixed incident X-ray energy as is used in XPS systems, as metal core orbitals (M) typically have higher binding energies than oxygen (O) (e.g 710 eV for Fe 2p3 orbitals compared to 530 eV for O 1s orbitals), the resulting photoelectrons from M will have lower electron kinetic energies and therefore their electrons could have reduced escape probability in the depths of the oxide film. This will lead to more photoelectrons emerging for O from the depths of the film, leading to quantitation difficulties when quantifying the relative amounts of M and O. In a situation where $NaNO_3$ may be coated on the oxide particles, this problem may be greatly exacerbated, as the M and oxide O elements may only be present at greater depths, under the surface nitrate coating, which will greatly attenuate the M and oxide O signals with respect to the Na, N and O signals from the nitrate. This indeed seems to be the case for these particulate products. Because of these problems, ratios of M to O in these samples are probably not absolutely accurate but changes in these ratios for different samples may be informative. However, as the same orbital in different metals (M) tend to have more similar binding energies (and therefore result in similar photoelectron kinetic energies and escape probabilities) and the metals in the oxide will tend to be located at similar depths in the samples, then quantitative analysis of the relative amounts of metals in the oxide by XPS measurement using the same orbitals will be expected to be more accurate. Therefore, the results presented in the following sections will concentrate on the analysis of major elements (Fe, Cr and Ni) in the oxide products, and on the ratios of these major metallic elements in the surface oxide films.

Also, detected on the surface of these particles was a high amount of C in the 0 oxidation state, C(0). It is worth noting that due to the surface sensitivity of the XPS method it is clear that there is a high amount of C on the outside of the particles. One possible source of carbon

is that the oxide on the steel particle surface may react with carbon dioxide, CO_2, in the air to form metal carbonates, CO_3^{2-}. If this were the source of carbon then a high amount of C would be expected when using both nitrate and chloride electrolytes, which is not found (see below), and a C valency of 4 would be expected from the XPS measurements, which is not the case. The amount of carbon in SS316 is 0.12 % (Table 1.1). It can also be noted that when machining the stainless steels with nitrate electrolyte that the machined surface of the steel appears black, and the black substance can be wiped away. If this substance were carbon, it would tend to suggest that C(0) is accumulating on the steel surface, as it is difficult to oxidise and therefore to electrochemically machine. Removal of the carbon would then be facilitated by the dissolution and removal of the surrounding metal matrix as well as possibly being dislodged by the high velocity of the electrolyte. It is likely that in the presence of chloride the carbon is removed from the steel surface due to the strong ligating properties of chloride ions, which favour the electrochemical oxidation and dissolution of the carbon. However, as nitrate is a relatively poor ligand, oxidation and dissolution is precluded. This carbon appears to be entrained into the surface of the metal oxide solid products, thus explaining its prevalence in the SS316 particles when machining with nitrate.

5.4.3.5 XPS analysis of the low chromium steels

The XPS spectra for SS410 particles in chloride and nitrate electrolytes are shown in Figures 5.31 and 5.32 respectively.

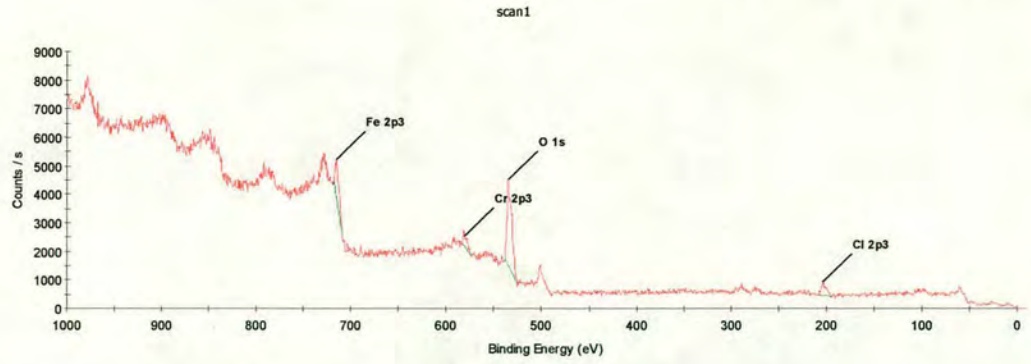

Name	Observed At.%	Specified At.%	Centre BE /eV ± 0.5 eV	Valency
Fe 2p3	6.49	85.50	712.47	+3
Cr 2p3	3.15	12.75	580.90	+3/6
O 1s	68.10	-	531.57	-2
Cl 2p3	22.26	-	203.00	-1

Figure 5.31: XPS spectra with table of results for SS410 solid dissolution particles machined with chloride electrolyte with no sputtering.

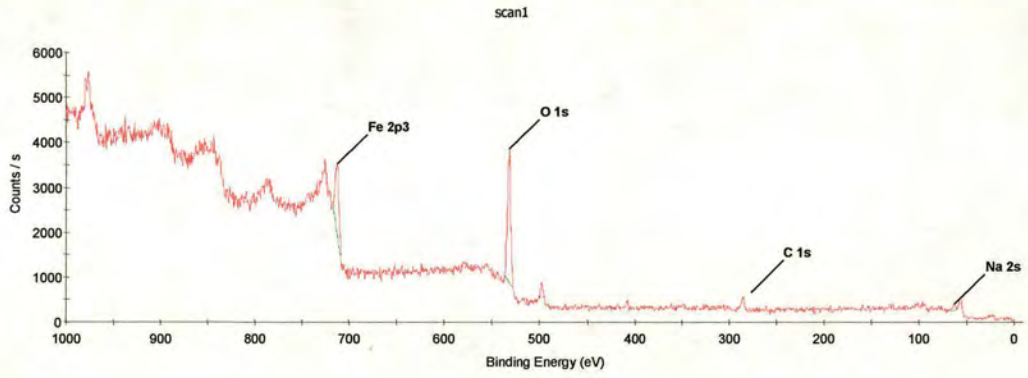

Name	Observed At.%	Specified At.%	Centre BE /eV ± 0.5 eV	Valency
Fe 2p3	10.33	85.50	712.70	+3
O 1s	62.93	-	531.55	-2
C 1s	9.04	0.14	283.54	0
Na 2s	17.70	-	62.50	+1

Figure 5.32: XPS spectra with table of results for SS410 solid dissolution particles machined with nitrate electrolyte.

These spectra for SS410 with chloride and nitrate (see discussion above) both show Fe in the +3 oxidation state. This is consistent with the valency of ECM dissolution for nitrate, but is not consistent with the ECM dissolution when using chloride electrolyte, when Fe(II) is produced (see Section 5.2.2). Therefore, this tends to suggest that Fe(II) undergoes further oxidation to Fe(III). This could either be in the electrolyte tank by air or when the particles are dried and air is sucked over the particles prior to XPS measurement. For nitrate, no Cr was detected in the solid products, consistent with the dissolution and formation of stable soluble Cr species as Cr(VI) (Section 5.4.1). When chloride was used then the formation of stable soluble Cr(VI) species has been shown not to occur by UV/Vis and dissolution via Cr(III) has been postulated (Section 5.2.2 and 5.2.3); in this case some Cr(VI) appears to be observed in the particles which is not what would be expected. However, this assignment may not be correct, as metals binding to halogens tend to have higher binding energies due to the high electronegativity of halogens. The halogens therefore decrease the electron density at the metal centre in a similar manner to a higher oxidation state. Therefore, $CrCl_3$ has a binding energy of 579.9 eV which is within the experimental error of the measured binding energy for Cr in this measurement; and may be responsible for the higher than expected binding energy rather than the higher oxidation state of Cr (VI).

The Cl^- detected was most likely due to the incorporation of chloride ions into the oxide layer of the particle as was postulated in Section 5.5. The higher binding energies observed for Fe(II) and Cr (III) support this hypothesis. The Fe to Cr ratio when using chloride is increased from 7Fe:1Cr in the bulk steel to 2Fe:1Cr in the particles. Therefore, there is approximately 3 times more Cr in the particles than in the bulk steel indicating that the Cr may be incorporated into the solid products rather than staying in solution as is the case with nitrate electrolyte.

For the nitrate electrolyte products, no significant incorporation of nitrate (as evidenced by there being no significant N peak on the XPS spectrum) was found for the products of ECM. This may be due to more efficient washing of the solid products. Also, a significant amount of C was detected (as was the case with SS316 and nitrate, see earlier for discussion) which was not the case when using chloride electrolyte (also as with SS316 and chloride). Therefore, as with SS316 the carbon may be coating the nanoparticle surface and inhibiting an accurate determination of the elemental composition of the particles.

However, with these results and the previous results (SS410 with chloride) it would be expected that there would be at least 25 % metal if all the products were MO_3 (M_2O_3 is probably more likely, as the binding energy of the O 1s orbital in Fe_2O_3 is consistent with the results found). The products seem to be essentially Fe particles with some additives. Therefore, the Fe and Cr content are very low possibly indicating heavily oxidised nanoparticles with most of the metal in the centre of the particle which cannot be detected.

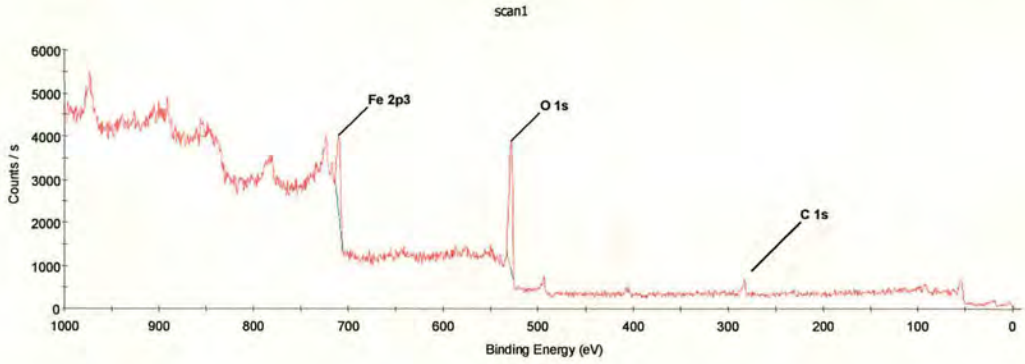

Name	Observed At.%	Specified At.%	Centre BE/ eV ± 0.5 eV	Valency
Fe 2p3	13.04	80.63	710.24	+3
C 1s	9.25	0.13	283.59	0
O 1s	77.67	-	528.74	-2

Figure 5.33: XPS spectra with table of results for J solid dissolution particles machined with nitrate electrolyte.

When using nitrate electrolyte with J (Figure 5.33), no significant amount of N was detected (as with SS410) suggesting that NO_3^- from the electrolyte is not incorporated into the particles to any significant extent; this is expected, due to its poor ligating properties. J with nitrate also showed Fe(III) to be present as expected (see Section 5.2.2). It is important to note that the two main elements present in all the particles and particularly J with nitrate electrolyte are iron and oxygen. This suggests that these particles may essentially consist of Fe_2O_3 (albeit with significant amounts of C). The importance of this will be discussed in Chapter 6. Again, C is present as with the previous steels results when using nitrate electrolyte. This seems to corroborate the hypothesis that the carbon present in the steel is not able to be removed from the steel surface by oxidative electrochemical dissolution during ECM, as for SS316 (see Section 5.4.3.1).

5.4.3.6 XPS analysis of the high chromium steels

The spectra and resulting quantitative results tables for the high chromium steels are now shown in Figures 5.34 and 5.35.

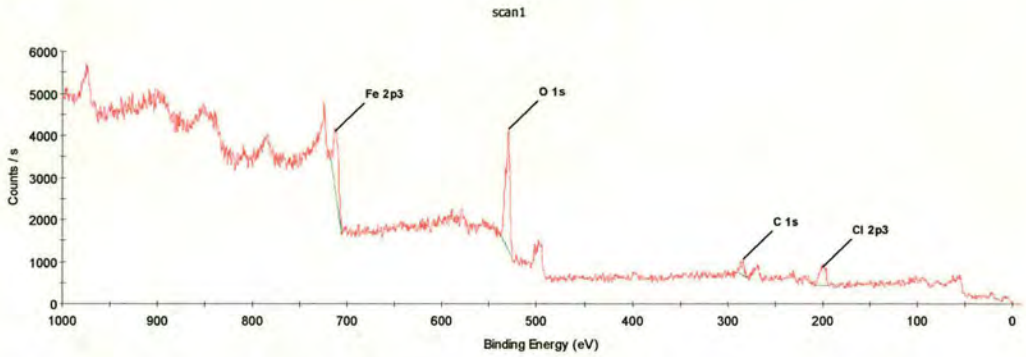

Name	Observed At.%	Specified At.%	Centre BE/ eV ± 0.5 eV	Valency
Fe 2p3	9.03	61.20	712.59	+3
C 1s	15.96	0.02	283.50	0
Cl 2p3	24.01	-	199.25	-1
O 1s	51.01	-	529.54	-2

Figure 5.34: XPS spectra with table of results for SD solid dissolution particles machined with chloride electrolyte.

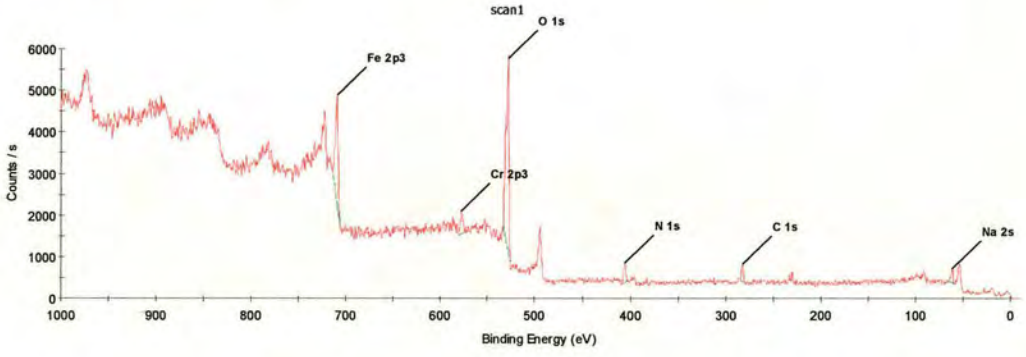

Name	Observed At.%	Specified At.%	Centre BE /eV ± 0.5 eV	Valency
Fe 2p3	8.22	61.20	709.50	+3
C 1s	9.02	0.02	282.50	0
N 1s	6.83	0.26	405.28	+5
O 1s	56.09	-	528.30	-2
Na 2s	17.74	-	61.00	+1

Figure 5.35: XPS spectra with table of results for SD solid dissolution particles machined with nitrate electrolyte.

As for the low Cr steels (see Section 5.4.3.5) significant amounts of C(0) were found when using nitrate electrolyte. However, C(0) was also observed with chloride for high Cr steels. This could be because the oxide layer for high Cr steels is known to remain intact under all conditions (see Section 5.2.1). Therefore, if the C present in the steel (0.02 % for SD) is not exposed to the chloride electrolyte though the onset of pitting then the chloride may not be able to ligate to the C(0) and therefore cannot promote oxidative dissolution from the steel surface. Therefore, the C(0) may be entrained in the electrolyte and incorporated into the particulate products. The structure of these particles is not known but it is possible that as before (see Section 5.4.3.4) the C may have accumulated on or near the outside of the particles, giving a artificially high amount of C when measured by XPS.

It is interesting that less than 2 % Cr was observed in the particulate products in both nitrate and chloride. This is consistent with the UV/vis results for nitrate and chloride as these high Cr steels have been shown by UV/vis studies to produce soluble stable CrO_4^{2-} products, and so significant Cr would not be expected in the particulate products (see Section 5.4.1). (Note, trace amounts of Cr were observed in the XPS spectrum of the products with nitrate (Figure 5.34)). For chloride, as with SS410 (see Section 5.4.3.5), there is a relatively large Cl^- peak when compared to O^{2-} indicating high Cl^- occupancy in the oxide lattice again.

5.4.4 Conclusion

The XPS results have showed that when machining the steels with nitrate electrolyte, then the solid particulate products contained significant amounts of C(0). This shows that C cannot be easily removed by electrochemical oxidation in nitrate and is most likely removed by dissolving all surrounding elements and entraining C in the flowing electrolyte. Given the abundance of C in the original steels and the surface sensitivity of XPS, this C(0) is most likely concentrated near the surface of the particles. However, no such C(0) is generally observed in chloride electrolyte products except in high Cr steels possibly indicating that chloride facilitates the ECM of carbon.

Generally, there is significant chromium content found in the products when using chloride electrolyte which is consistent with no soluble Cr product in Uv/vis results for chloride. However, no Cr is found in the solid products for chloride with high Cr steels or with nitrate electrolyte again consistent with the formation of soluble stable CrO_4^{2-} product from the

Uv/vis results. The results are consistent with solid haematite particles as products for iron machining which are consistent with powder XRD, Section 5.4.2.

The oxidation states of elements generally consistent with observed ECM dissolution valencies (e.g. Fe as (III), Cr as (VI) or (III)). One exception was the dissolution of low Cr steels in chloride, where apparent valencies of 3 from XPS were observed compared with 2 for ECM. This indicates that care must be taken with oxides containing significant Cl^-, where the association of the metal with the electronegative chloride ion may induce lower binding energies for oxidation state (II) for Fe which may be mistakenly assigned oxidation state (III).

The relative quantitation of M and O was problematic for thick oxides where the amount of M is consistently under estimated with respect to O, most probably due to the difference in the escape probability of the respective photoelectrons at any given depth in the oxide. However, changes in the amount of M between steels and the relative amounts of metals within an oxide may be able to be measured. The XPS experimental protocol used in this thesis was shown to be capable of detecting elements at greater than 2 % initial composition in the products. Longer acquisition times and/or greater X-ray intensities may be necessary to probe variation in the composition of the minor elements.

Therefore, XPS is a very appropriate technique for the analysis of solid oxide products from ECM. It is worth mentioning that no sputtering on the solid particulate products was carried out due to time constraints. However, it is possible that sputtering the particles would potentially give insight into the composition of the particles as a function of depth, particularly those with coating of C(0) and electrolyte salt (due to insufficient washing). Therefore, sputtering may be worth doing as part of future work (as long as the size of the particles is large compared to the sputter rate).

5.5 The Surface Dissolution Characteristics of Stainless Steels

In the light of the electrochemical, chemical and spectroscopic data collected in this chapter concerning the ECM of stainless steels, it is now worth considering the surface dissolution characteristics of the steels. According to the point defect model (PDM, see Section 1.16) the oxide layer is considered to be electrically neutral, dominated by a high electric field and containing a high concentration of point defects namely cation and anion vacancies. The rate of the oxide growth and breakdown is considered to be dependent upon the concentrations of these vacancies (Figure 5.36).

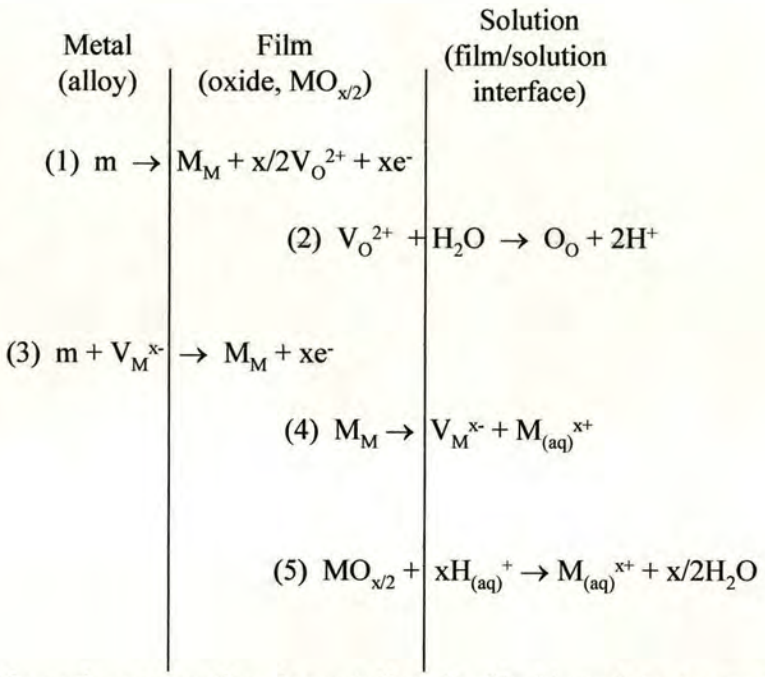

Figure 5.36: Schematic representing the metal/anodic film/electrolyte system according to the point defect model (PDM). m = metal atom, M_M= metal cation in cation site, O_O = oxygen ion in anion site, V_M^{x-} = cation vacancy, V_O^{2+} = anion vacancy. Reactions (1) and (2) describe the consumption and formation of anion (oxygen ion) vacancies at the film/solution and metal/film interface respectively. Reactions (3) and (4) describe the consumption and formation of cation vacancies at the metal/film and film/solution interface respectively. Reaction (5) describes the irreversible dissolution of the film at the film/solution interface.

At the metal/film interface, oxidation of the metal to a metal position in the oxide lattice takes place, along with simultaneous injection of oxygen vacancies (reaction (1)). The oxygen vacancies are then transported through the film to the film/solution interface where they react with adsorbed water (reaction (2)). Therefore, reactions (1) and (2) result in

growth of the oxide film. Also, metal vacancies are produced at the film/solution interface by ejection of a metal ion from the oxide lattice (reaction (4)). These can then travel through the oxide film and are then consumed at the metal/film interface as the metal vacancy is filled by oxidation and injection of a metal ion (reaction (3)). Thus reactions (3) and (4) result in the transpassive oxidative dissolution and transport of the metal through the oxide film (electrochemical machining). Destruction of the film can occur by the condensation of cation and anion vacancies, or by chemical reaction at the film/solution interface (reaction (5))[90 – 92].

Therefore, high valency dissolution (Sections 5.2.1, 5.2.2 and 5.2.3), Fe(III) and Cr(VI), is characteristic of transpassive dissolution through the oxide layer and low valency dissolution, Fe(II) and Cr(III), is characteristic of dissolution from ruptures/pits in the oxide film and is consistent with a loss of the oxide film.

However, halide ions (Cl^- in this case) can incorporate themselves into the oxide layer by occupying an anion vacancy [84 – 86, 136]. The film may respond to the loss of anion vacancies by generating cation vacancy/anion vacancy pairs via a Schottky pair reaction [84]. The anion vacancies in turn are filled by additional anions (Cl^- in this case) at the oxide film/solution interface to generate more cation vacancies. This process is autocatalytic, and a larger number of cation vacancies should lead to larger rates of transpassive dissolution in the presence of chloride. Whether or not the film breaks down depends on the relative rates with which the cation vacancies are transported across the barrier layer and are annihilated by emission of cations from the metal into the film. If this annihilation reaction is incapable of consuming the cation vacancies arriving at the metal/oxide film interface, the excess vacancies will condense and lead to the local detachment of the film from the underlying metal which could rupture the barrier layer leading to the formation of a pit [136, 145]. The results presented in this thesis suggest that this process is sufficient to remove the entire oxide layer locally on low chromium steels which are unable to effectively annihilate the cation vacancies. This leads to pit formation (Figure 5.37), and hence low valency dissolution can occur when using chloride electrolytes.

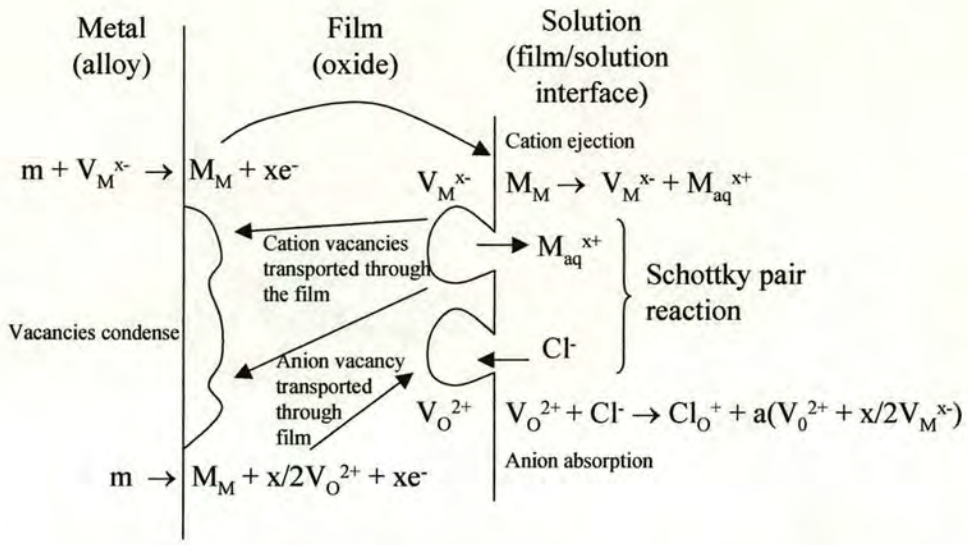

Figure 5.37: Diagram representing film breakdown due to the presence of chloride ions, where (V_0^{2+} + $x/2V_M^{x-}$) is the generation of the Schottky pairs and "a" is a factor which determines the number of Schottky pairs generated per Cl^- inserted. Inserting Cl^- into the oxide hole destabilises the lattice, straining it thus leading to pair generation. Therefore, the reaction is autocatalytic in that filling V_0^{2+} generates more V_O^{2+} to fill and each time this cycles round, more V_M^{x-} are generated. V_O^{2+} and V_M^{x-} are anion and cation vacancies respectively.

However, with high and intermediate chromium steels, the oxide film is thicker and/or more stable, and does not break down in the presence of chloride ions. Therefore, dissolution may occur via a transpassive mechanism in which the oxide film remains intact. This can occur as cation vacancies created at the film solution interface due to cation ejection, are transported across the surface film and filled by cation injection at the metal film interface. The rates of each of these processes therefore determines the overall rate of the ejection of metal cations (ECM dissolution) and each is controlled by the voltage drop in the region of oxide where reaction is occurring as well as the overall vacancy concentration. Changes in the measured values of V_0 therefore reflect changes in the overall voltages to drive these reactions. As the ECM current is given by the flux of cation vacancies from the film interface to the metal interface, decreased voltages (and hence decreased values of V_0) reflect enhanced rates of cation transport. This can be effected in a number of ways. At the metal surface, detachment of the oxide layer can occur due to cation vacancies condensing. At the film/solution interface the oxide layer can start to thin. In the film there can be an enhancement of diffusion and/or migration of species which compromise the barrier layer such as chloride,

by generating greater concentrations of vacancies. Such effects are probed by measuring the variation of I with V_0 (see Section 5.5.2) and the differences in V_0 values obtained for different steels under similar conditions (see Section 5.5.1).

5.5.1 Oxide film on steels

Surface films on steels have been considered to consist of an oxide with two distinct regions; an inner oxide layer which is rich in chromium (and can be considered to consist predominantly of Cr_2O_3) and an outer, more hydrated layer richer in iron [146, 147]. It is the inner, chromium-rich oxide layer that is considered to maintain the passivity of stainless steels, as ion diffusion through the relatively unhydrated and defect-free chromium oxide layer is slow [146, 147]. The thickness of this surface layer can be approximated from the XPS results with sputtering depth (the depth at which the M ratio becomes approximately that of the bulk) and as expected the higher the chromium content, then the thicker the oxide layer (Table 5.6). The un-machined surface of the steel was sputtered until the relative or absolute element concentrations were approximate to those that were known to be present in the steel.

Steel	Oxide thickness / nm (± 12 nm)
SS410 (low Cr)	24 (2 sputters)
J (low Cr)	36 (3 sputters)
Fe (no Cr)	36 (3 sputters)
SS316 (med Cr)	60 (5 sputters)
SD (high Cr)	96 (8 sputters)

Table 5.6: Comparison of oxide layer thickness on the different steels.

Therefore, from Table 5.6, it follows that the more Cr in the steel then the thicker the protective oxide layer as expected. As mentioned previously due to the differing hardness of the various elements in the steel then an absolute value of the oxide film thickness cannot be determined to high accuracy. However, estimations of the film thickness are provided with the number of sputters periods performed. Therefore, even if the exact values of the film thickness are relatively inaccurate, then the number of sputters performed still gives an accurate representation of the ratio of the film thicknesses between the different steels.

However, a more resistant (to diffusion) barrier is likely to have greater lattice energy and hence be more resistant to sputtering thus requiring more sputters to penetrate to the same depth. It is not known how much influence this effect has on the results.

The low chromium steels (J and SS410) have the thinnest oxide layer thus explaining the easy disruption of this layer by chloride ions (from electrolyte) resulting in low valency dissolution. The high chromium steels (D and SD) have a high enough concentration of chromium to sustain the oxide film under the most extreme conditions in this work. (i.e. chloride ions). However, SS316 has intermediate chromium content and therefore appears to show ECM characteristics intermediate between those of low chromium and high chromium steels. It is likely that in this case the chloride has sufficiently weakened the barrier layer to allow pitting to occur but is not enough on its own to cause pitting. The machined surface of 316 steel when using chloride electrolyte has been observed to have a split surface consisting of a smooth, shiny surface upstream with respect to the electrolyte flow, but with progressively more rough, dull pits growing with time and spreading from the downstream end of the electrolyte flow, particularly at low electrolyte flow rates and with recycled electrolyte (see Section 5.2.3). Another possible mechanism by which this pitting can occur is now described.

Chloride has previously been found to exist only in the outer layer of the film [148]. The first pits have been observed to initiate at sites where a small difference in film thickness occurs [149] by localised removal of the passive metal oxide surface. This could lead to the production of insoluble low valency metal chlorides, which precipitate onto the electrode surface [150], hindering the metal film regrowth mechanism and leading to pit growth and an increased area of low valency dissolution. With the growth of a pit, film thinning occurs around the pit and film thickening starts beneath the pit creating more sites for pits to initiate [149]. Harb [151] has investigated the effect of convection on the pitting behaviour of stainless steels, and has shown that high values of U (20 l min^{-1}) favour the removal of the metal chlorides from the electrode surface, promoting barrier oxide formation (repassivation), whereas low U (8 l min^{-1}) favours metal chloride precipitation and pit growth. These measurements were performed at U values, currents and voltages much lower than those applicable to ECM, but this explanation is consistent with the SS316 chloride ECM results. At high U dissolution at high valencies ($n_{Fe} = 3$, $n_{Cr} = 6$) occurs, consistent with dissolution through an oxide layer (i.e. a passivated surface). However, at low U, pitting corrosion and growth occurs, as shown by the growing importance of low valency

dissolution (Section 5.2.3). Therefore, a similar mechanism appears to occur under ECM conditions.

Typical V_0 values obtained from ECM experiments on stainless steels are presented in Table 5.7. V_0 measures the total voltage required at both electrodes to drive the surface electrochemical reactions (see Section 2.1). However, given that the tool reaction is most likely Equation 5.2 for all experiments, and that similar ECM currents are passed in all cases, the voltage required at the tool to drive Equation 5.3 ($E_{e,T} + \eta_T$ in Equation 5.6) can be considered to be similar in all cases. Therefore, observed variations in V_0 can be related to changes in the voltage at the workpiece surface required to drive the workpiece dissolution reaction, which will comprise the surface overpotentials at metal/film and film solution interfaces to drive the metal cation injection and ejection processes and an ohmic term required to drive ion migration through the oxide film, all of which are contained in the η_w term in Equation 5.6 (Figure 5.38).

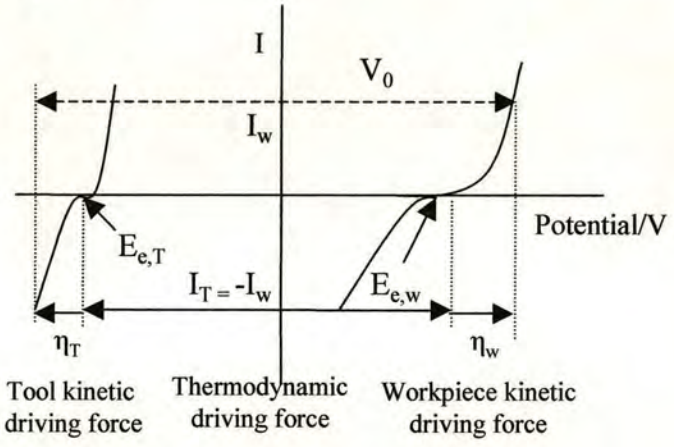

Figure 5.38 Representation of the workpiece and tool overpotentials where the tool has a relatively steep potential change compared to that of the workpiece (from Section 2.4).

Therefore, V_0 is given by

$$V_0 = E_{e,w} - E_{e,T} + \eta_w(I_w) - \eta_T(-I_w) \tag{5.6}$$

where η_w and η_t are the workpiece and tool overpotential terms respectively.

As the protective surface oxide layer contains a high proportion of chromium then it would be useful to look at chromium in more detail. Significant dissolution of Cr (particularly in

nitrate electrolytes) is occurring via the chromate ion, and this would be expected to increase the concentration of cation vacancies in the inner oxide layer, which would allow enhanced diffusion and migration of the cations formed from the oxidation and dissolution of the underlying metal atoms, resulting in stable ECM dissolution. Previously, it has been shown that at sufficiently high potentials (lower than those expected in the ECM experiments), trivalent Cr in the passive film tends to oxidise to hexavalent Cr [70]. When a critical amount is reached in the film, then transpassive dissolution begins. Therefore the Cr(VI) ejection reaction can be considered to be

Film/Solution interface $Cr(III) \rightarrow Cr(VI) + 3e^-$

$$Cr(VI) + xO^{2-} + (4-x)H_2O_{(l)} \rightarrow CrO_4^{2-}{}_{(aq)} + (8-2x)H^+$$

Therefore, the passive film is transformed into a transpassive film from which the dissolution of Cr as aqueous chromate(VI) species occurs (see Section 5.2). Transpassive dissolution of Fe(III) also occurs by the injection and ejection of Fe(III) at the metal/film and film/solution interfaces respectively. For nitrate electrolyte, visible absorption studies (see Section 5.4.1) demonstrated that oxidative dissolution of chromium metal during ECM occurs with the production of the chromate ion (CrO_4^{2-}, $n_{Cr} = 6$). This is consistent with the observed value of n_{Cr} obtained during ECM (see Section 5.2) and indicates that Cr is dissolving as CrO_4^{2-}. Comparison of the Pourbaix diagrams for iron [152] and for chromium [153] indicates that the potentials necessary to dissolve Cr from the workpiece surface as CrO_4^{2-} for a relatively non-coordinating ion such as nitrate would cause dissolution of Fe as Fe (III), although, as this analysis is based on pure metals, an extension to alloys must be attempted with care. This is consistent with the values of n_{Fe} observed in this work and with the oxidation state of Fe found in the XPS results (see Section 5.4.3.2).

It is also clear that in nitrate electrolyte, an increase in the chromium content of the steel results in an increase in V_0. This is to be expected, as increasing the proportion of chromium in the steel should lead to an increase in the thickness and barrier effectiveness of the inner layer, and an increase in the voltage required to drive cation migration ($\eta_w(I_w)$) through the film and produce stable ECM dissolution. This effect should result in an increase in the measured V_0 values as observed through Equation 5.6, and as is indeed seen in the results presented in Table 5.7. For both nitrate and chloride electrolytes, the results in Table 5.7 are grouped in order of decreasing chromium content in the stainless steel.

When using chloride electrolyte V_0 values obtained are significantly lower than those obtained when using nitrate electrolyte. It is known that chloride ions can insert into the surface oxide lattice (see Section 5.5), and it has been postulated that this autocatalytically produces increased cation lattice vacancies which would enhance the cation transport and dissolution rates, decreasing the effectiveness of the barrier layer [146, 147] and decreasing η_w and hence V_0 through Equation. (5.5). This is indeed observed. Also, it is likely that when using chloride electrolyte ($E_{e,w} - E_{e,T}$) may decrease because $E_{e,w}$ may decrease as the product of the dissolution reaction, $M^{x+}_{(aq)}$ is stabilised by the binding of the chloride ligand.

Steel	V_0 / V	V_0 Segment 2/ V	V_0 Segment 6/ V
D – High U, NO_3	15.7 ± 0.5	14.3 ± 0.5	15.8 ± 0.5
SS316 – High U, NO_3	9.7 ± 0.8	10.3 ± 0.8	9.8 ± 0.8
SS410-High U, NO_3	9.5 ± 0.8	9.9 ± 0.8	9.3 ± 0.8
J – High U, NO_3	7.5 ± 0.9	7.8 ± 0.9	7.3 ± 0.9
SD – High U, Cl	9.6 ± 0.8	8.5 ± 0.8	11.0 ± 0.7
D – Low U, Cl	9.2 ± 0.8	7.9 ± 0.9	11.7 ± 0.7
SS316 – High U, Cl[a]	5.7 ± 0.9	4.4 ± 1.0	6.3 ± 0.9
SS316- High U, Cl[b]	5.7 ± 0.9	4.8 ± 1.0	6.7 ± 0.9
SS410 – High U, Cl	4.0 ± 1.0	4.2 ± 1.0	3.1 ± 1.1
J – High U, Cl	5.6 ± 0.9	4.2 ± 1.0	5.7 ± 0.9

Table 5.7: Comparison of the V_0 values for the different materials under different flow regimes. [a] Results analysed up to $(t - t_0) = 300$ s. [b]The electrolyte was not recycled.

It is interesting that for the low chromium steels J and SS410, dissolution with reduced valency (as $n_{Fe} = 2$ and $n_{Cr} = 3$) occurs. This is characteristic of a surface which has lost its barrier chromium oxide protection, as soluble chromium (III) chloro species appear to be dissolving and V_0 is so low that low valency Fe dissolution can also occur. It is therefore apparent that alloy chromium content and chloride electrolyte content have opposing effects on the surface oxide barrier effectiveness.

Finally, it is worth considering what is the likely cause of the local removal of the surface oxide (the pitting event) for the intermediate steel SS316. It has previously been shown that

chloride can weaken the surface oxide sufficiently to make it susceptible to pitting in this case, but it remains to be demonstrated what the cause of the localised pitting events is. Experimentally, pitting occurs at the downstream end of the workpiece at low U (Section 5.2.3) and has been shown to be most likely due to the accumulation of products of the ECM reaction (Section 5.2.3). In order to test whether dissolved or precipitated products were of importance, two experiments were performed. The first consisted of adding the insoluble metal oxide and hydroxide products produced as a result of Equation 5.5 and obtained from filtering a recycled chloride electrolyte solution to a new chloride electrolyte solution. At high U, a transition from high to low valency was observed, starting at the downstream edge of the electrode. The second experiment involved performing the same ECM experiment using as electrolyte the filtrate of the recycled chloride solution. In this case, at high U the steel machined in a high valency state without any transition before 300 seconds. This is strong evidence that it is the solid products formed during ECM that are the cause of the pitting events. For the first experiment, it is interesting that the amount of solid product expected at the downstream edge of the electrode in this case is approximately the same as would be expected in the low U experiment, which is consistent with the particles being the cause of the pitting events in both cases (Figure 5.39).

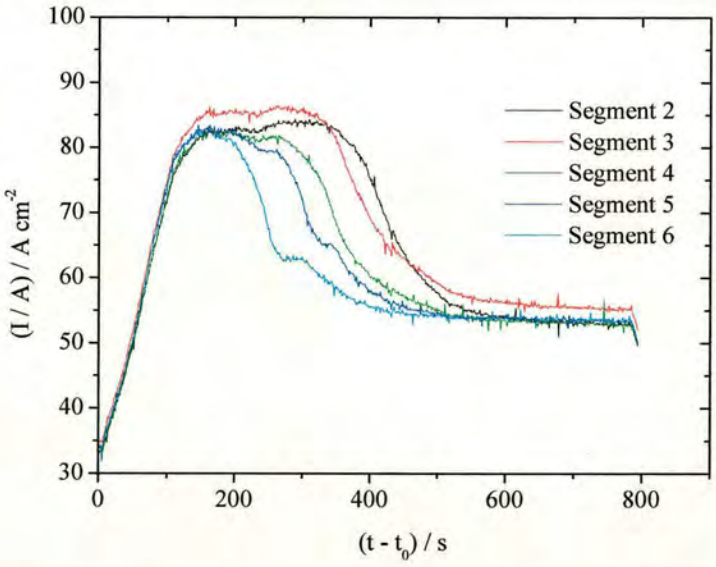

Figure 5.39: Experimental current transients for segments 2-6 for ECM of SS316 at high U with chloride electrolyte. In this experiment, solid products from a similar ECM experiment have been added to the electrolyte.

Beck and Chan [154] have produced a theoretical model analysing the effect of convection on the growth of pits. They predict that the critical value of U, U_{crit}, below which pit growth occurs depends upon the pit radius, r, as $r^{-4/3}$. This predicts that small pits should have a higher U_{crit} than large pits, which should effectively inhibit pit growth. However, this analysis does not allow for the lower value of U which can occur at the bottom of large pits, which has also been modelled [155] and could lead to the enhancement of pit growth. Thus pit growth may be dependent upon the initial formation of pits of a critical size. The impingement of particles has previously been suggested as one mechanism by which surface oxide film damage may occur [155], leading to pits of a critical size. Such damage may be as a result of the particle impacting with the surface. However, it may also be because of particles close to the surface inducing a local disturbance in the electrolyte flow, decreasing U to enable pit growth to a critical size.

5.5.2 Measurement of I vs V_0

The V_0 values previously calculated from the chronoamperometric theory (see Section 5.5.1) are average values over the length of the experiment and good fits (i.e. little variation in (V-V_0) with I) are observed because V is so large for these experiments at 24 V that V-V_0 does not vary appreciably [123]. This leads to an average value of V_0, which is insensitive to I, and therefore allows overall comparison of ECM voltages between different alloys [123]. This is consistent with the results for V_0 when carrying out ECM experiments at high applied voltages on the Nickel alloy In718 [123]. The observed independence of V_0 with I again indicated that changes in V_0 with I were small and within experimental error. However, at applied voltages, V, large enough to enable machining but small enough so that significant changes in V-V_0 occur during the experiment, chronoamperometric analysis allowed measurement of the variation of V_0 with I for In718 [123]. Previous results for In718 [123] indicated that Tafel behaviour was observed under ECM conditions but there was a relatively large scatter in the results due to the error in the applied voltage, V, due to the voltage source used in those measurements. Similar experiments were carried out in this work to assess the viability of measuring the I-V_0 characteristics of a stainless steel. The intermediate Cr steel, SS316 was chosen for these preliminary studies and an alternative voltage source (Section 3.2) was used which gave more accurate voltages so that V could be reduced to values approaching V_0 to enhance sensitivity, whilst minimising the error in these results.

Analysing parts of the current transients to provide information on the variation of V_0 during an experiment is useful because it can provide insight into the dissolution kinetics and mechanism (see Section 2.4). Every 400 data points were analysed and the current was taken as an average for the specified number of data points. A change in dissolution kinetics may then be attributed to changes in the structure and composition of the surface oxide film. As the average value of V was found to be 9.7 ± 0.8 V, experiments were performed at V = 11.0 V and f = 0.25 mm min^{-1} and than at V = 15.0 V and f = 1.00 mm min^{-1}, to enable V_0 values to be obtained at a range of ECM currents. Iterative fits to the chronoamperometric data were then performed according to the analysis in Section 2.8.2.

A plot of ln (I/A) against V_0 was then obtained for SS316. It is satisfying that the two plots obtained from the two experiments at relatively low and high values of f and different values of V meet at a common value of I and V_0, which gives support to the validity of this method of analysis. At low and high values of I, as with In718, I apparently has an exponential dependence on V_0. This is Tafel like behaviour, suggesting that the rate determining step is either the kinetics of ejection or insertion of metal ions at the film/solution or metal/film interface. The rate of these reactions will be controlled by that fraction of the voltage dropped at the interface. It is interesting that the Tafel gradients are much small than those typically found for surface electrochemical reactions, consistent with the fact that only a small fraction of total voltage drop at the working electrode is at this interface. It is also interesting that at intermediate currents, V_0 actually decreases with increasing I. This suggests that the overpotential rises monotonically with I/A, but instead for intermediate currents actually falls with rising I/A, before rising again (Figure 5.40).

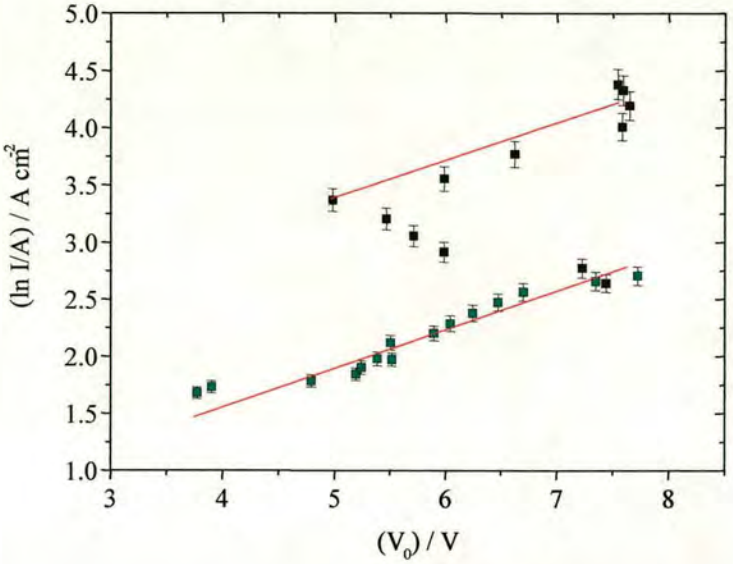

Figure 5.40: A plot of ln (I/A) vs V_0 for SS316 with nitrate electrolyte at high U. The first linear part of the plot was carried out at 11.0 V (blue) and the second decreasing part was carried out at 15.0 V (black). Therefore, there is good apparent correlation between the two voltages (within the error limits of k/f^2 and V should by the error bars).

Previous results for In718 [123] plotted ln (I/A) against k/f^2 and gave a straight line with a negative slope of $b \approx 1.4$ V indicating Tafel behaviour. The negative slope corresponds to the kinetics of the dissolution reaction increasing rapidly, such that the overall voltage required to drive the dissolution reaction falls. This indicates a thinning and/or increased conductivity in the barrier oxide layer, so that less of the voltage is required across this layer to drive the electrochemical dissolution reaction. This is good evidence for the importance of the barrier oxide layer in determining the dissolution kinetics and mechanism.

Therefore, V_0 does vary with I and parameterisation of this I versus V_0 behaviour is possible. It is worth considering how such an unusual variation of I with V_0 (a negative Tafel gradient) could be obtained. The rate of generation of cation vacancies and anion vacancies will be expected to increase with the voltage drop at the interfaces at which they are generated. The rate of generation of cation vacancies will be equal to

$$\text{Rate}(V_M^{x\cdot}) = k_4 x_M \qquad (5.7)$$

where k_4 is the rate constant for the ejection reaction (reaction (4) in Figure 5.36) and x_M is the occupancy of filled metal sites at the film/solution interface. The rate of generation of anion at the metal/film interface will be equal to

$$\text{Rate}(V_O^{2+}) = k_1 \tag{5.8}$$

where k_1 is the rate constant for reaction (1) in Figure 5.36.

The rate constants for these two processes will each depend on their interfacial potential drop, so that the rate constants are given by

$$k_1 \propto \exp(\alpha_1 x \Delta\phi_{f/s}) \tag{5.9}$$

$$k_4 \propto \exp(\alpha_4 x \Delta\phi_{m/f}) \tag{5.10}$$

where α_1 and α_4 are the transfer coefficients for reactions (1) and (4) respectively, x is the charge on the cation and $\Delta\phi_{m/f}$ and $\Delta\phi_{f/s}$ are the potential drops at the metal/film and the film/solution interfaces respectively. Therefore, the concentration of vacancies will be expected to increase as

$$[V_M^{x-}] \propto e^{(\alpha 1 x \Delta\phi f/s)} \tag{5.11}$$

$$[V_O^{2+}] \propto e^{(\alpha 4 x \Delta\phi m/f)} \tag{5.12}$$

However, the rate of lattice destabilisation which produces thinning or a less effective barrier oxide layer will be dependent on the rate of combination of cation and anion vacancies. This rate will be given by

$$\text{Rate} = k[V_M^{x-}][V_O^{2+}] \propto e^{(\alpha 1 x \Delta\phi m/f + \alpha 1 x \Delta\phi f/s)} \tag{5.13}$$

As V_0 increases, increasing the potential drop at both interfaces, the rate of thinning of the oxide layer would be expected to rise more rapidly with potential, and at higher currents, this reaction, which leads to oxide thinning, may become dominant and lead to a decrease in the value of V_0 required with increasing current.

A full study of these I/A vs V_0 characteristics for different steels would therefore give insight into what is controlling the dissolution process through these oxide layers. Additionally, it

also allows the full parameterisation of ECM such that I vs V_0 relationships can be measured; this is important as the complicated variation of values at high currents show that I vs V_0 data cannot simply be extrapolated from previously measured I-V_0 data measured at low currents.

5.5.3 Conclusion

These results indicate that the ECM dissolution characteristics of stainless steels are controlled by the nature of the surface oxide, which is primarily dependent upon their chromium content. Addition of "aggressive" ions such as chloride to the electrolyte can disrupt this surface layer and reduce the effectiveness of this surface barrier. Insoluble products of the ECM reaction can also compromise this barrier under certain conditions, leading to pitting corrosion and low valency dissolution. This is important in recycled electrolyte systems, which are typically used industrially. Although consideration of chromium content is of primary importance, it is known that the minor elements in the steels such as nickel also have some influence on surface oxide structure and stability. However, the influence of these elements on ECM dissolution appears to be minor. The determination of the effects (if any) of these elements would require the study of a wider range of steels.

The dissolution of the surface oxide can be explained in terms of the point defect model for ion transport in the surface oxide layer. This model has been proposed to explain the processes occurring during steel dissolution but these proposals were used to explain dissolution under much lower current and voltage conditions than those used in ECM. These results therefore demonstrate that the experimental system described can be used for the systematic collection and analysis of electrochemical and chemical data for dissolution under ECM conditions, allowing the measurement of ECM characteristics of a variety of steels or other alloy types and their correlation with composition. Furthermore, parameterisation of the I-V_0 characteristics of these alloys are possible, enabling more accurate simulation and modelling of the ECM process.

Chapter 6

Measurements of variations in efficiency in ECM

6.1 Introduction

It was reported by Doncasters plc that when machining J with nitrate electrolyte an unusual phenomenon is observed if the electrolyte is allowed to continuously recycle. Unusually high current densities were reported with apparent dissolving valencies of up to $n_{obs} = 9$ (where $n_{obs} = n/e$, see Section 2.11). This claim has been confirmed by experiments carried out in this thesis and detailed below and therefore an investigation into the possible cause of this "runaway current" effect has been carried out. An important point is that Doncasters plc only use nitrate electrolyte for all their industrial applications. J is widely used for industrial applications and the high dissolution currents which are produced by such high dissolving valencies are very expensive to maintain. Therefore, a solution to this problem was desirable and this was investigated by analysing the ECM characteristics of the J system with nitrate electrolyte.

6.2 Results and Discussion

Figure 6.1 shows the experimental segment currents when machining with new nitrate electrolyte at high U (for experimental conditions see Section 3.7). These current transients are considered to be typical and have been analysed in Section 5.2.2. However, there was a slight increase in current density at equilibrium from around 200 s onwards. At times before this increase, a valency of $n = 3.5 \pm 0.1$ was obtained for segments 2-6 from Equation 2.39, Section 2.8.2, which is consistent with dissolution of iron and chromium in their high valency states (Fe(III), $n_{Fe} = 3$ and Cr(VI), $n_{Cr} = 6$) across the entire workpiece surface, as this value is within experimental error of the mean valency of $n = 3.4$ which would be expected if the minor elements in these steels dissolved with a chemically reasonable average valency of $n = 3$.

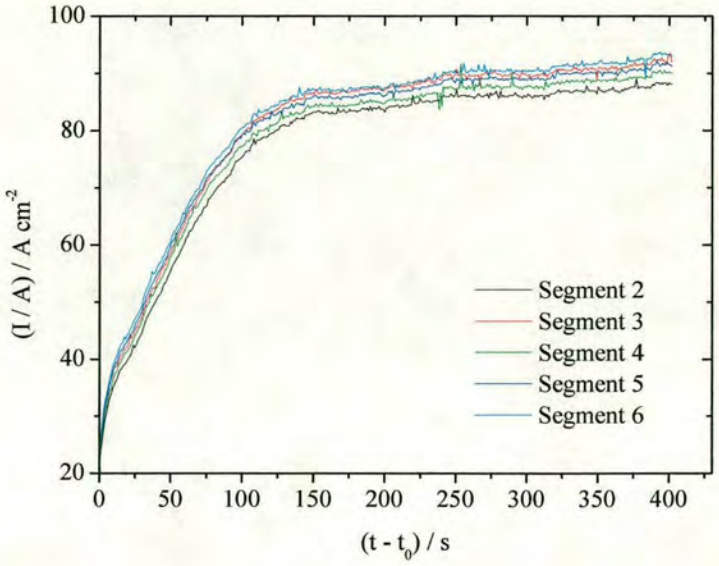

Figure 6.1: Experimental current transients for segments 2-6 for ECM of J at high U with nitrate electrolyte at a feed rate of 1.00 mm min^{-1}. The total thickness of J machined in this experiment was 6.1 mm.

The electrolyte used for this experiment was then used again for a repeat experiment. The same experimental conditions were used as before with the exception of using a new workpiece. The experimental current transients are shown in Figure 6.2. The initial part of the current transient exhibited the same characteristics as observed previously (Figure 6.1). A valency of n = 3.5 ± 0.1 was obtained for segments 2-6 at these early times, which is again consistent with dissolution of iron and chromium in their high valency states (Fe(III), $n_{Fe} = 3$ and Cr(VI), $n_{Cr} = 6$) across the entire workpiece surface. However, after around ~ 160 s, the current on segment 6 started to increase, followed by segment 5, 4, 3 and 2 in sequence. Therefore, the segment currents increased from downstream to upstream along the flow path length.

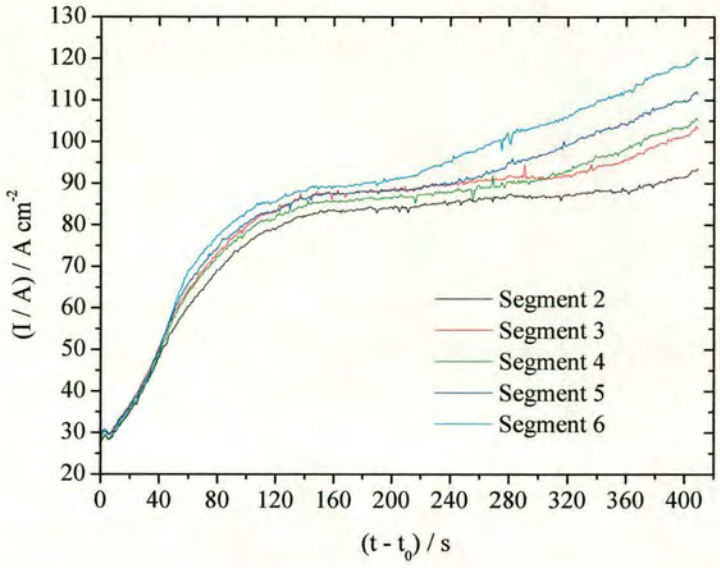

Figure 6.2: Experimental current transients for segments 2-6 for ECM of J at high U with once used nitrate electrolyte. The total thickness of J machined in this experiment was 6.1 mm.

The electrolyte was then reused again with the same experimental conditions, but with another new workpiece. Figure 6.3 shows the experimental current segments. The segment currents rose rapidly to a very high current density of ~140 A cm^{-2} before the currents split and continued to rise as observed in Figure 6.2. The segment current rise appeared to be linear; on performing a linear fit to the segment currents in Figure 6.2, slopes of 0.033 ± 0.002 A s^{-1} at segment 2, 0.060 ± 0.003 A s^{-1} at segment 3, 0.089 ± 0.004 A s^{-1} at segment 4, 0.120 ± 0.005 A s^{-1} at segment 5 and 0.141 ± 0.006 A s^{-1} at segment 6 were obtained. Therefore, the end segments have a greater slope as well as starting to rise first and the difference in slope between each of the segments is constant at 0.027 ± 0.002 A s^{-1}.

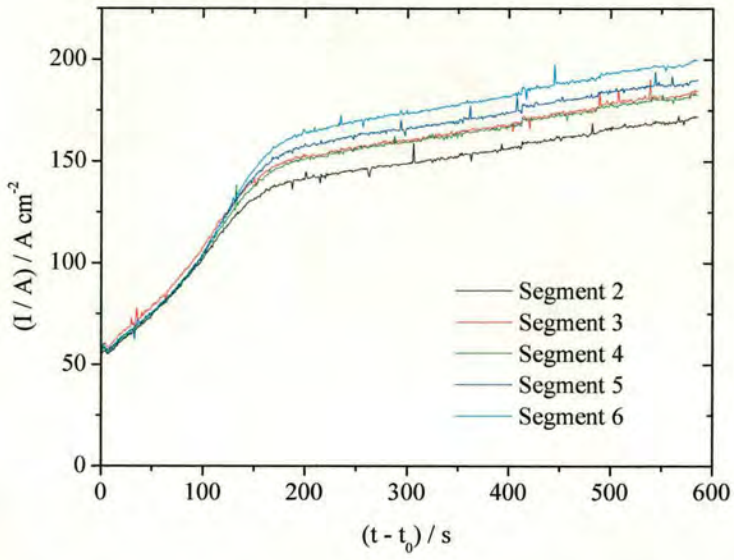

Figure 6.3: Experimental current transients for segments 2-6 for ECM of J at high U with twice used nitrate electrolyte. The feed rate was 0.5 mm min^{-1} and therefore the current was multiplied by 2 to be comparable to 1 mm min^{-1} experiments.

Performing the same linear analysis to the segment currents in Figure 6.3 gives a constant slope of 0.036 ± 0.003 A s^{-1}. Therefore, it appears that the segment currents begin to rise from the downstream end of the flow path and move back with decreasing slopes but with the same difference in slope. Once the segment currents reach a critical point then all the transients have the same slope and continue to rise. The valency at the end of this experiment at t = 400 s is $n_{obs} = 7.0 \pm 0.1$.

This steady increase in current with time is colloquially termed a "runaway current" effect. When performing the same experiment as previously, the only difference being that the nitrate electrolyte is not recycled in the system, therefore negating any build up of products in the electrolyte then no such "runaway current" behaviour is observed, Figure 6.4. Therefore, the "runaway current" effect would appear to be caused by the build-up of products in the electrolyte as the electrolyte is recycled through the system.

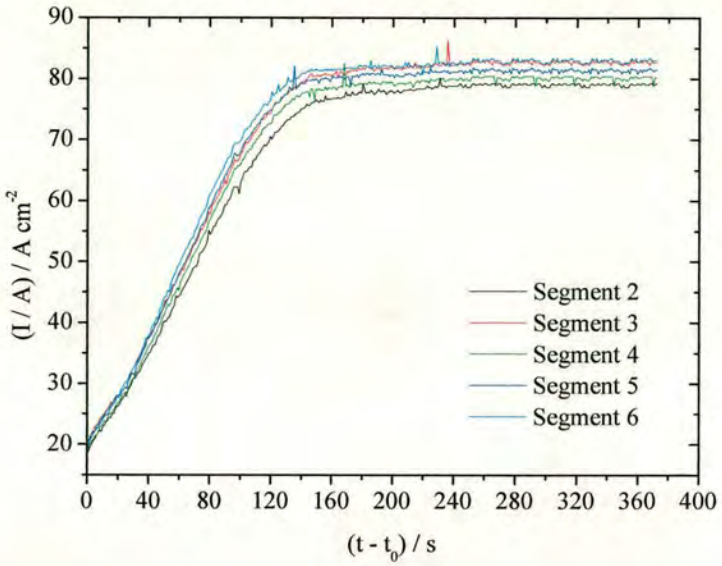

Figure 6.4: Experimental current transients for segments 2-6 for ECM of J at high U with nitrate electrolyte passed through the interelectrode gap once only.

6.3 Electrolyte filtering experiments

The cause of the "runaway current" was thought to be caused by products accumulating in the recycled electrolyte. When the electrolyte is not recycled then this "runaway effect" is not observed. Therefore, the dissolution products causing the "runaway" could be either one of the soluble products such as CrO_4^{2-} ions as observed previously (Section 5.4.1) when using nitrate or the insoluble products (Section 5.4.2 and 5.4.3) which have been observed to affect the machining of SS316 when machining with chloride. Therefore, two experiments were performed to determine which of the dissolution products was causing the "runaway effect". As in Section 5.5.1, these experiments involved separating used electrolyte into soluble and insoluble products by filtering the electrolyte. The first experiment involved using the filtered electrolyte, which should only contain soluble products (Figure 6.5). The second experiment used the filtered solid dissolution products in new electrolyte solution (Figure 6.6). A new workpiece was machined in each case. All machining conditions were the same as those used previously. In both cases the dissolution valency was found to be n = 3.3 ± 0.1 for segments 2-6 which is slightly lower than values previously observed (n = 3.5 ± 0.1) but is however still consistent with dissolution of iron and chromium in their high valency states (Fe(III), n_{Fe} = 3 and Cr(VI), n_{Cr} = 6) across the entire workpiece surface.

Initially from these results it appears that the hypothesis that the "runaway effect" is due to one of the dissolution products, either soluble or insoluble, is incorrect. Both experiments machined with the same dissolution valency and a significant "runaway effect" was not observed in either case.

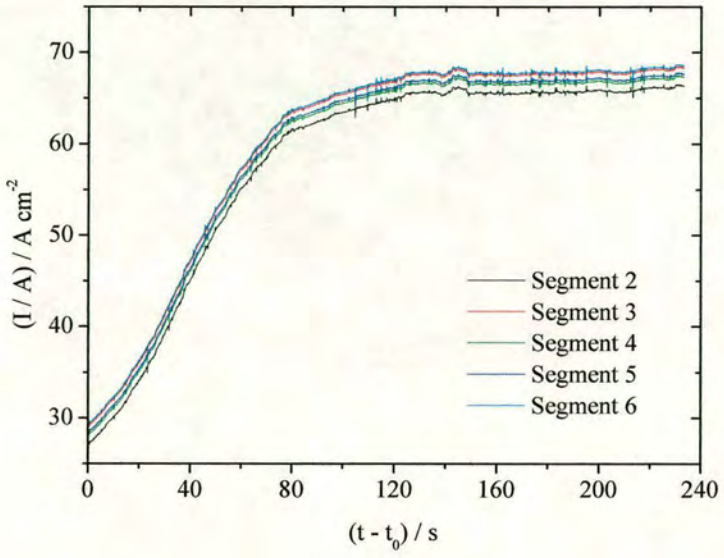

Figure 6.5: Experimental current transients for segments 2-6 for ECM of J at high U with old nitrate electrolyte with the solid dissolution products filtered from the electrolyte.

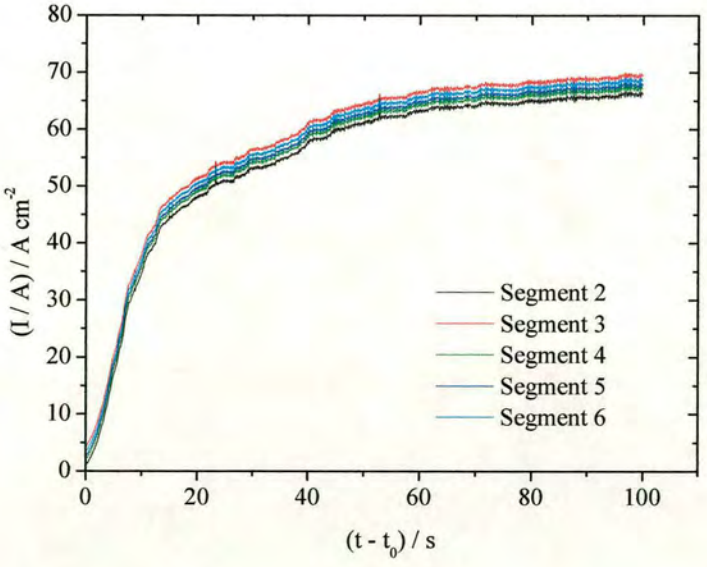

Figure 6.6: Experimental current transients for segments 2-6 for ECM of J at high U with new nitrate electrolyte and solid dissolution products added to the bulk electrolyte, 30 l in total.

From previous experiments when machining SS316 it was observed that the solid dissolution particles were causing the transition from high to low valency when using chloride. Therefore, it was strongly suspected that the particles were again causing the "runaway effect". A possible explanation as to why no effect was observed when the particles were added to new electrolyte is that the particles may be small in size and may have been able to aggregate or react in the electrolyte tank or during filtering. Such changes in morphology and chemical composition may be expected for small and/or reactive particles and may change the solid products sufficiently to preclude the "runaway effect". In this case, unlike for SS316 (Section 5.2.3) this separation experiment would not be able to determine unambiguously which of the products was responsible for the "runaway effect". However, it was seen in Section 5.2.3 when machining SS316 that particles can have a dramatic effect on the dissolution characteristics. The particles in the experiment were filtered (see Section 3.8 on sample preparation) and characterised by XRD in a similar manner to Section 5.4.2; they showed no XRD pattern below 600°C (with increasing pattern intensity up to 800 ^{0}C) indicating that the particles were probably amorphous or nanoparticles, which would be consistent with their reactivity.

6.4 Mixed electrolytes

As previously, ECM experiments were performed using chloride electrolyte. In this case, (Figure 5.6 of Section 5.2.2) the "runaway effect" was not observed and low valency dissolution occurred giving n = 2.1 ± 0.1, from Equation. 2.39. As iron is the major elemental component in this steel, this indicates that in this case iron and chromium dissolution is occurring in the low valency state (Fe(II), n_{Fe} = 2, Cr(III), n_{Cr} = 3). Therefore, one obvious solution to the problem of removing the "runaway effect" is to use chloride electrolyte. This has the further advantages that lower valency dissolution occurs which uses less current and is therefore cheaper to perform. However, this approach was not an option for Doncasters plc, who use a common ECM nitrate electrolyte system. Therefore, a possible solution to the "runaway effect" was desirable using nitrate electrolyte.

A possible alternative to using nitrate electrolyte would be the doping of nitrate electrolyte with a small amount of chloride electrolyte. This may have the further advantage of enabling the manipulation of the dissolution valency and finish during the ECM reaction. High valency machining (as is achieved with nitrate) can have certain advantages in producing a

high quality surface finish and therefore is desirable if this is required, which is why manufacturers use nitrate. Low valency dissolution (as found with chloride electrolytes) is however preferable for the majority of machining (roughing out) because although the finish is poorer, less current and power is required. It would therefore be desirable to use mixed chloride/nitrate electrolytes if judicious control of the ECM parameters could be used to produce low valency dissolution for roughing out, followed by high valency dissolution for a good surface finish, with little or no "runaway effect". The ECM characteristics of mixtures of chloride and nitrate electrolyte were therefore investigated, with constant overall ionic strength (2.56 M). A mixture of 50:50 (1.28 M:1.28 M) nitrate:chloride electrolyte was prepared and used initially. The ECM results are given in Figure 6.7.

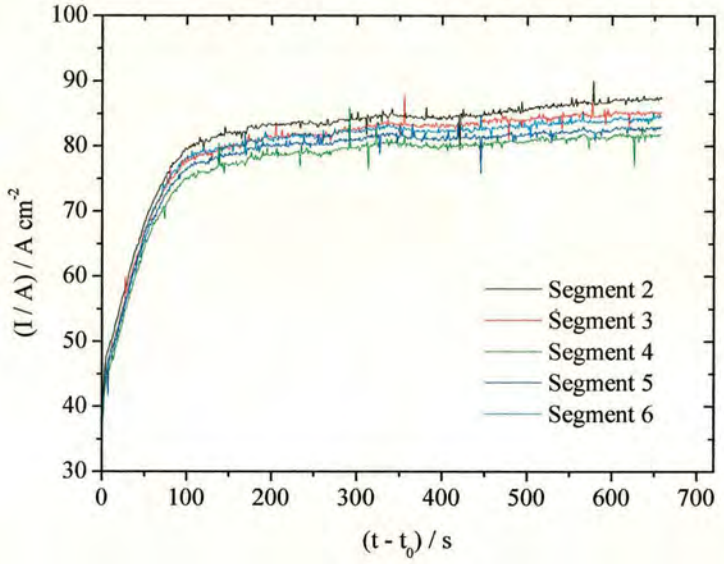

Figure 6.7: Experimental current transients for segments 2-6 for ECM of J at high U with 50 % nitrate and 50 % chloride electrolyte.

High valency machining was observed, but in contrast to pure nitrate, machining continued without any dramatic "runaway" in the current (compare with Figure 6.2). The segment currents could be seen to rise slightly and there was ~ 7 A cm^{-2} separation in the segment current densities. A constant increasing slope of 0.007 ± 0.002 A s^{-1} was calculated for each segment current. Therefore, although the dissolution valency was characteristic of nitrate, the chloride did appear to reduce the "runaway" current significantly. It seems likely that the chloro-substituted products and maybe nitro-chloro products produced in this reaction could be sufficiently different to prevent the "runaway" current.

Machining was then carried out with a 25:75 (0.64 M:1.92 M) mixture of nitrate:chloride (Figure 6.8).

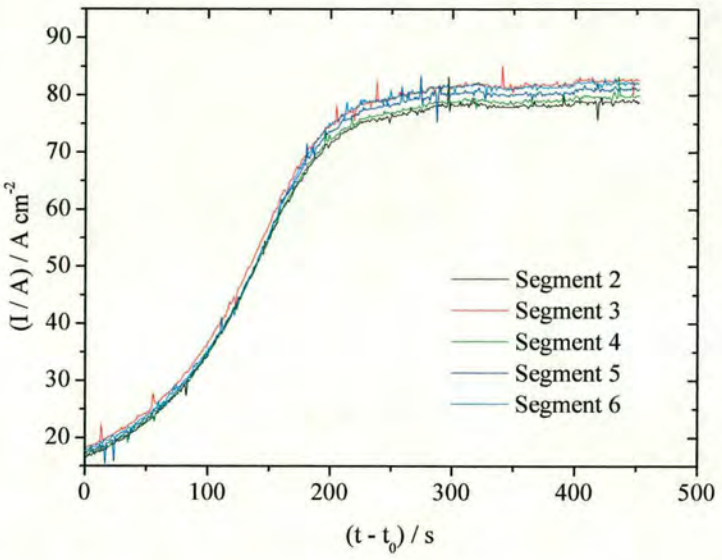

Figure 6.8: Experimental current transients for segments 2-6 for ECM of J at high U with 25 % nitrate and 75 % chloride electrolyte.

Again high valency dissolution was observed with less segment current density separation and constant slopes of 0.007 ± 0.002 A s^{-1} (same as for 50:50 experiment, Figure 6.7). Therefore, high valency machining could be achieved without any significant "runaway effect" by using a 25:75 or 50:50 mixed electrolyte of nitrate:chloride.

Finally, a 10:90 (0.26 M:2.30 M) ratio of nitrate to chloride was used (Figure 6.9) with the aim of trying to determine the point at which the dissolution valency became characteristic of chloride dissolution. Experimental results for ECM under these conditions are shown in Figure 6.9

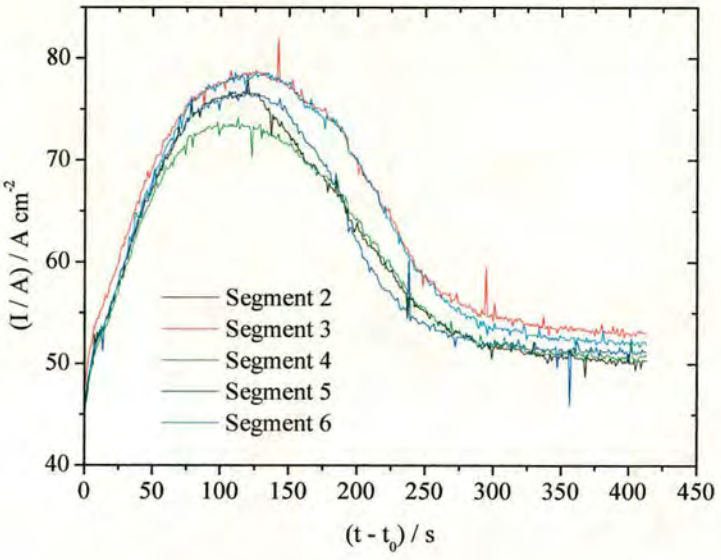

Figure 6.9: Experimental current transients for segments 2-6 for ECM of J at high U with 10 % nitrate and 90 % chloride electrolyte.

Initially the current transients approached the high valency current density of ~ 80 A cm^{-2} but then start to fall off after ~ 75 s. The current transients then levelled out at the low valency dissolution current of ~ 50 A cm^{-2} and appear to stabilise at this low valency. Therefore, it would appear to be possible to change the dissolution valency with mixed nitrate:chloride electrolytes, but only at relatively high chloride concentrations (90% chloride) which are impractical for Doncasters current machining methodology. It might be thought to be surprising that high dissolution valencies were still found at relatively low concentrations of nitrate, given the much enhanced ligating powers of chloride over nitrate. However, these results are entirely consistent with the results obtained for the ECM dissolution of SS316 (Section 5.2.3). In this case, it was found that there was a high to low valency transition for SS316 in chloride electrolyte induced by solid particulate products. This was explained by the chloride ions weakening the barrier oxide layer to an extent that pitting corrosion and low valency dissolution was occurring. It was also shown that chromium and chloride had antagonistic effects, with chromium increasing the oxide barrier effectiveness, and chloride compromising it. Jethete has a slightly lower Cr concentration than SS316, and it is therefore entirely consistent that such a high to low valency transition would occur at a slightly lower concentration of chloride ion in the electrolyte.

As mentioned previously (see Section 2.11) an assumption is often made that the efficiency, e = 1.0, is 100 % and therefore any change in current is due to a valency change. However,

in the case of J where the "runaway effect" is observed then it is very unlikely that J is dissolving with a valency of up to n = 9 as this is theoretically impossible when looking at the elements that constitute J (Table 1.1). Therefore, the only chemically reasonable alternative is that there is a short circuit reaction or other electrochemical reaction which does not result in ECM dissolution and causes the current to increase (Section 6.2). This increase can be shown in a plot of charge vs machining height of the workpiece. The theory behind this is explained in Section 2.12. The ultrasound system is used to measure the change in workpiece height as machining is in progress (see Section 3.5.4). This will now be discussed.

6.5 Measuring the efficiency (e)

A linear plot with a negative slope would be expected for 100 % efficiency when using Equation 2.71 in Section 2.12. If, however the efficiency is changing then the plot may curve away from linearity with the slope of the tangent to the curve giving the value of $n_{obs} = n/e$ at any time from Equation 2.71. The results from such an experiment is shown in Figure 6.10 for J.

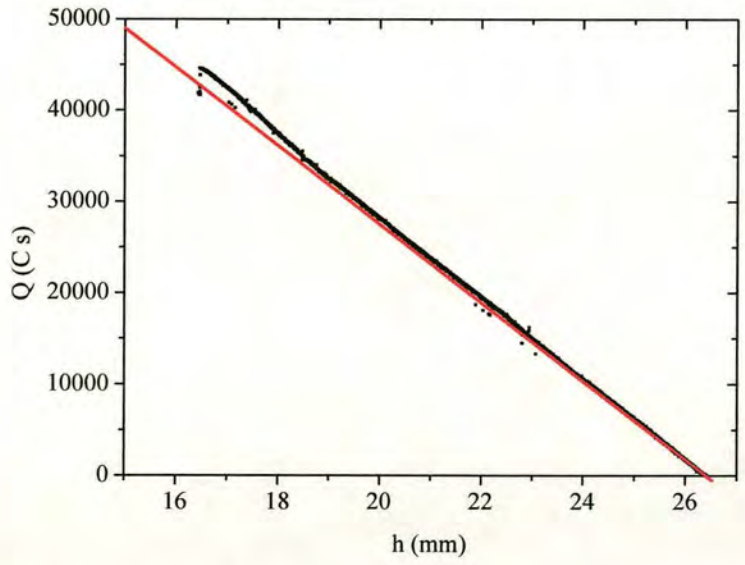

Figure 6.10: A plot of Q (C) vs h (mm) to show inefficiency for J with nitrate.

As expected the line does indeed curve away from linearity confirming that the efficiency is changing as machining progresses. The slope of the line at any point can be calculated from

the tangent to the graph and from this the observed valency can be calculated from Equation 2.39, Section 2.8.2 with n as n_{obs} in the Equation. Calculating the slope of the curve every 500 points or ~ 1.5 mm machining then the valency can be calculated as n/e = 3.9 ± 0.1 after 1.5 mm machining, n/e = 3.8 ± 0.1 after 3.0 mm machining, n/e = 4.0 ± 0.1 after 4.5 mm machining, n/e = 3.7 ± 0.1 after 6.0 mm machining, n/e = 3.8 ± 0.1 after 7.5 mm machining, n/e = 4.2 ± 0.1 after 9.0 mm machining and n/e = 4.2 ± 0.1 after 10.0 mm machining. If an efficiency of 100 % is assumed when the dissolution valency is n = 3.5 ± 0.1 then the efficiency can be calculated to decrease to e = 0.83 (83 %) after 10.0 mm machining. This is a significant reduction in efficiency and confirms the "runaway effect". However, the cause of this effect was still unknown.

The main element present in J is iron at 80.63 atomic %, as it is a relatively low Cr, high Fe steel. For comparison, a pure Fe workpiece was therefore machined under the same ECM conditions, to provide information on the cause of the "runaway effect". A pure iron workpiece was machined with nitrate electrolyte using the ultrasound gap measuring system.

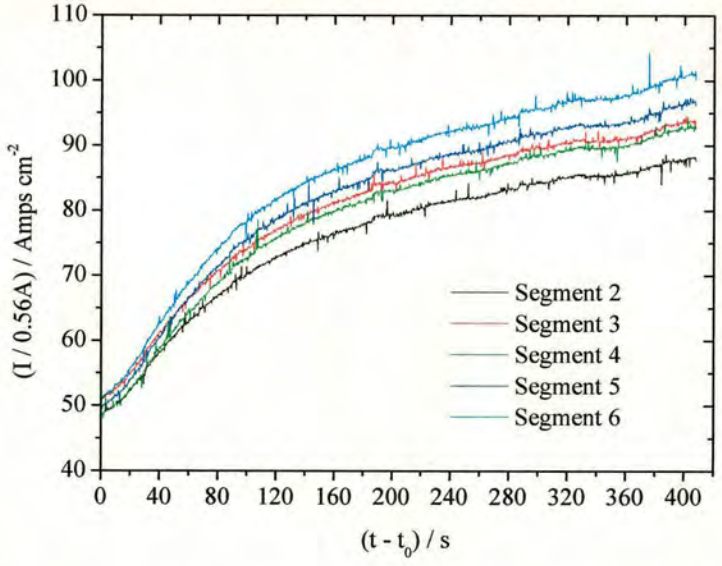

Figure 6.11: Experimental current transients for segments 2-6 for ECM of Fe at high U (16 l min^{-1}) with nitrate electrolyte at 0.56 mm s^{-1}. The currents are each divided by 0.56 accordingly to be comparable to 1 mm min^{-1} experiments

The current transients from machining Fe with fresh nitrate electrolyte (Figure 6.11) showed steadily increasing currents, a higher current density than would be expected for n = 3 from I_∞ and Equation 2.39, as well as an increase in current along the flow path length. The current continued to rise past 400 s, where typically the transients would have reached their equilibrium current after 130 s. This is also a "runaway effect". When machining J the runaway does not occur straight away as observed here. Therefore, the runaway effect is also observed when machining iron with nitrate electrolyte but more readily than J, which is suggestive that an iron product may be causing the "runaway effect". This is consistent with the XPS results of the dissolution particles for J (see Section 5.4.3.5) in that the only significant elements detected were iron and oxygen. As the ultrasound system was set to record over a 5 mm range then machining had to be stopped after 5 mm and the ultrasound reset, after which ECM was restarted. Resuming machining gave the second plot of current transients (Figure 6.12) which continues where Figure 6.11 ended. After a further 5 mm, a third machining plot was also recorded (Figure 6.13).

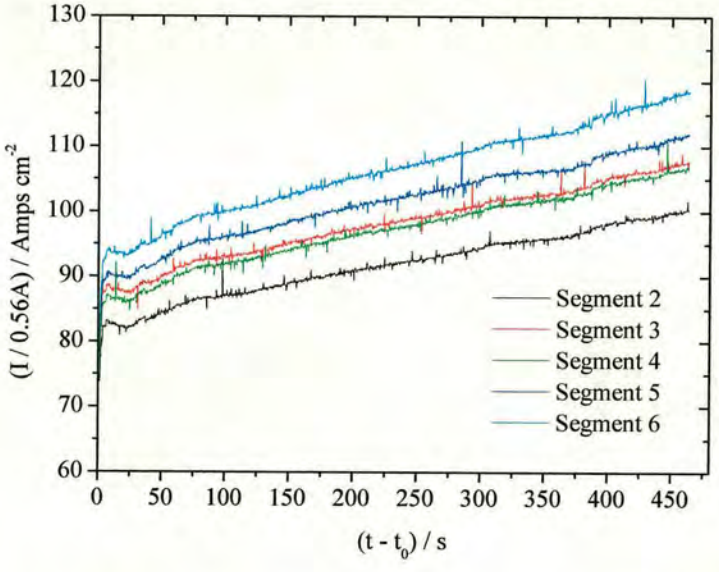

Figure 6.12: Experimental current transients for segments 2-6 for ECM of Fe at high U (16 l min^{-1}) with once used nitrate electrolyte at 0.56 mm s^{-1}. Therefore, the currents are multiplied accordingly to be comparable to 1 mm min^{-1} experiments.

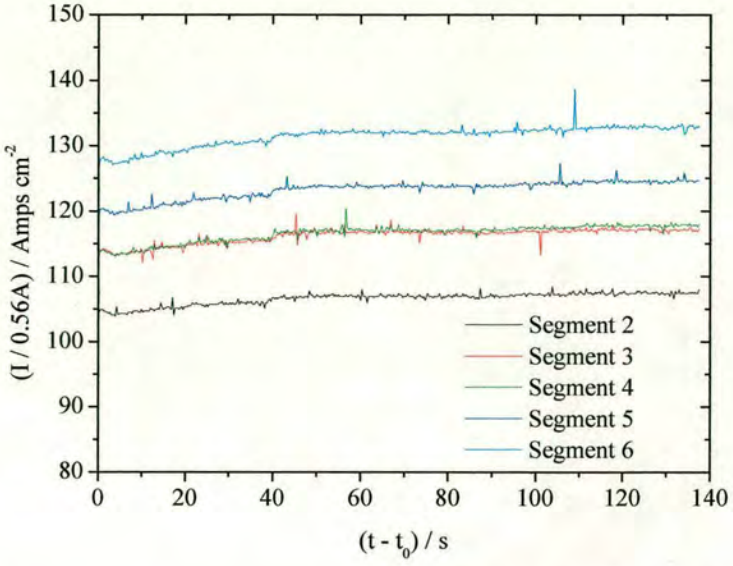

Figure 6.13: Experimental current transients for segments 2-6 for ECM of Fe at high U (16 l min^{-1}) with twice used nitrate electrolyte at 0.56 mm s^{-1}. Therefore, the current are multiplied accordingly to be comparable to 1 mm min^{-1} experiments.

The current transients for iron do appear to level off which was not previously observed with J. A calculated dissolution valency at this time was n/e = 4.8 at segment 2 rising to n/e = 6.0 at segment 6. This compares to typical dissolution valencies of n = 3.0 ± 0.1 which would be expected when machining with nitrate (Section 5.2.2). A comparable plot of Q vs h to J is shown in (Figure 6.14).

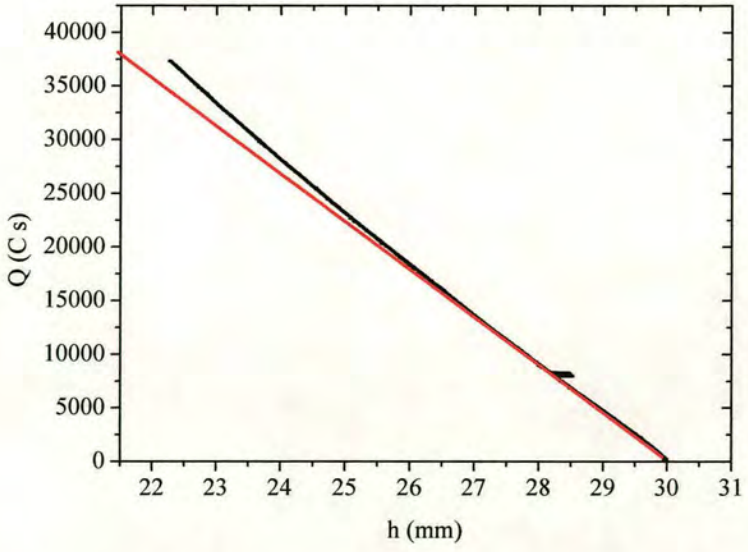

Figure 6.14: A plot of Q (C) vs h (mm) with nitrate for Fe.

As observed with J the plot deviates from linearity and curves away indicating an n/e and hence efficiency change. The slope of the line can be calculated at any point and therefore the valency can be calculated by using Equation 2.71. Calculating the slope every 500 points or ~ 1.5 mm machining then the valency can be calculated as n/e = 4.0 ± 0.1 at h = 1.5 mm, n/e = 3.8 ± 0.1 at h = 3.0 mm, n/e = 4.1 ± 0.1 at h = 4.5 mm, n/e = 4.1 ± 0.1 at h = 6.0 mm, n/e = 4.4 ± 0.1 at h = 7.0 mm and n/e = 4.6 ± 0.1 at h = 8.0 mm. If an efficiency of 100 % is assumed when the dissolution valency is n = 3.0 ± 0.1 then the efficiency can be calculated to decrease to e = 0.65 (or 65%). Again this is a significant decrease in efficiency and is greater than the decrease observed with J. It has been mentioned earlier (see Section 2.11) that there has been uncertainty as to whether an efficiency change was real or otherwise. As further evidence to show that this reduced efficiency is occurring with Fe (and J), then a plot of current, gap and time (Figure 6.15) was produced. If 100 % of the dissolution current was due to migration then the interelectrode gap would decrease as n_{obs} increased (as observed with Fe where n/e = 4.6). Plotting segment 6 for Fe and using the ultrasound data at segment 6 to calculate the interelectrode gap then Figure 6.15 is produced.

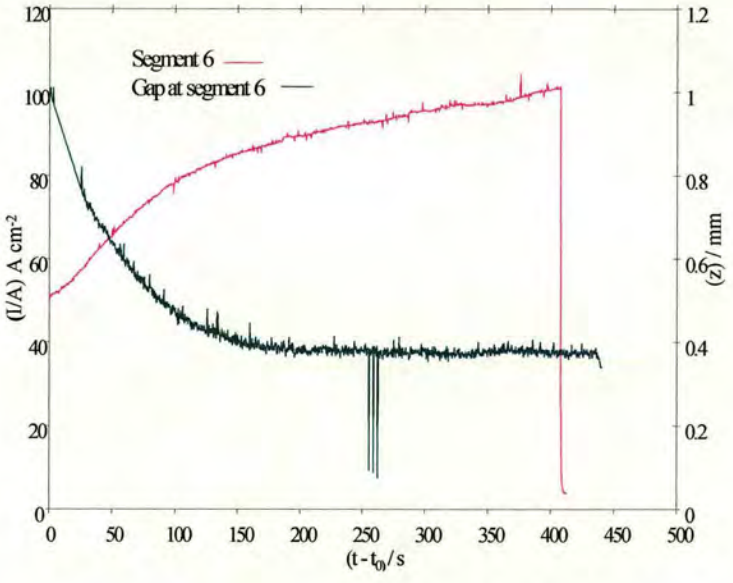

Figure 6.15: Experimental segment 6 for Fe with nitrate electrolyte at high U. The current is plotted with the interelectrode gap at segment 6 against time. As the current increases, the gap remains constant indicating the increase in current is not due to migration.

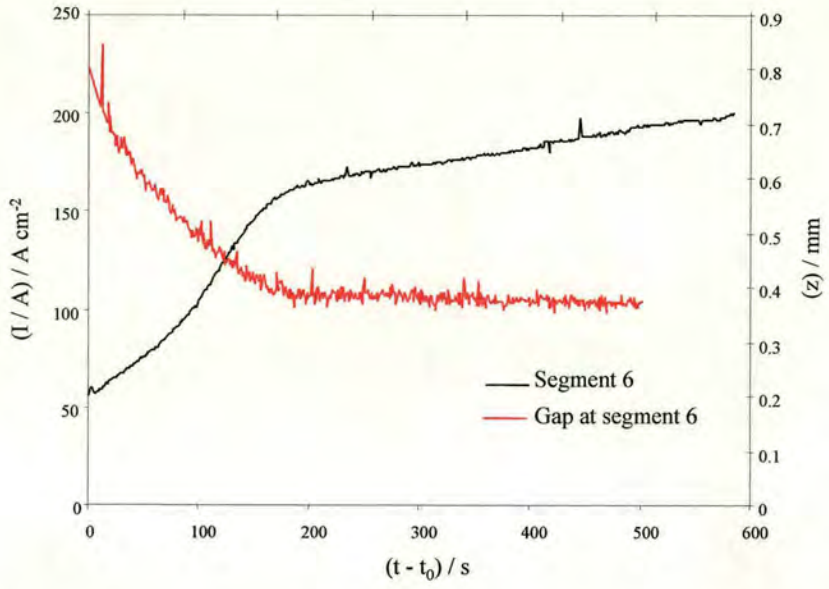

Figure 6.16: Experimental segment 6 for J with nitrate electrolyte at high U. The current is plotted with the interelectrode gap at segment 6 against time. As the current increases, the gap remains constant indicating the increase in current is not due to migration.

Therefore, as the current rises the gap remains constant. This demonstrates that any extra current produced is not governed by migration and is therefore due to some other process occurring in the gap. It also suggests that this reaction may involve neutral species (as they tend to be unaffected by migration). The chemical origin of this extra current will now be discussed in more detail.

6.6 Explanation of the inefficiency in Jethete

The cause of the runaway effect has been shown to be most likely due to iron, and it is postulated that like the valency change which is seen when machining SS316, these effects are most probably due to the solid dissolution products. In this case these are most likely to be iron dissolution products that are specific to nitrate electrolyte. The XRD spectra (see Section 5.4.2, Figure 5.21) and XPS data (see Section 5.4.3.5) for J solid products with nitrate showed distinctive differences to the other steel spectra with nitrate, showing iron-rich solid products with a different structure to the other steels. A highly probable dissolution product that could be produced in the interelectrode gap during machining is iron oxide, specifically $Fe^{III}_2O_3$ (see Section 5.4.2) as high valency dissolution is observed when

machining with nitrate. It has been previously observed that $Fe^{III}_2O_3$ acts as a catalyst when carrying out the following reaction [156].

$$e^-_{(aq)} + NH_{3(l)} \rightarrow NH_2^-_{(aq)} + \tfrac{1}{2}H_2 \qquad (6.1)$$

Thus the surface atoms of Fe_2O_3 (most likely the iron centres) can be considered to act as catalytic sites, where electron exchange occurs between the free electrons and ammonia, producing hydrogen. In the absence of this catalyst, free electrons are kinetically stable in ammonia solution. A catalyst acts to speed up both forward and reverse reactions, and as H_2O can be considered chemically similar to NH_3, it is therefore extremely plausible that these sites on Fe_2O_3 can enable the oxidation of H_2 to H^+, with the donation of electrons to the site.

$$\tfrac{1}{2}H_2 \rightarrow H^+ + e^- \qquad (6.2)$$

This could lead to the production of reduced metal centres in the metal oxide species. Such centres would tend to be reoxidised at the workpiece (either directly or via other Fe_2O_3 particles), whereas the protons produced would be reduced at the tool. This proposed reaction scheme is chemically plausible and would be a "short-circuit" reaction, producing increased current with no extra machining i.e. reduced efficiency (as the reduced and oxidised species produced at the tool and workpiece respectively undergo a redox reaction, producing species of reduced valency which can return to their respective electrodes to be rereduced and reoxidised respectively). It also involves neutral species which would not be able to transport by migration. It should also be noted that when machining iron with nitrate compared to Jethete with nitrate the runaway effect occurs instantly whereas when machining J a build up of dissolution products is required before the onset of the runaway. If iron oxide is produced in the gap then a critical concentration will be required before the runaway occurs. When machining J, other dissolution products will be present which could inhibit the formation of Fe_2O_3 and therefore it is consistent that it will take longer to build up to the required concentration of iron oxide to induce the runaway current. It should be remembered that other steels such as SS316, D and SD do not show this effect, despite the fact that each has Fe as its majority component, which demonstrates the sensitivity of this reaction to additives.

The short circuit reaction in this case could therefore be considered to be the reduction of iron oxide by hydrogen (produced at the tool)

$$Fe_2O_{3(s)} + 3H_{2(aq)} \rightarrow 2Fe_{(s)} + 3H_2O_{(l)} \quad (6.3a)$$

although the partial reduction of Fe_2O_3 to Fe(II) species may be more chemically reasonable e.g.

$$Fe_2O_{3(s)} + H_{2(aq)} \rightarrow 2FeO_{(s)} + H_2O \quad (6.3b)$$

$Fe_{(s)}$ (or Fe(II)) can then migrate back towards the workpiece where they can be reoxidised to produce Fe_2O_3 again via the reactions

$$Fe_{(s)} \rightarrow Fe(III) + 3e- \quad (6.4)$$

$$Fe(II)_{(s)} \rightarrow Fe(III) + e- \quad (6.5)$$

Fe(III) can then be reduced again by hydrogen produced at the tool according to Equation 6.3. Therefore, the redox reaction involving iron continues. Each time a cycle is completed more current is used, with no further dissolution and therefore the current will continue to increase and the efficiency decrease as observed. It is clear from the results presented for J that if such a cycle is present, multiple cycling can occur, as efficiencies of 0.5 and less can be obtained still with steadily decreasing efficiency (see Section 6.2). It would also seem that there is a point where the amount of cycling no longer increases when machining Fe with nitrate. This may be due to the solution reaching a constant concentration of catalytic particles, as particles sediment in the electrolyte tank. An alternative explanation would be that only Fe_2O_3 particles of a given size act as a catalyst (consistent with the filtration experiment, Section 6.2) and at high concentrations these particles may aggregate or flocculate, thereby reducing their catalytic effect.

If this hypothesis is correct then the cycle could be broken by adding a complexant which will bind to the dissolving Fe^{3+} ion to inhibit or prevent the formation of the Fe_2O_3 catalyst. Possible Fe^{3+} complexants are EDTA, citric acid and ascorbic acid [157]. Therefore, experiments were performed adding EDTA to the electrolyte to see if the "runaway effect" could be reduced and possibly prevented.

A variable flow experiment with iron in nitrate electrolyte was performed (Figure 6.17). As the flow rate is reduced then the concentration of products in the interelectrode gap would be expected to increase and therefore the "runaway current" should increase. This was observed.

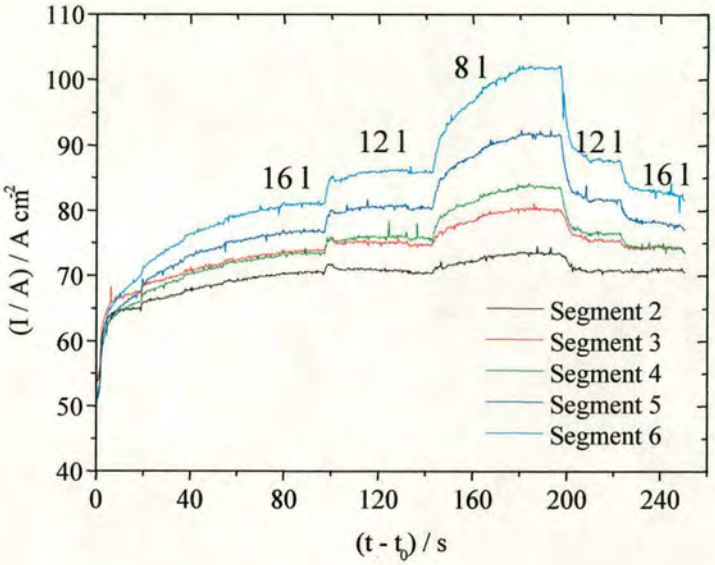

Figure 6.17: Experimental current transients for segments 2-6 for ECM of Fe at various flow rates (16-12-8-12-16 l min^{-1}) with nitrate electrolyte.

Adding EDTA to the bulk electrolyte should complex the Fe(III) species reducing this effect and may even prevent it from occurring. The reaction of iron with EDTA is

$$Fe^{3+} + EDTA^{4-} \rightarrow (Fe^{III}[EDTA])^{-} \qquad (6.6)$$

and thus Fe^{3+} reacts with EDTA with a 1:1 stoichiometry. Therefore, one can calculate the amount of EDTA required to react with the amount of Fe^{3+} produced by ECM dissolution. For pure iron, with an electrode area, A = 6.00 cm^2, and at a feed rate, f = 1.00 mm min^{-1}, the volume of Fe machined per minute is 6.00 cm^2 x 0.100 cm = 0.600 cm^3. The density of Fe, ρ = 7.874 g cm^{-3}, therefore the mass per minute dissolved under these conditions is 0.6 cm^3 x 7.87 g cm^{-3} = 4.72 g min^{-1} and the resulting molarity of Fe when using a flow rate of U = 16.0 l min^{-1} of electrolyte is 4.72 g min^{-1} / (55.85 g mol^{-1} x 16 l min^{-1}) = 0.0053 mol dm^{-3}, where 55.85 g mol^{-1} is the mass of one mole of Fe atoms. Under these conditions, therefore, a 0.0053 M EDTA solution should be just sufficient to complex all of the dissolving Fe^{3+} in the gap. This calculation assumes efficient mixing of the electrolyte, such that efficient

complexation occurs in the gap and complete conversion of Fe to $Fe(EDTA)^-$ occurs at the downstream edge of segment 7. A similar flow experiment to Figure 6.17 was therefore carried out with 0.0053 M EDTA added to the nitrate electrolyte. This is shown in Figure 6.18.

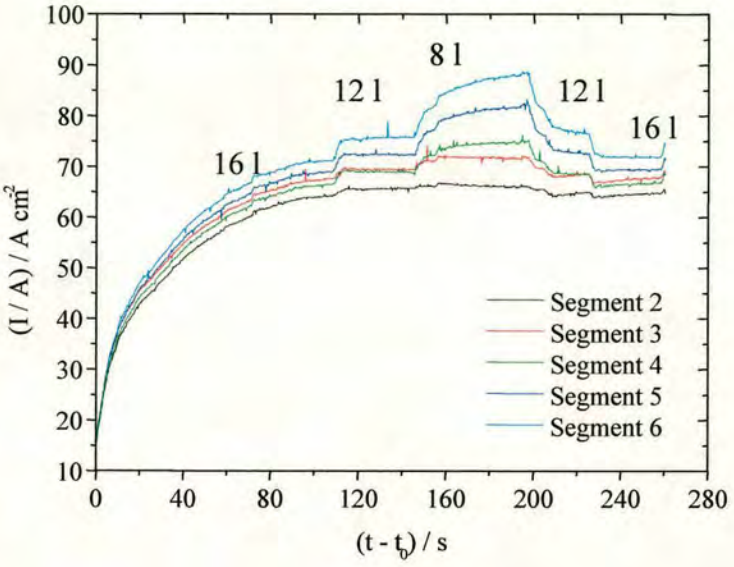

Figure 6.18: Experimental current transients for segments 2-6 for ECM of Fe at various flow rates (16-12-8-12-16 l min^{-1}) with nitrate electrolyte plus EDTA.

It is clear when comparing this experiment to Figure 6.17 that adding the stoichiometric amount of EDTA to complex the dissolving Fe(III) has produced a dramatic reduction in the "runaway effect" at 16 l min^{-1}. Each segment current appears to asymptotically approach the equilibrium current expected for Fe(III) dissolution, and there can be seen to be only a small increase in current along the flow path length, consistent with the production of some Fe_2O_3, most probably due to incomplete mixing of the Fe and EDTA reactants. This would seem to corroborate the catalytic Fe(III) theory advanced previously .

As the flow rate was reduced then the concentration of dissolving Fe^{3+} should increase at the same feed rate, and the concentration of EDTA in the electrolyte in the gap will be insufficient to bind to the Fe(III) produced, and Fe_2O_3 should start to be formed.. As would be expected in this case, increased currents are therefore observed with decreasing electrolyte flow rate as well as with increasing segment number at constant flow rate. However, on comparing Figures 6.17 and 6.18, there is still a noticeable reduction in the

extra current for each segment and the segment spread when machining iron with EDTA added to the nitrate electrolyte under these lower flow conditions. Therefore, the results seem to suggest that the EDTA is complexing the Fe(III), preventing the formation of Fe_2O_3 and therefore disrupting the "short-circuit" reaction cycle.

A similar experiment was then carried out using J with nitrate and EDTA (Figure 6.19). As the "runaway effect" is only observed after machining successive workpieces with J (see Section 6.2), in order to facilitate the quicker build up of products only half a tank of electrolyte was used (30 l). Therefore, the effect should occur twice as fast. 0.0263 M EDTA was also added. This is a five times higher concentration that for the Fe experiment, which should be enough to complex the dissolving Fe ions from J for 1125 seconds or 18.75 minutes. This corresponds to 18.75 mm of machined Fe, which at this reduced volume should be more than sufficient to see whether the "runaway effect" is prevented. ("Runaway" was observed after 13 mm of machining with 60 l of electrolyte, Section 6.2. It would therefore be expected after 6.5 mm or 390 seconds for 30 l of electrolyte).

The complexing reaction is as before

$$Fe^{3+} + EDTA^{4-} \rightarrow (Fe^{III}[EDTA])^{-} \qquad (6.7)$$

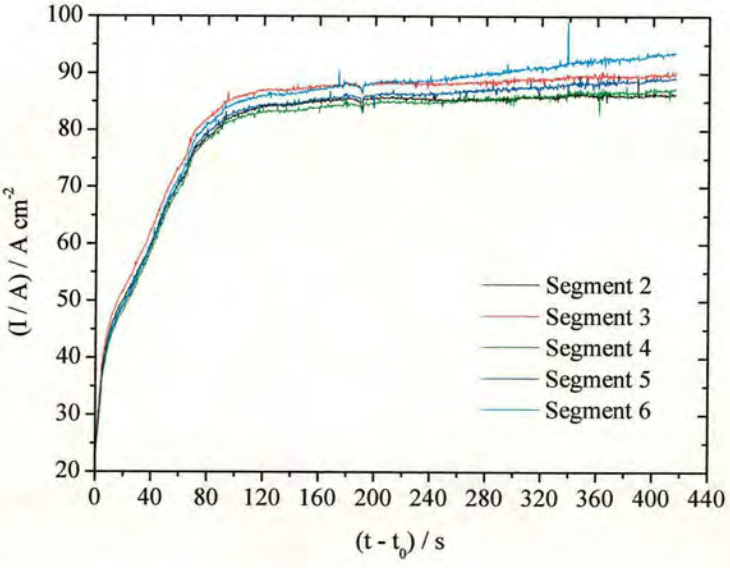

Figure 6.19: Experimental current transients for segments 2-6 for ECM of J at 16 l min^{-1} with nitrate electrolyte plus EDTA in 30 l total.

In fact, for J, each EDTA will complex a wide variety of dissolving metal ions M^{n+}. However, as the total concentration is calculated as for pure Fe, extra EDTA is present to complex these alloy elements. Therefore, they can be disregarded.

The results suggest that the EDTA has prevented the "runaway" from occurring. A high concentration of particles was present in the electrolyte after machining a workpiece for 5 mm and then using a new workpiece with the used electrolyte plus the addition of EDTA. There is a slight rise in current for segment 6 after ~ 200 s and there is a reduction in slope of segment 6 current (0.025 ± 0.002 A s^{-1}) compared with the slope when no EDTA is added (0.036 ± 0.003 A s^{-1}). A dissolving valency of $n = 3.8 \pm 0.1$ was found which was slightly higher than that previously observed with nitrate for the low chromium steels at $n = 3.5 \pm 0.1$. This is consistent with Fe dissolving with a valency of three, but may indicate dissolution of other metal alloy elements in J at higher valency than without EDTA. This would be consistent with the thermodynamic stabilisation of high valency oxidation states by complexation with EDTA.

6.7 Conclusion

The "runaway current" effect observed with J and nitrate electrolyte seems highly likely to be due to the formation of Fe_2O_3 in the interelectrode gap which acts as a catalyst to the short circuit reaction between the products from the workpiece and tool (Fe(III) and H_2). The products from this short-circuit reaction can then return to the workpiece and tool, donating and accepting electrons to regenerate the products of the workpiece and tool reactions. This cycle can occur repeatedly, and typically results in an extra current comparable to the dissolution current being passed, therefore causing a large inefficiency with $e < 1$. As this cycle depends on the amount of machined Fe_2O_3 product, the current continually rises (a "runaway current"). The inefficiency in the system was able to be independently measured and confirmed by using the ultrasound system to measure the change in workpiece height and plot this against the total charge passed to calculate e. Unlike the ECM reaction, the reaction rate of the cycle is not controlled by migration, as the increase in current is not accompanied by a corresponding change in gap. The catalytic cycle could be avoided by the addition of a complexant which bound to the Fe(III) thereby preventing the formation of solid Fe_2O_3. Trials were carried out on both Fe and J using nitrate with EDTA. The results suggest that the EDTA was binding to the dissolving Fe^{3+} in both systems and preventing the

catalytic cycle and hence the "runaway current". This additive or a similar complexing agent could be applied to the industrial machining process of J by nitrate electrolyte. Therefore, the addition of the additive has proved a success and highlights the importance of studying the chemistry of dissolution to enable the manipulation and control of parameters of the ECM process.

Chapter 7

Final Conclusions and Future Work

7.1 Conclusions

The following conclusions can be made from the work in this thesis:

1. Cell 99 has been used to demonstrate that the planar single tool and segments 2 – 6 from the segmented tool can be used to measure n and V_0 in an ECM system.

Cell 99 has been used to demonstrate that the planar single tool and segments 2 – 6 from the segmented tool are both equally valid when making measurements of n and V_0 in an ECM system. Segments 2 – 6 can also be used to measure the flow path variation whereas the planar single tool only provides an average value. However, segments 1 and 7 can be used to examine inlet and outlet erosion due to non-normal field lines and the limiting behaviour at short and long times can be parameterised and modelled. Segments 1 and 7 are harder to analyse theoretically to produce quantitative data at all times due to the overlapping segments, and the progressive effect of workpiece rounding but are no more difficult to explain as migration still governs dissolution.

2. Cell 2000 has been shown to be able to measure n and V_0 in an ECM system along the entire flow path length as well as providing the ability to sample electrolyte along the flow path length and make real time gap and workpiece height measurements with the ultrasound system.

Cell 2000 is an improved cell system which does not have overlapping end segments and hence does not suffer the theoretical problems for analysing segments 1 and 7. However, the inlet and outlet segments appear to suffer from minor hydrodynamic problems, which makes analysis of these segments more prone to error, especially at larger times. Cell 2000 is therefore capable of providing information about the ECM parameters along the entire flow path length. Combined with the chronoamperometric theory, the segmented tool in Cell 2000 is a powerful method for measuring the electrochemical dissolution characteristics of various workpiece materials along with the electrolyte sampling tubes and the real time interelectrode gap measurement system.

3. The experimental system can be used to collect electrochemical and chemical data under ECM conditions.

Although similar processes (chloride electrolyte inducing pitting which is dependent upon the integrity of the surface oxide layer) have been previously proposed as occurring during steel dissolution, it is significant that these proposals were previously invoked to explain dissolution under much lower current and voltage conditions than those appropriate to ECM. These results therefore demonstrate that the experimental system described can be used for the systematic collection and analysis of electrochemical and chemical data for dissolution under ECM conditions, allowing the measurement of ECM characteristics of a variety of steels and their correlation with composition.

4. The ECM dissolution characteristics of a family of alloys, in this case stainless steels, has been shown to be governed by the surface oxide layer.

These results indicate that the ECM dissolution characteristics of stainless steels are controlled by the nature of the surface oxide, which is dependent primarily upon their chromium content. Addition of "aggressive" ions such as chloride to the electrolyte can disrupt this surface layer and reduce the effectiveness of this surface barrier. Insoluble products of the ECM reaction can also compromise this barrier under certain conditions, leading to pitting corrosion and low valency dissolution. This is important in recycled electrolyte systems, which are typically used industrially.

5. The cause of the runaway current for J has been shown to be most likely due to an iron based oxide acting as a catalyst resulting in a short circuit reaction.

The runaway current effect observed with J and nitrate electrolyte seems highly likely to be due to the formation of Fe_2O_3 in the interelectrode gap which acts as a catalyst to the short circuit reaction. This cycle causes a large current to be passed that is not being used for dissolution therefore causing a large inefficiency. Therefore, the current continually rises unless this cycle is broken. The inefficiency in the system was able to be measured by using the ultrasound system to measure the change in workpiece height and plot this against the total charge passed to calculate e. The catalytic cycle was interrupted by the addition of a complexant which bound to the Fe(III) thereby preventing the formation of solid Fe_2O_3. Trials were carried out on both Fe and J using nitrate with EDTA. The results suggest that the EDTA was binding to the Fe(III) and preventing the runaway current.

6. XRD is not an effective method for analysing the solid dissolution products of ECM.

The solid dissolution products have to be annealed at a temperature of at least 600 ^{0}C in order to get a spectrum. This is most likely due to the solid particles being on the amorphous or nanocrystalline scale. It was shown that the use of an Argon flow stream whilst annealing seemed to be sufficient to prevent oxidation but heating to such high temperatures may have caused volatile components such as water of hydration in the sample to evaporate thus changing the products. Therefore, XRD is not an ideal method for analysing the products.

7. XPS is an effective method for analysing the solid dissolution products and the machined surface of the alloy.

The XPS results have showed that when machining the steels with nitrate electrolyte, then the solid particulate products contained significant amounts of C(0). This shows that C cannot be easily removed by electrochemical oxidation in nitrate and is most likely removed by dissolving all surrounding elements and entraining C in the flowing electrolyte. The oxidation states of elements are generally consistent with observed ECM dissolution valencies (e.g. Fe as (III), Cr as (VI) or (III)). The relative quantitation of M and O was problematic for thick oxides where the amount of M is consistently under estimated with respect to O, most probably due to the difference in the escape probability of the respective photoelectrons at any given depth in the oxide. However, changes in the amount of M between steels and the relative amounts of metals within an oxide may be able to be measured. The XPS experimental protocol used in this thesis was shown to be capable of detecting elements at greater than 2 % initial composition in the products. Longer acquisition times and/or greater X-ray intensities may be necessary to probe variation in the composition of the minor elements. Therefore, XPS is a very appropriate technique for the analysis of solid oxide products from ECM.

8. Visible absorption spectroscopy was effective in determining the oxidation state of Cr thus correlating with the observed current densities.

Visible absorption spectroscopy proved important in determining the valency state of Cr in the electrolyte tank and thereby confirming that Cr does dissolve with a valency of n = 6 when using nitrate electrolyte with approximately 100 % efficiency.

7.2 Future work

Possible future areas of expansion of the work in this thesis are:

1. The segmented tool system in Cell 2000 could be improved by removing all entry length hydrodynamic problems by changing the cell design and incorporating an entry length region to establish turbulent flow before entering the cell. Then segments 1 and 7 could be used in the chronoamperometric analysis. However, this may be difficult to do because of eroding surfaces.

2. The extension of the I/A vs V_0 analysis for ECM systems to a variety of different steels would provide insight into what is controlling the dissolution process through the oxide layer. Additionally, it would also allow the full parameterisation of ECM such that I vs V_0 relationships can be measured which is important as the complicated variation of values at high currents show that I vs V_0 data cannot simply be extrapolated from previously measured I-V_0 data measured at low currents.

Possible alternative analysis techniques that could be used to analyse the dissolution products are:

3. **Inductively coupled plasma (ICP).** This technique would be useful to analyse the used electrolyte. Any coloured products in the electrolyte can be determined by visible absorption spectroscopy. However, any colourless compounds cannot be detected by this method. Therefore, ICP could prove useful in this case to potentially identify any other dissolved metal complexes.

4. **XPS.** XPS analysis could be extended to sputter the solid dissolution products in order to gain information about the possible additional elements in the particles. This hypothesis could be tested with depth profiling. Extending the analysis of the dissolution products may enable the exact structure and composition of these products to be identified thus going some way to facilitate the disposal of these products safely.

References

[1] Dimiduk, D. M., Materials Science and Engineering A, 263 (2) (1999) 281.

[2] Larsen, J. M., Worth, B. D., Balsone, S. J. and Jones, J. W., Proc. TiAl applications; The Minerals, Metals and Materials Society, (1995) 821.

[3] Yamaguchi, M., Inui, H. and Kishida, K.. Materials Research Society Symp. Proc., 364 (1995) 3.

[4] Yoa, Z. and Marek, M., Materials Science and Engineering, A192/193 (1995) 994.

[5] Mantel, A. L. and Aspinwall, D. K., J. Mater Process Tech, 72(3) (1997) 413.

[6] Bentley, S.A., Goh, N.P. and Aspinwall, D.K., International Conference on Advances in Materials and Processing technologies, AMPT, (1999).

[7] Bentley, S.A. Mantel, A.L. Aspinwall, D.K., Intermetallics, 7 (1999) 967.

[8] Mantel, A. L., Aspinwall, D. K. and Wise, M. L. H., Institute of materials, UK, (1994) 244.

[9] Assessment of Electrochemical Machinability for Orthorhombic Titanium Aluminide, Edinburgh University Project Reference: DAC/EC21, (November 2000)

[10] Sharman A.R.C., Aspinwall D.K., Dewes R.C., Clifton D. and Bowen P, International Journal of Machine Tool and Manufacture, 41(11) (2001)1618.

[11] Benton, R. C. and Woodring, G. D., ASTME Paper No.3 (1965) 685.

[12] Debarr, A. E. and Oliver, D. Electrochemical Machining, (1968) Macdonald, London

[13] Kunz, H. G., Werkstatt u. Betrieb, 98 (1965) 355.

[14] Kelley, J., British Communications & Electronics, 11 (1964) 20.

[15] Gough, P. J. C., Engineers Digest, 27 (1966) 87.

[16] Debarr, A. E. and Oliver, D. Electrochemical Machining, Chapter 2 (1968) Macdonald, London.

[17] Lazarenko, B. R., Electrospark machining of metals, Consultants Bureau, (1964).

[18] Benedict, G. F., Nontraditional Manufacturing Processes, Marcel Dekker Incorporated (1987) January.

[19] Gurklis, J. A., Defense Metals Information Centre Report, Battelle Memorial Institute, 213 (1965).

[20] Risco, D.G and Davydov, A.D, J. Am. Soc. Mech. Eng. 64 (1993) 701.

[21] El Dardery, M.A, Int. J. Machine Tool Design Res. 22 (3) (1982) 147.

[22] Kellock, B, J. Machinary and Product. Eng. 140 (3604) (1982) 40.

[23] Chetty, O.V.K and Murthy Radhakrishan, R.V, Trans. ASME J. Eng. Ind. 103 (3) (1981) 341.

[24] Mileham, A.R., Harvey, S.J. and Stout K.J., J. Wear 109 (1986) 207.

[25] Gusseff, W., Method and apparatus for the electrolytic treatment of metals, British patent No. 335 003.

[26] Cleveland Twist Drill, Electrolytic sharpening, shaping and finishing of electrically conductive materials, British Patent No. 854 541.

[27] Rolls Royce, Manufacture of turbine and compressor blades, British Patent No. 846 278.

[28] Rolls Royce, Improvements relating to turbine and compressor blades, British Patent No. 846 279.

[29] Goyer, A. ECM: Little known, but very useful. Modern Machine Shop, (1988) April,.

[30] Debarr, A. E. and Oliver, D. Electrochemical Machining, (1968) Macdonald, London.

[31] Clifton, D., Process Characterisation for ECM, PhD thesis, University of Edinburgh, (2001).

[32] Kellock, B. Have a ball with a Cinderella process, Machinery and Production Engineering, (1982) May.

[33] Bjerketvedta, Dag., Roar Bakkea, Jan. and van Wingerdena, Kees., Gas Explosion Handbook, Journal of Hazardous Materials, 52 (1) (1997) 1-150.

[34] Larsson, C. N., Chapter 5, Electrochemical Machining, (1968) Macdonald, London.

[35] Proposal for a Council Directive on End-of-Life Vehicles, COM (97) 358.

[36] Jain, V. K. and Pandey, P. C. Tooling design for ECM Precision Engineering, 2 (1980) 195.

[37] Jain V.K. and Rajurkar K. P., Precision Engineering, 13(2) (1991) 111.

[38] Nilson, R. H. and Tsuei, Y. G., Transactions of ASME J. Applied Mechanics, 8(4) (1976) 54.

[39] Rolls Royce, Apparatus suitable for forming holes electrolytically in a metallic workpiece, British Patent No. 974 338.

[40] Rolls Royce, Electrode for forming holes electrolytically in a metallic workpiece, British Patent No. 974 339.

[41] Rolls Royce, Electrolytic shaping of metallic aerofoil blades, British Patent No. 937 737.

[42] Battelle Development, Electrolytic Cutting, British Patent No. 939 402.

[43] Clifton, D., Mill, F., Esanola, J., Kare, R. and Dover, W. D., J. of the Soc. for Underwater Technology, 24(4) (2000) 131-141.

[44] Clifton, D., Parameterisation and proof of concept study for ECM of PTT Assembly, Edinburgh University Project Reference: DAC/EC24, (October 2001)

[45] Clark, W. G. and McGeough, J. A., J. of Applied Electrochemistry, 7(4) (1977) 277.

[46] Hopenfield, J., Cole, R. R., J. Engineering for Industry, 88(4) (1966) 455.

[47] Thorpe J. F., Zerkle, R.D., Int. J. Mach. Tool Des and Res., 9 (1969) 131.

[48] Pramanik D. K., Agarwal R. A., De A. K., J. of the Inst. of Engineers, 57(5) (1977) 250.

[49] Jain V. K., Murgan S., Int. J of production Research, 24(2) (1986) 439.

[50] Landolt D., Muller R.H. and Tobias C.W., J. Electrochem. Soc., 118(1) (1971) 40.

[51] Davydov A. D. and Mirzoev R.A., Electrokhimiya, 8(10) (1972) 1463.

[52] Bannard, J., J. of Applied Electrochemistry, 7(1) (1976) 1.

[53] Landolt, D., J. Electrochem. Soc., 119(6) (1972) 708.

[54] Datta, M. and Landolt D., Electrochim. Acta, 25 (1980) 1263.

[55] Bejar, M. A. and Gutierrez, F., J. Mater. Processing Tech., 37 (1993) 691.

[56] Moir, P. G., Harvey, J., 16th MATADOR Conf., (1976) 257.

[57] Mileham, A. R., Jones, R. M., Harvey S. J., Production Points, Precsion Eng, 4(3) (1982) 168.

[58] Khairy, A., J. Materials Processing Technology, 58(2) (1995) 121.

[59] Machineability data centre, Machining data Handbook, third edition vol. 2 (1980).

[60] Bhattacharyya, B and Sorkhel, S. K., J. Materials Processing Technology, 86(2) (1999) 200.

[61] Hewidy, M.S. and Fattouh M., Int. J of production Research., 27 (6) (1989) 953.

[62] J. Hives and I. Rousar, J. of App. Electrochem., 24 (1994) 798.

[63] Hoare J. P., LaBoda M. A., McMillan M. L. and Wallace A. J., J. of Electrochem. Soc., 116 (2) (1969) 199.

[64] Haupt S. and Strehblow H. H., Corrosion. Sci. 37 (1995) 1.

[65] Brooks A.R., Clayton C.R., Doss K.and Lu Y.C., J. Electrochem. Soc. 133 (1986) 2459.

[66] da Cunha Belo M., Rondot B., Pons F., Le Hericy J. and Langeron J. P., J. Electrochem. Soc. 124 (1977).

[67] Lorang G., da Cunha Belo M., Simoes A. M. P., Ferreira M. G. S., J. Electrochem. Soc. 141 (1994) 12.

[68] Schmutz P.and Landolt D., Corros. Sci. 41 (1999) 2143.

[69] Asami K., Hasimoto K., Shimodaira S., Corrosion Sci, 18 (1978).

[70] Bojinov M., Fabricius, G., Laitinen, T., Makela, K., Saario, T and Sundholm, G., Electrochim. Acta., 46 (2001) 1339.

[71] Sukhotin A. M., Schlepakov M. N., Popov V. I., Sov. Electrochem. 21 (1985) 1582.

[72] Schmutz P. and Landolt D., Corros. Sci. 41 (1999) 2143.

[73] Olsson C. O. A., Hamm D., Landolt D., J. Electrochem. Soc. 147 (2000) 2563.

[74] Toney M.F., Davenport A.J., Joblonsky L., Ryan M.P.and Vitus C.M., Phys. Rev. Lett. 79 (1997) 4282.

[75] Oblonsky L.J., Ryan M.P.and Isaacs H.S., J. Electrochem. Soc. 145 (1998) 1922.

[76] Maurice V., Yang W.and Marcus P., J. Electrochem. Soc. 145 (1998) 909.

[77] Schmucki P., Virtanen S., Isaacs H.S., Ryan M.P., Davenport A.J., Boehni H.and Steinberg T., J. Electrochem. Soc. 145 (1998) 791.

[78] Wegrelius L., Falkenberg F.and Oleford I., J. Electrochem. Soc. 146 (1999) 1397.

[79] Bojinov M., Betova I.and Raicheff R.. J. Electroanal. Chem. 430 (1997) 169.

[80] Bojinov M., Fabricius G., Laitanen T. and Saario T., Electrochim. Acta. 44 (1999) 4331.

[81] Clayton C.R and Lu Y.C., J. Electrochem. Soc. 133 (1986) 2645.

[82] Lu Y.C., Clayton C.R.and Brooks A.R., Corros. Sci. 29 (1989) 881.

[83] Clayton C.R.and Lu Y.C., Corros. Sci. 29 (1989) 881.

[84] Urquidi M.and Macdonald D.D., J. Electrochem. Soc. 136 (1989) 555.

[85] Urquidi-Macdonald M.and Macdonald D.D., J. Electrochem. Soc. 136 (1989) 961.

[86] Macdonald D.D., J. Electrochem. Soc. 139 (1992) 3434.

[87] Muncaster R., Physics, Stanley Thornes Ltd (1994).

[88] Atkins P. W., Physical Chemistry, OUP (1994).

[89] Yagi K., chapter 13 in High-Resolution Transmission Electron Microscopy and Associated Techniques, Buseck et al, Oxford University Press (December 1988).

[90] Futamoto M., Surface Sci 150 (1985) 430.

[91] Venables J. A., Phil. Trans. Roy. Soc. Lond A318 (1986) 243.

[92] Browning R., J. Vac. Sci. Tech. A2 (1984) 1453.

[93] Liu J., Ultramicroscopy 52 (1993) 369.

[94] UK Surface Analysis Forum, http://www.uksaf.org/tech/xps.html, Christopher Walker KLA-Tencor, 686 Stirling Road, Slough, Berks., UK. (1998).

[95] Siegbahn K., Phil. Trans. Roy. Soc. London A, (1970) 33.

[96] Michigan State University, http://www.cem.msu.edu/~garrett/XPS.html, Simon J. Garrett, Department of Chemistry, Michigan State University, Michigan, USA (1999).

[97] Konig, W., Aachem, T. H., Humbs J., Annals of the CIRP, 25 (1) (1977) 83.

[98] Zhou, Y., Derby, J. J., Chemical Engineering Science, 50(17) (1995) 2679.

[99] Hardisty, H., Mileham, and A. R. and Shivani H., Proc. Inst. Mech. Engrs. Part B: J. Engineering Manufacture., 211(3) (1997) 197.

[100] Hardisty, H., Mileham A. R. and Suirvani, H., Proc. Inst. Mech. Engrs. Part B: J. Engineering Manufacture, 210(2) (1996) 109.

[101] Hardisty, H and Mileham A. R., Proc. Inst. Mech. Engrs. Part B- J. Engineering Manufacture, 213 (8) (1999) 787.

[102] Butt, R., Journal of computational and applied mathematics, 47(2) (1993) 151.

[103] Jain, V. K. and Pandey, P. C. Precision Engineering, 2 (1980) 23.

[104] Tsuei, Y. G., Yen, C. H. and Nilson R.H., American Soc. of Mech. Engineers, 3(1) (1977) 1.

[105] Deconinck J., Maggetto G., J. Electrochem Soc., 132(12) (1985) 2960.

[106] Tsuei, Y. G. and Nilson, R.H. Int. J. Mach. Tool Des and Res., 17(1) (1977) 169.

[107] Narayanan, O. H., Hinduja, S. and Nobel C. F., Int. J. Mach. Tool Des. Res., 26(3) (1986) 323.

[108] Konig, W., Aachen, T. H. and Humbs, J., Annals of the CIRP, 25(1) (1977) 83.

[109] Narayanan, O. H., Hinduja, B. E., and Nobel, C. F., Proc. Instn. Mech. Engrs, 200(C3) (1986) 195.

[110] Shuvra, D.A.S. and Ambar, K. M., Int. J. for numerical methods in engineering, 35(3) (1992) 1045.

[111] Nilson, R. H. and Tsuei, Y. G., J. of Engineering Mathematics, 8(4) (1974) 329.

[112] Butler J. A. V., Trans. Faraday Soc., 19 (1924) 734.

[113] Chao, C.Y., Lin, L. F. and MacDonald, D. D., J. Electrochem. Soc. 128(6) (1981) 1187.

[114] Brett, C. M. A, and Oliveira Brett, A. M. C. F., Comprehensive chemical kinetics, Elsevier, Amsterdam, 26 (1986) Chapter 5.

[115] R. B. Bird, W. E. Stewart and E. N. Lightfoot, Transport Phenomena, Wiley, New York (1960) 47.

[116] Levich V. G., Physicochemical Hydrodynamics, Prentice-Hall, Englewood Cliffs, (1962) 32.

[117] Newman J. S., Electrochemical Systems, Prentice-Hall, Englewood Cliffs, (1963).

[118] Schlicting, H., Boundary-Layer Theory, McGraw-Hill, New York, (1979) 555.

[119] Nikuradse, J.,Forsch. Geb. Ingenieurwes., 356 (1932).,

[120] Schlicting, H., Boundary-Layer Theory, McGraw-Hill, New York, (1979) 599.

[121] von Karmen, T., Z. Agnew. Math. Mech., 1 (1921) 244.

[122] Tipton H., Machine. & Prod. Eng. (1968) 325.

[123] Mount A.R., Eley K.L. and Clifton D., J. Appl, Electrochem., 30 (2000) 447.

[124] Mount, A. R., Howarth, P. S. and Clifton, D., J. Appl. Electrochem., 31 (2001) 1213.

[125] Datta, M., IBM J. of Res. and Develop. 37(2) (1993) 207.

[126] Clark W.G. and McGeough J.A., J. Appl. Electrochem. 7 (1977) 277.

[127] Datta M. and Landolt D., Electrochim. Acta, 25 (1980) 1263.

[128] Landolt D., J. Electrochem. Soc. 119 (1972) 708.

[129] Bejar M.A. and Gutierrez F., J. Mater. Proc. Tech., 37 (1993) 691.

[130] Laue M. v., Röntgenstrahlinterferenzen. Physikal. Zeir. 14 (1913) 1075.

[131] Bragg, W. H., and W. L. Bragg. Proc. R. Soc. Lond. 88 (1913) 428.

[132] Bragg, W. L., Proc. Camb.Phil. Soc. 17 (1913) 43.

[133] Massey, B. S. Mechanics of Fluids, 6th edition Chapman and Hall, London, 1995.

[134] Douglas, J. F. Gasiorek, J. M. Swaffield, J.A., Fluid Mechanics, third edition, Logman, London 1995.

[135] D. Clifton, A. R. Mount, G. M. Alder and D. Jardine, International J. of Machine Tools and Manufacture, 42 (2002) 1259.

[136] MacDonald D.D., J. Electrochem. Soc. 139 (1992) 3434.

[137] Haupt S. and Strehblow H. H., Corr. Sci., 37 (1995) 43.

[138] Landolt, D., J. Electrochem. Soc., 119 (1972) 708.

[139] Mount A. R., Howarth P. S. and Clifton D., J. Electrochem. Soc. 150(3) (2003) 63.

[140] von Karman T., Angew Z.. Math. Mech., 1 (1921) 244.

[141] Woodruff, D. P. and Delchar T. A., Modern Techniques of Surface Science, Cambridge Solid State Science Series (1994).

[142] Lopez, M. F., Guitierrez, A, Torres, C. L. and Bastidas, J. M., J. Mater. Res., 14 (3) (1999) 763.

[143] National Institute of Science and Technology (NIST), http://srdata.nist.gov/xps/main search menu.htm, U.S. Commerce Department's Technology Administration. (2003).

[144] Avantage data system - In depth explanation of functionality, Thermo VG Scientific (2001).

[145] Pagitsas M., Diamantopoulou A. and Sazou D., Electrochem. Comm. 3 (2001) 330.

[146] Brooks A.R., Clayton C.R., Doss K. and Liu Y.C., J. Electrochem. Soc., 133 (1986) 12.

[147] Lorang G., da Cunha Belo M., Simoes A.M.P. and Ferreira M.G.S., J. Electrochem. Soc., 141 (1994) 12.

[148] Szklarska-Smialowska Z., National Association of Corrosion Engineers, Houston, Texas, USA, (1986) 431.

[149] Sugimoto K., Matsuda S., Ogiwara Y. and Kitamura K., J. Electrochem. Soc. 132 (1985) 8.

[150] Alkire R. and Cangellari A., J. Electrochem. Soc., 130 (1983) 1252.

[151] Harb J.N., J. Electrochem. Soc., 133 (1986) 439C.

[152] Beverskog B. and Puigdomenech I., Corr. Science., 38 (1996) 2121.

[153] Beverskog B. and Puigdomenech I., Corr. Science., 39 (1997) 43.

[154] Beck T.R. and Chan S.G., Corrosion, 37 (1981) 665.

[155] Alkire R.C., Reise D.B. and Sani R.L., J. Electrochem. Soc., 131 (1984) 2795.

[156] Griffiths, L.E., PhD thesis, University of Edinburgh, (2002).

[157] Panias, M., Taxiarchou, I., Paspaliaris, A., and Kontopoulos A., Hydrometallurgy, 42 (1996) 257.

Appendix

Published papers:

(reprinted with the joint authors permission)

Mount A.R., Howarth P.S., Clifton D., The use of a segmented tool for the analysis of electrochemical machining, Journal of Applied Electrochemistry, 31 (2001) 1213.

Mount A.R., Clifton D., Howarth P., Sherlock A., An integrated strategy for materials characterisation and process simulation in electrochemical machining, Journal of Materials Processing Technology, 6670 (2003) 1.

Mount A.R., Howarth P.S., Clifton D., The Electrochemical Machining characteristics of Stainless Steels, Journal of The Electrochemical Society, 150(3) (2003) 63.

Journal of Applied Electrochemistry **31**: 1213–1220, 2001.

The use of a segmented tool for the analysis of electrochemical machining

A.R. MOUNT[1]*, P.S. HOWARTH[1] and D. CLIFTON[2]
[1]*Department of Chemistry;* [2]*Department of Mechanical Engineering, University of Edinburgh, King's Buildings, West Mains Road, Edinburgh EH9 3JJ, UK*
*(*author for correspondence, e-mail: a.mount@ed.ac.uk)*

Received 9 May 2001; accepted in revised form 14 August 2001

Key words: characterisation, current analysis, electrochemical machining, segmented tool

Abstract

A planar workpiece/planar segmented tool experimental configuration has been used to collect current–time data for the electrochemical machining (ECM) of Inconel 718 (In718) and stainless steel (SS316). As with previous measurements, theoretical analysis of the chronoamperometric data has been used to obtain values for the characteristic parameters of ECM under characteristic machining conditions, but the segmented tool allows this for each segment. These parameters are the valency, n, and k, from which the minimum voltage required to initiate machining, V_0, and the electrolyte conductivity, κ can be obtained. The variation of n, V_0 and κ between segments enables ECM conditions along the flow path length to be probed. Measurements on In718 in nitrate electrolyte have shown a small increase in electrolyte conductivity along the flow path. Tool segments which overlap the workpiece ends have been employed to measure edge effects in the ECM process; no significant edge effects were found when machining In718 in nitrate. The temporal and spatial dependences of a change in valency previously observed during the machining of SS316 have also been studied for the first time. Regions of low valency ($n = 2.1$) dissolution (downstream) and high valency (upstream, $n = 3.0$) dissolution were observed, with an intermediate region with monotonically decreasing valency where $3.0 > n > 2.1$.

1. Introduction

Increasing demand for high strength, low-weight, metallic and intermetallic alloys has led to an increasing requirement for metal cutting and forming processes able to cope effectively with such materials. Electrochemical machining (ECM), whereby metal is removed by the electrochemical dissolution of a workpiece material, offers many potential advantages over traditional methods of machining, as ECM is able to machine a material irrespective of hardness and is able to produce complex shapes at high metal removal rates. A high quality surface is produced without residual stresses or surface damage to the microstructure [1–5]. ECM is carried out by passing an electric current of up to 100 A cm^{-2} through an electrolyte flowing in the gap between an electrode tool (biased as the cathode) and workpiece (biased as the anode). As dissolution of the workpiece material occurs the tool electrode is advanced, at a controlled rate, to maintain removal of material.

Previous work [6] has demonstrated how chronoamperometric measurements of ECM using a planar workpiece/planar tool configuration with a constant tool feed rate can be analysed to obtain direct measurements of chemical parameters such as the electrolyte conductivity, the valency and the surface overpotential [7–11]. These are the crucial parameters for process simulation [12, 13] and tool design [14, 15] in ECM and they can also be used to give insight into the chemical dissolution processes occurring. Such measurements take no account of the variation of the nature and concentration of the ions in the flowing electrolyte across the workpiece surface during ECM. Upstream of the workpiece the electrolyte composition is the same as that in the electrolyte reservoir. However, as electrolyte flows across the workpiece surface, soluble metal ions are produced and electrolyte ions consumed, the temperature increases due to resistive heating [16] and the void fraction may increase due to gaseous products [17, 18]. These may lead to a progressive change in electrolyte conductivity and composition, which could induce variation in the ECM parameters with flow path length. This paper presents the analysis of flow path variation using a segmented tool system. A segmented tool (or sectional cathode) [19] has previously been reported for use in machining of large surface areas, with each segment under independent voltage control. However, this novel system has been developed to allow theoretical analysis of current transient data specifically to obtain ECM parameters along the flow path length.

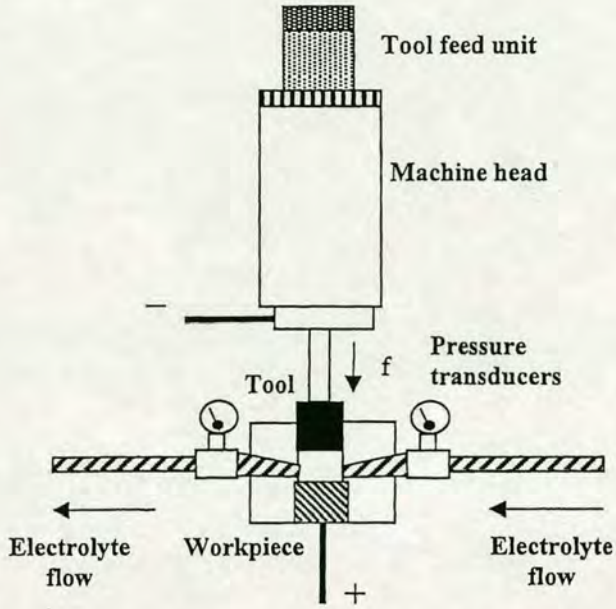

Fig. 1. The experimental configuration for the ECM machining experiments.

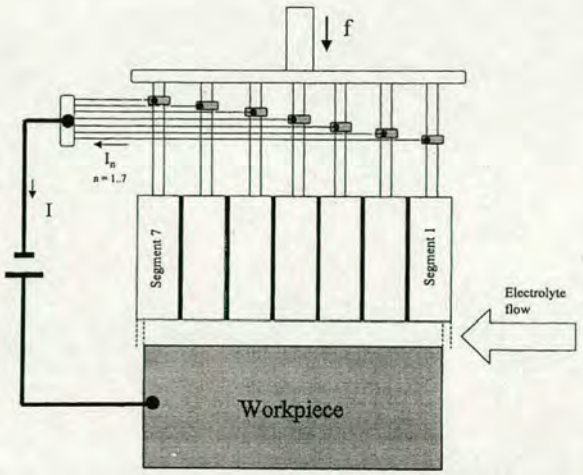

Fig. 2. The experimental configuration of the segmented tool system.

2. Experimental

The experimental setup for these measurements is as given previously ([6] and Figure 1). This consisted of a Transtec electrochemical machine, with an RDOA regulating transformer (Bonar Brentford Electric), a 600 A transformer (Goodyear), a Hydracell D25 electrolyte pump (Wanner Engineering Inc.), a type FT 13 (Platon Instrumentation) flow sensor and type HT (RS Components) current transducers. The data were collected using a PC with Intelligent Instruments (Burr–Brown) in house data logging system. A reservoir of 60 l of electrolyte was used, kept at 30 °C. As with the previous paper [6] the system under consideration is a planar tool moving at a constant feed rate, f, towards a planar parallel alloy workpiece, each of metallic area $A = 4.80\ \text{cm}^2$. However, in this work the tool was divided into seven separate coplanar electrodes (or segments) with relatively narrow insulation separating them (Figure 2). These were numbered segments 1–7 from upstream to downstream in the electrolyte flow as shown. Seven current transducers were used to detect the current for each segment and one transducer was used to measure the total combined current from all segments. All transducers were calibrated and the total current was consistently found to be equal to the sum of the segmented currents within experimental error (~0.5%). In contrast to previous studies [6], it should be noted that due to the introduction of insulation separating each segment, the overall length of the segmented tool in this setup was greater than the workpiece and hence segments 1 and 7 on the segmented tool overlapped the workpiece at each end. This had the advantage of enabling the measurement of edge effects, which have been suggested as being important in ECM [20].

The two electrolyte systems employed were a 2.56 mol dm^{-3} (15.0% w/v) aqueous solution of sodium chloride and a 2.56 mol dm^{-3} (21.7% w/v) aqueous solution of sodium nitrate (Anderson, Gibb and Wilson) and the workpiece alloys were SS316 and In718 (Haynes International Inc.). The certified compositions of these alloys are given in Table 1.

The initial electrode gap was measured by casting, using a polyether impression material (EPSE Permadyne). This initial gap was 0.80 mm for these experiments unless otherwise stated. A constant voltage, V, was applied between the workpiece and the tool. The electrolyte flow rate and feed rate, f, were also held constant throughout at 20.0 $\text{dm}^3\ \text{min}^{-1}$ and 1.00 mm min^{-1} respectively unless otherwise stated. Under these relatively high flow conditions, assuming that the movement of each electron in the external circuit results in the production of one anion and one cation in the electrolyte at the tool and the workpiece respectively and an upper limit for I_∞ of 350 A for these experiments, this corresponds to a maximum increase in ion concentration of 2.2×10^{-2} mol dm^{-3} during machining. From this the calculated change in electrolyte concentration is of the order of 1%. These conditions therefore ensure that the approximation of constant overall electrolyte concentration along the flow path length is reasonable.

Table 1. Composition in weight percent of In718 and SS316 alloys

Alloy	C	Fe	S	Al	P	Mn	Co	Cr	Cu	Mo	Ni	Si	Ti
SS316	0.12[a]	70.09	0.045[a]	–	0.045[a]	2.00[a]	–	17.00	–	2.50	8.00	0.02[b]	–
In718	0.05	18.45	–	0.48	–	0.22	0.17	18.16	0.02	2.96	53.32	0.10	1.02

[a] Maximum value; [b] Minimum value.

However, at lower flow rates, this approximation is less valid.

Fitting of the current–time transients I_2–I_6 was achieved by iteratively fitting the results to Equation (9), using the SigmaPlot plotting program (Jandel Scientific).

3. Results and discussion

3.1. *Calibration of the segmented tool apparatus*

The first test of the planar segmented tool/planar workpiece system was to compare and contrast its response to that of the planar single tool/planar workpiece. Previous studies [6] have shown that the planar single tool/planar workpiece configuration can successfully be used to obtain and analyse current–time data for the ECM of In718 in nitrate electrolyte at relatively high electrolyte flow rates and extract independent values for the machining parameters κ, V_0 and n. This suggests there is little significant variation in these ECM dissolution parameters across the workpiece surface, which greatly simplifies analysis for calibration. Theoretical analysis assumed the current to be governed by migration (an essential assumption for stable machining). Furthermore, since the tool and workpiece were parallel, of equal dimensions (area A) and separated vertically in this system, the field lines between the two electrodes could be assumed to be normal and vertical between the two electrodes (Figure 3a). The conductivity, κ, could be assumed to be constant [6] as the electrolyte flow rate was sufficient to minimise the change in concentration due to the build up of machining products and/or the loss of ions from the electrolyte, the temperature increase along the path length and the void fraction of evolved gases in the electrolyte, all of which can affect the conductivity. In this case, if the gap between the electrodes is z, the current across the electrolyte, I, is given by:

$$I = \frac{\kappa(V - V_0)A}{z} \tag{1}$$

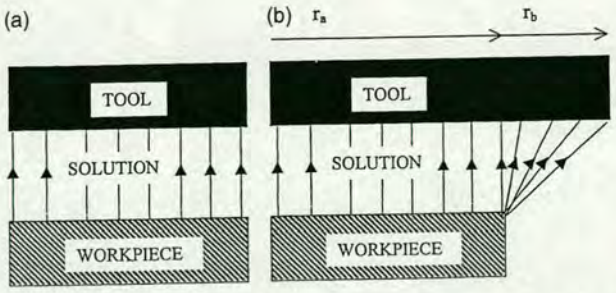

Fig. 3. Migration field lines (a) for the planar single tool system and for each of the segments 2–6 in the segmented tool system (b) for each of the end segments 1 and 7 in the segmented tool system. The distances corresponding to r_a and r_b are shown for segments 1 and 7. For these experiments $r_a = 4.69$ mm, $r_b = 1.31$ mm and hence $r_n = r_a + r_b = 6.00$ mm.

where V is the applied voltage, V_0 is that portion of the voltage required at the two electrodes to drive the electrode reactions (*vide infra*) and κ is the conductivity of the electrolyte. Assuming that all current leads to electrode dissolution (100% dissolution efficiency), this current is also the dissolution current of the workpiece, and therefore

$$I = \left[\frac{nFA\rho}{M}\right]\frac{dy}{dt} \tag{2}$$

where n is the average number of electrons required to be removed to dissolve each atom (the 'valency'), F is Faraday's constant (96 485 C mol^{-1}), ρ is the density of the workpiece material, dy/dt is the thickness of workpiece removed per unit time and M is the average molecular weight (the mass of 1 mol) of the workpiece material. It has been reported that efficiencies below 100% are obtained in some cases at low flow rates [16, 21–23], under which conditions n should be replaced by the more general term n/e in Equation (2), where e is the efficiency. However, efficiency has been observed to increase with flow rate and approach 100% ($e = 1$) at flow rates significantly lower than that employed throughout this work [21]. Furthermore, the measured invariance of n with current and interelectrode distance in this and previous work [6] (as demonstrated by the closeness of theoretical fits to the data) and the invariance of n with segment number (*vide supra*) all indicate a constant value of e, which would not be expected for efficiencies significantly below 100%.

The change in the interelectrode distance, z, is given by

$$\frac{dz}{dt} = \frac{dy}{dt} - f \tag{3}$$

and hence, combining Equations (1)–(3)

$$\frac{dz}{dt} = \frac{k}{z} - f \tag{4}$$

where

$$k = \left[\frac{\kappa(V - V_0)M}{nF\rho}\right] \tag{5}$$

Now at the equilibrium current, I_∞, (I when $t \to \infty$), when a steady-state current has been reached, z remains constant at z_∞ and $dz/dt = 0$; hence $f = k/z_\infty$,

$$I_\infty = \left[\frac{nFA\rho}{M}\right]f \tag{6}$$

and

$$\frac{dz}{dt} = k\left[\frac{1}{z} - \frac{1}{z_\infty}\right] \tag{7}$$

Equation (7) can be integrated from $t = t_i$, $z = z_i$ to $t = t$, $z = z$, to give

$$\ln\left[\frac{z_\infty - z_i}{z_\infty - z}\right] + \frac{z_i - z}{z_\infty} = \frac{k(t - t_i)}{z_\infty^2} \tag{8}$$

Substituting the appropriate values of I_i, I and I_∞ from Equation (1), one obtains

$$\ln\left[\frac{1 - \frac{I_\infty}{I_i}}{1 - \frac{I_\infty}{I}}\right] + \left[\frac{I_\infty}{I_i} - \frac{I_\infty}{I}\right] = \frac{f^2(t - t_i)}{k} \tag{9}$$

The initial time is often chosen to be as close as possible to the time at which the ECM voltage is applied to the electrode and tool feeding is commenced to ensure that the initial gap in these experiments can be approximated to that set before machining. In practice, this time is often the point at which the current stops its initial decrease, denoting the establishment of stable machining conditions. The values at this time (termed time zero) are given the subscript 0 in this paper to denote this.

For the planar segmented tool, Equation (9) should also apply to segments 2–6, with each of the segments having an identical electrode area, designated as $A = A_n$ and segment currents of $I_0 = I_{n,0}$ and $I_\infty = I_{n,\infty}$ in Equations (1), (2) and (6). Hence, each should give a similar current–time response to the planar single tool system. This is because the assumption of normal field lines between the workpiece and tool electrodes should largely apply to each of these segments, with the exception of the relatively thin intersegment insulating regions of the segmented tool. Since these insulating regions are small in area compared to the area of the segments (0.05 mm compared to 5.95 mm), they would therefore be expected to have a relatively small effect on the overall response. It is important to note that for segments 2–6, A_n corresponds to the area of one segment plus one intersegment insulating region, whilst for segments 1 and 7, A_n is the area of the segment plus half an insulating region, as this is the area of workpiece being eroded by each segment.

Figure 4 shows representative data for segments 2 and 6 for machining In718 with nitrate electrolyte, along with the iterative fits produced using Equation (9). Good fits to these data are obtained in all cases, from which values of f^2/k and $I_{n,\infty}$ (I_∞ for each segment, n) have been obtained. Furthermore, k/f^2 and $I_{n,0}$ data ($I_{n,0}$ being the initial current for segment n at the onset of machining) obtained for these fits can be compared to the values previously obtained using the planar single tool/planar workpiece configuration [6] (Figure 5). The single tool data showed that both k/f^2 and I_0 have a linear dependence with V, indicating approximately constant values of $V_0 = 5.4 \pm 0.4$ V, $\kappa = 0.20 \pm 0.010$ S cm^{-1} and $n = 3.0 \pm 0.2$ for the In718 system in nitrate electrolyte. The observed close correlation of the mean values of k/f^2 and I_0 for the segments at each value of V with those found from the previous single tool data demonstrates that ECM of In718 occurs with similar values of V_0, κ and n in both single and segmented tool experiments. Also, observed values of $I_{n,\infty}/A_n$ were found to be 72 ± 2 A cm^{-2} for all segments, in good agreement with I_∞/A values from the single tool experiments [6]. This confirms the applicability of the normal field line approximation to the segmented tool system and of Equation (9) to segmented tool data analysis for segments 2–6. This also validates the assumption of a constant efficiency for the dissolution reaction along the flow path length.

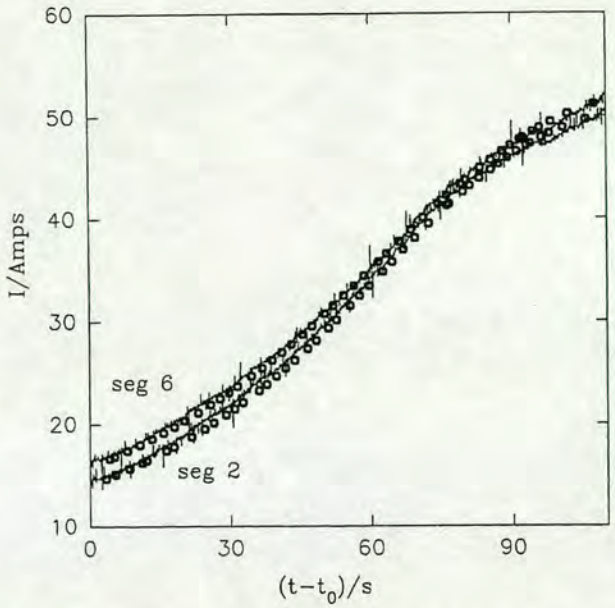

Fig. 4. Experimental current–time data (-) and theoretical fits to these data from Equation. (9) (o) for segments 2 and 6 for In718 in nitrate electrolyte at $V = 16$ V.

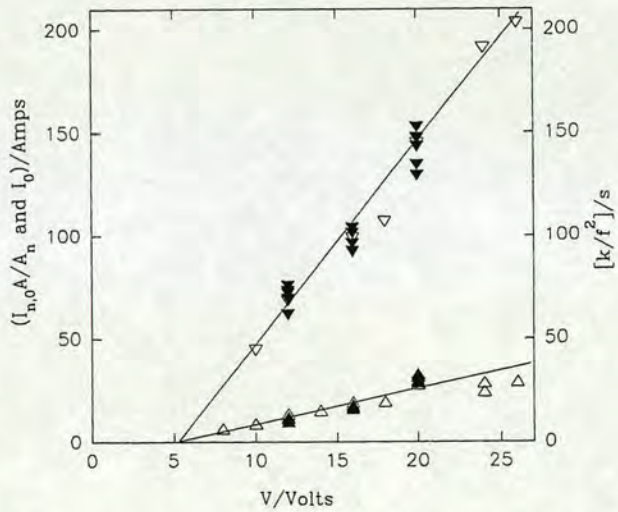

Fig. 5. Comparison of the values of $I_{n,0}$ and k/f^2 obtained for In718 in nitrate by the iterative fits to Equation (9) for each of segments 2–6 at $V = 12$, 16, 20 V (▼) with equivalent data (I_0 and k/f^2) obtained using the planar single tool (▽) from reference [6]. $I_{n,0}$ data have each been multiplied by A/A_n to account for the difference in area between the single tool and each segment of the segmented tool, allowing direct comparison with I_0 data. At each voltage the values of both $I_{n,0}$ and k/f^2 were observed to increase with segment number.

Notwithstanding this, on close examination of the data, there is a small but significant increase in the values of $I_{n,0}$ and k/f^2 with increasing segment number at each value of V. It should be emphasised that the increase observed with the segmented tool is sufficiently small to explain the previously observed reasonable fit of the overall current data for a single tool to a constant mean value of k [6] and to justify the assumption of a constant k across each segment. The total increase in k is of the order of 10% (independent of the applied voltage, V) between segments 2 and 6. This can be attributed either to a 10% increase in the conductivity, κ, and/or a 10% increase in the value of $(V - V_0)$, due to a decrease in V_0. A decrease in V_0 would be due to a change in the voltage required to drive the workpiece dissolution reaction, arising from a change in the nature of this reaction or in the reagent concentrations across the workpiece surface. Such a variation would be unlikely to produce the observed approximately linear increase in k observed with increasing segment number. Furthermore, this increase in $(V - V_0)$ would be expected to be sensitive to the magnitude of the applied voltage, V, leading to a dependence of the total increase of k on V, which is not observed. Thus the observed increase is not likely to be due to a significant change in V_0, but rather to an increase in κ. A small change in electrolyte composition and/or temperature is the most likely cause. Thus this system can be used to quantify small changes in k along the flow path length.

When considering segments 1 and 7, it is clear from Figure 3b that these tool segments overlap the workpiece, and that the migrational current will have a significant contribution from non-normal field lines. Initially, the migration can be modelled as two distinct areas. The first extends over a width r_a and depth l (which is the depth of all the segments) and is where segment and workpiece lie directly above one another and show normal field lines. The second area applies to the overlapping ends of the tool over a width r_b and depth l, and corresponds to field lines converging on the edge of the workpiece as shown. In this case, the current due to migration for segment 1 or 7, $I_{1,7}$, can be approximated as the sum of two terms (assuming a constant workpiece–tool distance of z throughout)

$$I_{1,7} = \frac{\kappa(V - V_0) l r_a}{z} + \kappa(V - V_0) l \int_0^{r_b} \frac{1}{\sqrt{r^2 + z^2}} \mathrm{d}r \quad (10)$$

where the segment width is equal to the sum of r_a and r_b. By making the substitution $r/y = \tan u$, one obtains

$$I_{1,7} = \frac{\kappa(V - V_0) l r_a}{z} + \kappa(V - V_0) l \int_0^{\tan^{-1}(r_b/y)} \sec u \, \mathrm{d}u \quad (11)$$

Integration gives

$$I_{1,7} = \frac{\kappa(V - V_0) l r_a}{z} + \kappa(V - V_0) l \left[\ln\left(\sec\left(\tan^{-1} \frac{r_b}{y} \right) + \frac{r_b}{y} \right) \right]$$

$$= \frac{\kappa(V - V_0) l r_a}{z} + \kappa(V - V_0) l \left(\ln \frac{\sqrt{2r_b^2 + z^2}}{z} \right) \quad (12)$$

and since $lr_n = A_n$, the area of segment $n = 2$–6, where r_n is the width of any of the segments n, by substitution one obtains [6]

$$I_{1,7} = \frac{I_n}{r_n} \left[r_a + B \ln \left(\frac{\sqrt{2r_b^2 + B^2}}{B} \right) \right] \quad (13)$$

where

$$B = \frac{z_\infty I_{n,\infty}}{I_n} = \frac{\kappa(V - V_0) A_n}{I_n} \quad (14)$$

from Equation (1), since I_n and $I_{n,\infty}$ are the current and equilibrium current (as t approaches infinity) for any of the segments $n = 2$–6 and z_∞ is the equilibrium distance between tool and workpiece. This means that B can be determined at any time for any segment n from the current I_n and either the values of z_∞ and $I_{n,\infty}$ or the values of κ and V_0 and the area of the segment, A_n. This allows the calculation of $I_{1,7}$ at any time from Equation (13) using the calculated values of B and the measured values of r_a, r_b, r_n and I_n. However, $I_{1,7}$ corresponds to the current that would be observed whilst maintaining a planar workpiece geometry. This will only rigorously apply at the onset of machining, as at the workpiece ends the increased migrational flux from the overlapping tool will lead to increased machining and an increasingly pronounced workpiece curvature, which has actually been observed after machining. The curvature causes an increased workpiece end to tool distance, resulting in a machining current less than that calculated in Equation (13). At longer times, machining conditions approach equilibrium, where there is no further change in either the tool–workpiece separation or the segment currents with time. Under these conditions, as the amount of metal dissolved from the workpiece per unit area by each segment will be the same and will exactly balance the feed rate, the currents for segments 1 and 7, $I_{1,7}$ will simply be given by

$$I_{1,7} = \frac{I_n r_a}{r_n} \quad (15)$$

with the particular condition as $t \to \infty$ of

$$I_{1,7,\infty} = \frac{r_a}{r_n} I_{n,\infty} \quad (16)$$

where $I_{1,7,\infty}$ and $I_{n,\infty}$ are the equilibrium machining currents for segments 1 or 7 and a neighbouring

segment, n, respectively. Thus experimental current–time transients obtained for segments 1 and 7 should be described by Equation (13) at short times and Equation (15) at long times, with a monotonic transition between these currents at intermediate times. This is indeed the case for both I_1 and I_7 (Figures 6 and 7),

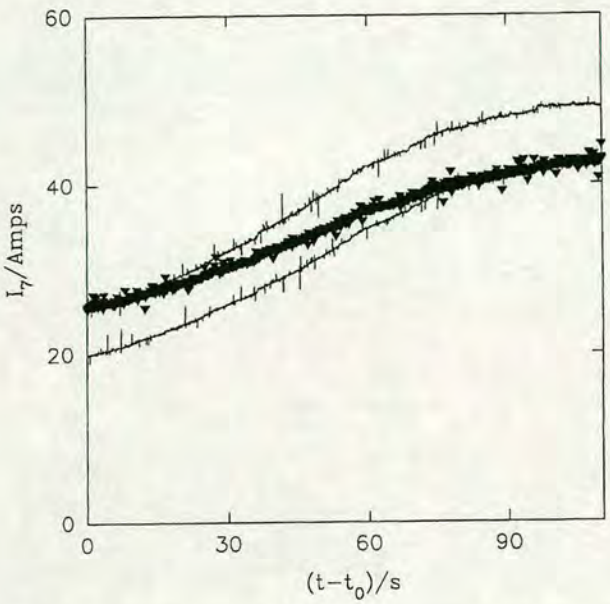

Fig. 6. Comparison of experimental current transient data for segment 7 (▼) measured at $V = 20$ V and an electrolyte flow rate of 16 dm^3 min^{-1} with theoretical data produced from Equation (13) (upper line) and Equation (15) (lower line) for ECM of In718 in nitrate electrolyte. Theoretical data for segment 7 have been calculated using Equation (13) and I_6 and z_∞ measured at segment 6.

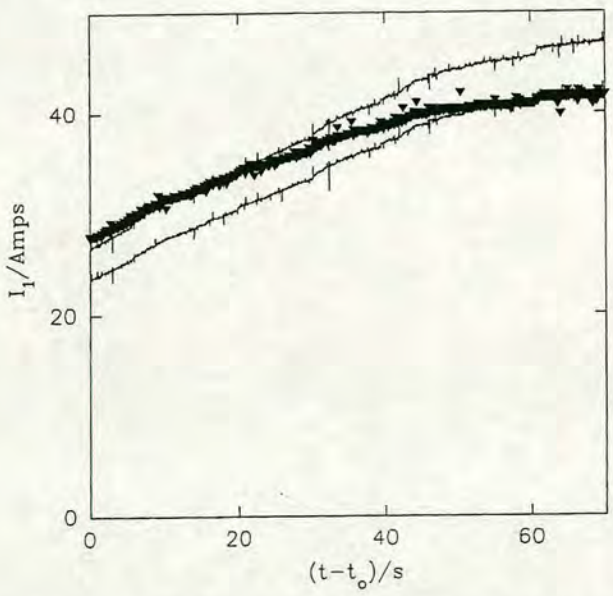

Fig. 7. Experimental current transient data for segment 1 (▼) measured at $V = 20$ V and an electrolyte flow rate of 22 dm^3 min^{-1} plotted against theoretical data produced from Equation (13) (upper line) and Equation (15) (lower line) for ECM of In718 in nitrate electrolyte. Theoretical data for segment 1 have been calculated using Equation (13) and I_2 and z_∞ measured at segment 2.

confirming the applicability of these models to these segments. I_1 can be seen to correlate closest with the currents predicted from segment 2 and I_7 with the currents predicted from segment 6, as the small differences in k observed on each segment necessitates comparison of neighbouring segments for the best correlation. This simple model does not incorporate any specific edge effects, as suggested by Landolt [20]. Thus, it is clear from the close correlation between theory and experiment that significant edge effects are not present in this system, and that correlation of experimental results obtained using the segmented tool system with theory could be used to probe these effects in other systems.

3.2. *ECM of SS316*

One application of the segmented tool is the measurement of changes in valency, such as those previously observed [24, 25] in the machining of stainless steel SS316 (En58J), where a smooth, bright surface was obtained at relatively high electrolyte flow rates and/or relatively low feed rates (low currents) and a dull, rough surface was produced at low flow rates and high currents (high feed rates). From consideration of the equilibrium erosion current and interelectrode gap, the bright surface was characterised as being due to Fe(III) and Cr(VI) dissolution and the dull surface to Fe(II) and Cr(III) dissolution. At intermediate flow rates, regions of shiny (upstream) and dull (downstream) surface were produced, with the proportion of shiny surface increasing with flow rate. This involved inspecting the workpieces after carrying out ECM for a fixed time at a variety of electrolyte flow rates [24]. Thus average valencies were produced and it was not possible to perform *in situ* measurements of the variation of this boundary position with time or to confirm the postulated variation of valency with flow path length. These spatially resolved and temporally resolved measurements have now been made using the segmented tool.

Figure 8 shows typical segmented tool current–time transients obtained from the ECM of SS316 under conditions analagous to fast flow rates, where a shiny surface finish was produced. As with In718 in nitrate electrolyte, similar current transients were observed for each segment, consistent with ECM occurring at a constant valency across the whole of the flow path length. Iterative fits to Equation (9) for each of the segments 2–6 produced a good fit to the experimental data, giving values of $I_{n,\infty} = 55 \pm 2$ A ($I_{n,\infty} = 75 \pm 3$ A cm^{-2}) in all cases. Since $M = 56.5$ g mol^{-1} and $\rho = 7.96$ g cm^{-3} for SS316, this gives a value of the valency from Equation (6) of $n = 3.0 \pm 0.1$ (assuming 100% efficiency of the machining process). This is consistent with the previous interpretation [24] of dissolution of the majority component as Fe(III) under these conditions. The values of k obtained both from I_0 and from k/f^2 produced by the iterative fits to Equation (9) were

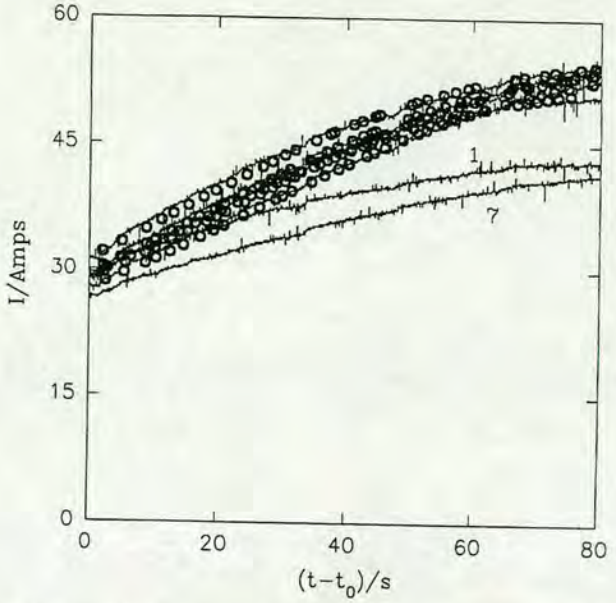

Fig. 8. Experimental current transient data (-) for segments 1–7 for ECM of SS316 at $V = 24$ V at an electrolyte flow rate of 22 dm^3 min^{-1}. Iterative fits to the current transient for segments 2–6 from Equation (9) are also shown (○). Segments 2–6 show a systematic decrease in I_0 with segment number. The transients for segments 1 and 7 are labelled.

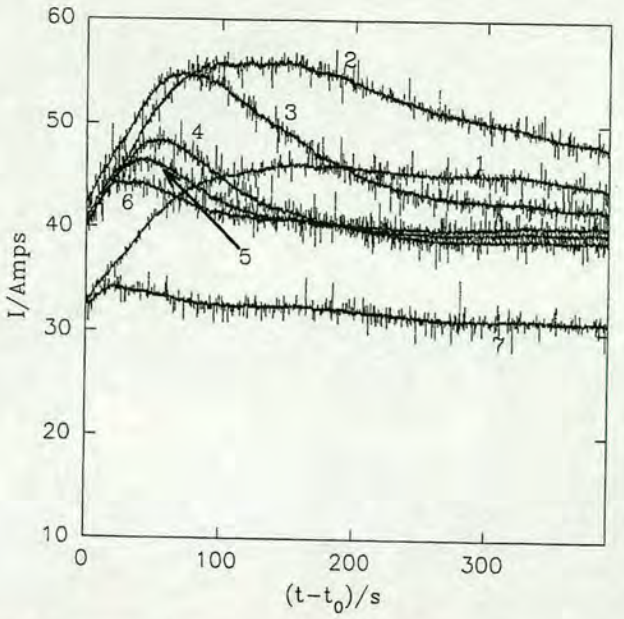

Fig. 9. Experimental current transient data (-) for segments 1–7 for ECM of SS316 at $V = 24$ V at an electrolyte flow rate of 16 dm^3 min^{-1}. The transient for each segment is labelled with the appropriate segment number.

observed to decrease by of the order of 10% from segments 2–6 (i.e. along the electrolyte path length), which is again sufficiently small to justify analysis with a constant κ for each segment. In contrast to the results for In718 in nitrate electrolyte, this is consistent with a small decrease in κ and/or an increase in V_0 along the electrolyte path length. For segments 1 and 7, $I_{n,\infty} = 44 \pm 1$ A, consistent with the calculated value from Equation (16) and $I_{n,\infty}$ of $I_{1,7,\infty} = 43 \pm 2$ A, which confirms that dissolution is occurring at the same valency across the whole of the workpiece surface. Substitution of the appropriate values of f^2/k, f, κ, ρ, V, M, n and F into Equation (5) gives a value of $V_0 = (12.4 \pm 0.5)$ V.

At slower flow rates, changes in valency are observed as expected (Figure 9). For $(t - t_0) \leqslant 150$ s, for segment 1, $I_{1,\infty}$=44 A and for segment 2, $I_{2,\infty}$= 57 A. This indicates that at equilibrium dissolution on these segments is occurring with $n = 3.0 \pm 0.1$ as before.

In contrast to segment 1, segment 7 shows very little change in ECM current with time, with $I_{7,\infty} = 31$ A. Since $I_\infty \propto n$ when comparing like segments, this corresponds to $n = 2.1 \pm 0.1$, entirely consistent with the previous interpretation of dissolution via Fe(II) downstream at low flow rates [24]. Furthermore, at times $(t - t_0) \geqslant 200$ s, a steady-state current of $I_{n,\infty} = 39 \pm 1$ A is established for segments 4–6, which also corresponds to $n = 2.1 \pm 0.1$, confirming that at these times for these segments dissolution occurs at this lower valency.

When comparing the current–time transients for segments 2–6, it is clear that there is a change in valency with time. Segment 2 shows a steady decrease in equilibrium current from $(t - t_0) \approx 160$ s onwards, attributable to a change in valency from $n = 3.0$ towards $n = 2.1$. Segments 3–6 show similar decreases, with significant deviation from the segment 2 transient at $(t - t_0) \approx 70$, 50, 35 and 25 s respectively. This deviation marks the progression of the 'boundary' between the areas machining at different valencies, which indicates that the boundary is moving upstream from segment 7 with time. Furthermore, the relatively slow decrease in each segment current with time indicates that the change in valency is not instantaneous, as does the observation that a decrease in valency is occurring on several segments simultaneously. Eventually, even the most upstream of segments is affected by this process, as evidenced by the observed decrease in current on segment 1 from $(t - t_0) \geqslant 300$ s. Further evidence for a gradual change has been acquired by terminating these experiments at different times and examining the workpiece surface. A clear correlation between the observed currents and the nature of the underlying workpiece surface was observed. Those segments with $n = 3.0$ had an underlying workpiece surface which was shiny, whilst for those with $n = 2.1$, the surface was dull. Those workpiece sections dissolving with $3.0 > n > 2.1$ had patches of shiny and dull surface, with the proportion of dull surface increasing as $n \rightarrow 2.1$. (However, even when the surface appeared completely dull, valencies above $n = 2.1$ could still be observed, indicating the presence of some areas of dissolution at increased valency). These observations therefore indicate that dissolution with a valency of $n = 2.1$ occurs initially on segment 7, producing a dull surface, and that this dull surface spreads progressively upstream across the workpiece surface with time, replacing dissolution with a valency of

$n = 3.0$, which is the cause of the shiny surface. These experiments show that, contrary to previous suggestions [24], this change in surface finish and overall dissolution valency occurs relatively slowly and simultaneously across several segments. We are presently investigating the chemistry of this dissolution process.

4. Conclusions

The results show that modification of a planar ECM system [6] to incorporate a segmented tool allows the variation of ECM parameters to be measured along the electrolyte flow path length. Variations in the electrolyte conductivity (κ, due to changes in electrolyte composition and/or temperature) and in the dissolution valency (n) have been measured, and the use of overlapping end segments has allowed edge effects (or throwing power effects) to be monitored. Such measurements are crucial to the parameterisation of the ECM of long flow-path length processes for industrial applications. Furthermore, these measurements can be made during machining, allowing both temporal and spatial changes to be monitored and giving insight into the time-dependent and current and voltage dependent electrochemical processes occurring which give rise to the ECM parameters observed.

Acknowledgements

We wish to thank EPSRC for support and for the provision of a studentship for PSH. We also gratefully acknowledge the support of Alan Cannon and Rolls-Royce plc and of Mike Yardley and Doncasters plc.

References

1. D.G. Risco and A.D. Davydov, *J. American Soc. Mech. Eng.* **64** (1993) 701.
2. M.A. ElDardery, *Int. J. Machine Tool Des. Res.* **22(3)** (1982) 147.
3. B. Kellock, *J. Machinery Product. Eng.* **140(3604)** (1982) 40.
4. O.V.K. Chetty and R.V. Murthy Radhakrishan, *Trans. of the ASME J. Eng. Ind.* **103(3)** (1981) 341.
5. A.R. Mileham, S.J. Harvey and K.J. Stout, *J. Wear* **109** (1986) 207.
6. A.R. Mount, K.L. Eley and D. Clifton, *J. Appl. Electrochem.* **30** (2000) 447.
7. A.K. Karimov, *J. Soviet Aeronautics* **28(3)** (1985) 105.
8. A.G. Makie, *J. Mathematical Anal. Apps.* **117(2)** (1986) 548.
9. J. Kozak, L. Dabrowski, K. Lubkowski and M. Rozenek, *Proc. 13th. Int. CAPE Conf.*, (Warsaw, 1997) p. 311.
10. H. Tipton, *Proc 5th Int. Confer. Adv. Machine Tool Des. Res.* (1964) 509.
11. A.D. Davydov and V.D. Kanshcheev, *Elektronnaya Obrabotka Materialov* (1985) 80.
12. H. Hardesty, A.R. Mileham and H. Shirrani, *Proc. Inst. Mech. Engrs.* **211B** (1997) 197.
13. O. Narayanan, S. Hinduja and C.F. Noble, *Int. J. Mach. Tool Des. Res.* **26** (1986) 323.
14. V.K. Jain and P.C. Pandey, *Precision Engr.* **2** (1980) 195.
15. G.M. Alder, D. Clifton and F. Mill, *Proc. Inst. Mech Engrs.* **214B** (2000) 745.
16. W.G. Clark and J.A. McGeough, *J. Appl. Electrochem.* **7** (1977) 277.
17. J. Hopenfield and R.R. Cole, *J. Eng. Ind.* **88** (1966) 455.
18. J. Hopenfield and R.R. Cole, *J. Eng. Ind.* **91** (1969) 755.
19. A.P. Shulepov, A.V. Kaptsov, V.A. Shmanev and V.G. Filimoshin, *Sov. Surf. Eng.* **5** (1987) 78.
20. D. Landolt, *J. Electrochem. Soc.* **119** (1972) 708.
21. M. Datta and D. Landolt, *Electrochim. Acta* **25** (1980) 1263.
22. D. Landolt, *J. Electrochem. Soc.* **119** (1972) 708.
23. M.A. Bejar and F. Gutierrez, *J. Mater. Processing Tech.* **37** (1993) 691.
24. P.J. Moir and S.J. Harvey, *Proc. of 16th Matador Conference* (1976) 275.
25. A.R. Mileham, R.M. Jones and S.J. Harvey, *Production Points, Precision Eng.* **4** (1982) 168.

ELSEVIER

Journal of Materials Processing Technology 6670 (2003) 1–6

Journal of Materials Processing Technology

www.elsevier.com/locate/jmatprotec

An integrated strategy for materials characterisation and process simulation in electrochemical machining

A.R. Mount[a,*], D. Clifton[b], P. Howarth[a], A. Sherlock[b]

[a]*Department of Chemistry, King's Buildings, West Mains Road, Edinburgh EH9 3JJ, UK*

[b]*Department of Mechanical Engineering, King's Buildings, West Mains Road, Edinburgh EH9 3JJ, UK*

Abstract

The analysis of current transients during electrochemical machining (ECM) at a planar workpiece planar tool configuration results in the determination of the important parameters for the ECM process. These have been used in finite difference simulation of the ECM process, which allows simulation of the current transients and tool and workpiece configurations at any time for non-planar configurations more applicable to industrial ECM. Small differences in the simulated and experimentally observed current transients are often observed, which can be attributed to variation of the combined ECM parameter k with current and electrolyte flow path length. Measurement of these variations has been achieved for In718 by current transient analysis of experimental data obtained from the ECM of a planar workpiece–planar segmented tool configuration. Variations in valency have also been measured for SS316 using this configuration. This information has then been used to improve the finite difference simulation. This approach has been shown to increase the accuracy of both materials characterisation and process simulation in ECM.

Keywords: Electrochemical machining; Characterisation; Finite difference; Process simulation

1. Introduction

Recent technological advances have lead to an increasing number of applications for high strength, low weight, metallic and intermetallic alloys. This has in turn led to an increasing requirement for metal cutting and forming processes able to cope effectively with such materials. Conventional milling or turning procedures can be problematic, as the necessarily high cutting forces often result in imperfections in shape and/or structure. They can also be uneconomic due to high tool wear and low machining rates. In electrochemical machining (ECM), the metal alloy (the anode or *workpiece*) is removed by electrochemical oxidation and dissolution, by applying a voltage which induces a current between the workpiece and a counter electrode (the cathode or *tool*). During this process the tool is advanced towards the workpiece at a controlled rate in an electrolyte solution, and control of the resulting workpiece form is achieved by ensuring migrational mass transport and using an appropriately shaped tool. For these advanced alloys, this has the advantages over many shaping processes of being able to machine efficiently despite their hardness and being able to produce complex shapes at high metal removal rates. Also, as the process involves controlled oxidation and dissolution of the metal from all points on the surface, with little increase in surface temperature, a high quality surface is produced without residual stresses or surface damage to the microstructure [1–5]. However, despite these advantages, ECM has yet to become the manufacturing process of choice for these systems. This is due in large part to the difficulty in predicting the tool shape and machining parameters necessary to produce a given workpiece profile. This problem can be considered in two parts; the generation and measurement of machining parameters for a particular workpiece–electrolyte system and the development of a simulation or modelling procedure [7–11] into which these parameters can be input in order to produce the required tool form for any given workpiece shape. In this paper, a method for determining ECM machining parameters by current transient measurements using a planar workpiece–planar tool system is presented. The application of these parameters to the machining of more complicated shapes is also considered by comparing simulated data obtained using a finite difference technique with data obtained experimentally.

* Corresponding author.
E-mail address: a.mount@cd.ac.ak (A.R. Mount).

0924-0136/03/$ – see front matter © 2003 Published by Elsevier Science B.V.
doi:10.1016/S0924-0136(03)00115-8

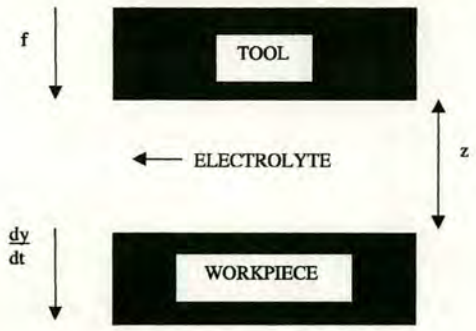

Fig. 1. The configuration for ECM.

2. Theory of current transients in the planar machining configuration

The theory for the analysis of current transients obtained using a planar workpiece–planar tool configuration has been detailed elsewhere [12]. For this system, the schematic set-up is as shown in Fig. 1.

The planar tool is fed at a constant feed rate, f, towards the workpiece, which is machining at a rate $\mathrm{d}y/\mathrm{d}t$. Electrolyte flows rapidly through the tool–workpiece gap. At long times or $t \to \infty$ (equilibrium), the separation of the electrodes, z, is z_∞ and $f = \mathrm{d}y/\mathrm{d}t$. The planar tool is of area A and moves towards a planar parallel workpiece, also of area A. It is assumed that the current is governed by migration (an essential assumption for stable machining). The simplest case is where the electrolyte is being pumped through the interelectrode gap (IEG) at high enough flow rate that the build up of machining products and/or the loss of ions from the electrolyte does not significantly affect the electrolyte conductivity, which can therefore be assumed to remain constant across the tool and workpiece throughout the experiment. Since the gap between the electrodes is z, and the applied voltage is generally sufficient for the establishment of field lines perpendicular to the electrodes, the migrational current across the electrolyte, I, is given by:

$$I = \frac{\kappa(V - V_0)A}{z} \tag{1}$$

where V is the applied voltage, V_0 the voltage required at the two electrodes to drive the reaction and κ the conductivity of the electrolyte. Assuming that this current produces solely workpiece dissolution, this current is also the dissolution current of the workpiece, and therefore

$$I = \left[\frac{nFA\rho}{M}\right]\frac{\mathrm{d}y}{\mathrm{d}t} \tag{2}$$

where n is the number of electrons transferred per dissolving atom (the "valency"), F the Faraday (96,487 C mol^{-1}), ρ the density of the workpiece material, $\mathrm{d}y/\mathrm{d}t$ the thickness of workpiece removed per unit time and M the average molecular weight (the mass of 1 mol of the workpiece material with the workpiece composition). The change in the inter-electrode distance, z, is given by:

$$\frac{\mathrm{d}z}{\mathrm{d}t} = \frac{\mathrm{d}y}{\mathrm{d}t} - f = \frac{k}{z} - f \tag{3}$$

where

$$k = \left(\frac{\kappa(V - V_0)M}{nF\rho}\right) \tag{4}$$

For I_∞ (I when $t \to \infty$), a constant current is reached and z remains constant at z_∞ as $\mathrm{d}z/\mathrm{d}t = 0$; hence $f = \mathrm{d}y/\mathrm{d}t = k/z_\infty$. Thus

$$\frac{I_\infty}{A} = \frac{nF\rho f}{M} \tag{5}$$

and

$$\frac{\mathrm{d}z}{\mathrm{d}t} = k\left[\frac{1}{z} - \frac{1}{z_\infty}\right] \tag{6}$$

This equation can be integrated from $t = i$, $z = z_i$ to $t = t$, $z = z$, to give

$$\ln\left[\frac{z_\infty - z_i}{z_\infty - z}\right] + \frac{z_i - z}{z_\infty} = \frac{k(t - t_i)}{z_\infty^2} \tag{7}$$

or from Eq. (1)

$$\ln\left[\frac{1 - (I_\infty/I_i)}{1 - (I_\infty/I)}\right] + \left[\frac{I_\infty}{I_i} - \frac{I_\infty}{I}\right] = \frac{k(t - t_i)}{z_\infty^2} = \frac{f^2(t - t_i)}{k} \tag{8}$$

where I_i, I_∞ and I are the initial current, the equilibrium current and the current at $t = t_i$, ∞ and t, respectively. Judicious choice of these currents allows analysis of ECM parameters to obtain values of f^2/k and I_i.

3. Experimental

The experimental apparatus used in these measurements is as detailed in [6]. The solution flow was controlled by means of a Hydriacell D25 pump (Wanner Engineering); the flow sensor was a type FT 13 (Platon Instrumentation) and the current transducers were of type HT (RS components). The data were collected using a 486 PC (Viglen) and Intelligent Instruments (Burr-Brown) in house data logging system combined with the Visual Designer software (Intelligent Instruments). The experimental set-up involved a reservoir of 60 l of electrolyte, thermostatically controlled at 30 °C. The planar anode, or workpiece, was of width 1.20 cm and length (along the electrolyte flow path) 4.00 cm, giving a total area of 4.80 cm^2. The planar single tool was a copper–tungsten alloy of the same dimensions and area. Experimental feed rates, f, were set at 1.00 mm min^{-1} throughout unless otherwise stated.

4. Electrochemical machining

Fig. 2 shows typical current transient data for the machining of In718 alloy. In this figure, currents are reported as

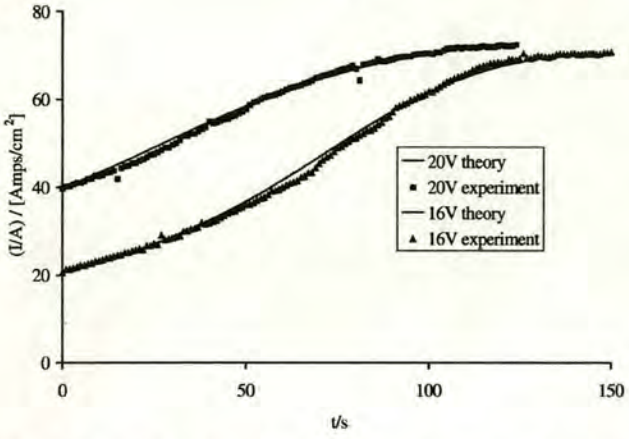

Fig. 2. Comparison of typical theoretical and experimental current transients for the ECM of In718 at applied voltages of 16 and 20 V, with an electrolyte of 21.7% (w/v) of aqueous sodium nitrate, flowing at 20 l min^{-1} and $f = 1.0$ mm min^{-1}.

current densities, I/A and the initial gap between the tool and the workpiece was 0.80 mm. Theoretical data were produced by iterative fitting to Eq. (8), with values of $t = i$ and I_i being fixed at the experimental values as close to the application of the machining voltage as possible, when stable machining started to occur. As with all other ECM current transients in this paper, time, t, is measured with respect to this chosen value of t_i. Iterative error minimisation involved using the experimental currents, I, to iteratively minimise the error in the calculated values of t from Eq. (8) with respect to the experimental times, t.

It is clear that this process produces close agreement between experiment and theory. Furthermore, values of I_∞ and f^2/k are produced for each iterative fit. As expected from Eq. (5), for a constant feed rate (in this case $f = 1.0$ mm min^{-1}) I_∞/A was found to be independent of applied voltage at 70 ± 2 A cm^{-2} for In718. As $\rho = 8.228$ g cm^{-3} and $M = 59.79$ g mol^{-1} in this case, this gives a constant value for the valency of $n = 3.0 \pm 0.2$.

The values of the parameters f^2/k and I_i are also important, as they can be used to determine a value for V_0. This is shown in Fig. 3, where k/f^2 and I_i have been plotted as a function of the applied voltage, V, for both chloride and nitrate electrolytes. Each of these electrolyte concentrations is equivalent, at 2.56 mol dm^{-3}. t_i was again chosen to be as close as possible to the onset of stable machining, to ensure that $z_i = 0.80$ mm (the initial gap) in each case.

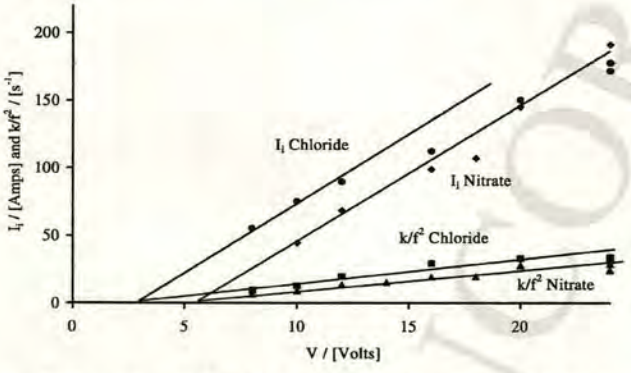

Fig. 3. Plot of I_i and k/f^2 against the applied voltage, V, for 21.7% (w/v) aqueous sodium nitrate and 15% (w/v) aqueous sodium chloride electrolyte.

From Eqs. (1) and (4), both k/f^2 and I_i should be proportional to $(V - V_0)$. Thus for each electrolyte, as V_0 is relatively insensitive to changes in V [12], if there is no change in surface reaction, both lines should intercept at a common V-axis intercept of V_0. This is clearly the case for the nitrate electrolyte, where an intercept of $V_0 = 5.4 \pm 0.4$ V is obtained. The low V data for chloride also show similar behaviour, with an intercept of $V_0 = 3.0 \pm 0.4$ V. The gradients of each of the lines can be used to determine a value for the conductivity of the electrolyte, κ, which was found to be 20 ± 1 S m^{-1} for both the nitrate and chloride electrolytes. This is consistent with previous measurements on these electrolytes [13]. However, at high V, both the k/f^2 and I_i data for chloride show systematic deviations from their lines, which indicates a significant increase in V_0. This can be attributed to a change in the nature of the anodic dissolution reaction.

5. Finite difference simulation of non-planar ECM configurations

It is important to assess whether these ECM parameters obtained from a planar machining configuration can be generalised to more typical non-planar configurations and other tool feed regimes. A 2D simulation of the ECM process was therefore undertaken using a time-stepped finite difference approach. It is assumed that changes in the electric field distribution within the gap occur much faster than any changes in the geometry. Thus the Laplace field equation can be solved using the finite difference method for a fixed tool and workpiece geometry. The tool and workpiece geometries are represented by interpolation splines. At each node of the workpiece spline the derivative of the potential in the direction normal to the surface is calculated. From this the current density and hence the removal rate according to Faraday's laws is calculated. Thus the change in the workpiece geometry for a small time-step Δt can be calculated. The workpiece spline is then reformed for the new geometry ready for the next time-step. This can be repeated for as long as necessary, often until equilibrium machining occurs (as evidenced by the attainment of a constant current and the invariance of the workpiece shape with time). This process simply requires the input of the ECM parameters V_0, n, κ obtained from the planar ECM configuration experiments, plus the appropriate values of z_i, V, A and f for the experiment. Fig. 4 shows as an example of the calculated and experimentally observed current transients obtained for ECM of a planar In718 workpiece in 15% (w/v) aqueous sodium chloride electrolyte using a stepped tool. In this example the feed rate, f, was also increased from 0.5 to 0.8 mm min^{-1} during the transient.

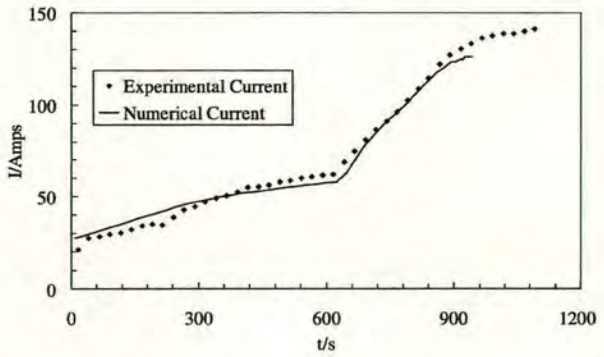

Fig. 4. Comparison of experimental and numerical current transients for a planar In718 workpiece using 15% chloride electrolyte and a stepped tool with an applied voltage of 16 V.

The reasonable agreement between the numerical and experimental current transients demonstrates the success of this approach. Furthermore, this procedure allows comparison between the numerical and experimental workpiece shapes at equilibrium machining. This is shown in Fig. 5, along with the tool shape used in these experiments. Again, reasonable agreement between numerical simulation and experiment can be seen. The small deviation observed between theory and experiment shown in Figs. 4 and 5 is most likely attributable either to changes in V_0 or κ with ECM current or to changes in these parameters along the electrolyte flow path length. Improved simulation would therefore require measurement of these parameters as a function of these variables. The former effect has been measured by iterative fitting of small sections of the current transient (for which V_0 and κ can be assumed to be constant) to Eq. (8) [12]. The latter has been studied by the use of a segmented tool (Section 6).

6. Planar segmented tool–planar workpiece ECM system

At slower flow rates and higher ECM currents, the consumption and production of ions during ECM would be expected to change significantly the composition of the electrolyte, which may result in variation in the ECM parameters along the flow path. In order to study this, a planar segmented tool system has been constructed, as shown in Fig. 6 [14]. Here the planar tool is divided into seven distinct segments of similar area along the flow path length, each separated by a relatively thin insulating gap.

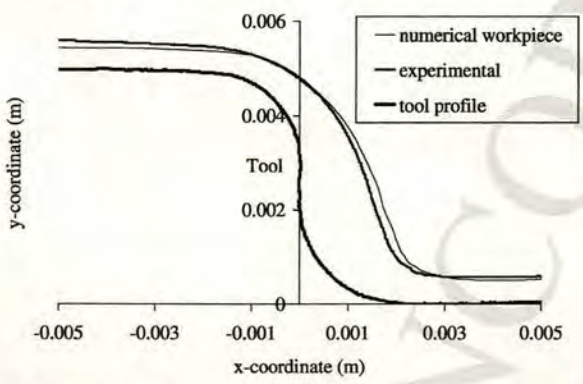

Fig. 5. Tool profile and numerical and experimental workpiece profiles for the In718 ECM experiment in Fig. 4.

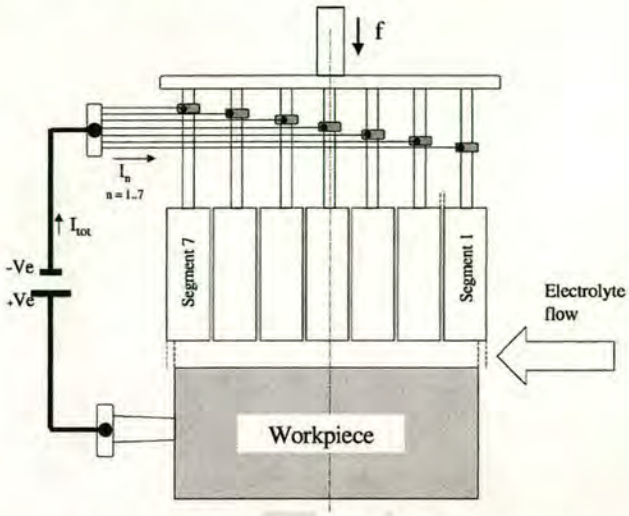

Fig. 6. The planar segmented tool–planar workpiece system.

The ECM current through each segment, I_n, is measured individually during the experiment, with n having values from 1 to 7 for the seven segments. Segment 1 corresponds to the most upstream segment in the electrolyte flow and Segment 7 the most downstream. Fig. 7 shows a typical response for the ECM of In718 in 21.7% sodium nitrate using this system.

As expected, Segments 2–6 produce current transients that can be fitted to Eq. (8), using the appropriate value of the area, A, of each segment, and each gives the same value of I_∞ within experimental error, indicating no significant change in valency across the workpiece surface. However, the values of I_i (and k/f^2 produced from the iterative fits) can be seen to show a small but significant increase with

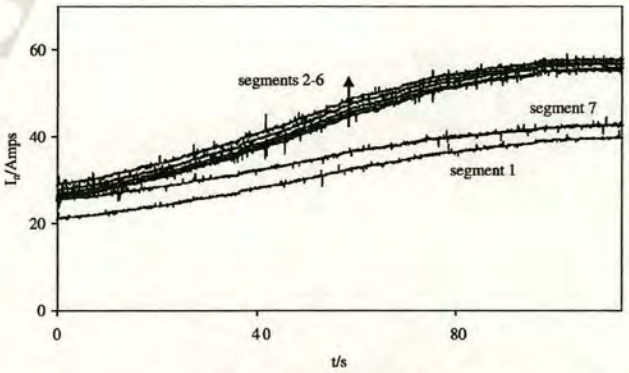

Fig. 7. Segment current transients for the ECM of a planar In718 workpiece in 21.7% nitrate. The applied voltage, V, was 20 V, the starting gap was 0.8 mm and the electrolyte flow rate was 16 l min^{-1}.

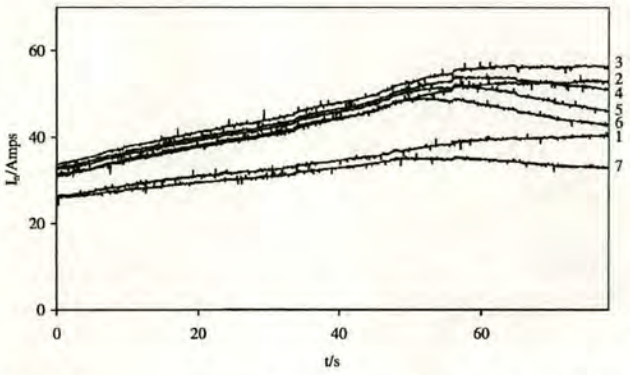

Fig. 8. Segment current transients for the ECM of a planar SS316 workpiece in 15% sodium chloride electrolyte. The segment numbers for each transient are shown to the right of the diagram.

increasing segment number, indicative of an increase in the value of k. This is most likely due to a small but significant increase in κ, which can be attributed to the production of soluble ionic products (metal ions at the workpiece, hydroxide ions at the tool) along with a small increase in the electrolyte temperature along the path length in the IEG due to resistive heating [15,16]. In this case these effects clearly outweigh the decrease in κ which would be expected if the hydrogen gas evolved at the tool produced a significant accumulated void fraction in the electrolyte [17]. It should be noted that Segments 1 and 7 produce different current transients. This is because they overlap the workpiece edges (Fig. 6). This produces a lower effective area and hence equilibrium current for these two segments compared to Segments 2–6. Furthermore, there is significant contribution from non-perpendicular field lines between the overlapping portion of Segments 1 and 7 and the workpiece edge at larger values of z. As a result, the workpiece edges become rounded during machining and the current transients for Segments 1 and 7 show a different form from Eq. (8), which has been considered elsewhere [14]. Despite this difference in form, the increased value of I_i for Segment 7 compared with Segment 1 can still clearly be seen in Fig. 7, which confirms the increase in k measured for the other segments along the flow path length.

The segmented tool can also be used to study ECM under conditions where a change in valency occurs along the electrolyte path length. A good example is the ECM of the stainless steel SS316 (EN 58J) in sodium chloride electrolyte. Previous measurements [18,19] have shown that a valency change, attributed to a change in dissolution valencies from Fe(III), Cr(VI) to Fe(II), Cr(III) occurs and that under suitable conditions of electrolyte flow, feed rate, and applied voltage, equilibrium machining can produce two different zones of stable ECM machining, each with their own characteristic valency and surface finish. Fig. 8 shows typical current transients obtained for ECM of an SS316 workpiece using the planar segmented tool under conditions where this occurs, i.e. an applied voltage, V, of 25 V, a starting gap of 0.8 mm and an electrolyte flow rate of 16 l min^{-1}.

As for In718, a small increase in κ is observed along the electrolyte path length at early times. However, as machining progresses and the current increases and the value of z decreases, a critical point is reached for segments further down the flow path where the valency decreases, as evidenced by the decrease in the machining current. This is consistent with previous observations [18]. It is clear from these data that this decrease occurs earliest on Segment 7 and progressively later with decreasing segment number, with little discernible change in valency for Segment 1 throughout its transient. This suggests that this change in valency is as a result of the change in electrolyte composition along the path length as a result of machining. Furthermore, the change can be seen to be progressive, with the valency decreasing smoothly, rather than stepping from one limiting value to another. Such observations allow the valency to be determined as a function of electrolyte path length and ECM current across the workpiece.

7. Conclusions

The use of a planar workpiece planar tool configuration to measure and analyse current transients allows the determination of the parameters important in ECM. Segmentation of the tool allows the dependency of these parameters on electrolyte flow length to be determined. Using finite difference process simulation, it has been shown that these parameters can then be used in the simulation of non-planar configurations applicable to practical ECM. Together, this forms an integrated strategy for ECM characterisation and process development.

Acknowledgements

The authors would like to thank the British government funding body, EPSRC, Rolls-Royce plc and Doncasters plc for providing the funding for this work. Thanks also go to Mikel Agirre for carrying out some of the experiments on the stepped tool.

References

[1] D.G. Risco, A.D. Davydov, J. Am. Soc. Mech. Eng. 64 (1993) 701.
[2] M.A. ElDardery, Int. J. Mach. Tool Des. Res. 22 (1982) 147.
[3] B. Kellock, J. Mach. Prod. Eng. 140 (3604) (1982) 40.
[4] O.V.K. Chetty, R.V.M. Radhakrishan, Trans. ASME J. Eng. Ind. 103 (3) (1981) 341.
[5] A.R. Mileham, S.J. Harvey, K.J. Stout, J. Wear 109 (1986) 207.
[6] W. Konig, T.H. Aachem, J. Humbs, Ann. CIRP 25 (1977) 83.
[7] Y. Zhou, J.J. Derby, Chem. Eng. Sci. 50 (1995) 2679.
[8] R. Butt, J. Comput. Appl. Math. 47 (1993) 151.
[9] V.K. Jain, P.C. Pandey, Precis. Eng. 2 (1980) 23.

[10] H. Hardisty, A.R. Mileham, H. Shivani, Proc. Inst. Mech. Engrs. B 211 (1997) 197.
[11] H. Hardisty, A.R. Mileham, Proc. Inst. Mech. Engrs. B 213 (1999) 787.
[12] A.R. Mount, K. Eley, D. Clifton, J. Appl. Electrochem. 30 (2000) 447.
[13] C.N. Larsson, in: A.E. De Barr, D.A. Oliver (Eds.), Electrochemical Machining, MacDonald, London, 1968, p. 108.
[14] A.R. Mount, P.S. Howarth, D. Clifton, J. Appl. Electrochem., submitted for publication.
[15] W.G. Clark, J.A. McGeough, J. Appl. Electrochem. (1977) 277.
[16] J.F. Thorpe, R.D. Zerkle, J. Mach. Tool Des. Res. 9 (1969) 131.
[17] J. Hopenfield, R.R. Cole, J. Eng. Ind. 88 (1966) 455.
[18] P.G. Moir, J. Harvey, Proceedings of 16th MATADOR Conference, 1976, p. 275.
[19] A.R. Mileham, R.M. Jones, S.J. Harvey, Precis. Eng. 4 (1982) 168.

Journal of The Electrochemical Society, **150** (3) D63-D69 (2003)
0013-4651/2003/150(3)/D63/7/$7.00 © The Electrochemical Society, Inc.

The Electrochemical Machining Characteristics of Stainless Steels

A. R. Mount,[a,z] P. S. Howarth,[a,*] and D. Clifton[b]

[a]*Department of Chemistry,* [b]*Department of Mechanical Engineering, University of Edinburgh, King's Buildings, Edinburgh, EH9 3JJ, UK*

A systematic study of a variety of stainless steels [SS316, SS410, Jethete (J), Duplex (D), and Super Duplex (SD)] has been performed, measuring their electrochemical machining (ECM) characteristics in chloride and nitrate electrolytes. Theoretical current/time analysis using a segmented tool was used to determine the dissolution valencies, n, and overpotentials, V_0, along the flow path length. Electrolyte samples from the interelectrode gap, taken at intervals along the flow path, and the bulk were analyzed for conductivity, pH, and visible absorption. The results indicate that the ECM dissolution characteristics of stainless steels are controlled by the surface oxide structure, which is primarily determined by the chromium content. Typically, the high chromium steels D and SD were found to machine with high primary elemental valencies (consistent with $n_{Fe} = 3$ and $n_{Cr} = 6$), resulting in the production of soluble CrO_4^{2-}. However, for the low chromium steels J and SS410, low valency dissolution (consistent with $n_{Fe} = 2$, $n_{Cr} = 3$) occurred with chloride electrolyte, and this was also found for the intermediate chromium steel SS316 at low electrolyte flow and recycled electrolyte. These results have been explained by the disruption caused to the surface barrier oxide layer by chloride ions and solid ECM products, which allow low valency dissolution to take place. Significant accumulation of these products occurred when performing electrolyte recycling, which is commonly used in industry.
 [DOI: 10.1149/1.1545463]

Manuscript submitted February 13, 2002; revised manuscript received September 10, 2002. Available electronically January 31, 2003.

Electrochemical machining (ECM) is the process of metal removal by the electrochemical dissolution of a workpiece material. It has many potential advantages over traditional machining methods, particularly where high strength, low weight, metallic, and intermetallic alloys are used. It can machine a material irrespective of hardness without causing any undue stresses or surface damage. High machining rates and complex shapes are also possible.[1-5] ECM is carried out by passing a current (typically of the order of 100 A cm^{-2} to ensure industrially viable machining rates) between an electrode tool (cathode) and a workpiece (anode) across a gap through which an electrolyte is passed. The workpiece is then fed toward the tool as dissolution occurs at a controlled rate in order to maintain metal removal.

The ECM reaction induces progressive change in the electrolyte composition along the flow path length. This typically causes changes in the related physicochemical properties and hence changes in ECM dissolution characteristics along the flow path length. For example, changes in ECM gap along the flow path have been measured at constant applied voltage and attributed to electrolyte joule heating[6,7] and gas bubble formation at the tool.[8] However, there have not been corresponding measurements of chemical changes along the flow path length and their influence on the ECM characteristics. Furthermore, such measurements have been made after the termination of ECM, and hence provide a snapshot of the ECM characteristics on termination only, and not mapping of these characteristics throughout the ECM process.

This paper describes a novel ECM system which has been developed to enable such in-line physicochemical characterization of ECM along the flow path length. This uses chronoamperometry[9] to give direct measurements of the physical parameters which characterize ECM *i.e.*, electrolyte conductivity, overpotential, and workpiece valency.[10-14] A segmented tool is used[15] each electrode of which provides in-line information on these ECM parameters at a specified point along the flow path length, while electrolyte sampling (during ECM) along the flow path length provides corresponding chemical information.

Experimental data is also presented on the application of this system to the characterization of stainless steels (SS). Marked changes in the dissolution characteristics of SS 316 (SS316) have been measured[16,17] under ECM conditions (~100 A cm^{-2}), with a boundary along the flow path length being observed, delineating areas with different surface finishes, consistent with different dissolution mechanisms and different valencies. The position of the boundary was shown to be sensitive to electrolyte flow conditions, but these measurements were not in-line (and hence could not readily be used to map ECM parameters) and were not related to the chemistry of the ECM process. Similar variations in the electrochemical dissolution characteristics of iron, chromium, and lower chromium steel alloys have also been measured.[18] Although these were in-line measurements, they were at relatively low current densities (<30 A cm^{-2}) and did not attempt to probe the variation in observed physicochemical parameters along the flow path length.

This paper presents a systematic study of the physicochemical ECM parameters within the stainless steel family of alloys, probing the effect of changes in elemental alloy composition.

Experimental

The setup is as described in previous work.[9] The data was collected using a Dell PC containing an Intelligent Instruments (Burr-Brown) in-house data logging system. A reservoir of 60 L of electrolyte was used, initially at 30°C. The cell (Fig. 1) consisted of a planar workpiece (the alloy) moving at a constant feed rate, f, towards a parallel planar segmented tool of copper chrome. Each of these electrodes was of length 4.00 cm and width 1.50 cm, giving an overall area for each: $A = 6.00$ cm^2. The segmented tool had seven segments, independently powered and monitored, numbered with segment 1 at the electrolyte flow inlet and segment 7 at the flow outlet. Tubes (0.4 mm inside diam) enabled electrolyte sampling in the interelectrode gap (Fig. 1), at three positions along the flow path length [the inlet tube (IT) in the gap above segment 2, the middle tube (MT) above segment 4, and the outlet tube (OT) above segment 6]. Typical flows in these tubes were both calculated and measured as being less than 1% of the total electrolyte flow, ensuring sampling without significant perturbation of the electrolyte flow.

The electrolytes used were a 15.0 % w/v solution of sodium chloride or a 21.7% solution of sodium nitrate (each 2.56 mol dm^{-3}; Anderson, Gibb, and Wilson) as appropriate. Electrolyte conductivity was measured using a 4010 conductivity meter (Jenway). This incorporates a temperature probe such that all conductivity values are produced at a constant reference temperature of 25°C. The bulk conductivity of the sodium chloride and sodium nitrate electrolytes were measured as $\kappa = 0.20 \pm 0.1$ S cm^{-1} at 25°C, in good agreement with previous measurements.[9] pH measurements were performed using a Hydrus 300 digital meter (Fisherbrand).

* Electrochemical Society Student Member.
[z] E-mail: A.Mount@ed.ac.uk

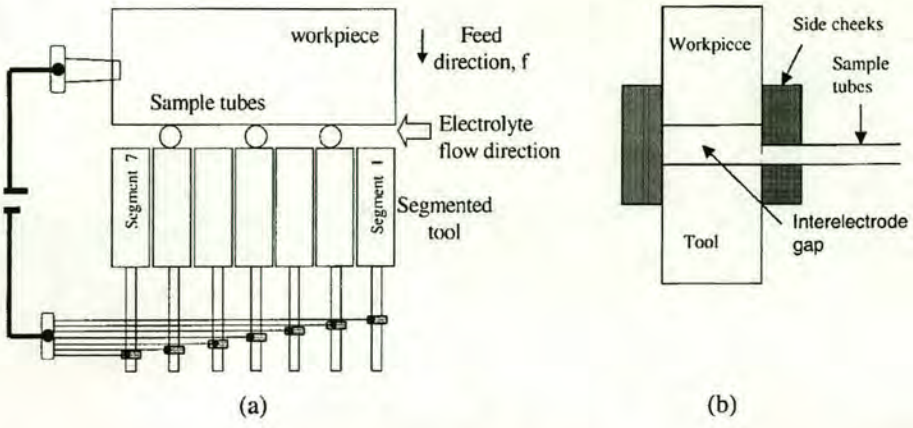

Figure 1. Experimental configuration of the segmented tool system (a) front view (b) end view from the end face of segment 7 (flow out of page). The positions of the tubes used to sample the flow are shown (○).

The workpiece materials studied were Jethete (J), SS 316 and 410 (SS316 and SS410), Duplex (D), and Super Duplex (SD), with compositions (atom w %) as given in Table I. The initial electrode gap was 0.80 mm, a constant voltage, $V = 24.0$ V, was applied between the tool and the workpiece and $f = 1.00$ mm min^{-1} unless otherwise stated. The electrolyte flow rate, U, was either 20.0 L min^{-1} (high U) or 8.0 L min^{-1} (low U) and the electrolyte was recycled (the typical industrial arrangement) unless otherwise stated. The planar segmented tool was calibrated as shown in previous work.[15] Iterative fits to the experimental I_n, t data for each segment, n, were performed using Eq. 1[9,15]

$$t = \frac{k}{f^2}\left[\ln\left(\frac{1 - \frac{I_{n,\infty}}{I_{n,0}}}{1 - \frac{I_{n,\infty}}{I_n}}\right) + \left(\frac{I_{n,\infty}}{I_{n,0}} - \frac{I_{n,\infty}}{I_n}\right)\right] + t_0 \quad [1]$$

where k is

$$k = \frac{\kappa M(V - V_0)}{nF\rho} \quad [2]$$

Analysis of the chronoamperometric transients was performed by nonlinear regression with iterative fitting to obtain k/f^2 (and hence k) and $I_{n,\infty}$[9] using the Levenberg-Marquardt algorithm in Origin 6.1 (OriginLab). To avoid charging effects, the initial time (t_0) and current ($I_{n,0}$) were chosen to be the earliest time after the voltage was applied when stable machining conditions were reached. It has been shown previously[15] that Eq. 1 can be applied to segments 2-6, as edge effects are unimportant and it can be assumed that there are normal field lines between the workpiece and the tool. In this case, the effective area of each segment includes one intersegment insulation region, of area 0.0075 cm^2. However, this equation does not always apply to the end segments 1 and 7,[15] so analysis of the variation of ECM parameters along the electrolyte flow path is confined to measurements on segments 2-6.

For each segment, the average valency, n, was calculated from the equilibrium machining current[9,15] using

$$n = \frac{I_{n,\infty}M}{AFf\rho} \quad [3]$$

The average valency can then be subdivided into individual valencies for each element in the alloy

$$n = \sum_i n_i x_i \quad [4]$$

An efficiency of 100% (a fractional efficiency, e, of 1) was assumed throughout the work presented here. There have been reports[6,19-21] that efficiencies below $e = 1$ are obtained in some cases at low U, in which case the numerator of Eq. 3 should include e. However, efficiency has been observed to increase with U and would be expected to approach $e = 1$ at U values lower than those used throughout this work.[15,19] Measurements on the nature and amount of the ECM products as a function of the ECM current have been used to test this assumption (see the section on characterization of the ECM products of SS). Furthermore, the relatively high U values employed in this work ensure that electrolyte flow effects on the current distribution are negligible.[8]

Results and Discussion

SS are iron chromium alloys, typically with greater than 10 atom wt % chromium. This chromium induces the formation of a protective oxide film on the metal surface. Since ECM dissolution characteristics would also be expected to be determined largely by the surface oxide layer, the steels are categorized in terms of their chromium content.

ECM of SD and D.—SD (25.58 % Cr) and D (23.00 % Cr) are both high chromium steels, with chromium contents greater than 20%. For each electrolyte and all segments (2-6), both steels machined with equilibrium currents which produce an overall valency,

Table I. Composition in atomic weight percent of SSJ, SS316, SS410, D, and SD.

Alloy	Fe	Cr	Ni	Mo	Mn	Cu	C	S	P	Si	N	V	W
J	80.63[b]	12.50[a]	3.00[a]	2.00[a]	0.90[a]	-	0.13[a]	0.02	0.03	0.35	0.04[a]	0.40[a]	-
SS410	85.50	12.75	0.23	0.01	0.72	0.08	0.14	0.02	0.04	0.49	0.02	-	-
SS316	70.09	17.00	8.00	2.50	2.00	-	0.12	0.05	0.05	0.02	-	-	-
D	63.52[b]	23.00[a]	6.50[a]	3.50[a]	2.00[a]	0.20[a]	0.03[a]	0.02[a]	0.03[a]	1.00[a]	0.20[a]	-	-
SD	61.20	25.58	6.98	3.57	0.63	0.60	0.02	-	0.02	0.47	0.26	-	0.65

[a] Maximum amount.
[b] Minimum amount.

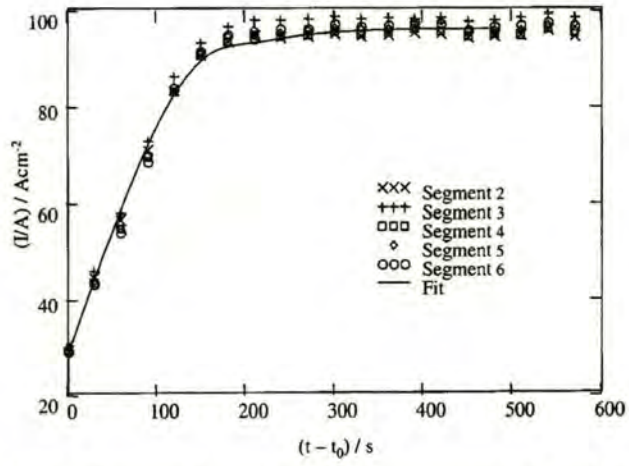

Figure 2. Experimental current transients for segments 2-6 for ECM of SD at low U with chloride electrolyte.

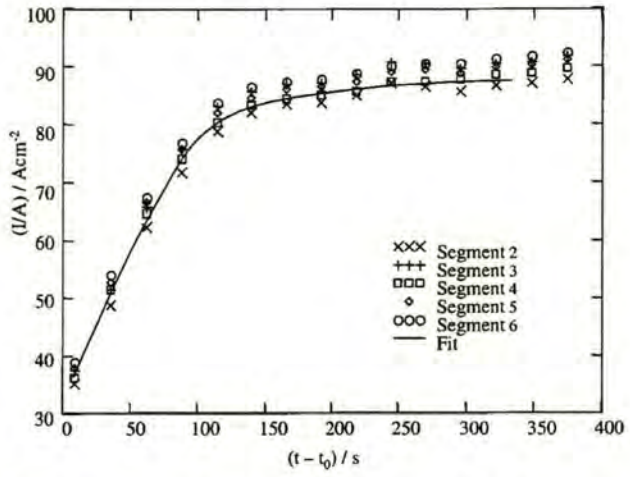

Figure 4. Experimental current transients for segments 2-6 for ECM of J at high U with nitrate electrolyte.

$n = 3.8 \pm 0.1$ (Fig. 2 and 3) across the entire workpiece surface. From Eq. 3 and 4, this is consistent with dissolution of iron in its high valency state [Fe(III),$n_{Fe} = 3$] and of dissolution of chromium in its high valency state [Cr(VI),$n_{Cr} = 6$], if it is assumed that the minor elements in the alloy (*i.e.*, all elements excluding Fe and Cr, Table I) dissolve with an average valency of $n = 3 \pm 1$. This is both chemically reasonable and consistent with previous interpretations of the ECM valencies of SS.[16,17] For these and all subsequent electrolyte and steel systems, substitution of the values of k/f^2, f, κ, ρ, V, M, n and F into Eq. 2 enabled V_0 to be calculated for each current/time transient. Representative values for these and all other steels are tabulated in Table III (vide infra).

ECM of J and SS410.—(12.50 % Cr) and SS410 (12.75 % Cr) are both low chromium steels, containing less than 15% chromium. When carrying out ECM with nitrate electrolyte, a valence of $n = 3.5 \pm 0.1$ was obtained for segments 2-6 for both materials (Fig. 4). This is again consistent with dissolution of iron and chromium in their high valence states [Fe(III), $n_{Fe} = 3$, and Cr(VI), $n_{Cr} = 6$] across the entire workpiece surface, as this value is within experimental error of the mean valence of $n = 3.4$ which would be expected if the minor elements in these steels dissolved with a chemically reasonable average valence of $n = 3$. However for chloride electrolyte, dissolution with a lower valence occurs (Fig. 5) giving $n = 2.1 \pm 0.1$, obtained from Eq. 3. Because iron is the major elemental component in these steels, this indicates that in this case iron dissolution is occurring in its low valence state [Fe(II), $n_{Fe} = 2$] and also suggests that chromium (and some of the minor elements) may be dissolving in lower valence states than with nitrate. It has been postulated previously[16,17] that Cr dissolves as Cr(III), $n_{Cr} = 3$ under these conditions. It is interesting to note that our results would be consistent with this postulation if the average valence of the minor elements were $n = 2 \pm 1$ (Table I).

ECM of SS316.—SS316 (17.00% Cr) contains an intermediate chromium content (between 15 and 20%). ECM with nitrate gives an average valence of $n = 3.6 \pm 0.1$ for segments 2-6 (Fig. 6). Within experimental error, this is again consistent with dissolution of iron and chromium in their high valence states [Fe(III), $n_{Fe} = 3$, and Cr(VI), $n_{Cr} = 6$], if the overall valence of the minor elements is $n = 3 \pm 1$. For chloride at high U, at short times, $(t - t_0) < 400$ s, (Fig. 7) a similar value of n within experimental error was obtained as for nitrate. However, at longer times [(t

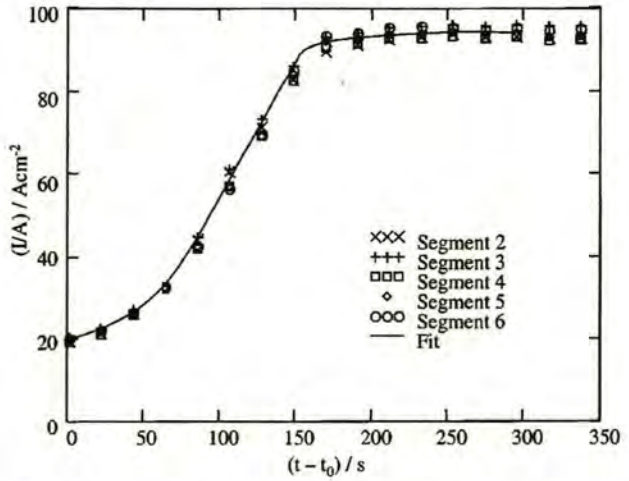

Figure 3. Experimental current transients for segments 2-6 for ECM of D at high U for nitrate electrolyte at a start gap of 1.6 mm.

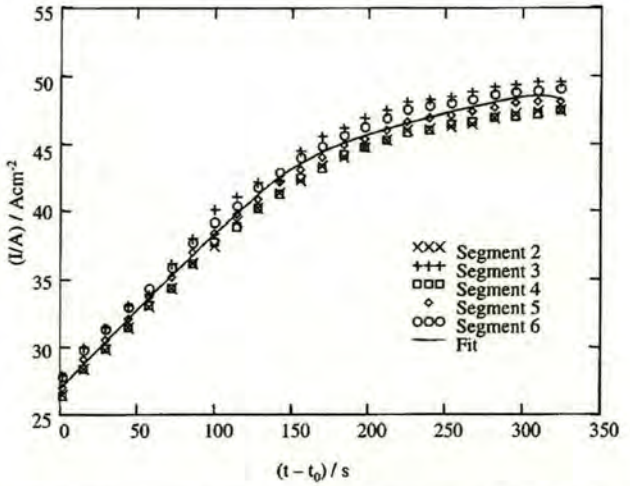

Figure 5. Experimental current transients for segments 2-6 for ECM of SS410 at high U with chloride electrolyte at a start gap of 1.6 mm.

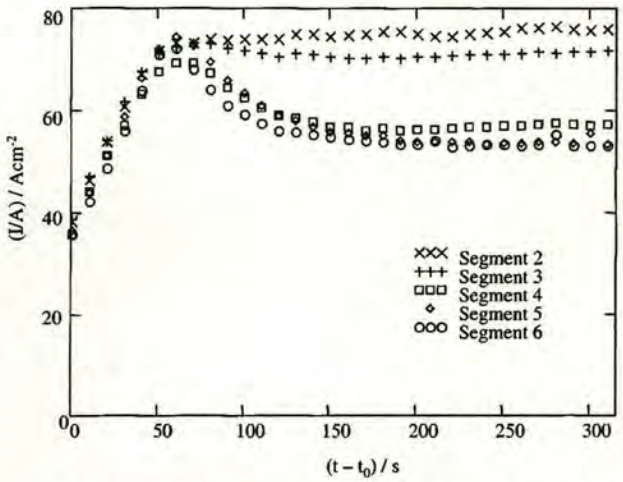

Figure 9. Experimental current transients for segments 2-6 for ECM of SS316 at low U with chloride electrolyte without recycling.

Characterization of the ECM products of SS.—Analyses of the electrolyte composition before ECM, along the flow path length during ECM (from IT, MT, and OT) and in the recirculating tank after ECM were performed. For all experiments and all samples, the conductivity of the electrolytes were measured as $\kappa = 0.20 \pm 0.1$ S cm^{-1} at 25°C within experimental error. These values are in agreement with those measured for bulk chloride and nitrate electrolyte previously both before and during ECM,[9] and indicate that conductivity is not a sensitive measure of the degree of product accumulation in these systems. This underlines the fact that significant conductivity changes would be expected only when there are significant differences in conductivity between reactants and products. Typical values of the pH of these electrolyte samples are given in Table II. The bulk pH of the electrolyte was typically found to lie in the range pH 8 ± 1 both before and after ECM experiments, consistent with the expected pH variation of the water supply. However, the pH of samples taken from IT, MT, and OT was often significantly outside this range. Although mixing of these electrolyte samples would be expected in these sample tubes, for those experiments with equilibrium gaps significantly greater than 0.4 mm, the tubes would sample electrolyte from closer to the tool surface than the workpiece; these pH values are shown in italics (Table II). They tend to be greater than those for experiments that sample electrolyte products from both the workpiece and the tool. This is to be expected, as at the tool the reduction reaction

$$H_2O_{(aq)} + e^- \rightarrow \frac{1}{2}H_{2(aq)} + OH^-_{(aq)} \quad [5]$$

will generate hydroxide ions and increasing the local pH. At the workpiece, the general reaction

$$M_{(s)} \rightarrow M^{n_m+}_{(aq)} + n_m e^- \quad [6]$$

occurs, with each metal ion, M, dissolving with its own characteristic valency, n_m. Subsequent metal oxide and hydroxide formation

$$M^{n_m+}(H_2O)_{y(aq)} \rightarrow M^{(n_m-x)+}(OH)_x(H_2O)_{y-x(aq)} + xH^+_{(aq)} \quad [7]$$

would then generate an acidic pH near the workpiece. Along the electrolyte flow path length, electrogenerated products will tend to convect and migrate from their respective electrode towards the opposite electrode. Away from the thin diffusion layer present at each electrode surface,[22] turbulent flow enhances this mixing, and the reaction

$$M^{n_m+}_{(aq)} + n_m OH^-_{(aq)} \rightarrow M(OH)_{n_m(s)} \quad [8]$$

would be expected to occur, producing soluble and insoluble metal hydroxides and (following dehydration) metal oxides. Such reactions would be expected to produce a significantly lower pH near the center of the gap compared to near the tool, as hydroxide ions are consumed. Overall, this would produce more acidic pH values for OT (and MT) than IT, if significant reaction according to Eq. 8 occurs within the sampling volume of the sample tube. Such increases in acidity are indeed found (Table II), indicating the importance of Eq. 8 within the interelectrode gap during ECM.

Visible absorption measurements have also been performed on IT, MT, and OT samples to identify and characterize absorbing metal dissolution products in the electrolyte. A typical series of absorption spectra for the electrolyte samples obtained during the equilibrium machining of SS410 in nitrate electrolyte are shown in Fig. 10. The close correspondence of these spectra to the visible absorption spectrum of a reference basic chromate ion (CrO_4^{2-}) solution (Fig. 10a) is strong evidence that chromate is present in each sample. For a constant current density and electrochemical reaction type across the workpiece surface, the concentration of stable products should increase linearly with flow path length. This linear increase in absorption is observed for samples IT, MT, and OT in Fig. 10b, c, and d. The increase in absorption between neighboring tubes, when compared with the absorption peak height of the chromate calibration solution of known concentration (Fig. 10a), gives an average increase in chromate concentration between neighboring tubes of $(1.4 \pm 0.1) \times 10^{-4}$ M. By considering f, U, ρ, M, and x_{Cr} for SS410, a theoretical increase in chromate concentration has been calculated between neighboring tubes as 1.5×10^{-4} M. This assumes no electrochemical reduction of accumulated chromate ion at the tool, which would lead to a reduction in this calculated value toward that observed experimentally. The reasonably close correspondence of this calculated value to the experimentally observed value indicates that chromate is the major chromium product of ECM dissolution in this case, and is stable in the electrolyte. This is consistent with the interpretation (the section on ECM of J and SS410) that $n_{cr} = 6$ and with the assumption that the efficiency of the ECM reaction, $e \approx 1$.

Furthermore, the bulk electrolyte CrO_4^{2-} concentration after one circulation was comparable to that obtained at OT, confirming the stability of the CrO_4^{2-} product. It is interesting that in contrast to nitrate, experiments with chloride electrolyte showed no detectable

Table II. A comparison of selected electrolyte sample pH values obtained when carrying out equilibrium ECM of steels under different flow regimes. The IT, MT, and OT sample tubes are located with their inside edge at the edge of the tool surface. At equilibrium gaps greater than the tube diameter (0.4 mm), the samples from these tubes will therefore be unrepresentative of the overall electrolyte composition in the gap and will be expected to contain more products from the tool reaction than the workpiece reaction. Gaps significantly less than 0.4 mm would be expected to contain more products from the workpiece reaction. Those samples with gaps greater than 0.4 mm are therefore shown in italics.

Steel/flow conditions and electrolyte	pH (IT)	pH (MT)	pH (OT)
D-high U, Cl	8.74	10.02	2.65
SD-high U, Cl	6.38	10.40	3.52
J-high U, Cl	*10.83*	*10.40*	*6.23*
J-high U, NO_3	*9.08*	*8.69*	*7.26*
SS410-high U, NO_3	*10.09*	*8.02*	*10.39*
SS410-high U, Cl	*10.58*	*10.37*	*9.47*
SS316-high U, NO_3	10.02	8.53	10.08
SS316-high U, Cl	10.59	11.42	2.75
SS316-low U, Cl	*11.50*	*11.68*	*7.02*

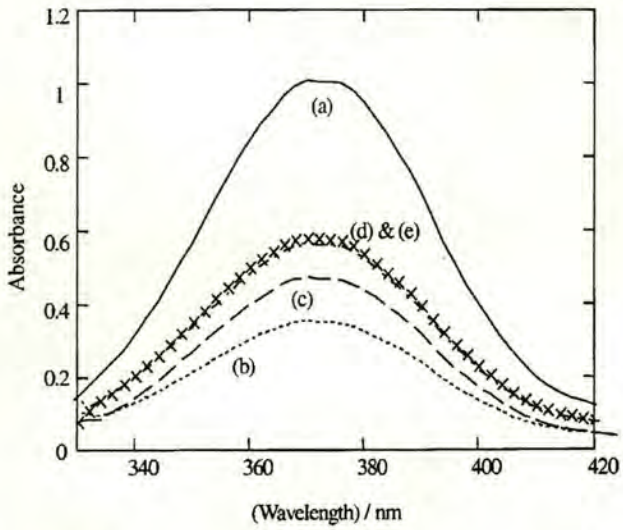

Figure 10. (a) The spectrum of 2.0×10^{-4} M CrO_4^{2-} in 5.0×10^{-3} M NaOH. Also shown is the visible absorption spectra of samples taken from the sample tubes (b) IT (c) MT (d) OT (e) bulk electrolyte after one complete circulation for ECM of SS410 at high U with nitrate electrolyte. These samples were diluted by a factor of 5.

absorption for chromate in any of the electrolyte samples, which suggests alternative chloro-substituted dissolution products.

The surface dissolution characteristics of SS.—Typical V_0 values obtained from ECM experiments on SS are presented in Table III. V_0 measures the total voltage required at both electrodes to drive the surface electrochemical reactions. However, given that the tool reaction is most likely Eq. 5 for all experiments, and that similar ECM currents are passed in all cases, the voltage required at the tool to drive Eq. 5 will be similar in all cases. Therefore, observed variations in V_0 can be related to changes in the voltage at the workpiece surface required to drive the workpiece dissolution reaction. These will comprise the surface overpotential required to drive the electrochemical reaction and an ohmic voltage term required to drive ion migration through any surface resistive film. For both nitrate and chloride electrolytes, the results in Table III are grouped in order of descending chromium content in the SS. For nitrate electrolytes, it is clear that relatively high V_0 values are obtained, which increase with increasing Cr content. Surface films on steels have been considered to consist of an oxide with two distinct regions; an inner oxide layer which is rich in chromium (and can be considered to consist predominantly of Cr_2O_3) and an outer, more hydrated layer richer in iron.[23,24] It is this inner, chromium-rich oxide layer that is considered to maintain the passivity of SS, as ion diffusion through the relatively unhydrated and defect-free chromium oxide layer is slow.[23,24] Increasing the Cr content would be expected to decrease ion mobility through this layer, increasing the voltage required to drive ECM dissolution, and increasing V_0 as observed.

Table III. Comparison of the V_0 values for the different materials under different flow regimes.

Steel	V_0/V	V_0 Segment 2/V	V_0 Segment 6/V
D-high U, NO_3	15.7 ± 0.5	14.3 ± 0.5	15.8 ± 0.5
SS316-high U, NO_3	9.7 ± 0.8	10.3 ± 0.8	9.8 ± 0.8
SS410-high U, NO_3	9.5 ± 0.8	9.9 ± 0.8	9.3 ± 0.8
J-high U, NO_3	7.5 ± 0.9	7.8 ± 0.9	7.3 ± 0.9
SD-low U, Cl	9.6 ± 0.8	8.5 ± 0.8	11.0 ± 0.7
D-low U, Cl	9.2 ± 0.8	7.9 ± 0.9	11.7 ± 0.7
SS316-high U, Cl[a]	5.7 ± 0.9	4.4 ± 1.0	6.3 ± 0.9
SS316-high U, Cl[b]	5.7 ± 0.9	4.8 ± 1.0	6.7 ± 0.9
SS410-high U, Cl	4.0 ± 1.0	4.2 ± 1.0	3.1 ± 1.1
J-high U, Cl	5.6 ± 0.9	4.2 ± 1.0	5.7 ± 0.9

[a] Results analyzed up to $(t - t_0) = 300$ s.
[b] The electrolyte was not recycled.

In comparison, although the corresponding V_0 values obtained when using chloride electrolyte show a similar pattern with Cr content, the value for each steel is significantly lower than with nitrate. It is known that chloride ions can insert into the surface oxide lattice, and it has been postulated that this produces both cationic and anionic lattice vacancies which enhance ion transport and dissolution rates, decreasing the effectiveness of the barrier layer[25,26] and reducing the voltage required for ion migration. Furthermore, as chloride has good ligating abilities it will tend to coordinate to the dissolving metal ions, resulting in chloro-coordinated products, with little chromate ion production (as observed in the section on characterization of the ECM products of SS). This will tend to decrease the overpotential required for dissolution. Both effects will produce the observed lowering of V_0. It is interesting that for the low chromium steels J and SS410, the lowest values of V_0 are obtained, and as a consequence, dissolution with reduced valence (as $n_{Fe} = 2$ and $n_{Cr} = 3$) occurs. This is characteristic of a surface which has lost effective barrier oxide protection. As expected, it is apparent that alloy chromium content and chloride electrolyte content have opposing effects on the surface oxide barrier effectiveness.

SS316 has intermediate chromium content and therefore appears to show ECM characteristics intermediate between those of low chromium and high chromium steels. It is likely that in this case, the chloride has sufficiently weakened the effectiveness of the barrier layer to allow pitting to occur. Initiation of pitting corrosion is considered to start by localized removal of the metal oxide barrier layer. This leads to the production of insoluble low valency metal chlorides, which precipitate onto the electrode surface,[27] hindering metal repassivation and leading to pit growth and an increased area of low valence dissolution. Harb[28] has investigated the effect of convection on the pitting behavior of SS, and has shown that high values of U favor the removal of the metal and chloride ions from the electrode surface, inhibiting metal chloride precipitation and promoting barrier oxide formation (repassivation), whereas low U favors metal chloride precipitation and pit growth. It is interesting that although these measurements were performed at U values, currents, and voltages much lower than in these studies, this explanation is consistent with the SS316 chloride ECM results. At high U, dissolution at high valencies ($n_{Fe} = 3$, $n_{Cr} = 6$) occurs, consistent with dissolution through an oxide layer (*i.e.*, a passivated surface). However, at low U, pitting corrosion and growth occurs, as shown by the growing importance of low valence dissolution (see the section on ECM of SS316).

Finally, it is worth considering what is the likely cause of the local removal of the surface oxide (the pitting event). Experimentally, pitting occurs at the downstream end of the workpiece at low U (the section on ECM of SS316) and has been shown to be most likely due to the accumulation of products of the ECM reaction (the section on Effect of electrolyte recirculation). In order to test whether dissolved or precipitated products were of importance, two experiments were performed. The first consisted of adding the insoluble metal oxide and hydroxide products produced as a result of Eq. 8 and obtained from filtering a recycled chloride electrolyte solution to a new chloride electrolyte solution (Fig. 11). At high U, a transition from high to low valence was observed, starting at the downstream edge of the electrode. The second experiment involved performing the same ECM experiment using as electrolyte the filtrate of the recycled chloride solution. In this case, at high U, the steel machined in a high valency state without any transition before 300 s as in Fig. 7. This is strong evidence that it is the solid products formed during ECM that are the cause of the pitting events. For the

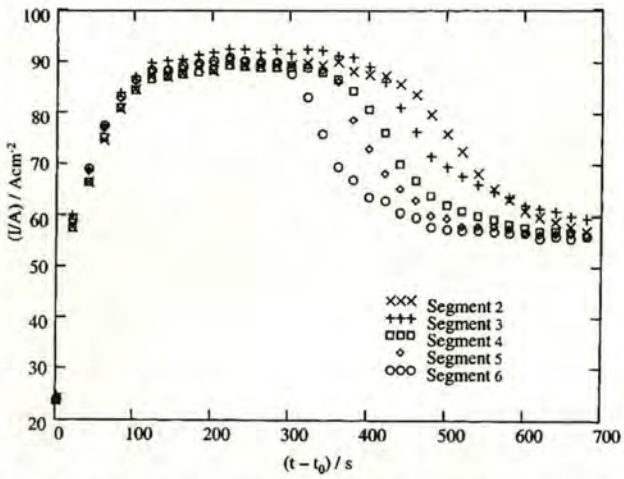

Figure 11. Experimental current transients for segments 2-6 for ECM of SS316 at high U with chloride electrolyte. In this experiment, solid products from a similar ECM experiment have been added to the electrolyte.

first experiment, it is interesting that the amount of solid product expected at the downstream edge of the electrode in this case is approximately the same as would be expected in the low U experiment (Fig. 8), which is consistent with the particles being the cause of the pitting events in both cases.

Beck and Chan[29] have produced a theoretical model analyzing the effect of convection on the growth of pits. They predict that the critical value of U, U_{crit}, below which pit growth occurs, depends upon the pit radius, r, as $r^{-4/3}$. This predicts that small pits should have a higher U_{crit} than large pits, which should effectively inhibit pit growth. However, this analysis does not allow for the lower value of U which can occur at the bottom of large pits, which has also been modeled[30] and has been shown to lead to the enhancement of pit growth. Thus pit growth may be dependent upon the initial formation of pits of a critical size.

The impingement of particles has previously been suggested as one mechanism by which surface oxide film damage may occur,[27] leading to pits of a critical size. Such damage may be as a result of the particle impacting with the surface. However, it may also be as a result of particles close to the surface inducing a local disturbance in the electrolyte flow, decreasing U to enable pit growth to a critical size.

Conclusion

These results indicate that the ECM dissolution characteristics of SS are controlled by the nature of the surface oxide, which is dependent primarily upon their chromium content. Addition of "aggressive" ions such as chloride to the electrolyte can disrupt this surface layer and reduce the effectiveness of this surface barrier. Insoluble products of the ECM reaction can also compromise this barrier under certain conditions, leading to pitting corrosion and low valency dissolution. This is important in recycled electrolyte systems, which are typically used industrially. Although consideration of chromium content is of primary importance, it is known that the minor elements in the steels such as nickel also have some influence on surface oxide structure and stability. The influence of these elements on ECM dissolution appears to be minor; however determination of the effects, if any, of these elements would require the study of a wider range of steels.

Although it is reassuring that similar processes have been previously proposed as occurring during steel dissolution, it is significant that these proposals were previously invoked to explain dissolution under much lower current and voltage conditions than those appropriate to ECM. Therefore, these results demonstrate that the experimental system described in this paper can be used for the systematic collection and analysis of electrochemical and chemical data for alloy dissolution under ECM conditions, allowing the measurement of the physicochemical characteristics along the flow path length and their temporal variation.

Acknowledgments

We wish to thank EPSRC for their support. We also gratefully acknowledge the support of Alan Cannon and Rolls Royce plc and of M. Yardley and Doncasters plc.

One of the authors, A. R. Mount, assisted in meeting the publication costs of this article.

List of Symbols

A	area of each electrode (segment or total)
F	Faraday constant
f	tool feed rate
I	current
I_0	the exchange current for the electrochemical reaction
M	average molecular mass of the workpiece
n	average valency of dissolving workpiece
n_i	valence of constituent workpiece element i
t	time
U	electrolyte flow rate
V	applied voltage
V_0	proportion of voltage required to drive electrochemical reactions at the electrodes (the effective overpotential)
x_i	mole fraction of constituent workpiece element i

Greek

κ	electrolyte conductivity
ρ	density of the workpiece material

Subscripts

∞	value as time approaches infinity
0	value at designated time zero
n	segment number

References

1. D. G. Risco and A. D. Davydov, *J. Am. Soc. Mech. Eng.*, **64**, 701 (1993).
2. M. A. ElDardery, *Int. J. Mach. Tool Des. Res.*, **22**, 147 (1982).
3. B. Kellock, *J. Machin. Product. Eng.*, **140**, 40 (1982).
4. O. V. K. Chetty and R. V. Murthy Radhakrishan, *Trans. ASME J. Eng. Ind.*, **103**, 341 (1981).
5. A. R. Mileham, S. J. Harvey and K. J. Stout, *J. Wear*, **109**, 207 (1986).
6. W. G. Clark and J. A. McGeough, *J. Appl. Electrochem.*, **7**, 277 (1977).
7. J. F. Thorpe and R. D. Zerkle, *Int. J. Mach. Tool Des. Res.*, **9**, 131 (1969).
8. J. Hopenfield and R. R. Cole, *J. Eng. Ind.*, **88**, 455 (1966).
9. A. R. Mount, K. L. Eley, and D. Clifton, *J. Appl. Electrochem.*, **30**, 447 (2000).
10. A. K. Karimov, *J. Sov. Aeronaut.*, **28**, 105 (1985).
11. A. G. Makie, *J. Math. Anal. Appl.*, **117**, 548 (1986).
12. J. Kozak, L. Dabrowski, K. Lubkowski, and M. Rozenek, in *Proceedings of the 13th International Computer-Aided Production Engineering Conference*, p. 311, June 9-14, 1997.
13. H. Tipton, in *Proceedings of the 5th International Conference on Advances in Machine Tool Design And Research*, University of Birmingham, (p. 509, Sept 1964).
14. A. D. Davydov and V. D. Kanshcheev, *Elektronnaya Obrabotka Materialov*, , 80 (1985).
15. A. R. Mount, P. S. Howarth, and D. Clifton, *J. Appl. Electrochem.*, **31**, 1213 (2001).
16. P. J. Moir and S. J. Harvey, in *Proceedings of the 16th Matador Conference*, p. 275 (1976).
17. A. R. Mileham, R. M. Jones, and S. J. Harvey, *Production Points, Precis. Eng*, **4**, 168 (1982).
18. E. Rosset, M. Datta, and D. Landolt, *J. Appl. Electrochem.*, **20**, 69 (1990).
19. M. Datta and D. Landolt, *Electrochim. Acta*, **25**, 1263 (1980).
20. D. Landolt, *J. Electrochem. Soc.*, **119**, 708 (1972).
21. M. A. Bejar and F. Gutierrez, *J. Mater. Process. Technol.*, **37**, 691 (1993).
22. T. von Karman, *Z. Angew. Math. Mech.*, **1**, 244 (1921).
23. A. R. Brooks, C. R. Clayton, K. Doss, and Y. C. Liu, *J. Electrochem. Soc.*, **133**, 12 (1986).
24. G. Lorang, B. M. da Cunha, A. M. P. Simoes, and M. G. S. Ferreira, *J. Electrochem. Soc.*, **141**, 12 (1994).
25. D. D. MacDonald, *J. Electrochem. Soc.*, **139**, 3434 (1992).
26. S. Haupt and H. H. Strehblow, *Corros. Sci.*, **37**, 43 (1995).
27. R. Alkire and A. Cangellari, *J. Electrochem. Soc.*, **130**, 1252 (1983).
28. J. N. Harb, *J. Electrochem. Soc.*, **133**, 439C (1986).
29. T. R. Beck and S. G. Chan, *Corrosion (Houston)*, **37**, 665 (1981).
30. R. C. Alkire, D. B. Reise, and R. L. Sani, *J. Electrochem. Soc.*, **131**, 2795 (1984).